Multiscale Modeling of Blood Flow and Soft Matter

by

Dmitry A. Fedosov

Sc.M., Applied Mathematics, Brown University, USA, 2007
Sc.M., Aerospace Engineering, Pennsylvania State University, USA, 2004
B.S., Mathematics, Novosibirsk State University, Russia, 2002

Thesis

Submitted in partial fulfillment of the requirements for
the Degree of Doctor of Philosophy
in the Division of Applied Mathematics at Brown University

May 2010

Abstract of "Multiscale Modeling of Blood Flow and Soft Matter," by Dmitry A. Fedosov, Ph.D., Brown University, May 2010

This work presents multiscale modeling of blood flow and polymer suspensions which requires the use of heterogeneous modeling approaches. A hybrid method based on coupling the Molecular Dynamics (MD) method, the Dissipative Particle Dynamics (DPD) method, and the incompressible Navier-Stokes (NS) equations is developed and is called the Triple-Decker algorithm. MD, DPD, and NS are formulated in separate subdomains and are coupled via an overlapping region by communicating state information at the subdomain boundaries. The triple-decker algorithm is verified for several prototype flows such as Couette, Poiseuille, and lid-driven cavity flow.

A three-dimensional multiscale red blood cell (RBC) model is developed and is able to predict RBC mechanics, rheology, and dynamics in agreement with experiments. Based on an analytic theory, the modeled membrane properties can be uniquely related to the experimentally established RBC macroscopic properties without any adjustment of parameters. The developed model is applied to modeling infected RBCs in malaria where RBC membrane properties can dramatically change. Blood flow is simulated in microtubes for different diameters and hematocrit values. The blood flow model captures the well-known Fahraeus and Fahraeus-Lindquist effects and cell-free layers measured in experiments. Blood flow in malaria is characterized by the adhesion of infected RBCs to the vascular endothelium. The adhesive dynamics of infected RBCs in malaria is simulated based on the stochastic bond formation/dissociation model and compares well with experimental observations.

Depletion layers in dilute polymer solutions in micro- and nano-channels are investigated for various conditions and compare well with the asymptotic lattice theory solution of depletion near a repulsive wall. In Poiseuille flow, polymer migration across the streamlines results in two symmetric off-center peaks in the center-of-mass distribution which identify the preferred chain positions across the channel. Steady state rheological properties of semi-dilute polymer solutions and melts are obtained with the Reverse Poiseuille flow (RPF) which is demonstrated to be an accurate and convenient virtual rheometer for complex fluids. For isothermal solutions the material functions satisfy the principle of time-concentration superposition, while for undiluted chains the temperature dependence is reconciled by the principle of time-temperature superposition.

This dissertation by Dmitry A. Fedosov is accepted in its present form
by the Division of Applied Mathematics as satisfying the
dissertation requirement for the degree of Doctor of Philosophy

Date........................ ....
Professor George Em Karniadakis, Director

Recommended to the Graduate Council

Date........................ ....
Professor Bruce Caswell, Reader

Date........................ ....
Professor Martin Maxey, Reader

Approved by the Graduate Council

Date........................ ....
Sheila Bonde
Dean of the Graduate School

The Vita of Dmitry A. Fedosov

Education

- Sc.M. Applied Mathematics, Brown University, USA, 2007.
- Sc.M. Aerospace Engineering, Pennsylvania State University, USA, 2004.
- Sc.B. Mathematics with Honors, Novosibirsk State University, Russia, 2002.

Awards and fellowships

- Simon Ostrach fellowship, Brown University, 2009.
- Academic fellowship, Brown University, 2004.

Publications

Articles in peer-reviewed journals

1. D. A. Fedosov, B. Caswell and G. E. Karniadakis, *"A multiscale red blood cell model with accurate mechanics, rheology, and dynamics"*, Biophysical Journal (submitted, 2009).
2. D. A. Fedosov, B. Caswell and G. E. Karniadakis, *"Systematic coarse-graining of spectrin-level red blood cell models"*, Computer Methods in Applied Mechanics and Engineering, (submitted, 2009).
3. D. A. Fedosov, B. Caswell and G. E. Karniadakis, *"Steady Shear Rheometry of DPD models of Polymer Fluids in Reverse Poiseuille Flow"*, Journal of Chemical Physics, (submitted, 2009).
4. D. A. Fedosov and G. E. Karniadakis, *"Triple-Decker: Interfacing Atomistic-Mesoscopic-Continuum Flow Regimes"*, Journal of Computational Physics, 228(4), 1157-1171, 2009.
5. W. Pan, D. A. Fedosov, B. Caswell and G. E. Karniadakis, *"Hydrodynamic Interactions for Single DPD Particles, and their Clusters and Filaments"*, Physical Review E, 78(4), 046706, 2008.

6. D. A. Fedosov, B. Caswell and G. E. Karniadakis, *"DPD Simulation of Depletion Layer and Polymer Migration in Micro- and Nano-Channels for Dilute Polymer Solutions"*, Journal of Chemical Physics, 128(14), 144903, 2008. Selected for publication in Virtual Journal of Nanoscale Science & Technology, 17(17), April 28 2008.

7. D. A. Fedosov, I. V. Pivkin and G. E. Karniadakis, *"Velocity Limit in DPD Simulations of Wall-Bounded Flows"*, Journal of Computational Physics, 227(4), 2540-2559, 2008.

8. A. A. Alexeenko, D. A. Fedosov, D. A. Levin, S. F. Gimelshein, and R. J. Collins, *"Transient Heat Transfer and Gas Flow in a MEMS-based Thruster"*, Journal of Microelectromechanical Systems, 15(1), 181-194, 2006.

9. A. A. Alexeenko, D. A. Fedosov, D. A. Levin, S. F. Gimelshein, and R. J. Collins, *"Performance Analysis of Microthrusters Based on Coupled Thermal-Fluid Modeling and Simulation"*, Journal of Propulsion and Power, 21(1), 95-101, 2005.

10. T. Ozawa, D. A. Fedosov, D. A. Levin, S. F. Gimelshein, *"Quasi-Classical Trajectory Modeling of OH Production in Direct Simulation Monte Carlo"*, Journal of Thermophysics and Heat Transfer, 19(2), 235-244, 2005.

Articles in conference proceedings

1. D. A. Fedosov, B. Caswell and G. E. Karniadakis, *"Multiscale modeling of blood flow in cerebral malaria"*, Proceedings of ASME 2010 First Global Congress on NanoEngineering for Medicine and Biology, NEMB, 2010.

2. D. A. Fedosov, B. Caswell and G. E. Karniadakis, *"Coarse-Grained Red Blood Cell Model with Accurate Mechanical Properties, Rheology and Dynamics"*, Proceedings of the Engineering in Medicine and Biology Society, EMBC, 2009 Annual International Conference of the IEEE, 2009.

3. D. A. Fedosov, B. Caswell and G. E. Karniadakis, *"Dissipative Particle Dynamics Simulation of Polymer- and Cell-Wall Depletion in Micro-Channels"*, Proceedings of the XV International Congress on Rheology: The Society of Rheology 80th Annual Meeting, AIP Conference Proceedings, 1027(1), 612-614, 2008.

4. D. A. Fedosov, B. Caswell and G. E. Karniadakis, *"Reverse Poiseuille Flow: the Numerical Viscometer"*, Proceedings of the XV International Congress on Rheology: The Society of Rheology 80th Annual Meeting, AIP Conference Proceedings, 1027(1), 1432-1434, 2008.

5. D. A. Fedosov, S. V. Rogazinsky, M. I. Zeifman, M. S. Ivanov, A. A. Alexeenko, and D. A. Levin, *"Analysis of Numerical Errors in the DSMC Method"*, Proceedings of the Rarefied Gas Dynamics: 24th International Symposium on Rarefied Gas Dynamics, AIP Conference Proceedings, 762(1), 589-594, 2005.

6. T. Ozawa, D. A. Fedosov, and D. A. Levin, *"Modeling of OH Product Distributions Using QCT-MD and BL Models in a Bow Shock"*, Proceedings of the Rarefied Gas Dynamics: 24th International Symposium on Rarefied Gas Dynamics, AIP Conference Proceedings, 762(1), 902-907, 2005.

7. T. Ozawa, D. A. Fedosov, D. A. Levin, and S. F. Gimelshein, *"Use of Quasi-Classical Trajectory Methods in the Modeling of OH Production Mechanisms in DSMC"*, AIAA Paper 2004-0336, 42nd AIAA Aerospace Sciences Meeting, 2004.

8. A. A. Alexeenko, D. A. Levin, D. A. Fedosov, S. F. Gimelshein, and R. J. Collins, *"Coupled Thermal-Fluid Modeling of Micronozzles for Performance Analysis"*, AIAA Paper 20034717, 39th AIAA/ASME/SAE/ASEE Joint Propulsion Conference and Exhibit, 2003.

9. A. A. Alexeenko, D. A. Levin, D. A. Fedosov, S., F. Gimelshein, R. J. Collins, *"Coupled Thermal-Fluid Analyses of Microthruster Flows"*, AIAA Paper 20030673, 41st Aerospace Sciences Meeting and Exhibit, 2003.

Book chapters

1. D. A. Fedosov, B. Caswell and G. E. Karniadakis, Dissipative particle dynamics modeling of red blood cells, in *"Computational Hydrodynamics of Capsules and Cells"* edited by C. Pozrikidis, Chapman & Hall/CRC (in press, 2009).

Conference presentations

1. 62^{nd} Annual Meeting of the APS Division of Fluid Dynamics, *"Multiscale modeling of blood flow in cerebral malaria"*, Minneapolis, MN (November 2009).

2. 81st Annual Meeting of The Society of Rheology, *"A numerical simulation study of rheology and dynamics of healthy red blood cells and parasitized by Plasmodium falciparum"*, Madison, WI (October 2009).

3. 31st Annual International Conference of the IEEE Engineering in Medicine and Biology Society, *"Coarse-Grained Red Blood Cell Model with Accurate Mechanical Properties, Rheology and Dynamics"*, Minneapolis MN (September 2009).

4. 5th International Workshop on Meshfree Methods for Partial Differential Equations, *"Triple-Decker: Interfacing Atomistic-Mesoscopic-Continuum Flow Regimes"*, Bonn, Germany (August 2009).

5. 10th US National Congress on Computational Mechanics, *"Multiscale Modeling of Blood Flow in Cerebral Malaria"*, Columbus, OH (July 2009).

6. SIAM Conference on Computational Science and Engineering, *"Multiscale Modeling in Complex Fluids and Soft Matter"*, Miami, FL (March 2009).

7. SIAM Conference on Computational Science and Engineering, *"Unsteady 3D Flow Simulations in Cranial Arterial Tree"*, Miami, FL (March 2009).

8. SIAM Conference on the Life Sciences, *"Triple-Decker: Interfacing Atomistic-Mesoscopic-Continuum Flow Regimes in Biological Fluids"*, Montreal, QC Canada (August 2008).

9. 79th Annual Meeting of The Society of Rheology, *"DPD simulation of depletion layer and polymer migration in micro- and nano-channels for dilute polymer solutions"*, Salt Lake City, UT (October 2007).

10. 3rd International Conference for Mesoscopic Methods in Engineering and Science, *"Reynolds number limit in DPD simulations of wall-bounded flows"*, Hampton, VA (July 2006).

To my family:
my parents Larisa and Anatoly,
my wife Kathrin,
my daughter Maria,
and my brother Vladimir.

Acknowledgments

I would like to thank my advisor, Professor George Em Karniadakis, for his guidance and support during my PhD studies at Brown University. I am also very thankful to him for providing a virtually unlimited access to supercomputer resources and for excellent opportunities to visit scientific conferences to present our research.

I would like to thank my co-advisor, Professor Bruce Caswell, for his guidance and expert advice. He made an indispensable contribution to my understanding and knowledge of the fields of rheology and complex fluids.

I am grateful to Professor Martin Maxey for being on my thesis committee, reading through my research, and providing useful feedback and suggestions.

I would like to express my gratitude to all faculty members of the Division of Applied Mathematics for their scientific advice and the great courses offered in the division. I also thank the staff of the division for their tremendous help in any paperwork and division activities.

My gratitude is extended to all present and past CRUNCH group members and friends for numerous interesting discussions on scientific and private matters and for sharing their experience. I also thank them for a friendly and collaborative environment in the group.

I would like to acknowledge the funding support which made the research presented in this thesis possible:

- NIH grant R01HL094270,
- NSF grant CBET-0852948,
- NSF grant DUE-0734234,
- NSF grant OCI-0636336,
- NSF grant DMS-0510799,
- ONR grant N00014-04-0007.

Last but certainly not least, I would like to express my deepest gratitude to my family. My parents, Larisa and Anatoly, and my brother, Vladimir, have unconditionally supported me throughout all these years. They never questioned my choice to study in the USA

so far from home. I thank my wife Kathrin for her love and tremendous support and encouragement during the five years at Brown University. She was also patient enough to read through my thesis. My daughter Maria, who was born just several months ago, gave me a lot of joy and smiles while simultaneously writing the thesis and babysitting her.

Contents

List of Tables

List of Figures

Chapter 1

Introduction

Understanding natural phenomena as well as modern biomedical and engineering applications requires research across multiple disciplines with the simultaneous use of experiments, theories, and numerical simulations. Multiscale modeling is an interdisciplinary rapidly developing area with its applications in various fields such as engineering, physics, biology, medicine, etc. Many realistic problems require accurate modeling across several orders of magnitude in spatiotemporal scales. Examples include the Physiome Project [3], blood circulation and hemorheology [160], cytoadhesion in malaria [36, 11] and in inflammation processes [185, 125], and polymer melts and solutions [43]. Such multiscale applications often necessitate simultaneous modeling of a certain level of microscopic or mesoscopic details with a surrounding macroscopic flow.

Classical numerical methods are limited in their applications to certain ranges of space and time scales. Atomistic methods such as the Molecular Dynamics (MD) and the Monte Carlo (MC) techniques provide a detailed system description on the level of a single atom; however such simulated systems are restricted to very small sizes and times on the order of nanometers and nanoseconds due to a demanding computational expense. Mesoscopic approaches such as Dissipative Particle Dynamics (DPD) [105, 92], the Lattice Boltzmann method (LBM) [187], Brownian dynamics (BD) [62, 171], and Smoothed Particle Hydrodynamics (SPH) [12, 195] provide a "coarse-grained" description of a simulated system with respect to an atomistic representation by retaining some molecular details which are required to capture the physics of that system. They allow for a significantly expanded range of simulated space and time scales in comparison with atomistic methods, but their upper limit in spatiotemporal scales remains and depends on the level of coarse-graining used. Larger space and time scales are accessible by continuum approaches such as the Navier-Stokes (NS) equations. These methods rely on the continuum assumption and are likely to fail when molecular details of a simulated system are of physical importance.

Hybrid multiscale algorithms attempt to merge several existing methods that cover different ranges of space and time scales. They may offer a potential solution for bridging between various spatiotemporal scales. Several recently developed hybrid methods include MD-NS coupling [151, 148, 44, 93, 207], and MD-LBM [84, 55]. Such algorithms undergo constant developments and improvements; however, up to date, they are substantially restricted in their applications. Thus, current hybrid algorithms are able to adequately simulate some Newtonian fluid flows, while efficient multiscale approaches for flows of complex and biological fluids which are of great interest are yet to be developed.

Our contribution to the development of hybrid multiscale approaches is the triple-decker algorithm which bridges all three levels of descriptions, namely atomistic via MD, mesoscopic via DPD, and continuum via NS. It is based on the domain decomposition framework and allows for an efficient decoupling of space and time scales. Currently, the triple-decker algorithm is proved to accurately simulate steady flows of Newtonian fluids.

Nevertheless, the major part of this work is devoted to a development of a multiscale red blood cell (RBC) model which is then applied to blood flow modeling under healthy conditions and in malaria disease. In addition, soft matter systems such as dilute and semi-dilute polymer solutions and melts are investigated for various flow conditions. These models may further be incorporated into the triple-decker algorithm framework to enable hybrid simulations of complex and biological fluid flows.

1.1 Blood flow

Blood is a concentrated suspension containing RBCs or erythrocytes, white blood cells (WBCs) or leukocytes, platelets, and blood plasma with a number of suspended macromolecules and chemical elements. The blood volume fraction of RBCs is approximately 45%, of WBCs below 1%, while the rest of the volume roughly consists of the Newtonian-like plasma. Thus, RBCs yield the most contribution to the non-Newtonian characteristics of blood such as shear-dependent viscosity and non-zero normal stress differences.

Blood flow is the main mechanism for the transport of oxygen, nutrients, waste products, molecules, and cells which are vital for the functioning of the whole organism. Changes in normal blood flow circulation which occur in many blood related diseases and disorders such as malaria, sickle cell anemia, and diabetes may lead to serious organism malfunctioning or death. Blood flow features under healthy conditions and in various diseases and disorders can provide indispensable information for understanding many biological processes and for the development of new efficient drugs and treatments. This has motivated an enormous scientific effort in blood flow modeling.

Blood flowing in large vessels with a characteristic diameter greater than approximately 1 mm is often modeled as a Newtonian fluid with a constant viscosity due to the high shear rates in such vessels [31]. However, in vessels with a diameter smaller than 1 mm non-Newtonian properties of blood are likely to be of importance in blood flow modeling [211]. In this regime, continuum modeling of blood flow may still provide a good approximation for vessel diameters larger than about $100 - 200$ μm if an appropriate non-Newtonian fluid model is used. Nonetheless, continuum modeling of blood flow in vessels of diameters smaller than 100 μm is not adequate and requires explicit modeling of RBCs.

RBCs are highly deformable, non-nucleated biconcave discs with a diameter of approximately 8 μm and a thickness of 2 μm. RBC deformability is the main factor which allows them to pass through very narrow capillaries with a diameter as small as 3 μm. Therefore, this property has to be incorporated in simulations in order to accurately reproduce blood flow in microcirculation. Due to persistent computational challenges many of the developed RBC models are two-dimensional [188, 162, 15]. These models can provide relevant qualitative information about the blood flow in microcirculation; however, their quantitative predictions are likely to be unreliable since realistic RBCs are inherently three-dimensional. Several three-dimensional models of RBCs were recently developed [150, 53, 159]. Nonetheless, their use in blood flow modeling is limited due to the computational expense such that the maximum number of simulated RBCs is on the order of $O(10^2)$. In addition, some adjustable parameters have to be chosen for these models.

The multiscale RBC model developed in this work is constructed as a network of springs and incorporates realistic mechanical and rheological properties measured in experiments [190, 167]. The model parameters are computed based on a semi-analytic analysis of membrane network deformations which completely eliminates the adjustment of model parameters. The RBC model is able to accurately describe the mechanics, rheology, and dynamics of healthy RBCs and RBCs in malaria. Blood flow is simulated in microtubes and in microfluidic devices with characteristic sizes up to 100 μm. The developed parallel code allows for efficient simulations of RBC suspensions with $O(10^4)$ RBCs.

Blood flow in malaria is significantly affected by an increased membrane stiffness of RBCs infected by Plasmodium (Pf) parasites and their cytoadherence to vascular endothelium [23, 140, 190]. The developed blood flow model is used to quantify an increase in blood flow resistance in malaria compared with that under healthy conditions. In addition, an adhesive dynamics model is introduced to capture the adherence of Pf-parasitized RBCs to ligand-coated walls found in experiments [11].

1.2 Soft matter

Soft matter includes a variety of materials whose physical characteristics are comparable with thermal fluctuation forces such that they undergo active thermal motion. Complex and non-Newtonian fluids are examples of *soft matter* which includes physical systems such as polymers, colloids, foams, gels, some biomaterials, etc. A strong interest in such materials is driven by the fact that they yield a wide range of physical properties depending on various conditions such as local flow characteristics and temperature. Many soft matter materials show intermediate behavior between solids and simple Newtonian liquids, while their behavior can drastically change even at a modest deformation.

Behavior of soft matter materials is not always dictated by their atomic or molecular structure, because some physical arrangements may be formed on a mesoscopic level which may influence macroscopic properties of such materials. Therefore, simulations of soft matter materials often require multiscale resolution of physical processes which occur at the mesoscale. Detailed atomistic modeling is computationally too expensive to be able to resolve physics at the mesoscale, while continuum methods do not consider any structures at the mesoscale due to the continuum assumption. This has motivated the development of efficient mesoscopic methods such as DPD, LBM, BD, and SPH.

We employ the DPD method for modeling dilute and semi-dilute polymer solutions, melts, as well as RBCs and blood flow discussed above. DPD is a particle mesoscopic method where each particle corresponds to a cluster of molecules moving together in a Lagrangian fashion subject to soft potentials. In contrast to the MD method, DPD employs much larger time steps and particle sizes because of the soft particle interactions. In particular, the DPD method appears to be successful in simulations of complex fluids, such as suspensions of polymers, DNA, colloids, and cells [91, 193, 73].

Dilute polymer solutions are modeled in micro- and nano-channels. Polymer depletion layers and polymer migration in Poiseuille flow are investigated using the bead-spring model in the DPD method. A new efficient method which can be used to obtain steady state rheological properties of a simulated material is developed and applied to semi-dilute polymer solutions and melts. Rheometry of materials often utilizes a variety of experimental techniques in order to obtain reliable rheological measurements over a wide range of flow characteristics, concentrations, and temperatures. In contrast, only a few methods in numerical rheometry are available and hence, further development is needed. The proposed method for steady-state, rheological measurements is an alternative method in numerical rheometry. It allows one to expand the range of measured rheological properties in simulations and provides additional confirmation for the accuracy of existing methods in numerical rheometry.

1.3 Dissertation outline

In this section an outline of the thesis is provided along with a short description of the research work performed in each chapter.

Chapter 2: The triple-decker algorithm for coupling atomistic, mesoscopic, and continuum flow regimes. It includes

- the MD-DPD-NS coupling algorithm and descriptions of these methods,
- modeling of non-periodic boundary conditions such as inflow and outflow for MD and DPD methods,
- Couette and Poiseuille flow simulations with MD-DPD-NS coupling across them,
- the lid-driven square cavity flow using all three levels of descriptions,
- the treatment of the cavity corner singularity in the NS method by simulating the cavity corner with DPD,

- an algorithm modification which allows zero overlapping thickness among coupled subdomains in special cases,
- Couette flow for immiscible fluid layers with different viscosities.

Chapter 3: A three-dimensional multiscale RBC model which captures realistic mechanical and rheological properties, and dynamics. The developed model is used to simulate RBCs under healthy conditions and in malaria disease. This chapter contains

- four RBC models with different spring definitions,
- a theoretical analysis of the membrane properties which eliminates the adjustment of model parameters,
- a method for modeling membrane viscosity to render RBC membrane viscoelastic properties,
- membrane-solvent no-slip boundary conditions which allow for separate internal/external solvents through dynamic bounce-back reflections of fluid particles on the RBC membrane,
- RBC modeling on a spectrin level ($N_v \sim 27000$) and highly coarse-grained RBCs represented with several hundred vertices,
- RBC stretching simulations in comparison with optical tweezers experiments [190],
- a stress-free RBC model which eliminates artifacts due to surface triangulation,
- a comparison of a single spring extension of the spectrin-level RBC model with the spectrin extension obtained in coarse-grained MD simulations [142],
- mechanical properties of infected RBCs in malaria,
- rheological properties of healthy and Pf-parasitized RBCs obtained with twisting torque cytometry in comparison with optical magnetic twisting cytometry in experiments [167, 133],
- the rheology of healthy and Pf-parasitized RBCs through measurements of membrane thermal fluctuations in comparison with experiments [10, 158],

- simulations of the RBC creep test and recovery,
- the dynamics of RBCs in shear flow, tumbling and tank-treading behavior,
- the dynamics of RBCs in Poiseuille flow in a tube of 9 μm diameter and transition to parachute shape.

Chapter 4: Blood flow modeling under healthy conditions and in malaria, and adhesive dynamics of leukocytes and Pf-parasitized RBCs. The chapter includes

- blood flow in microtubes of various tube diameters for different hematocrit values,
- blood flow velocity profiles and RBC density distributions,
- the Fahraeus effect,
- the Fahraeus-Lindquist effect,
- cell-free layers in blood flow,
- increased resistance of blood flow in malaria,
- blood flow in a microchannel with a constriction for different constriction lengths and widths, viscosities of the suspending medium, RBC membrane rigidities, and hematocrit values,
- an adhesive dynamics model based on the stochastic bond formation/dissociation,
- various states of adhesive dynamics of leukocytes in shear flow,
- the adhesive dynamics of Pf-parasitized RBCs in comparison with that on ICAM-1 and on mammalian CHO cells found in experiments [11],
- the effect of membrane properties on RBC adhesive dynamics,
- the influence of a rigid parasite inside RBCs on their adhesive dynamics in shear flow,
- the adhesion of Pf-parasitized RBCs in a rectangular microflow chamber.

Chapter 5: Modeling of depletion layer and polymer migration in micro- and nanochannels for dilute polymer solutions. It contains

- polymer models and DPD boundary conditions,

- depletion layers depending on the polymer model, quality of the solvent, wall-polymer interactions, channel width, and the number of monomers representing the polymer,
- a comparison of simulated depletion layers with the analytic solution for an ideal chain [58],
- shape characteristics of polymers across the channel,
- polymer migration in Poiseuille flow for different Pe and Re numbers,
- polymer shapes in Poiseuille flow,
- polymer migration in solvents of different quality.

Chapter 6: Reverse Poiseuille flow (RPF) - a steady state numerical rheometer for complex and non-Newtonian fluids. This chapter includes

- a RPF method description,
- steady state rheological measurements such as the shear dependent viscosity and the first and second normal stress coefficients,
- rheological properties of mono-disperse polymer melts,
- rheological properties of semi-dilute polymer solutions,
- the time-concentration superposition for polymer solutions,
- the time-temperature superposition principle for polymer melts and a consistent DPD model to satisfy this principle.

We conclude in chapter 7 with brief remarks. In addition, the thesis contains several appendices. Appendix A presents the derivation of RBC nodal forces from the energies defined in chapter 3. Appendix B includes mathematical details of the analysis of the macroscopic properties of a hexagonal network, while appendix C describes reflections of solvent particles at moving triangular faces on the RBC surface required for membrane-solvent boundary conditions. Appendices D and E contain brief manuals that instruct how to construct initial conditions for simulations and how to run the developed code.

Chapter 2

Triple-Decker: Interfacing Atomistic-Mesoscopic-Continuum Flow Regimes

2.1 Introduction

As mentioned in the thesis introduction 1 fluid flow modeling on an atomistic level via Molecular Dynamics (MD) or Monte Carlo (MC) methods is extremely limited due to large computational cost. At much larger scales than those at the atomistic or molecular level a continuum assumption is valid, and continuum approaches (e.g., Navier-Stokes (NS) equations) for fluid flows are used. However, between atomistic and continuum scales lies an intermediate range called *mesoscopic*, which exhibits features of both, the atomistic and the continuum regimes. It covers a range, where the continuum description is not yet appropriate, and the atomistic representation is not feasible due to a system size. Figure 2.1 shows a schematic plot of length and time scales corresponding to different regimes. The overlaps between the rectangles indicate that there are no definite borders between the neighboring descriptions. However, gaps between some of the regimes are apparent; for example between the atomistic and the continuum.

To bridge the existing gaps, multiscale hybrid approaches have to be developed to provide a unified description from nanoscales to larger scales. The majority of existing multiscale methods [151, 81, 148, 44, 93, 207, 204] attempt to "glue" together atomistic and

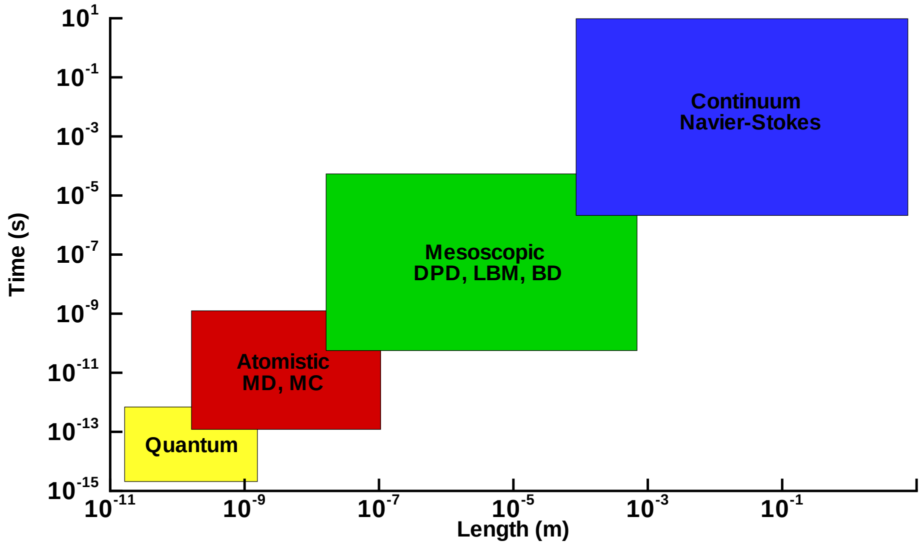

Figure 2.1: A schematic plot of various spatiotemporal scales covered by different descriptions (quantum, microscopic, mesoscopic, and continuum) with several examples of typical methods used.

continuum approaches corresponding to MD and NS, respectively. Remarkably, the mesoscopic level is simply omitted in the atomistic/continuum paradigm. Over the last decade, there has been great progress in developing efficient numerical methods for the mesoscopic regime; the examples are the Lattice Boltzmann method (LBM) [187], the Dissipative Particle Dynamics (DPD) [105, 92], and the Smoothed Particle Hydrodynamics (SPH) [12, 195]. A few attempts have been made recently to couple atomistic and mesoscopic descriptions directly, specifically MD and LBM [84, 55]. However, to the best of our knowledge, there is no published hybrid atomistic-mesoscopic-continuum method for multiscale flow phenomena, which would combine the advantages of all three levels of description.

There are two main coupling approaches:

1. The *flux-exchange* method [151, 81, 148, 44] is based on the flux exchange between continuum and particle domains.
2. The *state-exchange* method [93, 207, 204, 84, 55] is based on the alternating Schwarz method [182].

More specifically, the flux-exchange method is based on the direct exchange of flux information in the overlap domain between the particle region and the continuum region, and relies on the matching of fluxes of mass, momentum and energy. In the state-exchange method the state information between the particle simulation and the NS equations is transferred through an overlap region where the particles' dynamics is constrained; the constrained dynamics is often imposed via a dynamic relaxation technique [204]. The alternating Schwarz method is used to solve sequentially the problems in the continuum and atomistic domains, and state exchange is performed until convergence is achieved. The main difficulty here is the extraction and imposition of the required state information in particle-based methods. The extraction of the mean flowfield properties requires sampling of flow characteristics over some region and often over a time interval. This fact makes the application of the flux-exchange model difficult and favors the alternating Schwarz method. However, the Schwarz method appears to be more restrictive in the case of dynamic simulations of unsteady flows.

The choice of a particular multiscale algorithm depends strongly on the flow problem. Several algorithm characteristics (e.g., performance, applicability, robustness) may be considered. The main requirement for all available algorithms is conservation of mass, momentum and energy. For instance, conservation of momentum and energy in particle-based methods is often imposed on average and is not satisfied at every fixed point of time. The applicability of a particular algorithm may be restricted, for example, to steady flows as well as to a certain range of flow regimes. The algorithm robustness includes the ability of the hybrid method to efficiently decouple length and time scales. Both of the aforementioned coupling approaches lead to a reasonably good decoupling of spatial scales. However, the state-exchange method enables less restrictive temporal coupling than the flux-exchange method. Here, we employ the state-exchange method for coupling atomistic, mesoscopic, and continuum formulations.

In this chapter we describe the triple-decker algorithm, which couples atomistic, mesoscopic, and continuum formulations. Details of atomistic modeling via MD, mesoscopic via DPD, and continuum via NS are given. Simulation results of the triple-decker algorithm for Couette, Poiseuille and lid-driven cavity flows are presented. Finally, we conclude with a brief discussion.

2.2 Triple-Decker algorithm

In this section we describe the coupling mechanism. The hybrid coupling technique used here is based on a domain decomposition similar to the Schwarz alternating method [182]. The flow domain is decomposed into three (or potentially more) overlapping regions: an atomistic region described by MD, a mesoscopic region described by DPD, and a continuum region represented by spectral element discretization of the incompressible NS equations.

A schematic of the domain decomposition (left) and the time progression (right) is shown in figure 2.2. Each subdomain is subject to Dirichlet velocity boundary conditions (BCs).

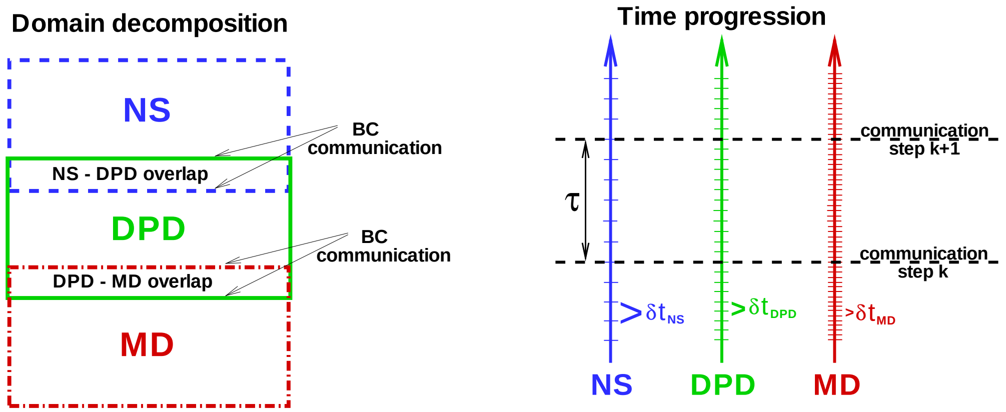

Figure 2.2: A schematic of the MD-DPD-NS domain decomposition (left) and the time progression (right).

The integration in each region is performed independently, and coupling among different subdomains is done through BC communications. As an example, in figure 2.2 BCs for the DPD region will be provided from both MD and NS regions, and in turn, BCs for the MD and NS subdomains will be extracted from the DPD region. The communication with necessary BCs information among subdomains is done every τ in time progression as shown in figure 2.2 (right). Note that the time τ between two successive communications may correspond to a different number of time steps for the three descriptions. For instance, figure 2.2 (right) shows the smallest time step δt_{MD} chosen for the MD simulation, a larger δt_{DPD} for DPD, and the largest time step δt_{NS} for the Navier-Stokes formulation, which illustrates an effective temporal decoupling. In addition, the time interval τ can be manually set and potentially changed during simulation depending on the flow development, i.e., prescribe small τ for transient flow and larger τ for steady state. There are many possible communication patterns which can be used for the simulation progressing in time. Figure 2.3 presents the sequential communication pattern among the subdomains. Hence, the time integration can be performed in the chosen order such that one subdomain is advanced during τ, BCs are passed to the second subdomain, and in turn the second subregion is integrated during τ, and so forth. As an alternative, one could run all the subdomains simultaneously and carry out BCs communications every τ. The algorithm allows one to freely select subdomain dimensions (e.g., length, width), timestep for integration and, if needed, fluid properties (e.g., viscosity for multi-layer fluid), because the subdomains are integrated separately and are coupled only through BCs.

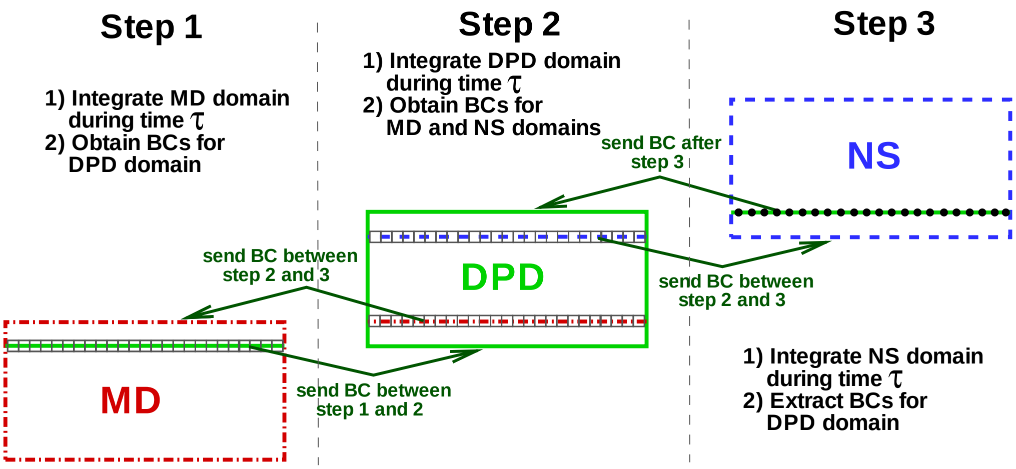

Figure 2.3: A sample communication pattern for the MD-DPD-NS coupling. Sequential integration of the subdomains.

An extraction of BCs from particle subdomains such as MD and DPD involves *velocity averaging*. A number of cells is present along the line of interest, where the local velocity field is sampled, and the averaging is carried out during a number of timesteps. However, one has to be aware of the associated statistical error E_v, which depends on the number of samples M_v, the corresponding cell average $\bar{v}$ and standard deviation $\sigma(v)$ of desired flow properties. Hadjiconstantinou et al. [94] obtained an *a priori* estimate for the number of samples M_v required to measure the average of velocities in a cell of volume V for fixed error E_v, as follows

$$M_v = \frac{k_B T}{\bar{v}^2} \frac{1}{\bar{\rho} V E_v^2}, \tag{2.1}$$

where $\bar{\rho}$, T and k_B are the average density, temperature and Boltzmann constant, respectively. Note that one sample ($M_v = 1$) corresponds to the averaging over $\bar{n}V = \frac{\bar{\rho}}{m}V$ particle velocities or over all particles in volume V during a single time step, where $\bar{n}$ is the average number density and m is the particle mass. This formula provides the correct estimate assuming that the samples are statistically independent, which is generally not valid for MD and DPD fluids if sampling is performed every timestep. If the samples are correlated, the number of samples required to estimate the average of velocity is equal to

$$M_v^c = 2\frac{\tau_v}{\delta t}M_v, \tag{2.2}$$

where τ_v is the autocorrelation time [109]. The autocorrelation time is proportional to the fluid self-diffusion coefficient D because of the Green-Kubo relation: $D = \frac{1}{3}\int_0^\infty A_v(t)dt$, where $A_v(t)$ is the velocity autocorrelation function defined as $A_v(t) = Ce^{-t/\tau_v}$, where C is a constant. We have used the above equations in order to determine the number of samples required to keep the error E_v below 5%.

2.2.1 Atomistic region via Molecular Dynamics

The atomistic region is necessary in flow parts where the continuum formalism breaks down or where atomistic level physics needs to be captured. We model the atomistic subdomain using MD, but in combination with the DPD thermostat [105, 92]. Next, we describe the MD method and the imposition of BCs.

2.2.1.1 MD governing equations with DPD thermostat

The molecular dynamics system consists of N point particles of mass m_i, position $\mathbf{r}_i$ and velocity $\mathbf{v}_i$. The particles evolve according to Newton's second law of motion

$$d\mathbf{r}_i = \mathbf{v}_i dt, \qquad d\mathbf{v}_i = \frac{1}{m_i}\sum_{j\neq i}(\mathbf{F}_{ij}^{LJ}dt + \mathbf{F}_{ij}^{D}dt + \mathbf{F}_{ij}^{R}\sqrt{dt}), \tag{2.3}$$

where $\mathbf{F}_{ij}^{LJ} = \nabla U(r_{ij})$ are Lennard-Jones interparticle forces and $\mathbf{r}_{ij} = \mathbf{r}_i - \mathbf{r}_j$, $r_{ij} = |\mathbf{r}_{ij}|$. $\mathbf{F}_{ij}^{D}$ and $\mathbf{F}_{ij}^{R}$ are dissipative and random forces, which define the DPD thermostat described in the DPD method, see section 2.2.2. Soddemann et al. [184] showed that it is advantageous to use the DPD thermostat in MD as it is completely local and allows *longer timesteps* compared to conventional thermostats without sacrificing accuracy. The Lennard-Jones potential is given by

$$U(r_{ij}) = 4\epsilon \left[\left(\frac{\sigma_{MD}}{r_{ij}} \right)^{12} - \left(\frac{\sigma_{MD}}{r_{ij}} \right)^{6} \right], \tag{2.4}$$

where ϵ and σ_{MD} are energy and length characteristic parameters, respectively. All interactions vanish beyond a *cutoff radius* r_c. The equations of motion were integrated using the modified velocity-Verlet algorithm [92].

2.2.1.2 MD for non-periodic systems

Here we describe a model which imposes non-periodic BCs in MD. Two main issues are considered: (i) correct imposition of local velocity at the boundary, and (ii) control of local disturbance effect on density, pressure and temperature.

Figure 2.4 shows a schematic boundary conditions with the involved forces used for particle methods. An enforcement of local velocity at the boundary is subdivided into imposition of the normal v_n and the tangential v_t components of velocity. The tangential component of velocity at the boundary is enforced through an *adaptive shear force* (see figure 2.4): each particle with distance $h < r_c$ from the boundary is subject to a tangential force $F_t^k(h)$ depending on the distance h. The force is defined as

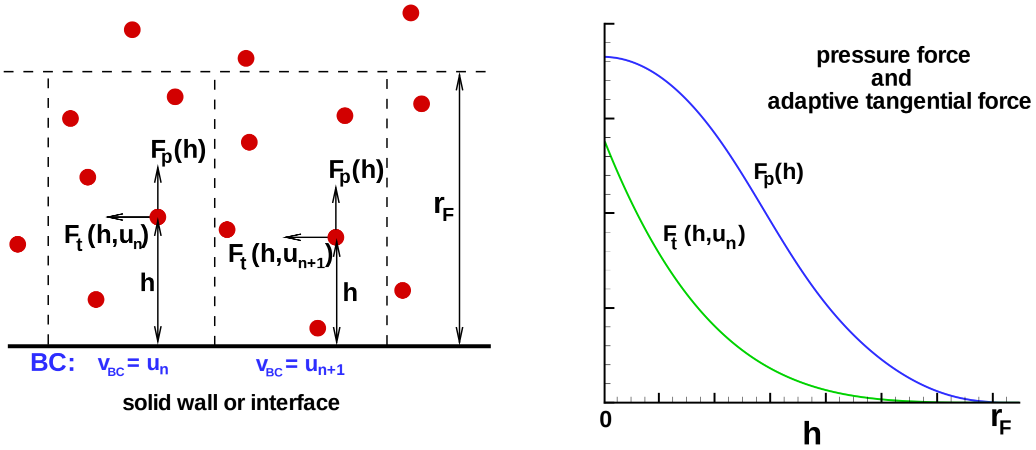

Figure 2.4: A schematic of boundary conditions used in particle methods such as MD and DPD (left). The sample profiles of the pressure and adaptive tangential forces (right).

$$F_t^k(h) = C_k(\Delta v_t) w(h), \tag{2.5}$$

where k is the iteration number, $C_k(\Delta v_t)$ is an adaptive force *strength* and $w(h)$ is a *weight function* defined as $w(h) = (1 - \frac{h}{r_c})^4$. The adaptive force strength is calculated iteratively as $C_{k+1} = C_k + \alpha \Delta v_t$, where α is a *relaxation parameter* which can be set to a constant value similar to [151] or calculated adaptively as proposed in [204]. In this work we set the relaxation parameter to $\alpha = 1.0$, but future work will incorporate a dynamic approach. Here, we define $\Delta v_t = v_t^{BC} - v_t^{est}$ with v_t^{BC} the assigned velocity at the boundary and v_t^{est} an estimated flow velocity at the boundary. The near-boundary velocity profile is estimated by local cell averaging of particle velocities during every m time steps. Next, v_t^{est} is calculated by extrapolation from the estimated near-boundary velocity profile, and recalculation of the adaptive shear force is performed. Here, we employ a first-order extrapolation based on two points in the near-boundary region. In general, higher order extrapolation can be implemented, however it requires estimation of larger number of points in the near-boundary velocity profile. After a number of iterations, we find that $\Delta v_t \simeq 0$, so that C_k and $F_t^k(h)$ converge to a constant value, which leads to the proper tangential BC velocity $v_t = v_t^{BC}$.

Imposition of the normal velocity component v_n is carried out by *particle insertions and reflections* similarly to [207]. Particles that strike the boundary are *specularly* reflected in a frame of reference attached to the moving boundary. The collision time is calculated as $t' = (x^k - x_{BC})/(v_{BC} - v^k)$, where x_{BC} and v_{BC} are the boundary position and the boundary speed, and x^k and v^k are the position and the normal velocity of a particle. If a particle crosses the boundary ($0 \leq t' \leq \delta t_{MD}$) during one time step, a new particle velocity and position are computed according to the following equations

$$v^{k+1} = 2v_{BC} - v^k, \qquad x^{k+1} = x^k + t'v^k + (\delta t_{MD} - t')v^{k+1}. \tag{2.6}$$

Note that only the normal to the boundary component is updated, while the two tangential to the boundary components (in 3D) remain unchanged. After particle reflection is completed, the average number of particles that have left the domain is equal to the particle flux through the boundary $n\delta t_{MD} A v_n$, where n is the number density and A is the area. Particles that have left the domain are deleted. At the inflow particles are inserted into near boundary layer according to the particle flux through the boundary using the *USHER* algorithm [45]. The *USHER* algorithm provides numerical stability of the insertion procedure and minimizes local disturbances in fluid properties. Inserted particle velocities are drawn from a Maxwellian distribution according to the local boundary velocity. In addition, we added an *adaptive normal force* of similar type as in equation (2.5). However, we found that the insertion and reflection of particles appears to be sufficient to enforce a correct normal velocity at the boundary, so the adaptive normal force was turned off in most of our calculations. Note that insertion and reflection of particles does not conserve instantaneous momentum, however the total system momentum is conserved *on average*.

We now address the second issue of minimizing local disturbances in fluid properties. As we mentioned before, the *USHER* algorithm works well for the particle insertion. However, another problem is *erroneous* density fluctuations near the boundary, which appear due to an imbalance of forces from the surrounding fluid (a particle near the boundary interacts with a not-fully spherical region of fluid particles). In order to compensate for the force imbalance, we apply the following pressure force in the near-boundary region (see figure 2.4) similarly to [207, 74]:

$$F_p(h) = -n \int_{V_s \setminus V_{ex}(h)} \frac{\partial U}{\partial r} g(r) dV, \tag{2.7}$$

where V_s is the sphere volume, $V_{ex}(h)$ is a volume excluded from the sphere by the boundaries, and $g(r)$ is the radial distribution function. The calculation of the above integral requires computing the radial distribution function for the specific fluid used in the simulations. Note that the pressure force $F_p(h)$ can be also calculated directly from an equilibrium simulation for a fictitious boundary.

2.2.2 Mesoscopic region via Dissipative Particle Dynamics

The mesoscopic region might cover the flow region where the continuum formalism is not valid while a fully atomistic simulation is not feasible due to computational cost. The mesoscopic subdomain is modeled through the DPD method described next.

2.2.2.1 DPD governing equations

DPD is a mesoscopic particle method and, unlike MD, each DPD particle represents a *molecular cluster* rather than an individual atom, and can be thought of as a soft lump of fluid. Similarly to MD, the DPD system consists of N point particles of mass m_i, position $\mathbf{r}_i$ and velocity $\mathbf{v}_i$. DPD particles interact through three forces: conservative ($\mathbf{F}_{ij}^C$), dissipative

($\mathbf{F}_{ij}^D$), and random ($\mathbf{F}_{ij}^R$) forces given by

$$\begin{aligned}
\mathbf{F}_{ij}^C &= F_{ij}^C(r_{ij})\hat{\mathbf{r}}_{ij}, \\
\mathbf{F}_{ij}^D &= -\gamma\omega^D(r_{ij})(\mathbf{v}_{ij}\cdot\hat{\mathbf{r}}_{ij})\hat{\mathbf{r}}_{ij}, \\
\mathbf{F}_{ij}^R &= \sigma\omega^R(r_{ij})\frac{\xi_{ij}}{\sqrt{dt}}\hat{\mathbf{r}}_{ij},
\end{aligned} \tag{2.8}$$

where $\hat{\mathbf{r}}_{ij} = \mathbf{r}_{ij}/r_{ij}$, and $\mathbf{v}_{ij} = \mathbf{v}_i - \mathbf{v}_j$. The coefficients γ and σ define the strength of dissipative and random forces, respectively. In addition, ω^D and ω^R are weight functions, and ξ_{ij} is a normally distributed random variable with zero mean, unit variance, and $\xi_{ij} = \xi_{ji}$. All forces are truncated beyond the cutoff radius r_c, which defines the length scale in the DPD system. The conservative force is given by

$$F_{ij}^C(r_{ij}) = \begin{cases} a_{ij}(1 - r_{ij}/r_c) & for \quad r_{ij} \leq r_c, \\ 0 & for \quad r_{ij} > r_c, \end{cases} \tag{2.9}$$

where a_{ij} is the conservative force coefficient between particles i and j.

The random and dissipative forces form a thermostat and must satisfy the fluctuation-dissipation theorem in order for the DPD system to maintain equilibrium temperature T [64]. This leads to:

$$\omega^D(r_{ij}) = \left[\omega^R(r_{ij})\right]^2, \qquad \sigma^2 = 2\gamma k_B T, \tag{2.10}$$

where k_B is the Boltzmann constant. The choice for the weight functions is as follows

$$\omega^R(r_{ij}) = \begin{cases} (1 - r_{ij}/r_c)^k & for \quad r_{ij} \leq r_c, \\ 0 & for \quad r_{ij} > r_c, \end{cases} \tag{2.11}$$

where $k = 1$ for the original DPD method. However, other choices (e.g., $k = 0.25$) for these envelopes have been used [74, 71, 193] in order to increase the viscosity of the DPD fluid.

The time evolution of velocities and positions of particles is determined by Newton's second law of motion similarly to MD method, which is integrated using the modified velocity-Verlet algorithm [92].

2.2.2.2 Boundary conditions in DPD

Non-periodic boundary conditions in the DPD region are imposed analogously to the MD region. The tangential component of velocity is enforced through the adaptive shear force $F_t^k(h)$. Imposition of normal velocity component is performed by insertion and reflection of particles as described in section 2.2.1. However, here the *USHER* algorithm is omitted. We found that the system remains stable with *random* insertions. Moreover, a disturbance to the local properties appears to be on the order of several percent which is similar to deviations introduced by the thermostat. No special algorithm is required for insertions because of soft particle interactions in DPD compared to hard MD particle interactions. In order to minimize near-boundary density fluctuations we use a similar pressure force $F_p(h)$ as for the MD subdomain.

2.2.3 Continuum model

The continuum part of the hybrid system is governed by the incompressible NS equations in the form

$$\frac{\partial \mathbf{u}}{\partial t} + (\mathbf{u} \cdot \nabla)\mathbf{u} = -\frac{1}{\rho}\nabla p + \nu \nabla^2 \mathbf{u}, \qquad \nabla \cdot \mathbf{u} = 0, \tag{2.12}$$

where $\mathbf{u}$ is the fluid velocity, ρ is the density, p is the pressure and ν is the kinematic viscosity. At the boundary we specify Dirichlet velocity boundary conditions. The NS equations are solved using the spectral/hp element discretization implemented in the parallel solver NEKTAR [110].

2.3 Simulation results

We test the triple-decker algorithm for three flows: Couette, Poiseuille and lid-driven cavity flow. We compare the hybrid simulation results with an exact solution for the Couette and Poiseuille flows, and with numerical solution for the cavity flow obtained by a highly resolved spectral element discretization of the NS equations.

2.3.1 Couette and Poiseuille flows

We apply the MD-DPD-NS algorithm to the cases of Couette and Poiseuille flows. Figure 2.5 shows a sketch of the domain used in both simulations. The fluid is confined between

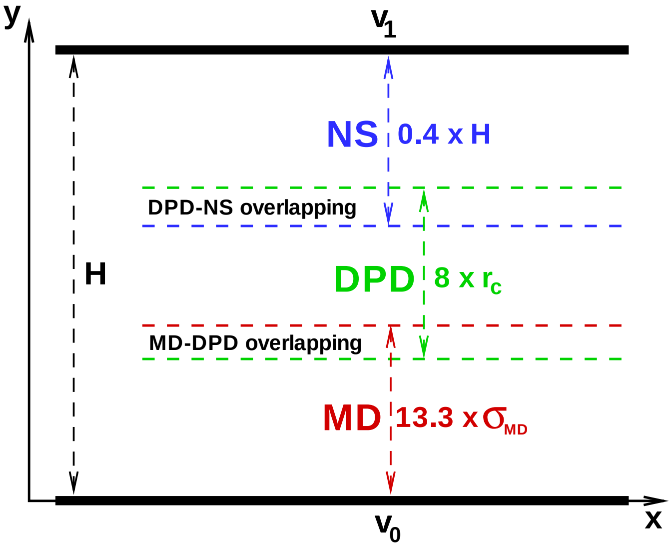

Figure 2.5: Sketch for the Couette and Poiseuille flow domain.

two parallel walls placed at $y = 0$ and $y = H = 20$ with velocities v_0 and v_1, respectively. For the case of Couette flow we set $v_0 = 0$, $v_1 = 5$, and for Poiseuille flow $v_0 = v_1 = 0$. Table 2.1 presents the parameters used in the MD and DPD regions. The domain is assumed to be periodic in x direction, and for MD and DPD also in z direction. The width of MD, DPD and NS layers was set to $13.3 \times \sigma_{MD}$, $8 \times r_c$ and $0.4 \times H$, respectively. The timestep in all regions was chosen to be 0.005 and the kinematic viscosity ν was equal to 0.576 in common (for all three descriptions) non-dimensional units. The viscosity in case of MD and DPD was calculated using the periodic Poiseuille flow method of [14]. In the case of Poiseuille flow the fluid is driven by a constant pressure gradient equal to 0.03 (non-dimensional units). The overlapping regions have thickness $\delta = 2$. The thickness of overlap is a free parameter, however it may have a strong effect on the flow convergence. While it is desirable to have a minimal overlap due to the computational expense, δ must be greater

region	ϵ	σ_{MD}	a	n	r_c	γ	σ	k_BT	k (eq. 2.11)
MD	0.3	0.6	N/A	3	1	4.5	3	1	1.0
DPD	N/A	N/A	25	3	1	4.5	3	1	0.221

Table 2.1: MD and DPD simulation parameters. MD-DPD-NS coupling for Couette and Poiseuille flows.

than zero because the overlapping region is responsible for the propagation of information among regions with different formulations. For instance, in case of the Couette flow (figure 2.5) the flow development is initiated at the upper wall and propagates downwards through the NS region. Having $\delta = 0$ would not allow propagation of flow development in the DPD region. In addition, $\delta \sim 0$ might provide an extremely slow flow development. Several tests we performed suggest that the overlapping region should approximately have a thickness on the order of 10% of the flow characteristic length.

The coupling process was performed every time $\tau = 0.5$ which corresponds to 100 timesteps. The coupling time τ was chosen according to equations (2.1) and (2.2) as follows: Here $k_B T = 1$, $\bar{v} = 2.5$, $\bar{\rho} = 3.0$, $V = 10 \times 10 \times 0.5 = 50$ and $E_v = 0.05$ lead to $M_v = 0.427$, which corresponds to averaging over approximately 64 particle velocities. The autocorrelation time $\tau_v = 0.45$ yields $M_v^c = 77$. Taking into account that some estimated velocities are below 2.5 we set the number of samples to 100 timesteps. One iteration of the algorithm corresponds to the flow integration during time τ and is performed as follows: The NS solver is advanced during the time τ and BCs are extracted and passed to the DPD subdomain. Then, DPD is advanced during τ and BCs are passed to the MD and NS regions (see figure 2.5). Next, the MD subdomain is integrated during time τ and BCs for the DPD region are extracted. Thus, a single iteration of the triple-decker algorithm corresponds to the sequence of region integrations $NS \rightarrow DPD \rightarrow MD$. The choice of the sequence is solely based on the type of flow, such that the flow development propagates from the moving wall downwards through the $NS \rightarrow DPD \rightarrow MD$ regions to the stationary lower wall. Note that for the case of Poiseuille flow an analogous sequence $MD \rightarrow DPD \rightarrow NS$ can be selected due to symmetry. This type of iteration is performed until the system relaxes to a steady state solution. The number of iterations required to reach steady state depend on many factors, such as flow and fluid properties (e.g., viscosity, Reynolds number, geometry), the relative geometric complexity of different domains, the overlapping regions (e.g., thickness, complexity), the BC relaxation technique, etc. Here the number of iterations to reach steady state was on the order of $O(10^2)$. After the steady state was reached, we carried out averaging of the flow field over 10^5 time steps.

Figure 2.6 presents hybrid simulation results of Couette and Poiseuille flows. We find an excellent agreement of the triple-decker method results with the exact solution. In addition, we have observed *no density fluctuations* across the channel. However, this system

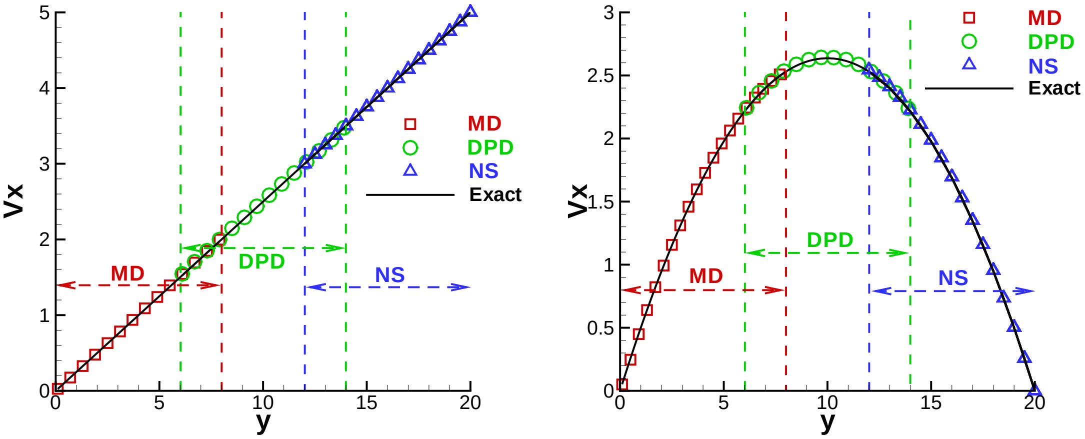

Figure 2.6: Couette (left) and Poiseuille (right) flow velocity profiles.

corresponds to a relatively simple coupling among regions. It only requires to impose a tangential velocity at the boundary while the normal velocity component remains zero. Note that no particle insertions are performed in the above simulations. Nevertheless, these results verify the correctness of the adaptive shear forcing for imposing the proper tangential velocity at the boundary.

2.3.2 Lid-driven square cavity flow

We selected the well-known lid-driven square cavity flow to test the more general hybrid model system. The Reynolds number of this flow is defined as $Re = \frac{VL}{\nu}$, where V is the velocity of the moving lid and L is the height of the cavity. Figure 2.7 shows a sketch of the simulation domain. The MD and DPD parameters are the same as in table 2.1. The MD computational subdomain was set to $83.3\sigma_{MD} \times 25.0\sigma_{MD} \times 16.7\sigma_{MD}$, the DPD subdomain to $50r_c \times 25r_c \times 10r_c$, and the NS subdomain to $L \times 0.6L$, where $L = 50$ is the characteristic length. In terms of common non-dimensional units the MD subdomain covers the region $[0, 50] \bigcap [35, 50]$, the DPD subdomain is $[0, 50] \bigcap [20, 45]$ and the NS subdomain is $[0, 50] \bigcap [0, 30]$, respectively (see figure 2.7). The overlapping regions were set with a thickness of 20% of the characteristic length L. The MD and DPD regions were assumed to be periodic in the z direction. The parameters described next are in common non-dimensional units: The kinematic viscosity was 0.576, and the velocity of the moving lid was set to $V = 0.576$, which corresponds to $Re = 50$. The timestep in the MD and DPD

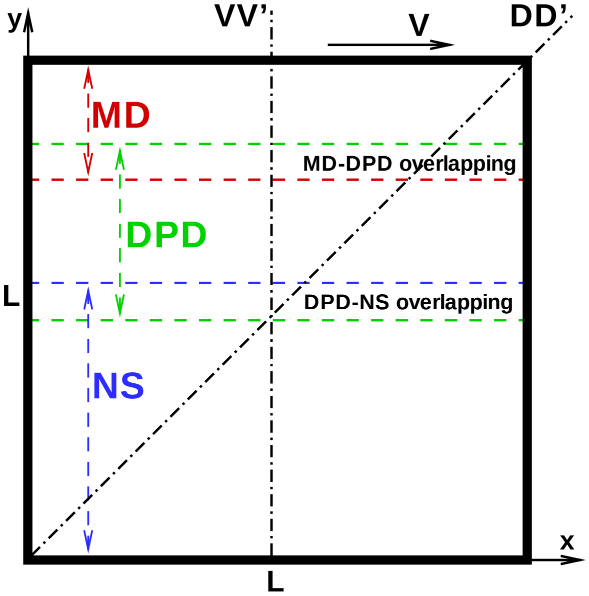

Figure 2.7: Lid-driven square cavity flow domain sketch. Comparison of results is performed along the cuts VV' and DD'.

regions was set to 0.005, and in the NS region to 0.015.

Here, the sequence of one iteration was $MD \rightarrow DPD \rightarrow NS$ due to the flow propagation from the moving lid to the bottom of the cavity. The inter-region communication was done every time $\tau = 2.25$, which corresponds to 450 timesteps in case of the MD and DPD regions, but to 150 timesteps for the NS subdomain. Similarly to the Couette and Poiseuille flow system, we estimate here $M_v = 48.225$ (eq. 2.1) with $\bar{v} = 0.576$, $E_v = 0.05$ and $V = 1.66 \times 0.5 \times 10 = 8.33$, and therefore $M_v^c = 8680$ (eq. 2.2) with the autocorrelation time $\tau_v = 0.45$. Our choice of $\tau = 2.25$ or 450 timesteps corresponds to the error of approximately 22%, which was done for the purpose of a faster flow convergence to a steady state. However, after steady state was reached, we performed several iterations of the algorithm with each iteration of 9000 timesteps and set the error level below 5% in order to refine the steady state solution. The number of iterations to reach steady state was considerably increased compared to the case of Couette and Poiseuille flows due to the flow complexity and was approximately 500. Also, having the overlapping region thickness less than 10% of the characteristic length yielded a slightly under-developed flow comparable with the flow at a lower Reynolds number (e.g., $Re = 45$). We attribute this to the flow complexity at the interfaces which can be affected by an artificially reduced propagation of the information through a thin overlapping region. In addition, we applied a correction to the boundary velocities extracted from the MD and DPD regions in order to set the total mass flux through the interface to zero (total domain mass conservation). The correction is found to be on the order of several percent of the velocity magnitudes.

Figure 2.8 shows hybrid simulation results of the $Re = 50$ square cavity flow extracted along the VV' (at the half of the domain) and DD' lines (see figure 2.7). Results obtained by employing only the full NS equations are plotted with the solid lines, MD results by square symbols, DPD by circles and NS by triangles. The hybrid model solution agrees very well with the highly accurate spectral element solution. Here, velocities at the boundaries contain non-zero tangential as well as normal components. This simulation serves as a rigorous verification of the proposed triple-decker algorithm. In addition, figure 2.9 presents the number density profiles extracted along the VV' and DD' lines. The number density in the MD and DPD regions is normalized by the bulk density. In the NS region we assume it to be constant and equal to one as we solve the incompressible NS equations. Note that the number density is uniform along the VV' cut, however we observe a slight density increase in the upper right corner in case of the DD' cut, where there is particle accumulation in the corner due to the MD fluid being slightly compressible at sufficiently high flow velocity [189]. The influence of the particle accumulation in a wall-bounded geometry on the flow solution was thoroughly studied in the case of the DPD method in [74], where an empirical criterion was established that identifies the maximum allowed flow velocity below which an accurate DPD solution can be obtained. Here, an analogous criterion suggests that the

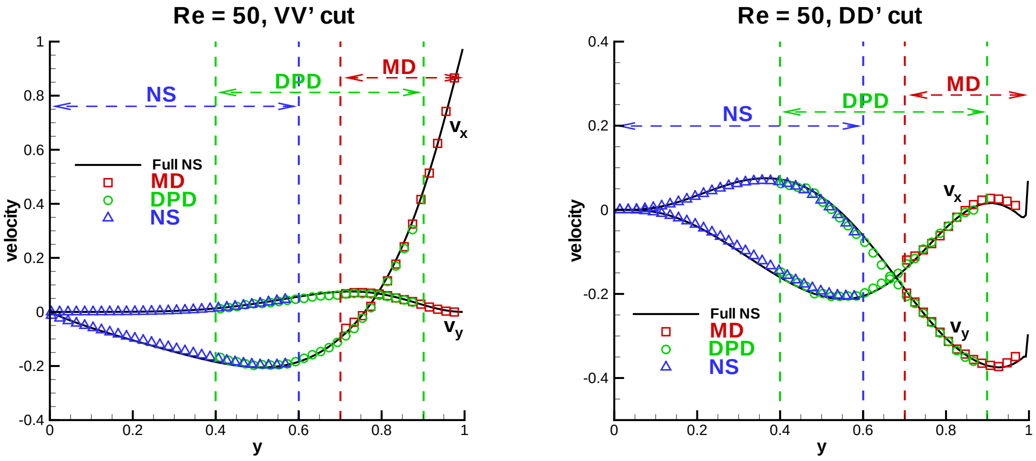

Figure 2.8: Velocity profiles extracted along VV' (left) and DD' (right) lines. The coordinates and velocities are normalized by the characteristic length and velocity, respectively. $Re = 50$.

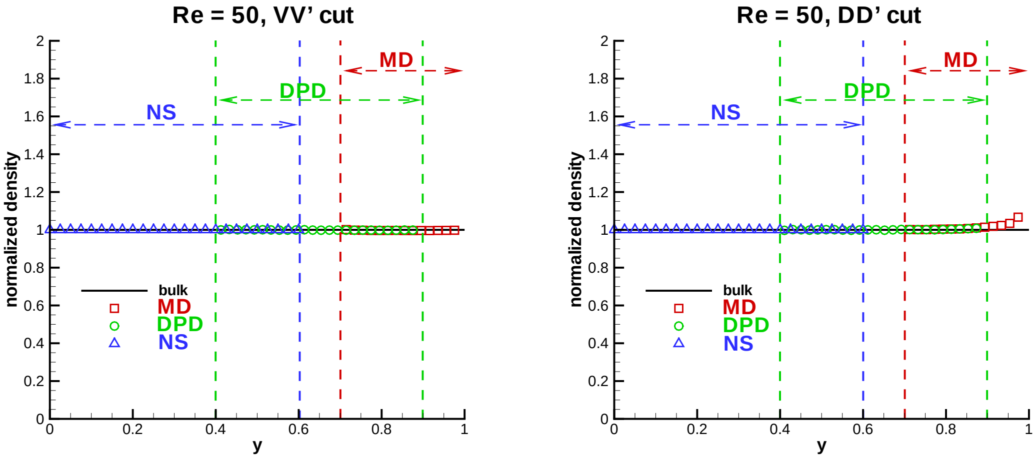

Figure 2.9: Number density profiles extracted along VV' (left) and DD' (right) lines. The number density is normalized by the bulk density in the case of the MD and DPD regions, and is assumed to be 1 in the NS domain. $Re = 50$.

maximum density in the corner normalized by the bulk density should be bounded by 2.0, which corresponds to the maximum lid velocity of approximately 5.0. The values in our simulation are far below the above limits, which justifies why the particle accumulation in the corner has a negligible effect on the flow solution.

Next, we present simulation results of the square cavity flow where the MD, DPD and NS subdomains utilize different non-dimensional characteristic lengths and contain immiscible fluids with different viscosity. However, the Reynolds number of 50 was matched in all regions by scaling the boundary velocities during inter-region communications. For example to scale the velocities for DPD extracted from the MD region, we use the following formula:

$$v_{DPD}^{BC} = v_{MD}^{BC} \frac{L_{MD}}{L_{DPD}} \frac{\nu_{DPD}}{\nu_{MD}}, \tag{2.13}$$

where L_{MD} and L_{MD} are the characteristic lengths of the MD and DPD regions, and ν_{MD}, ν_{DPD} are the fluid viscosities. Table 2.2 summarizes the simulation parameters used in the MD and DPD regions. The MD computational subdomain was set to $100\sigma_{MD} \times$

region	ϵ	σ_{MD}	a	n	r_c	γ	σ	k_BT	k (eq. 2.11)
MD	1.0	1.0	N/A	0.6	2.94	2.5	3	1.8	1.0
DPD	N/A	N/A	25	3	1	4.5	3	1	0.25

Table 2.2: MD and DPD simulation parameters for the cavity flow. Immiscible fluids.

$30\sigma_{MD} \times 10\sigma_{MD}$, the DPD subdomain to $40r_c \times 20r_c \times 10r_c$ and the NS to $L \times 0.6L$ with the characteristic lengths $L_{MD} = 100\sigma_{MD}$, $L_{DPD} = 40r_c$ and $L_{NS} = L = 10$. In non-dimensional units the aforementioned regions correspond to $100 \times 30 \times 10$ (MD), $40 \times 20 \times 10$ (DPD) and 10×6 (NS), respectively. The simulation domain was similar to that in the figure 2.7 with the overlapping regions having thickness of 20% of the characteristic length, and the MD and DPD regions were set to be periodic in the z direction. The fluid viscosities were $\nu_{MD} = 2.44$, $\nu_{DPD} = 0.54$ and $\nu_{NS} = 0.2$, and the velocity of the moving lid in the MD subdomain was set to $V = 1.22$, which corresponds to $Re = 50$. The timestep in the MD and DPD regions was set to 0.00375, and in the NS region to 0.015.

The sequence of one iteration was $MD \rightarrow DPD \rightarrow NS$ similar to the previous cavity flow simulation. The inter-region communication was done after the state of the system advances past time $\tau = 0.75$, which corresponds to 200 timesteps in case of the MD and DPD regions, but to 50 timesteps for the NS subdomain. Here, $M_v = 24.28$ (eq. 2.1) with $\bar{v} = 1.22$, $E_v = 0.05$ and $V = 3.32 \times 1.0 \times 10 = 33.2$, and therefore $M_v^c = 3237$ (eq. 2.2) with the autocorrelation time $\tau_v = 0.25$. After steady state was reached with initial inter-communication time $\tau = 0.75$, similarly to the previous cavity flow case, in order to refine the steady state solution we performed several iterations with inter-communication time $\tau = 15$ and set the error below 5% .

Figure 2.10 shows hybrid simulation results of the $Re = 50$ square cavity flow with immiscible fluids extracted along the VV' and DD' lines. The hybrid model solution agrees

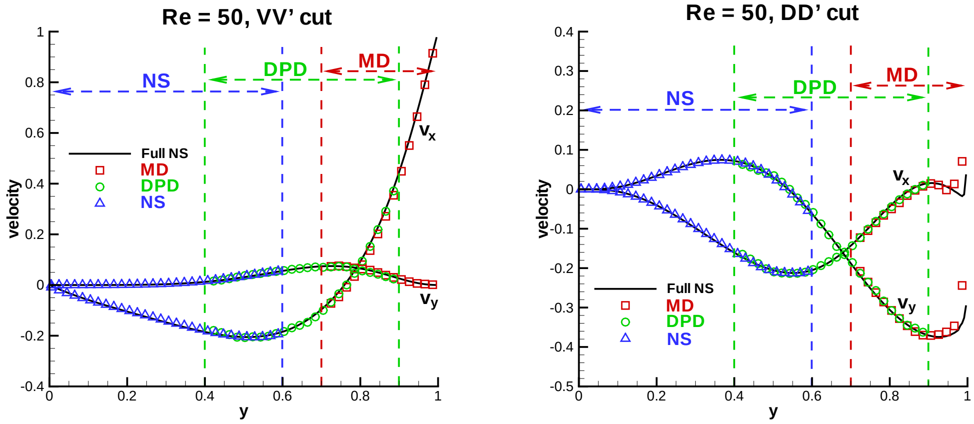

Figure 2.10: Velocity profiles extracted along VV' (left) and DD' (right) lines. The coordinates and velocities are normalized by the characteristic length and velocity, respectively. $Re = 50$. Immiscible fluids.

very well with the highly accurate spectral element solution. In addition, figure 2.11 presents the number density profiles extracted along the VV' and DD' lines. The number density

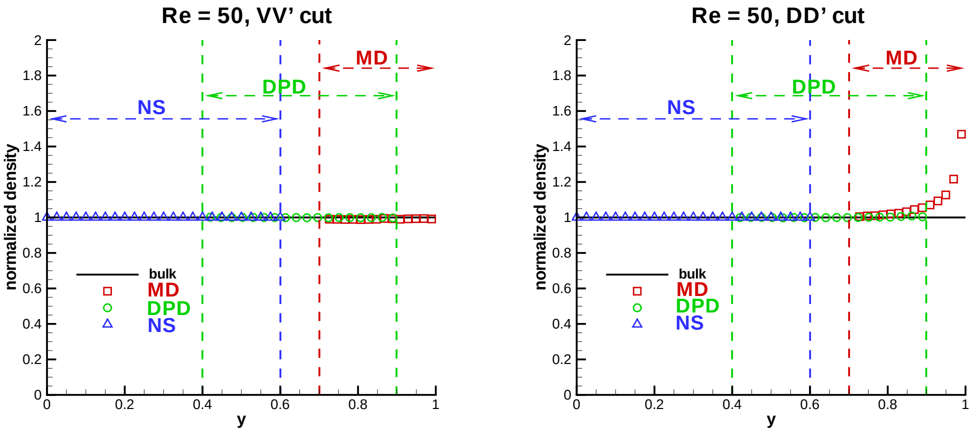

Figure 2.11: Number density profiles extracted along VV' (left) and DD' (right) lines. The number density is normalized by the bulk density in case of the MD and DPD regions, and is assumed to be 1 in the NS domain. $Re = 50$. Immiscible fluids.

is nearly constant along the VV' cut, however we observe a density increase in the corner in case of the DD' cut. The MD fluid is slightly compressible which permits the particle accumulation in the corner. Here, the normalized density in the corner is higher compared to the cavity flow described above due to a higher velocity of the moving lid. To illustrate the density increase in the corner we provide a normalized density contour plot in figure 2.12. Using our empirical criterion [74] we estimate that the maximum allowed flow velocity

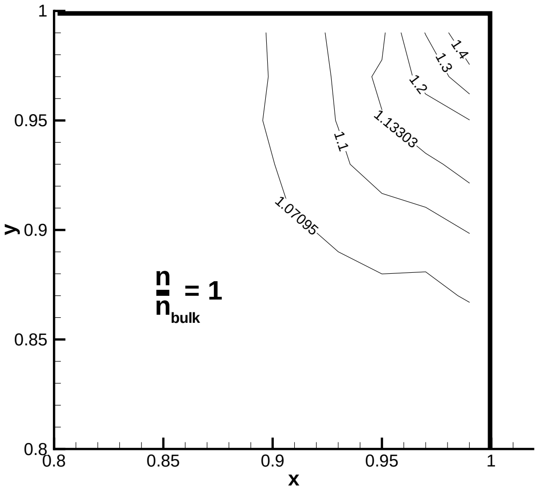

Figure 2.12: Contour plot of normalized density in the corner. Immiscible fluids.

below which an accurate solution can be obtained is 6 or the maximum density in the corner is 2.5. Our values are within the stated limits, and therefore particle accumulation in the corner has a negligible effect on the flow solution.

Next, we present an additional cavity test that employs only DPD and NS regions; figure 2.13 shows the domain sketch. We place the DPD subdomain in the right upper corner where we have discontinuous velocity at the boundary. The cavity corner singularity was studied systematically in [118, 146, 147] for the case of MD and NS methods. In general, the NS numerical solution in the small neighborhood of such singularity is erroneous and it often gives rise to numerical instability [172]. However, the DPD method does not have such a problem. Note that the left upper corner could be done analogously.

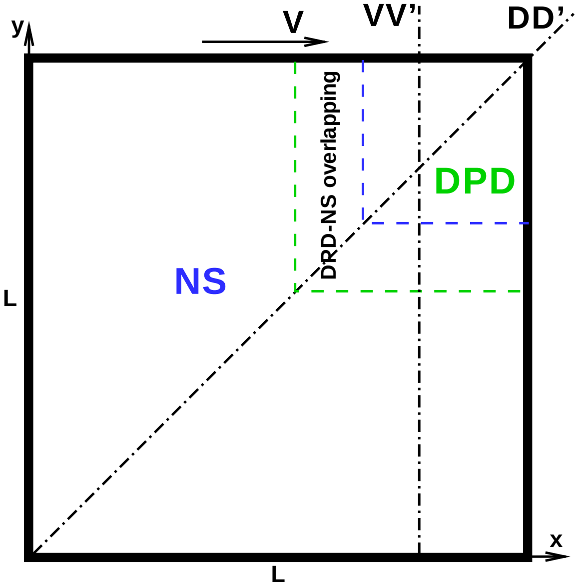

Figure 2.13: Lid-driven square cavity flow domain sketch. NS-DPD coupling. Comparison of results is performed along the cuts VV' and DD'.

Here the DPD region covers the area of $\{35 \leq x \leq 50\} \bigcap \{35 \leq y \leq 50\}$ in the right upper corner of the cavity. The NS region is 50×50 excluding the $\{40 \leq x \leq 50\} \bigcap \{40 \leq y \leq 50\}$ subregion. The overlapping region thickness is equal to 5, which corresponds to the aforementioned 10% of the characteristic length $L = 50$. The DPD parameters used in this simulation were the same as outlined in table 2.2. The kinematic viscosity for both descriptions was $\nu = 0.54$ and the timestep was set to 0.01 in non-dimensional units. The inter-region communication was carried out every $\tau = 1.0$. Figure 2.14 shows velocity profiles extracted along the VV' ($x = 42.5$) and DD' lines for the flow at $Re = 100$. Results

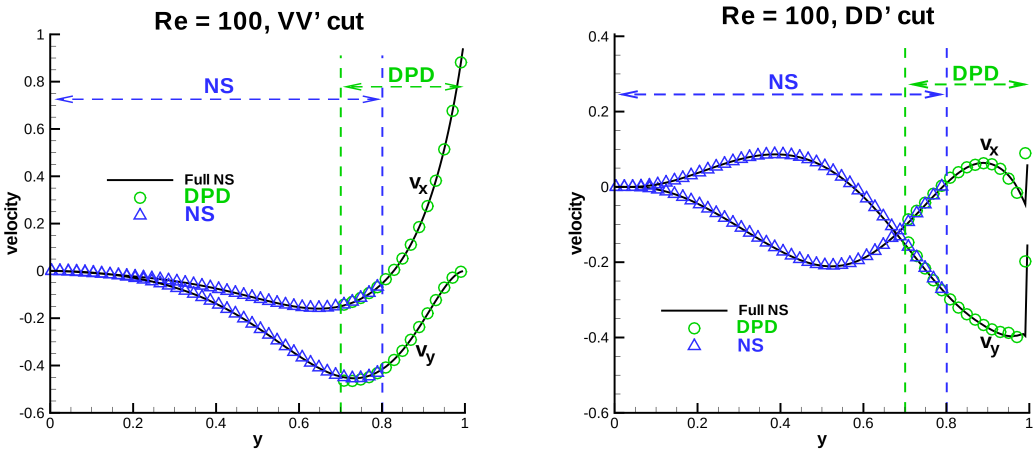

Figure 2.14: Velocity profiles extracted along VV' (left) and DD' (right) lines. The coordinates and velocities are normalized by the characteristic length and velocity, respectively. $Re = 100$.

obtained by the full NS description are plotted with solid lines, DPD results with circles and NS with triangles. We find an excellent agreement of the hybrid model results with the highly accurate full NS simulation results. Figure 2.15 presents the number density profiles extracted along the VV' and DD' lines. The number density in the DPD region is

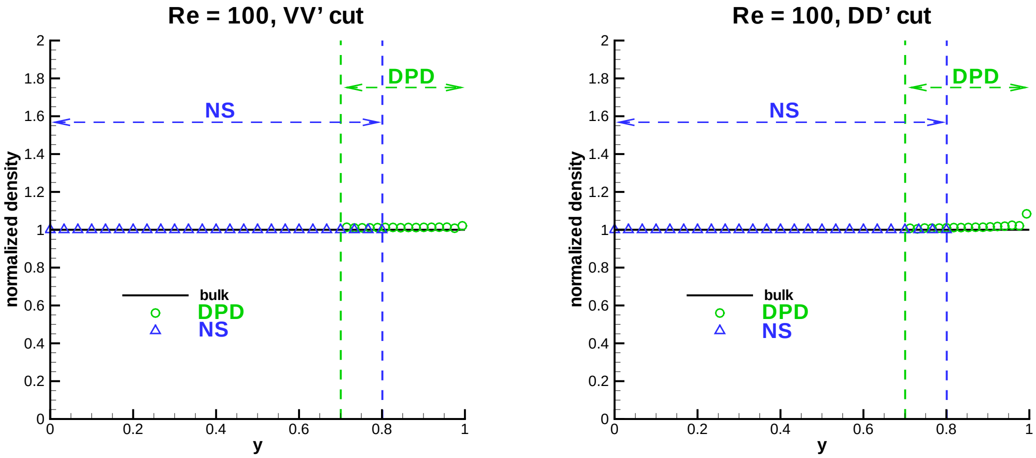

Figure 2.15: Number density profiles extracted along VV' (left) and DD' (right) lines. The number density is normalized by the bulk density in case of the DPD region, and is assumed to be 1 in the NS domain. $Re = 100$.

normalized by the bulk density, and in the NS region is assumed to be one. The number density in the domain is nearly uniform, and has only a small deviation in the corner due to the reasons mentioned before. Finally, to illustrate that in the case of the full NS simulation the incompressibility constraint is not satisfied in the small neighborhood of velocity discontinuity point (in the corner) we calculate the divergence of the velocity field. Figure 2.16 presents the divergence of velocity extracted along the DD' line. Nevertheless, we find that for the DPD case the mass in the corner is nearly conserved. The slightly non-zero value of the divergence of velocity is probably due to the particle accumulation effect in the corner described in detail in [74].

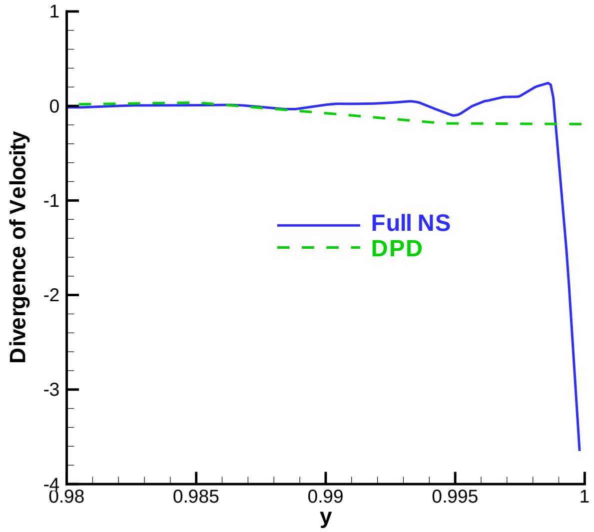

Figure 2.16: $\nabla \cdot \mathbf{v}$ extracted along DD' line for the cases of full NS and DPD. $Re = 100$.

2.3.3 Zero overlapping thickness

The triple-decker algorithm presented above requires a non-zero overlapping thickness of the subdomains with different formulations. However, a slight modification of the algorithm enables us to employ zero overlapping thickness, which can be thought of as an interface. Figure 2.17 shows the Couette flow domain (left) and the time progression (right) sketch with zero overlapping thickness. The two walls are placed at $y = 0$ and $y = H = 20$ with velocities $v_0 = 0$ and $v_1 = 5$, respectively. The lower half of the domain contains MD fluid and the upper half DPD fluid, and corresponding parameters are described in table 2.1. The domain is assumed to be periodic in the x and z directions. The boundary conditions at the walls are enforced similarly through the aforementioned adaptive shear force, the pressure force and the specular reflection. However, at the interface we employ the adaptive shear

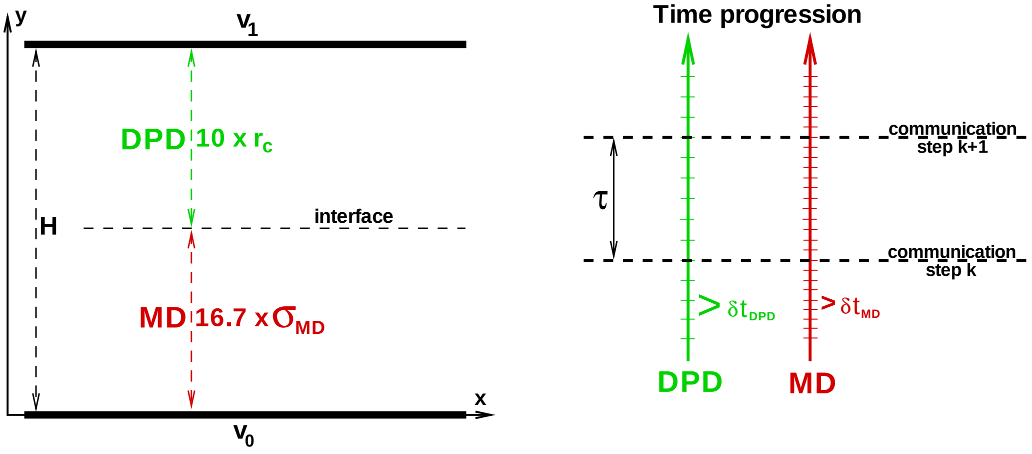

Figure 2.17: Couette flow domain (left) and the time progression (right) sketch. Zero overlapping thickness.

forcing, the definition of which is modified in order to enforce continuous velocity across the interface. Hence, Δv_t in equation (2.5) is defined as $\Delta v_t = v_t^{MD} - v_t^{DPD}$, where v_t^{MD} and v_t^{DPD} are the estimated flow velocities at the interface from the MD and DPD regions, respectively. The same iterative procedure (eq. (2.5)) is performed until Δv_t converges to zero, which leads to the continuous velocity across the interface. The adaptive shear force $F_t^k(h)$ is applied in both regions near the interface in counter directions (for instance, positive x direction in the MD near-interface layer and negative x direction in the DPD region).

Figure 2.18 presents simulation results of Couette flow for the case of zero overlapping thickness. We find an excellent agreement of the results (MD is represented by squares and DPD by circles) with the exact solution (solid line). In this case, the MD and DPD fluids have the same viscosity, and therefore yield the expected linear velocity profile across the channel. In figure 2.18 we also plot Couette flow results with the MD fluid (triangles) having a lower viscosity compared to that of the DPD fluid (stars), which approximates Couette flow for immiscible fluid layers. This test verifies that the adaptive shear force leads to the continuous velocity and shear stress across the interface. In addition, we have observed a uniform density across the channel.

Having zero overlapping thickness among the subdomains is computationally more advantageous compared to the system having non-zero overlaps. However, the example shown above corresponds to zero velocity flux through the MD-DPD interface, and it is not yet

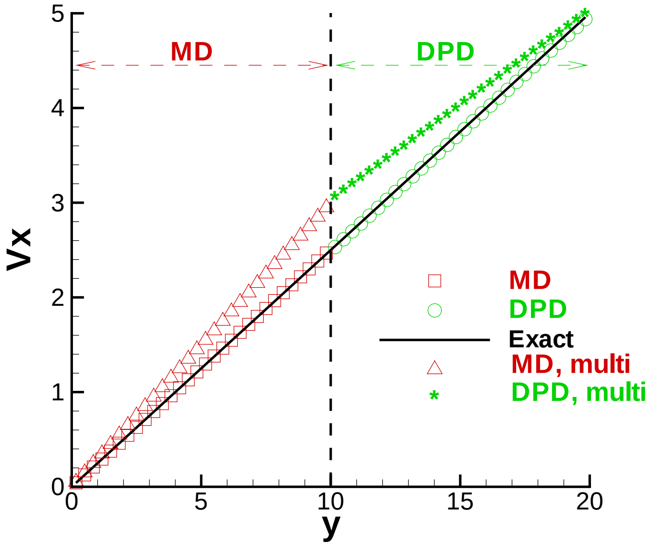

Figure 2.18: Couette flow velocity profiles. Zero overlapping thickness.

clear how to properly impose non-zero normal velocity at the interface in case of arbitrary flow. To this end, the algorithm with zero overlapping thickness is limited at present to simple flows having an interface along the streamlines.

2.4 Summary

In this chapter we have presented a hybrid multiscale method, which is able to cover a broad range of spatiotemporal scales starting from molecular to mesoscopic and to continuum. The molecular region employs the MD method, the mesoscopic utilizes the DPD method, and the continuum is described by the incompressible NS equations.

The scheme is based on the domain decomposition used in the Schwarz alternating method. The corresponding subdomains communicate by passing velocity boundary conditions, which are extracted from one region and subsequently imposed in a receiving region. The choice of a communication pattern among regions with different formulations can be set by a user depending on geometry and flow type. In order to extract flowfield information from particle-based formulations we need to perform averaging during a number of timesteps, which can be varied depending on the characteristic flow velocity and temperature. Imposition of non-periodic boundary conditions involves particle insertion and deletion, specular wall reflection and body force terms. Particles are inserted according to the USHER algorithm in MD region and randomly in near-boundary layer in DPD region. The number of inserted particles corresponds to the particle flux at the boundary. The velocities are drawn from an equilibrium Maxwellian distribution. Body forcing includes a boundary pressure force in order to minimize near-boundary density fluctuations, and an adaptive shear force which enforces the tangential velocity component of boundary conditions.

The algorithm is verified for the Couette, Poiseuille and lid-driven cavity flow simulations. The results show very good agreement with analytic and reference solutions. In addition, we showed that the hybrid algorithm can be applied in singularity regions for the NS formulation such as corners in the lid-driven square cavity. Moreover, we presented a spatiotemporal decoupling by utilizing different region dimensions and timesteps in simulations. Finally, we discussed a minimal modification of the algorithm which allowed us to have zero overlapping thickness among the regions with different formulations.

Even though the simulation results presented in this chapter were done for two-dimensional flows, we do not see any restrictions to extend the hybrid algorithm to three-dimensional flow cases. Furthermore, future work should consider an extension of algorithm to more complex fluids such as polymeric and biological fluids and suspensions. This type of problems might require more sophisticated particle insertion and body forcing algorithms and potentially the inclusion of additional intra- and inter-molecular, electrostatic and excluded volume interactions. In addition, such systems might need an inter-exchange with more detailed information, for instance polymeric stresses. In turn, in the continuum region the incompressible NS equations might need to be substituted by more appropriate visco-elastic continuum non-Newtonian fluid models.

Chapter 3

Modeling red blood cells: single cell mechanics, rheology, and dynamics in health and malaria disease

3.1 Introduction

The healthy human red blood cell has a biconcave shape with an average diameter of 7.8 μm. Its membrane consists of a lipid bilayer with an attached cytoskeleton formed by a network of the protein spectrin linked by short filaments of actin. The lipid bilayer is considered to be nearly viscous and area preserving [83], while the membrane's elasticity is attributed to the attached spectrin network, as is the integrity of the entire RBC when subjected to severe deformations in capillaries as small as 3 μm.

Advances in experimental techniques have allowed accurate measurements of red blood cell (RBC) properties down to the nanometer scale. They include micropipette aspiration [205, 50], RBC deformation by optical tweezers [101, 190], RBC edge flicker microscopy [186], tracking of fluorescent nanometer beads attached to the RBC [123], optical magnetic twisting cytometry (OMTC)[167], three-dimensional measurement of membrane thermal fluctuations [161, 158], and observations of RBCs immersed in both shear and in pressure-driven flows [79, 4, 191, 196]. Micropipette aspiration and optical tweezers techniques tend to deform the whole RBC membrane directly, while RBC edge flicker microscopy and tracking of fluorescent nanobeads attempt to extract the mechanical properties from passive observations of thermal fluctuations. The first two techniques yield the macroscopic interfacial shear modulus of healthy cells in the range of $2 - 12\ \mu N/m$, while the thermal fluctuations techniques predict the shear modulus to be one to two orders of magnitude smaller than those from the RBC deformation experiments. Recent theoretical developments offer explanations for the discrepancies in experimental results. Li et al. [127] suggest that metabolic activity or large strains may induce a continuous rearrangement of the erythrocyte cytoskeleton. Consequently, in their model the RBC membrane exhibits strain hardening or softening depending on certain conditions. Moreover, the cytoskeleton attachments diffuse within the lipid bilayer, but the diffusion is negligible at short time scales. Gov [87] proposed an active elastic network model in which the metabolic activity affects the stiffness of the cell through the consumption of adenosine triphosphate (ATP). The activity induced by ATP would appear to greatly affect membrane undulations [88] with resultant fluctuations equivalent to a three-fold increase of the temperature. This argument is in contrast with recent experiments [66] which found no ATP dependence of RBC properties or its membrane fluctuations.

Optical magnetic twisting cytometry and three-dimensional measurement of membrane thermal fluctuations furnish measurements of membrane rheological properties (e.g., the complex modulus). The evidence provided by these experiments is sufficient to characterize the complex mechanical response of the membrane to be viscoelastic. In addition, the experimental findings show that RBCs subjected to large deformations are characterized by a nonlinear mechanical response. Thus, the objective of this chapter is to demonstrate a consistent multiscale RBC model which is able to successfully capture the known mechanics, rheology, and dynamics of RBCs. While membrane strain hardening or softening and the metabolic activity can be incorporated into this model their effects are beyond the scope of this work.

Our RBC model is constructed by a network of springs combined with bending energy and constraints for surface-area and volume conservation. Figure 3.1 illustrates the difference between network and continuum based models, which are characterized by different parameters. Atomic force microscopy experiments [194, 192] have shown that the spectrin network of RBCs is highly irregular compared to the regular hexagonal network and has

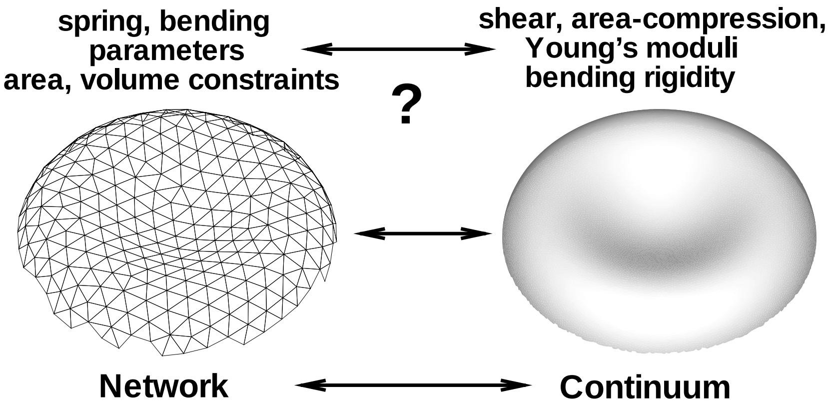

Figure 3.1: A sketch of network and continuum models.

varying lengths of interconnections. The multiscale RBC model at the spectrin level, where each spring in the network corresponds to a single spectrin tetramer with the equilibrium distance between two neighboring actin connections of about 75 nm, corresponds to an *effective* spectrin network since it is regular, i.e. nearly hexagonal. On the other hand, the RBC network can also be highly coarse-grained with equilibrium spring lengths of up to approximately $500 - 600$ nm. Theoretical analysis of the hexagonal network yields its elastic and dynamic properties, and completely eliminates adjustment of multiscale model parameters. The current theoretical results for the spectrin-level model [42] underestimate the effective membrane Young's modulus by about 50%.

Recently several RBC models have been developed: at the continuum scale [83, 65, 162, 57], at the discrete spectrin level [48, 126], and on the mesoscopic scale [150, 53, 56, 159]. Fully continuum (both fluid and solid) models suffer from non-trivial coupling between nonlinear solid deformations and fluid flow with their consequent computational expense. This has motivated the rapid development of "semi-continuum" models [162, 57] of deformable particles which use immersed boundary or front-tracking techniques. In these a membrane is represented by a set of points which are tracked in Lagrangian fashion, and are coupled to an Eulerian discretization of the fluid domain resulting in the same viscosity of both inside and outside the cell. These models often employ simplified treatments of the elastic membrane, and therefore fail to capture the known viscoelastic properties of real RBCs. In addition, continuum models omit some phenomena at the mesoscopic and microscopic scales such as membrane thermal fluctuations which are known to affect RBC rheology and dynamics [149]. On the molecular level, detailed spectrin models of RBCs are much limited by the demanding computational expense. This motivates us to focus on an accurate mesoscopic model of RBCs.

Several mesoscopic methods have been developed [150, 53, 56, 159] for modeling deformable particles such as RBCs. Dzwinel et al. [56] modeled an RBC as a volume of elastic material with an inner skeleton. This does not account for the main structural element of the RBC, namely a membrane filled with fluid, and therefore it fails to properly capture the dynamics of RBCs, such as tumbling and tank-treading behavior observed in shear flow [4, 181]. The three other aforementioned methods [150, 53, 159] employ an approach very similar to ours in which the RBC is represented by a network of springs in combination with bending rigidity and constraints for surface-area and volume conservation. Dupin et al. [53] couple the discrete RBC to a fluid described by the Lattice Boltzmann method [187]. In spite of very promising results, their model employs the same external and internal fluids and does not account for membrane viscosity and thermal fluctuations. Noguchi and Gompper [150] reported very interesting results on the dynamics of vesicles and RBCs obtained with Multiparticle Collision Dynamics [132] but not entirely in the physiologically correct regime. Pivkin and Karniadakis [159] used Dissipative Particle Dynamics (DPD) [105] to simulate a coarse-grained RBC model which is the starting point of this work. Below, we will present a general multiscale RBC model which incorporates major improvements in its mechanical and rheological properties and in its dynamics.

The proposed framework will be also used in the modeling of RBCs in malaria. Malaria is an infectious disease caused by a Plasmodium parasite. It is common for tropical and subtropical regions resulting in several million deaths per year. One of the most serious forms of malaria is caused by the Plasmodium falciparum (Pf) that infects RBCs. Intra-erythrocytic development of the parasite includes three stages from the earliest to the latest: ring → trophozoite → schizont. Infected RBCs show progressing changes in their mechanical and rheological properties, and morphology [38, 180] as the parasite develops. Progression through the stages leads to considerable stiffening of the RBC membrane as found in optical tweezers stretching experiments [190] and in diffraction phase microscopy by monitoring thermal fluctuations [158]. Moreover, Pf development results in vacuoles formed inside of RBCs reducing the cell volume. Thus, at the final stage (schizont) infected RBCs are often observed to have a “near spherical” shape, while the preceding stages maintain their biconcavity. These changes greatly affect rheological properties and dynamics of Pf-parasitized RBCs, and lead to obstructions of small capillaries [180] impairing the ability of RBCs to circulate. In addition, recent experiments [133] showed that the temperature elevation from the physiological value (37^o C) to the febrile (41^o C) leads to an additional significant stiffening of parasitized RBCs.

Section 3.2 presents a complete theoretical analysis of a membrane network model implementing specified macroscopic membrane properties without any parameter adjustment for different spring models and arbitrary levels of coarse-graining. Section 3.3 provides results on the cell mechanics for healthy and Pf-parasitized RBCs. In addition, we propose a stress-free model, which eliminates non-vanishing local artifacts, such as the dependence of mechanical properties on triangulation quality and equilibrium shape stability for realistic membrane bending rigidity; the latter is often compensated with artificially high bending stiffness. Rheological properties of the modeled RBCs (healthy and infected) are tested in section 3.4 using twisting torque cytometry, membrane thermal fluctuations, a whole RBC creep test followed by the cell recovery. RBC dynamics in shear and Poiseuille flows is studied in section 3.5, and is compared with the theoretical predictions of RBC motion [4, 181]. We discuss quantitative accuracy of those theories since they utilize strong simplifications. The results are summarized in section 3.6.

3.2 Red blood cell modeling framework

The cell membrane is represented by a viscoelastic network which is filled and surrounded by separate fluids. For the simulations we employ the Dissipative Particle Dynamics (DPD) method [105], see section 2.2.2 for details. The membrane model is general enough to be used with other simulation techniques such as Brownian dynamics, lattice Boltzmann, multiparticle collision dynamics, and the immerse-boundary method.

3.2.1 Viscoelastic membrane model

The cell model structure is defined by a two-dimensional triangulated network on a membrane surface that is characterized by a set of points with Cartesian coordinates $\{\mathbf{x}_i\}$, $i \in 1...N_v$ which are vertices of the two-dimensional triangulated network. The vertices are connected by N_s springs (edges) forming N_t triangles. Potential energy of the system is given by

$$V(\{\mathbf{x}_i\}) = V_{in-plane} + V_{bending} + V_{area} + V_{volume}. \tag{3.1}$$

The in-plane energy term includes the elastic energy stored in the membrane as follows,

$$V_{in-plane} = \sum_{j \in 1 \ldots N_s} U_s(l_j) + \sum_{k \in 1 \ldots N_t} \frac{C_q}{A_k^q}, \tag{3.2}$$

where l_j is the length of the spring j, A_k is the area of the k-th triangle, and the constant C_q and exponent q will be defined further. Note that spring forces in membrane (the first sum in equation (3.2)) are a combination of conservative elastic forces, that may be expressed in terms of an energy potential $U_s(l_j)$, and dissipative forces that are defined in section 3.2.4. Thus, the first sum defines the contribution of viscoelastic springs, while the second sum contains a hydrostatic elastic energy of the triangular membrane patches. Different spring models can be used here, and their performance will be discussed in section 3.3. However, we highlight two *nonlinear* spring models: the wormlike chain (WLC) and the finitely extensible nonlinear elastic (FENE) spring, the attractive potentials of which are given, respectively, by

$$U_{WLC} = \frac{k_B T l_m}{4p} \frac{3x^2 - 2x^3}{1 - x}, \qquad U_{FENE} = -\frac{k_s}{2} l_m^2 \log\left[1 - x^2\right], \tag{3.3}$$

where $x = l/l_m \in (0, 1)$, l_m is the maximum spring extension, p is the persistence length, $k_B T$ is the energy per unit mass, and k_s is the FENE spring constant. Note that when the distance between two connected points approaches l_m, the corresponding spring force goes to infinity, and therefore it limits the maximum extension to l_m. It is important to point out that both WLC and FENE springs exert purely attractive forces, thus they produce a triangular area compression, while the second term in equation (3.2) provides triangular area expansion. The minimum energy state of a single triangle corresponds to an equilibrium spring length l_0, which depends on the spring parameters and C_q. The relationship between these parameters and the equilibrium length can be derived by energy minimization [48] or by setting the Cauchy stress obtained from the virial theorem [7] to zero [42]. We obtained the following expressions for WLC and FENE springs, respectively,

$$C_q^{WLC} = \frac{\sqrt{3} A_0^{q+1} k_B T (4x_0^2 - 9x_0 + 6)}{4pql_m(1 - x_0)^2}, \qquad C_q^{FENE} = \frac{\sqrt{3} A_0^{q+1} k_s}{q(1 - x_0^2)}, \tag{3.4}$$

where $x_0 = l_0/l_m$ and $A_0 = \sqrt{3}l_0^2/4$. These formulas allow us to calculate the strength of the second term in equation (3.2) for the given equilibrium length and spring parameters. Another choice is to select a spring with a specific equilibrium length (e.g., harmonic spring, WLC or FENE in combination with a repulsive potential), and then set C_q to zero. We now introduce an energy potential which defines a repulsive force in the form of a power function (POW) of the separation distance l as follows

$$U_{POW}(l) = \begin{cases} \frac{k_p}{(m-1)l^{m-1}} & m > 0, \quad m \neq 1, \\ -k_p \log(l) & m = 1, \end{cases} \tag{3.5}$$

where k_p is the POW force coefficient and m is the exponent. The combination of WLC or FENE with the POW force defines a spring with nonzero equilibrium length, and will be called WLC-POW and FENE-POW, respectively. The strength k_p can be expressed in terms of the equilibrium length l_0 and the WLC or FENE parameters by equating the corresponding forces. The combination of WLC or FENE with the second term of the in-plane energy in equation (3.2) will be denoted as WLC-C and FENE-C. The viscous contribution of each spring will be defined below.

The bending energy is defined as,

$$V_{bending} = \sum_{j \in 1 \ldots N_s} k_b \left[1 - cos(\theta_j - \theta_0)\right], \tag{3.6}$$

where k_b is the bending constant, θ_j is the instantaneous angle between two adjacent triangles having the common edge j, and θ_0 is the spontaneous angle.

The last two terms in equation (3.1) define the area and volume conservation constraints given by

$$\begin{aligned} V_{area} &= \frac{k_a(A - A_0^{tot})^2}{2A_0^{tot}} + \sum_{j \in 1 \ldots N_t} \frac{k_d(A_j - A_0)^2}{2A_0}, \\ V_{volume} &= \frac{k_v(V - V_0^{tot})^2}{2V_0^{tot}}, \end{aligned} \tag{3.7}$$

where k_a, k_d and k_v are the global area, local area and volume constraint constants, respectively. The terms A and V are the total instant area and volume of the RBC, while A_0^{tot} and V_0^{tot} are the desired total area and volume, respectively. The second term of the V_{area}

energy corresponds to local area dilatation.

The nodal forces corresponding to the above energies are derived from the following formula

$$\mathbf{f}_i = -\partial V(\{\mathbf{x}_i\})/\partial \mathbf{x}_i, \qquad i \in 1...N_v. \tag{3.8}$$

Exact force expressions are derived analytically in appendix A.

3.2.2 Macroscopic elastic properties

Several parameters must be chosen in the membrane network model. To eliminate adjustment of the model parameters a relationship between them and corresponding network macroscopic properties (see fig. 3.1) has to be derived. Theoretical analysis of the hexagonal network is presented further to obtain its linear macroscopic properties with respect to the selected network parameters. We extend the linear analysis of a two-dimensional sheet of springs built with equilateral triangles [42]. Figure 3.2 shows an element of the hexagonal network with the central vertex **v** placed at the origin. From the virial theorem (see chapter 2 of [7]), the Cauchy stress at the vertex **v** surrounded by the area element $S = 2A$ is given by

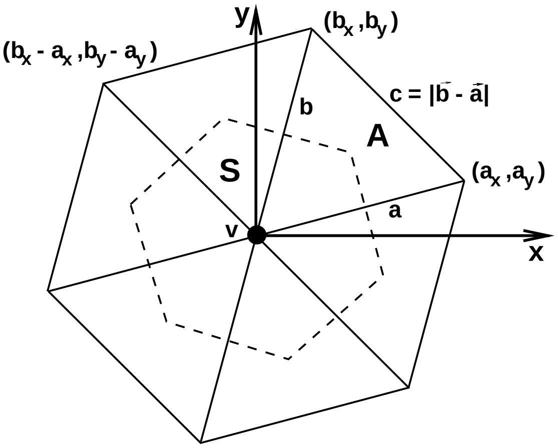

Figure 3.2: An element of the hexagonal network with the central vertex **v** placed at the origin.

$$\tau_{\alpha\beta} = -\frac{1}{2A}\left[\frac{f(a)}{a}a_\alpha a_\beta + \frac{f(b)}{b}b_\alpha b_\beta + \frac{f(c)}{c}c_\alpha c_\beta\right] - \\ -\left(q\frac{C_q}{A^{q+1}} + \frac{k_a(A_0^{tot} - N_t A)}{A_0^{tot}} + \frac{k_d(A_0 - A)}{A_0}\right)\delta_{\alpha\beta}, \tag{3.9}$$

where $f(\cdot)$ is the spring force, α, β can be x or y, $\vec{c} = \vec{b} - \vec{a}$, N_t is the total number of triangles, and $A_0^{tot} = N_t A_0$. In general, N_t cancels out and the global and local area contributions to the stress can be combined as $-(k_a + k_d)(A_0 - A)/A_0 \delta_{\alpha\beta}$. *Note that the linear analysis in [42] did not take into account the global and local area contributions to the stress which significantly affect the final results.* The linear shear modulus can be derived by applying a small engineering shear strain γ to the configuration in figure 3.2, followed by the first derivative of shear stress $\mu_0 = \frac{\partial \tau_{xy}}{\partial \gamma}|_{\gamma=0}$. The shear deformation is area-preserving, and therefore only spring forces contribute to the membrane shear modulus. For different spring models, we obtained the following expressions for μ_0 (see appendix B for details):

$$\begin{aligned}
\mu_0^{WLC-C} &= \frac{\sqrt{3} k_B T}{4 p l_m x_0} \left(\frac{3}{4(1-x_0)^2} - \frac{3}{4} + 4x_0 + \frac{x_0}{2(1-x_0)^3} \right), \\
\mu_0^{FENE-C} &= \frac{\sqrt{3} k_s}{2} \left(\frac{x_0^2}{(1-x_0^2)^2} + \frac{2}{1-x_0^2} \right), \\
\mu_0^{WLC-POW} &= \frac{\sqrt{3} k_B T}{4 p l_m x_0} \left(\frac{x_0}{2(1-x_0)^3} - \frac{1}{4(1-x_0)^2} + \frac{1}{4} \right) + \frac{\sqrt{3} k_p (m+1)}{4 l_0^{m+1}}, \\
\mu_0^{FENE-POW} &= \frac{\sqrt{3}}{4} \left(\frac{2 k_s x_0^2}{(1-x_0^2)^2} + \frac{k_p (m+1)}{l_0^{m+1}} \right).
\end{aligned} \tag{3.10}$$

The linear-elastic area-compression modulus K can be calculated from the area expansion with the resulting in-plane pressure given by

$$P = -\frac{1}{2}(\tau_{xx} + \tau_{yy}) = \frac{3 l f(l)}{4A} + q \frac{C_q}{A^{q+1}} + \frac{(k_a + k_d)(A_0 - A)}{A_0}. \tag{3.11}$$

Then, the compression modulus K is defined as

$$K = - \left. \frac{\partial P}{\partial \log(A)} \right|_{A=A_0} = - \left. \frac{1}{2} \frac{\partial P}{\partial \log(l)} \right|_{l=l_0} = - \left. \frac{1}{2} \frac{\partial P}{\partial \log(x)} \right|_{x=x_0}. \tag{3.12}$$

Using equations (3.11) and (3.12) we derive the linear area-compression modulus for different spring models (see appendix B for details) as follows

$$\begin{aligned}
K^{WLC-C} &= \frac{\sqrt{3}k_BT}{4pl_m(1-x_0)^2}\left[\left(q+\frac{1}{2}\right)(4x_0^2-9x_0+6)+\frac{1+2(1-x_0)^3}{1-x_0}\right]+k_a+k_d,\\
K^{FENE-C} &= \frac{\sqrt{3}k_s}{1-x_0^2}\left[q+1+\frac{x_0^2}{1-x_0^2}\right]+k_a+k_d,\\
K^{WLC-POW} &= 2\mu_0^{WLC-POW}+k_a+k_d,\\
K^{FENE-POW} &= 2\mu_0^{FENE-POW}+k_a+k_d.
\end{aligned} \tag{3.13}$$

Note that if $q = 1$ we obtain the expressions $K^{WLC-C} = 2\mu_0^{WLC-C} + k_a + k_d$ and $K^{FENE-C} = 2\mu_0^{FENE-C} + k_a + k_d$. Generally, for a nearly incompressible sheet of springs the area constraint coefficients have to be large such that $k_a + k_d \gg \mu_0$, and hence $K \gg \mu_0$.

The Young's modulus Y for the two-dimensional sheet can be expressed through the shear and area-compression moduli as follows

$$Y = \frac{4K\mu_0}{K+\mu_0}, \qquad Y \to 4\mu_0, \quad if \quad K \to \infty, \tag{3.14}$$

with the Poisson's ratio ν given by

$$\nu = \frac{K-\mu_0}{K+\mu_0}, \qquad \nu \to 1, \quad if \quad K \to \infty. \tag{3.15}$$

The above expressions are consistent with the incompressibility assumption enforced through the condition $k_a + k_d \gg \mu_0$. In practice, we use the values $\mu_0 = 100$ and $k_a + k_d = 5000$ which provide a nearly incompressible membrane with Young's modulus about 2% smaller than its asymptotic value of $4\mu_0$. All analytical expressions for μ_0, K and Y were numerically verified by shearing, area expanding and stretching tests of the regular two-dimensional sheet of springs. In addition, it is important to note that the modeled sheet appears to be *isotropic* for small shear and stretch deformations; however, it is *anisotropic* at large deformations.

3.2.3 Membrane bending rigidity

The bending resistance of an elastic sheet is often described by the macroscopic model of Helfrich [100], the energy of which is given by

$$E_c = \frac{k_c}{2}\int_A (C_1 + C_2 - 2C_0)^2 dA + k_g \int_A C_1 C_2 dA, \tag{3.16}$$

where C_1 and C_2 are the local principal curvatures, C_0 is the spontaneous curvature, and k_c and k_g are the bending rigidities. Note that the second term in equation (3.16) is constant for closed surfaces.

The relationship between the model bending coefficient k_b and the macroscopic bending rigidity k_c is derived for the case of a spherical shell. Figure 3.3 shows two equilateral triangles with the edge length a and vertices resting on the surface of a sphere of radius R. The angle between the triangle normals $\mathbf{n}_1$ and $\mathbf{n}_2$ is equal to θ. In case of the spherical shell the total energy in equation (3.16) is given by

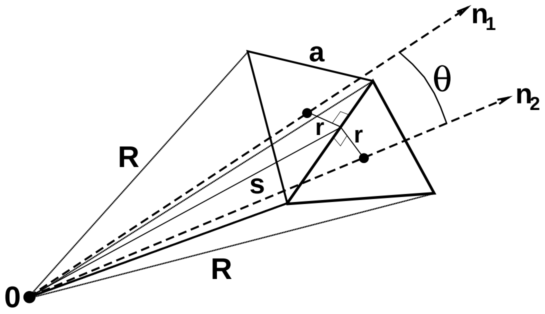

Figure 3.3: Two equilateral triangles placed on the surface of a sphere of radius R.

$$E_c = 8\pi k_c (1 - C_0/C_1)^2 + 4\pi k_g = 8\pi k_c (1 - R/R_0)^2 + 4\pi k_g, \tag{3.17}$$

where $C_1 = C_2 = 1/R$ and $C_0 = 1/R_0$. For the network model the energy of a triangulated sphere is equal to

$$V_{bending} = N_s k_b [1 - cos(\theta - \theta_0)] \tag{3.18}$$

in the notations defined above. Expansion of $cos(\theta - \theta_0)$ in Taylor series around $(\theta - \theta_0)$ provides us with the leading term as follows

$$V_{bending} = N_s k_b (\theta - \theta_0)^2/2 + O((\theta - \theta_0)^4). \tag{3.19}$$

From the sketch in figure 3.3 we find that $2r \approx \theta R$ or $\theta = a/(\sqrt{3}R)$, and analogously $\theta_0 = a/(\sqrt{3}R_0)$. Furthermore, $A_{sphere} = 4\pi R^2 \approx N_t A_0 = \sqrt{3}N_t a^2/4 = \sqrt{3}N_s a^2/6$, and thus $a^2/R^2 = 8\pi\sqrt{3}/N_s$. Finally, we obtain

$$V_{bending} = \frac{N_s k_b}{2}\left(\frac{a}{\sqrt{3}R} - \frac{a}{\sqrt{3}R_0}\right)^2 = \frac{N_s k_b a^2}{6R^2}\left(1 - \frac{R}{R_0}\right)^2 = \frac{4\pi k_b}{\sqrt{3}}\left(1 - \frac{R}{R_0}\right)^2. \tag{3.20}$$

Equating the macroscopic bending energy E_c for $k_g = -4k_c/3$, $C_0 = 0$ [128] and $V_{bending}$ yields the relation $k_b = 2k_c/\sqrt{3}$ in agreement with the continuum limit. The spontaneous angle θ_0 is set according to the total number of vertices N_v on the sphere. It can be shown that $\cos(\theta) = 1 - 1/[6(R^2/a^2 - 1/4)]$, $N_s = 2N_v - 4$, and thus the corresponding bending stiffness k_b and the spontaneous angle θ_0 are given by

$$k_b = \frac{2}{\sqrt{3}}k_c, \qquad \theta_0 = cos^{-1}\left(\frac{\sqrt{3}(N_v - 2) - 5\pi}{\sqrt{3}(N_v - 2) - 3\pi}\right). \tag{3.21}$$

3.2.4 Membrane viscosity

So far a purely elastic membrane was defined; however, the RBC membrane is known to be viscoelastic. Next, we describe the viscous component of viscoelastic springs in equation (3.2). The addition of dissipative and random forces into springs fits naturally in the DPD method since inter-particle dissipative interactions are an intrinsic part of the method. The implementation of the dissipative and random interactions as in equation (2.8) appears to be insufficient. The contribution from inter-particle relative velocity $\mathbf{v}_{ij}$ projected on their connecting vector is negligible for small dissipative coefficients γ, while large values of γ affect the numerical stability of the method. Better performance is achieved with a viscous spring dissipation term $-\gamma\mathbf{v}_{ij}$, for which the fluctuation-dissipation balance needs to be invoked to maintain the equilibrium membrane temperature k_BT.

Further, the general framework of the fluid particle model [63] is employed with the following definitions

$$\begin{aligned} \mathbf{F}_{ij}^D &= -\mathbf{T}_{ij}\cdot\mathbf{v}_{ij}, \quad \mathbf{T}_{ij} = A(r_{ij})\mathbf{1} + B(r_{ij})\mathbf{e}_{ij}\mathbf{e}_{ij}, \\ \mathbf{F}_{ij}^R dt &= \sqrt{2k_BT}\left(\tilde{A}(r_{ij})d\overline{\mathbf{W}_{ij}^S} + \tilde{B}(r_{ij})\frac{tr[d\mathbf{W}_{ij}]}{3}\mathbf{1} + \tilde{C}(r_{ij})d\mathbf{W}_{ij}^A\right)\cdot\mathbf{e}_{ij}, \end{aligned} \tag{3.22}$$

where $tr[d\mathbf{W}_{ij}]$ is the trace of a random matrix of independent Wiener increments $d\mathbf{W}_{ij}$, and $d\overline{\mathbf{W}_{ij}^S} = d\mathbf{W}_{ij}^S - tr[d\mathbf{W}_{ij}^S]\mathbf{1}/3$ is the traceless symmetric part, while $d\mathbf{W}_{ij}^S = [d\mathbf{W}_{ij} + d\mathbf{W}_{ij}^T]/2$ is the symmetric part. $A(r)$, $B(r)$, $\tilde{A}(r)$, $\tilde{B}(r)$, and $\tilde{C}(r)$ are scalar functions having the following relation

$$\begin{aligned} A(r) &= \frac{1}{2}\left[\tilde{A}^2(r) + \tilde{C}^2(r)\right], \\ B(r) &= \frac{1}{2}\left[\tilde{A}^2(r) - \tilde{C}^2(r)\right] + \frac{1}{3}\left[\tilde{B}^2(r) - \tilde{A}^2(r)\right]. \end{aligned} \tag{3.23}$$

Note that if $\tilde{A}(r) = \tilde{C}(r) = 0$ and $B(r) = \gamma$ the standard dissipative and random forces are recovered (see section 2.2.2).

We define $A(r) = \gamma^T$ and $B(r) = \gamma^C$ resulting in $\mathbf{T}_{ij} = \gamma^T\mathbf{1} + \gamma^C\mathbf{e}_{ij}\mathbf{e}_{ij}$, where γ^T and γ^C are the dissipative coefficients. Using this definition the dissipative interactions become as follows

$$\mathbf{F}_{ij}^D = -\left[\gamma^T\mathbf{1} + \gamma^C\mathbf{e}_{ij}\mathbf{e}_{ij}\right]\cdot\mathbf{v}_{ij} = -\gamma^T\mathbf{v}_{ij} - \gamma^C(\mathbf{v}_{ij}\cdot\mathbf{e}_{ij})\mathbf{e}_{ij}, \tag{3.24}$$

where the first term provides a desirable viscous contribution, while the second term is analogous to the dissipative force in DPD. From the definitions above the random interactions are given by

$$\mathbf{F}_{ij}^R dt = \sqrt{2k_BT}\left(\sqrt{2\gamma^T}d\overline{\mathbf{W}_{ij}^S} + \sqrt{3\gamma^C - \gamma^T}\frac{tr[d\mathbf{W}_{ij}]}{3}\mathbf{1}\right)\cdot\mathbf{e}_{ij}. \tag{3.25}$$

Note that this equation imposes the condition $3\gamma^C > \gamma^T$. The defined dissipative and random forces in combination with an elastic spring constitute a viscoelastic spring whose equilibrium temperature k_BT is constant.

To relate the membrane shear viscosity η_m and the dissipative parameters γ^T, γ^C we subject the element of the hexagonal network (fig. 3.2) to a constant shear rate $\dot{\gamma}$ considering only viscous contribution of the dissipative force in equation (3.24). The shear stress τ_{xy} at short times can be well approximated as follows

$$\begin{aligned} \tau_{xy} = -\frac{1}{2A_0}\left[\gamma^T\dot{\gamma}\left(a_y^2 + b_y^2 + c_y^2\right) + \frac{\gamma^C\dot{\gamma}}{l_0^2}\left((a_xa_y)^2 + (b_xb_y)^2 + (c_xc_y)^2\right)\right] = \\ = \dot{\gamma}\left(\sqrt{3}\gamma^T + \sqrt{3}\gamma^C/4\right). \end{aligned} \tag{3.26}$$

The derivation of the equalities above is similar to that of the macroscopic shear modulus described in appendix B in detail. Hence, the membrane viscosity is given by

$$\eta_m = \frac{\tau_{xy}}{\dot{\gamma}} = \sqrt{3}\gamma^T + \frac{\sqrt{3}\gamma^C}{4}. \tag{3.27}$$

The relation above indicates that γ^T accounts for a large portion of viscous contribution than γ^C, and therefore γ^C is set to $\gamma^T/3$ in all simulations that follow.

3.2.5 Membrane-solvent boundary conditions

The described membrane model is filled and surrounded by different solvents that are represented by a collection of interacting particles. Figure 3.4 shows a snapshot of a RBC simulation in equilibrium. In order to impose appropriate boundary conditions (BCs) for the external/internal fluids on the membrane two matters need to be addressed:

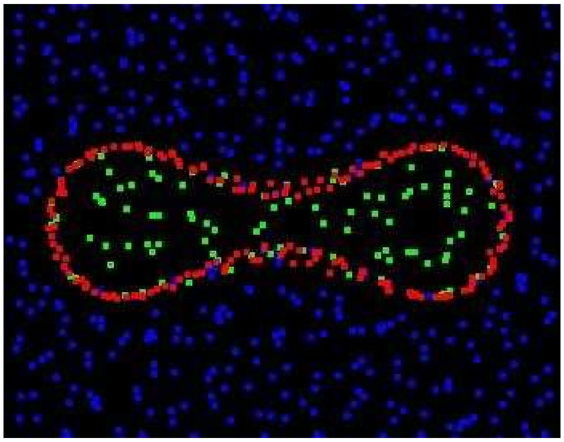

Figure 3.4: A slice through a sample equilibrium simulation with RBC vertices drawn by red particles, external fluid particles in blue, and the internal fluid in green.

i) membrane impenetrability to prevent mixing of the internal and the external fluids,

ii) no-slip BCs imposed by pairwise point interactions of the fluid and membrane particles.

Bounce-back reflections of fluid particles at the moving membrane triangular plaquettes impose the membrane impenetrability (see appendix C for details). In addition, bounce-back reflections of fluid particles result in a smaller slip at the membrane surface than, for example, specular reflections; however, no-slip is not guaranteed. Thus, dissipative interactions between the fluid and the membrane are needed to be enhanced to achieve no-slip at the membrane surface. For this purpose, the DPD dissipative force between fluid particles and membrane vertices has to be properly set.

Calculation of the dissipative force coefficient γ is based on the idealized case of linear shear flow over a flat plate. Under the continuum assumption the total shear force on the area A of the plate is equal to $A\eta\dot{\gamma}$, where η is the fluid's viscosity and $\dot{\gamma}$ is the local constant shear rate. To mimic the membrane surface a number of wall particles is distributed on the plate with a hexagonal configuration. The force on a single wall particle of such a system exerted by the surrounding fluid under shear can be expressed as

$$F_v = \int_{V_h} n g(r) F^D dV, \tag{3.28}$$

where F^D is the DPD dissipative force between fluid and wall particles, n is the fluid number density, $g(r)$ is the radial distribution function of fluid particles with respect to the wall particles, and V_h is the half sphere volume of fluid above the plate. Thus, the total shear force on the area A in this case is equal to $N_A F_v$, where N_A is the number of plate particles enclosed by the area A. The equality of $N_A F_v = A\eta\dot{\gamma}$ results in the expression of the dissipative force coefficient γ in terms of the fluid density and viscosity, as well as the wall density N_A/A, while under the assumption of linear shear flow the shear rate cancels out. This formulation results in satisfaction of the no-slip BCs for the linear shear flow over a flat plate. It also serves as an excellent approximation for no-slip at the membrane surface in spite of the assumptions made. Note that in the absence of conservative interactions between fluid particles and the membrane vertices, the radial distribution function takes a simple form $g(r) = 1$ and the integral above can be taken analytically.

3.2.6 Membrane triangulation

The average unstressed shape of a single RBC measured in the experiments in [65] is biconcave and is described by

$$z = \pm D_0 \sqrt{1 - \frac{4(x^2+y^2)}{D_0^2}} \left[a_0 + a_1 \frac{x^2+y^2}{D_0^2} + a_2 \frac{(x^2+y^2)^2}{D_0^4} \right], \tag{3.29}$$

where $D_0 = 7.82\ \mu m$ is the cell diameter, $a_0 = 0.0518$, $a_1 = 2.0026$, and $a_2 = -4.491$. The area and volume of this RBC is equal to 135 μm^2 and 94 μm^3, respectively. We have investigated three types of triangulation strategies:

- *Point charges*: N_v points are randomly distributed on a sphere surface, and the electrostatic problem of point charges is solved while the point movements are constrained on the sphere. After equilibrium is reached, the sphere surface is triangulated, and conformed to the RBC shape according to equation (3.29).
- *Advancing front*: The RBC shape is imported into commercially available grid generation software Gridgen [1] which performs the advancing front method for the RBC surface triangulation.
- *Energy relaxation*: First, the RBC shape is triangulated following the point charges or advancing front methods. Subsequently, relaxation of the free energy of the RBC model is performed while the vertices are restricted to move on the biconcave shape in equation (3.29). The relaxation procedure includes only in-plane and bending energy components and is done by flipping between the two diagonals of two adjacent triangles.

The triangulation quality can be characterized by two distributions: i) distribution of the link (edge) lengths, ii) distribution of the vertex degrees (number of links in the vertex junction). The former is characterized by the value $d(l) = \sigma(l)/\bar{l}$, where $\bar{l}$ is the average length of all edges, and $\sigma(l)$ is the standard deviation. The latter defines the regularity of triangulation by providing the relative percentage of degree-n vertices $n = 1 ... n_{max}$. Note that the regular network, from which the mechanical properties were derived, has only degree-6 vertices. Table 3.1 presents the *average* mesh quality data for different triangulation methods. Better mesh quality corresponds to a combination of smaller $d(l)$, higher percentage of degree-6, and smaller percentage of any other degree vertices, and is achieved for a larger number of points N_v. It seems that the best quality is reached with the energy relaxation method whereas the advancing front triangulation yields the lowest quality, which will be discussed further below.

Method	$d(l)$	degree-6	degree-5 and degree-7	other degrees
point charges	$[0.15, 0.18]$	$90\% - 95\%$	$5\% - 10\%$	0%
advancing front	$[0.13, 0.16]$	$45\% - 60\%$	$37\% - 47\%$	$3\% - 8\%$
energy relaxation	$[0.05, 0.08]$	$75\% - 90\%$	$10\% - 25\%$	0%

Table 3.1: Mesh quality for different triangulation methods.

3.2.7 Coarse-graining

For systematic coarse-graining the parameters of the fine or spectrin-level model have to be defined. Atomic force microscopy results [194, 192] show that each actin junction complex exists every $3000 - 5000$ nm^2. Taking into account that the average RBC area is equal to $A = 135$ μm^2 [65] we obtain that the RBC spectrin network has about $27000 - 45000$ junction complexes which represent the total number of vertices N_v in the spectin-level model. The spectrin-level model in this chapter is built by $N_v = 27344$ junction complexes. The effective equilibrium spectrin length l_0 is estimated as follows

$$A = N_t \cdot A_0 = (2N_v - 4) \cdot A_0 = (2N_v - 4) \cdot \frac{\sqrt{3}l_0^2}{4}, \tag{3.30}$$

and is equal to 75.5 nm. Note that l_0 lies in the range $59 - 76$ nm based on the number of junction complexes $27000 - 45000$. In order to define the maximum spectrin extension it is more convenient to set the value of the ratio $x_0 = l_0/l_m$, which is equal to 2.2 for the WLC models and 2.05 for FENE, and it governs the nonlinear spectrin response. This yields $l_m = 166.1$ nm for WLC and 154.8 nm for FENE models. Using the defined lengths and equation (3.10) with $\mu_0 = 6.3$ $\mu N/m$ we obtain the persistence length $p = 18.7$ nm for the WLC-C model at room temperature $T = 23^oC$ and the spring constant $k_s = 2.4$ $\mu N/m$ in case of the FENE-C model. The persistence length estimated here is about 2.5 times longer than $p = 7.5$ nm chosen in [42, 159]; however, both values are within the range obtained from experiments [20]. In part this difference can be reconciled by a choice of the effective spectrin-level model. From equation (3.10) for the WLC-C model we find that in order to have the same macroscopic shear modulus for a fixed x_0 but for a different number of the actin junction complexes N_v in the spectrin-level representation, the product pl_0 has to be kept constant. This implies that for a smaller number of vertices ($N_v = 27344$ in this case) the equilibrium spectrin length would increase while the persistence length becomes smaller. In addition, the estimated parameters depend on the spring model, such that for the cases of the WLC-POW and the FENE-POW models we obtain $p = 14.68\ nm$ and $k_s = 3.06\ \mu N/m$, respectively, while the power force parameter k_p found by equating the corresponding spring forces for $l_0 = 75.5\ nm$ is equal to $1.66 \times 10^{-27}\ Nm^2$ and $1.73 \times 10^{-27}\ Nm^2$ for the POW exponent $m = 2$.

Systematic RBC coarse-graining yields a model represented by a smaller number of vertices compared to the spectrin-level model, which is called the "fine" model further in the text. Equating the areas of the coarse-grained and fine models, we obtain the equilibrium and the maximum extension lengths (l_0 and l_m) for the coarse-grained RBC as follows

$$l_0^c = l_0^f \sqrt{\frac{N_v^f - 2}{N_v^c - 2}}, \qquad l_m^c = l_m^f \sqrt{\frac{N_v^f - 2}{N_v^c - 2}}, \tag{3.31}$$

where the superscripts c and f correspond to coarse-grained and fine models, respectively. For a fixed x_0 the shear and area-compression moduli remain unchanged for the coarse-grained model if the parameters are adjusted as follows

$$p^c = p^f \frac{l_0^f}{l_0^c}\ (WLC), \qquad k_s^c = k_s^f\ (FENE), \qquad k_p^c = k_p^f \left(\frac{l_0^c}{l_0^f}\right)^{m+1}\ (POW). \tag{3.32}$$

The equations (3.31, 3.32) define a complete set of parameters required for the model at an arbitrary coarse-graining level derived from the fine model.

3.2.8 Scaling of model and physical units

We now outline the scaling procedure, which relates the model's non-dimensional units to physical units. First, the equilibrium spring length $l_0 = l_0^M$ is chosen in our model units, where the superscript M denotes "model" and $[l_0^M] = r^M$ defines model length scale. Another parameter we are free to select is the imposed shear modulus $\mu_0 = \mu_0^M$ with $[\mu_0^M] = N^M/r^M = (k_BT)^M/(r^M)^2$, which will provide a scaling base. Use of WLC and FENE springs requires the maximum extension length l_m^M to be set; however, it is more convenient to set the ratio $x_0 = l_0^M/l_m^M$. Further we will show that the choice of x_0 does not affect the linear elastic deformation, but it governs the RBC nonlinear response at large deformations. For given l_0^M, μ_0^M and x_0 we can calculate the required spring parameters for a chosen model using equation (3.10). Then, the area-compression modulus K^M and the Young's modulus Y^M are found for the calculated spring parameters and given area constraint parameters (k_a and k_d) using equations (3.13, 3.14).

Once the model parameters are set, we can define the length scale based on the cell diameter $D_0^M = (L_x^M + L_y^M)/2$, where $[D_0^M] = r^M$ and L_x, L_y are the cell diameters in the x and y directions found from the equilibrium simulation of a single cell with the obtained model parameters. The length scale based on l_0^M appears to be inappropriate because, in general, the cell dimensions will depend on the relative volume-to-area ratio and to some extent on the current triangulation artifacts (discussed below). As an example, we can define an RBC and a spherical capsule with the same l_0^M, while the cell sizes would greatly differ. However, in general, D_0^M is proportional to l_0^M for fixed volume-to-area ratio. The real RBC has an average diameter $D_0^P = 7.82\ \mu m$ (superscript P denotes "physical"), and therefore the following length scale is adapted

$$r^M = \frac{D_0^P}{D_0^M} m, \tag{3.33}$$

where m stands for "meters". Further, the Young's modulus is used as the main scale parameter. Matching the model and physical Young's modulus $Y^M\ \frac{(k_BT)^M}{(r^M)^2} = Y^P\ \frac{(k_BT)^P}{m^2}$ provides us with the energy unit scale as follows

$$(k_BT)^M = \frac{Y^P}{Y^M}\frac{(r^M)^2}{m^2}(k_BT)^P = \frac{Y^P}{Y^M}\left(\frac{D_0^P}{D_0^M}\right)^2 (k_BT)^P. \tag{3.34}$$

In general, if the membrane is nearly incompressible, the scaling based on the shear modulus is exactly the same as above. After we determined the model energy unit (as an example for room temperature $T = 296\ K$), we calculate the bending rigidity k_b in model energy units using equation (3.21). In addition, we define the force scale, N^M, by

$$N^M = \frac{(k_BT)^M}{r^M} = \frac{Y^P}{Y^M}\frac{D_0^P}{D_0^M}\frac{(k_BT)^P}{m} = \frac{Y^P}{Y^M}\frac{D_0^P}{D_0^M}N^P. \tag{3.35}$$

Scaling of model and physical mechanical properties does not require an explicit definition for the time scale as outlined above; however, it is necessary for the membrane rheology and dynamics. The scaling between model and physical times is defined as follows

$$\tau = \left(\frac{t_i^P}{t_i^M} \right)^{\alpha} s = \left(\frac{D_0^P}{D_0^M} \frac{\eta^P}{\eta^M} \frac{Y_0^M}{Y_0^P} \right)^{\alpha} s, \qquad t_i = \frac{D_0 \eta}{Y_0}, \tag{3.36}$$

where τ is the model time, η is a characteristic viscosity, t_i is the intrinsic time, and α is the scaling exponent. Note that α characterizes time scale dependence, and is not necessarily equal to one with numerous examples in rheology.

3.3 RBC mechanical properties

The elastic shear modulus μ_0 measured experimentally lies between 2 and 12 $\mu N/m$ and the bending modulus k lies between 1×10^{-19} and 7×10^{-19} J, which corresponds to the range of $25 - 171$ $k_B T$ based on the room temperature $T = 23^o C$. Since the precise geometry is often not known, the discrepancies in the measurements arise, in part, from overly simplified geometrical models used to extract values from the measured forces. In such cases, accurate numerical modeling can provide a valuable aid in experimental parameter quantification.

In recent optical-tweezers stretching experiments [190] the RBC behavior was modeled as a hyperelastic material together with the finite element method (FEM). From the FEM simulations a membrane shear modulus μ_0 in the range $5 - 12$ $\mu N/m$ was obtained. This corresponds to the Young's modulus of $Y = 3\mu_0 = 15 - 36$ $\mu N/m$ due to the use of a three-dimensional membrane model. Dao et al. [42] performed coarse-grained molecular dynamics (CGMD) simulations of the spectrin-level cytoskeleton which yielded a worse comparison to the experimental stretching response than FEM. Their derivation of the shear modulus μ_0 and the area-compression modulus K did not take into account the area constraint providing the estimated area-compression modulus to be $K = 2\mu_0$. This results in a Young's modulus underprediction by about 50% and explains the poor performance of the spectrin-level model in comparison with FEM.

3.3.1 RBC stretching: success and problems

Next, we performed RBC stretching simulations and compared the results with the experimental data of RBC deformation by optical tweezers [190]. Here, we used the average RBC diameter of $D_0^P = 7.82$ μm. The aforementioned FEM simulations of RBC membrane [190] showed an agreement with the experimental data for $\mu_0^P = 5.3$ $\mu N/m$; however, we found that a slightly better correspondence of the results was achieved for $\mu_0^P = 6.3\ \mu N/m$ and $Y^P = 18.9\ \mu N/m$ (two-dimensional properties of the three-dimensional elastic model), which we selected to be the targeted properties. Table 3.2 shows a set of the model and physical RBC parameters using the coarse-graining procedure described in section 3.2.7. In all cases $\mu_0^M = 100$, while x_0 was equal to 2.2 for the WLC models and 2.05 for the FENE models, and the exponents $q = 1$ (eq. (3.2)) and $m = 2$ (eq. (3.5)). The area and volume constraints coefficients were set to $k_a = 5000$, $k_d = 0$, and $k_v = 5000$ for WLC-C and FENE-C models, while $k_a = 4900$, $k_d = 100$, and $k_v = 5000$ for the WLC-POW model. The triangulation for all N_v was performed using the energy relaxation method. The imposed Young's modulus for all cases was $Y^M = 392.453$, which is about 2% lower than that in the incompressible limit $Y^M = 4\mu_0^M = 400$. Using equation (3.34) we found the energy unit $(k_BT)^M$ based on $(k_BT)^R$ at room temperature $T = 296\ K$. The bending rigidity k_c was set to $2.4 \times 10^{-19} J$, which seems to be a widely accepted value and is equal to approximately $58(k_BT)^R$. The total RBC area A_0^{tot} was equal to $N_t\frac{\sqrt{3}}{4}(l_0^M)^2$, where N_t is the total number of triangle plaquettes with the area $A_0 = \frac{\sqrt{3}}{4}(l_0^M)^2$. Note that for all triangulations used here $N_t = 2N_v - 4$. The total RBC volume V_0^{tot} was found according to the following scaling $V_0^{tot}/(A_0^{tot})^{3/2} = V^R/(A^R)^{3/2}$, where $V^R = 94\ \mu m^3$ and $A^R = 135\ \mu m^2$ according to the average RBC shape described by equation (3.29).

Model	N_v	l_0^P	p^P or k_s^P	l_0^M	D_0^M
WLC-C	500	5.58×10^{-7}	2.53×10^{-9}	0.56	8.267
WLC-C	1000	3.95×10^{-7}	3.58×10^{-9}	0.4	8.285
WLC-C	3000	2.28×10^{-7}	6.19×10^{-9}	0.23	8.064
FENE-C	500	5.58×10^{-7}	2.4×10^{-6}	0.56	8.265
WLC-POW	500	5.58×10^{-7}	1.99×10^{-9}	0.56	8.25

Table 3.2: RBC physical (“P” in SI units) and simulation (“M” in model units) parameters.

The RBC was suspended in a solvent which consists of free DPD particles with the number density $n = 3$. Note that the macroscopic solvent properties (e.g., viscosity) were not important here, because we were interested in the final cell deformation for every constant stretching force. Thus, we allowed enough time for the RBC to reach its final deformation state without close monitoring of the stretching dynamics. Meanwhile, the solvent maintained the temperature at the constant value of $(k_BT)^M$.

Figure 3.5 shows a sketch of the RBC before and after deformation. The total stretching force F_s^P was in the range 0...200 pN, which was scaled into model units F_s^M according to equation (3.35). The total force F_s^M was applied to $N_+ = \epsilon N_v$ vertices (drawn as small black spheres in figure 3.5) of the membrane with the largest x-coordinates in the positive x-direction, and correspondingly $-F_s^M$ was exerted on $N_- = N_+$ vertices with the smallest x-coordinates in the negative x-direction. Therefore, a vertex in N_+ or N_- was subject to the force $f_s^M = \pm F_s^M/(\epsilon N_v)$. The vertex fraction ϵ was equal to 0.02 corresponding to a contact diameter of the attached silica bead $d_c = 2\ \mu m$ used in experiments. The contact diameter was measured as $\left(\max_{ij}|y_i^+ - y_j^+| + \max_{ij}|y_i^- - y_j^-|\right)/2$, where y_i^+, y_j^+ and y_i^-, y_j^- are the y-coordinates of vertices in N_+ and N_-, respectively. The simulations for the given force range were performed as follows: i) $B = 16$ was chosen, which defines the force increment $\Delta F_s^P = 200\ pN/B$ with corresponding ΔF_s^M. ii) The loop $i = 1...B$ was run with the stretching force $i{\cdot}\Delta F_s^M$ during time 2τ each. The time τ was long enough in order for the RBC to converge to the equilibrium stretched state for the given force. Thus, the time $[0, \tau]$ was the transient time for convergence, and during time $[\tau, 2\tau]$ the deformation response was calculated. The axial diameter D_A was computed over time τ as $|x_{max} - x_{min}|$, where x_{max} is the maximum x position among the N_+ vertices, while x_{min} is the minimum among N_-. The transverse diameter D_T was calculated as $2 \times \max_{i=1...N_v}\sqrt{(y_i - c_y)^2 + (z_i - c_z)^2}$, where c_y, c_z are the y and z center of mass coordinates.

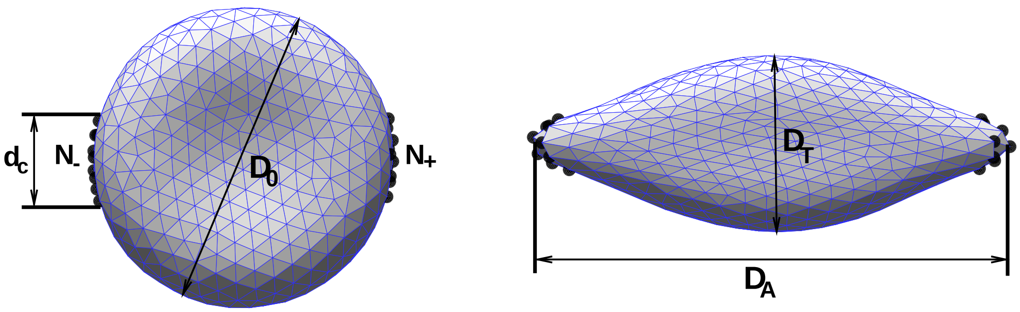

Before stretch **After stretch**

Figure 3.5: RBC sketch before and after deformation.

Figure 3.6 presents the RBC stretching response for a different number of vertices N_v (left) and spring models (right) with RBC parameters from table 3.2; also included are experimental results [190] and the spectrin-level RBC model results of [42]. Independent of the number of vertices or spring model we find excellent agreement of the simulation results with the experiment. A noticeable disagreement in the transverse diameter may be partially due to experimental errors arising from the fact that the optical measurements were performed from a single observation angle. RBCs subjected to stretching may rotate in y-z plane as observed in our numerical simulations, and therefore measurements from a single observation angle may result in underprediction of the maximum transverse diameter. However, the simulation results remain within the experimental error bars. The solid line in figure 3.6 corresponds to the spectrin-level RBC [42] of a similar type employing the WLC-C model. Their derivation of linear elastic properties did not include a contribution of the area constraint, which results in the Young's modulus being underpredicted by about 50%. From the region of small near-linear deformation ($0 - 50\ pN$), it is apparent that the solid line corresponds to a membrane with a larger Young's modulus compared to the experiment. In addition, the ratio x_0 was set to 3.17, which results in near-linear elastic deformation, and ignores the nonlinear RBC response at large deformations. Finally, we note that the FENE-C model appears to be less stable (requires a smaller time step) at large deformations due to a more rapid spring hardening compared to WLC-C. The WLC-POW model performs similarly to WLC-C; however, a weak local area constraint ($k_d > 0$)

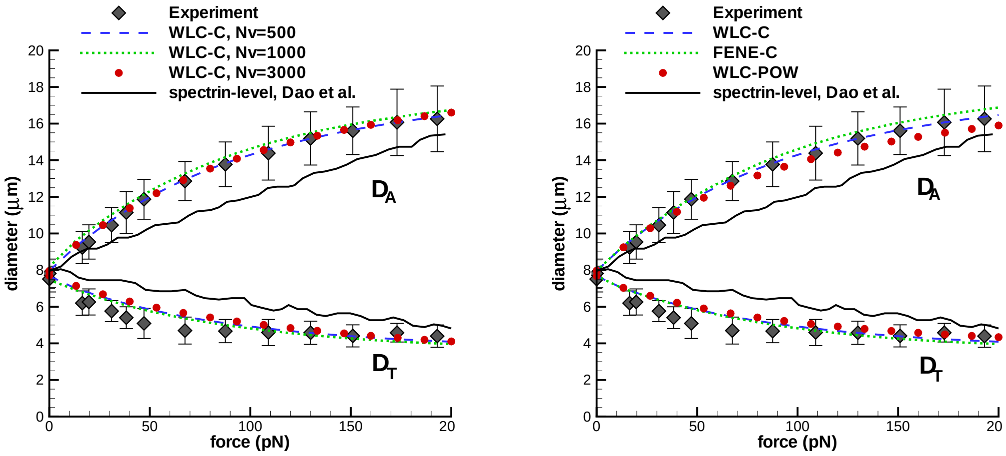

Figure 3.6: Computational results for *different* N_v (left) and *spring models* (right) compared with the experiments in [190] and the spectrin-level RBC model in [42].

may be required for stability at large deformations as it mimics the second in-plane force term in equation (3.2) for the WLC-C model. Figure 3.7 demonstrates typical RBC shape evolution from equilibrium (0 pN force) to 100 pN total stretching force for different N_v using the WLC-C model. Note that the RBCs show local anomalous surface features (hills) in equilibrium which are due to local membrane stresses since it is not possible to have regular hexagonal triangulation of the RBC surface with equal edges. The strength of the local buckling depends on the relative interplay of the in-plane elasticity and bending rigidity. Increase of the membrane bending stiffness results in a smoother RBC surface, while a decrease would result in a more buckling. However, this feature seems to be less pronounced for higher N_v. Other membrane models yield similar shapes.

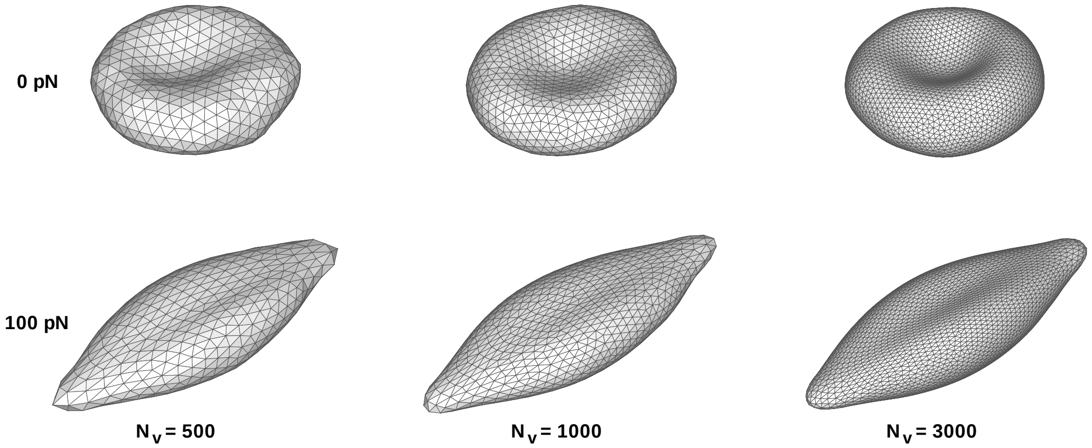

Figure 3.7: RBC shape evolution at *different* N_v and *total stretching forces* for the WLC-C model.

Despite the demonstrated success of the RBC models, several problems remain due to the fact that the membrane is not stress-free. Figure 3.8 shows the RBC response of the WLC-C ($N_v = 500$) model for different stretching directions (left) with energy relaxation triangulation and the RBC response for models with different triangulations (right). While the RBC triangulated through the energy relaxation method gives satisfactory results with differences in the stretching response on the order of $5-8\%$, RBCs triangulated by other methods show a much greater discrepancy with the experiment. Figure 3.9 shows the RBC shapes at equilibrium and at the stretching force of 100 pN for point charges, advancing front triangulations (WLC-C model), and for a “stress-free” model introduced in the next section. The RBCs triangulated by point charges and advancing front methods show pronounced

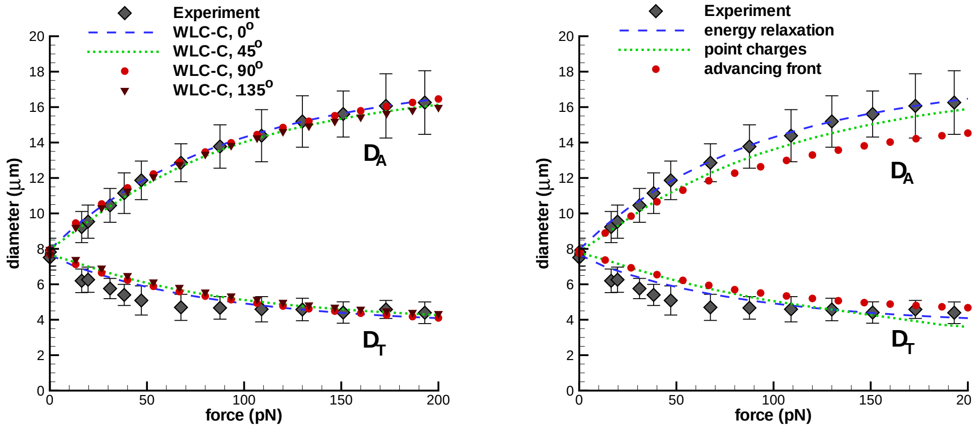

Figure 3.8: RBC stretching along lines with *different orientation angles* (left) and *triangulation methods* (right) compared with the experiments in [190].

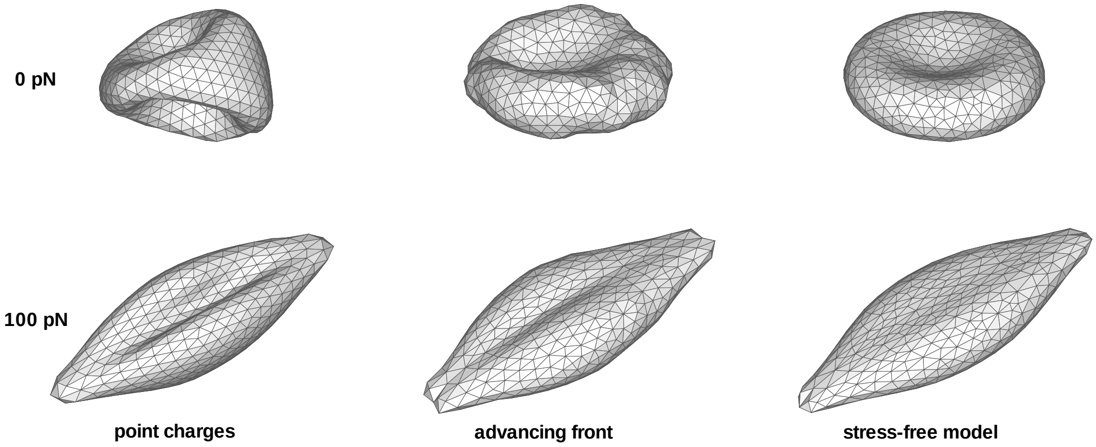

Figure 3.9: RBC shape evolution for *different triangulations* and the *stress-free model* introduced in the next section.

buckling and a non-biconcave shape for realistic bending and elastic RBC properties due to stronger local stresses arising from more irregular triangulation when compared to the energy relaxation mesh. In order to obtain a smooth biconcave shape the membrane bending rigidity has to be set to about $500(k_BT)^R$ and $300(k_BT)^R$ for point charges and advancing front methods, respectively, which is much higher than the bending rigidity of the real RBC of about $58(k_BT)^R$. Local buckling features are less pronounced for stretched cells since the membrane is subject to strong stretching stresses. Moreover, figure 3.8 shows that these models have higher effective elastic moduli than those measured, as they are subject to a higher membrane stress at equilibrium due to triangulation artifacts. Also, they appear to yield a stronger stretching anisotropy $(10 - 15\%)$ compared to the free energy relaxation method. The effect of local stresses on the membrane equilibrium shape appears to be a drawback for existing models [126], which is often compensated by setting artificially high values for the bending rigidity. Figure 3.9 also shows the corresponding RBC shapes (advancing front triangulation) with a "stress-free" model which proves to be independent of triangulation and will be proposed next.

3.3.2 Stress-free membrane model

To eliminate the aforementioned membrane stress anomalies we propose a simple "annealing" procedure. For each spring we define l_0^i $i = 1...N_s$ which are set to the edge lengths after the RBC shape triangulation, since we assume it to be the equilibrium state. Accordingly we define $l_m^i = l_0^i \times x_0$ and A_0^j $j = 1...N_t$ for each triangular plaquette. The total RBC area $A_0^{tot} = \sum_{j=1...N_t} A_0^j$ and the total volume V_0^{tot} is calculated from the RBC triangulation. Then, we define the average spring length as $\bar{l}_0 = \sum_{i=1...N_s} l_0^i$, and the average maximum spring extension as $\bar{l}_m = \bar{l}_0 \times x_0$; these are then used in the linear elastic properties estimation using equations (3.10 and 3.13). Here, we omit the WLC-C and FENE-C models because it may not be possible to define a single in-plane area expansion potential (the second force term in equation (3.2)) which would define different individual equilibrium spring lengths for a triangle with distinct sides. However, for the WLC-POW and FENE-POW models the individual equilibrium spring length can be simply defined. Based on given $\bar{l}_0$, $\bar{l}_m$ and μ_0^M the WLC or FENE spring parameters (p or k_s) can be calculated analogously to the previous model and then set to the same value for all springs. Then, the individual power force coefficients k_p^i $i = 1...N_s$ (eq. (3.5)) are defined for each spring in order to set the given equilibrium spring lengths l_0^i. An additional generalization of the model is to define individual spring parameters (p^i or k_s^i) and the power force coefficients k_p^i for all springs. Here, a system of two constraints (equilibrium length l_0^i and imposition of μ_0^M) needs to be solved for every spring. However, computational results did not differ for both stress-free approaches for the studied membranes.

We perform tests using the WLC-POW model for different triangulation methods and number of vertices. Table 3.3 shows a set of the model and physical RBC parameters. Other parameters are $\mu_0^M = 100$, $x0 = 2.2$, $m = 2$ (eq. (3.5)), $k_a = 4900$, $k_d = 100$, and $k_v = 5000$. Figure 3.10 presents simulation results for $N_v = 500$ with different triangulations (left) and

N_v	l_0^P	p^P	$\bar{l}_0^M$	D_0^M
27344	7.55×10^{-8}	14.68×10^{-9}	0.15	15.87
9128	1.31×10^{-7}	8.48×10^{-9}	0.13	8.12
3000	2.28×10^{-7}	4.86×10^{-9}	0.23	8.07
1000	3.95×10^{-7}	2.81×10^{-9}	0.4	8.07
500	5.58×10^{-7}	1.99×10^{-9}	0.56	8.06
250	7.8×10^{-7}	1.4×10^{-9}	0.79	8.08
100	1.25×10^{-6}	8.88×10^{-10}	1.23	8.05

Table 3.3: RBC physical ("P" in SI units) and simulation ("M" in model units) parameters. Stress-free model.

a range of the number of vertices N_v from 100 to 27344 (right). A substantial improvement

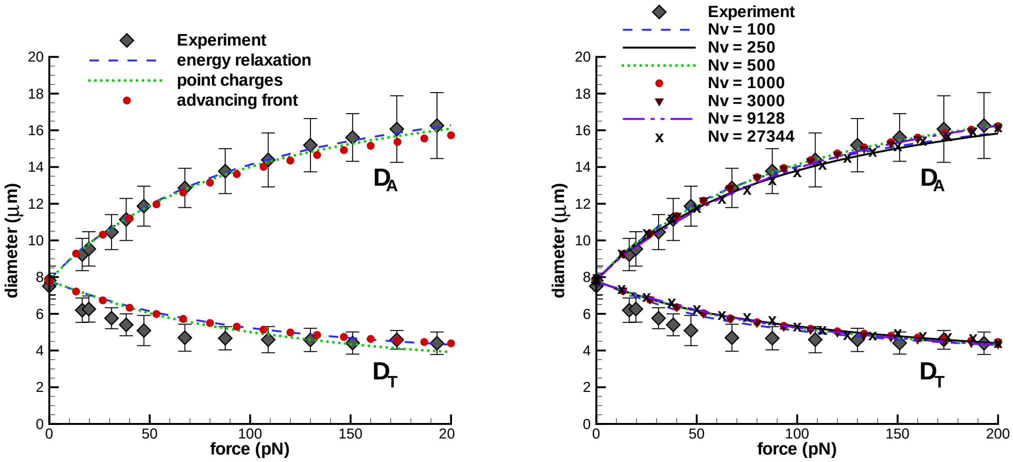

Figure 3.10: Stress-free RBC model for different triangulation methods with $N_v = 500$ (left) and number of vertices with the energy relaxation triangulation (right) compared with the experiments in [190].

is observed when compared with the results in figure 3.8 (right). Note that the stress-free model, when probed along different stretching directions results in deviation in the stretching response on the order of 1% for the free energy triangulation method and about $3 - 5\%$ for the other triangulation techniques. In addition, the stress-free model eliminates equilibrium shape artifacts for different triangulations shown in figure 3.9, and can be used even in cases of much lower bending rigidity. The stretching response for different number of vertices shows excellent agreement with the experimental results. Here, $N_v = 27344$ corresponds to a spectrin-level of RBC modeling as in [126], while $N_v = 100 - 500$ is a highly coarse-grained RBC. Figure 3.11 presents RBC shapes for the cases of high coarse-graining and spectrin-level models. Even though the coarse-grained model of $N_v = 100$ yields correct mechanical deformation results, it does not provide an accurate or smooth RBC shape description, which can be of importance in RBC dynamics. We suggest the minimum N_v to be used for the RBC model should be about $250 - 300$.

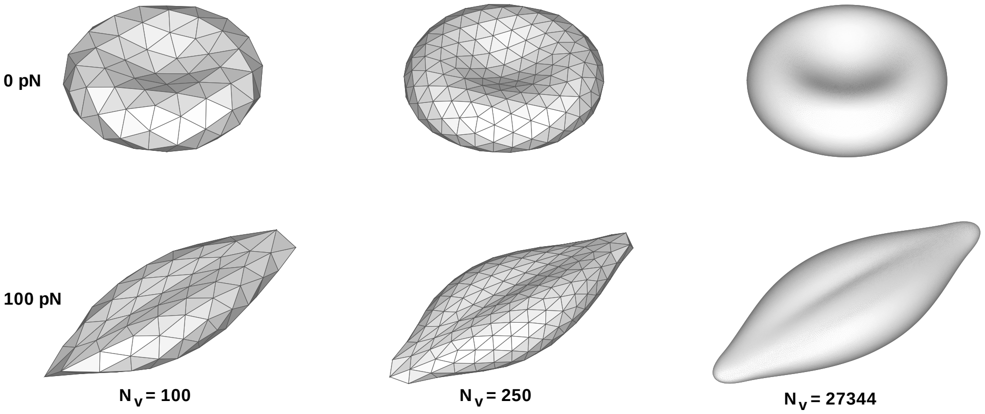

Figure 3.11: RBC shapes for highly coarse-grained models ($N_v = 100,\ 250$) and the spectrin-level model ($N_v = 27344$).

The dependence of the RBC deformation response on the ratio x_0 and on the number of vertices N_+, N_- (figure 3.5) is shown in figure 3.12. As mentioned above, small RBC

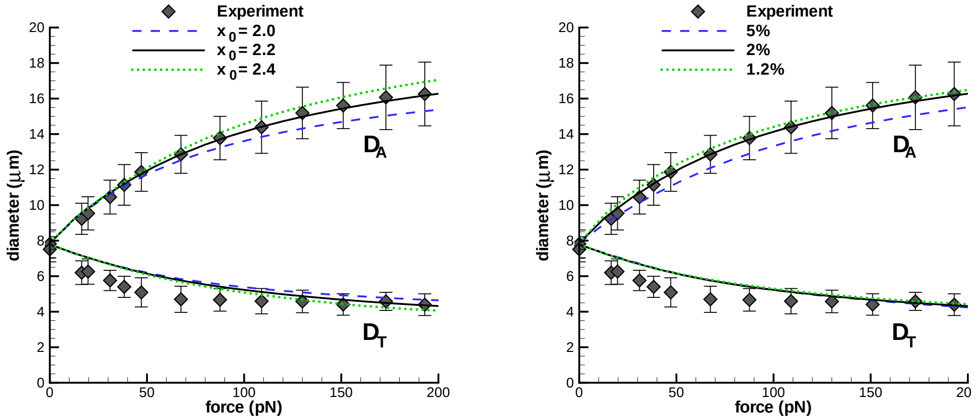

Figure 3.12: The stretching response of the stress-free RBC model for different ratio x_0 (left) and number of vertices in percents which are subject to the stretching force (right) compared with the experiments in [190].

deformations are independent of the ratio x_0; however, at large deformations this parameter plays a significant role and governs the nonlinear RBC response. In addition, figure 3.12 (right) shows that the RBC response is sensitive to the fraction of vertices (shown in percent) to which the stretching force is applied. It is equivalent to changing d_c in figure 3.5, which characterizes the attachment area of the silica bead in the experiments.

3.3.3 Comparison with a single spectrin tetramer

It is rather remarkable that RBCs can be accurately modeled with just a few hundred points, which is about one hundred times computationally cheaper than the spectrin-level RBC model, where $N_v \sim 27000$. At the spectrin-level of RBC modeling, each spring represents a single spectrin tetramer, and therefore the spring force WLC-POW should mimic the spectrin tetramer deformation response. We are not aware of any experimental single spectrin stretching results; however, in [142] this has been done by means of numerical simulation using coarse-grained molecular dynamics (CG-MD). Figure 3.13 compares the single spectrin-tetramer stress-strain response to the spring force of the spectrin-level RBC model. The “WLC-POW fit” curve assumes that the maximum extension spring length is 200 nm as in the CG-MD simulations of [142], which corresponds to $l_0 = 91$ nm with $x_0 =$

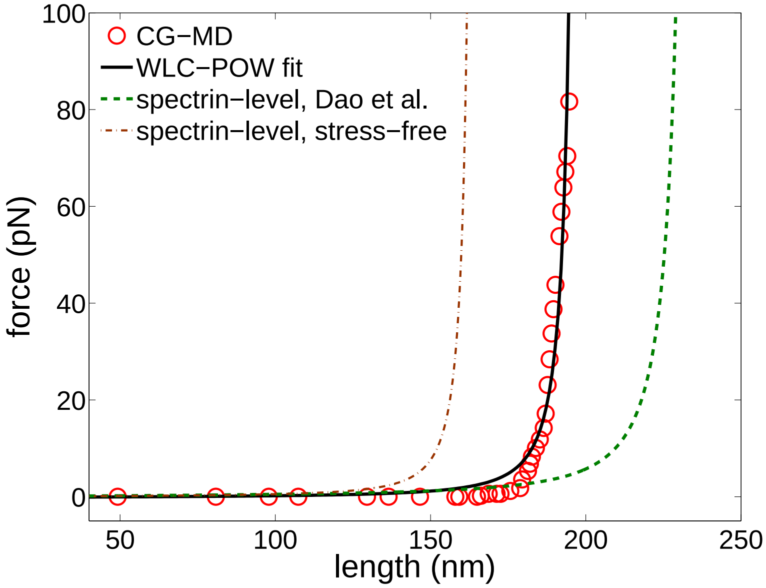

Figure 3.13: A single spectrin-tetramer stress-strain response [142] compared to the spring force of the spectrin-level RBC model.

2.2. This equilibrium length corresponds to an effective spectrin-level model represented by $N_v = 18826$ (eq. (3.30)) actin junction complexes, which is lower than that found in atomic force microscopy experiments [194, 192]. The dashed line in figure 3.13 corresponds to the spring force of the spectrin-level model in [42] with parameters $l_0 = 75\ nm$, $x_0 = 3.17$, and $l_m = 237.75\ nm$ which results in about 50% underprediction of the macroscopic Young's modulus. Finally, the dash-dotted line corresponds to our stress-free spectrin-level model with $N_v = 27344$. The discrepancy between the CG-MD and the spectrin-level models arises from great variability in the spectrin structure characterized by variable spectrin lengths and numbers of actin junction complexes. As discussed in the coarse-graining section 3.2.7 for the effective spectrin-level model, the equilibrium spectrin length is directly related to the number of junction complexes. However, the spectrin-level model spans a wide range in terms of the number of junction complexes, i.e. $27000 - 45000$, as documented in [194, 192].

3.3.4 Pf-parasitized RBCs

One of the main characteristics of the malaria disease is progressive changes in RBC mechanical properties and geometry. Progression through the parasite development stages (ring → trophozoite → schizont) leads to a considerable stiffening of infected RBCs in comparison with healthy ones [190, 158]. In addition, the schizont stage is often characterized by "near spherical" RBC shape, while the preceding stages maintain their biconcavity.

Figure 3.14 shows a comparison of simulation results of healthy and parasitized RBCs at different stages compared with the optical tweezers experiments [190]. The simulation results were obtained with the stress-free model ($N_v = 500$) having $\mu_0 = 6.3\ \mu N/m$ for the healthy RBC, 14.5 for the ring stage, 29 for the trophozoite, and 60 $\mu N/m$ for the schizont, which is consistent with the experiments [190, 158]. The ratio x_0 is equal to 1.8 for the infected RBCs. The bending rigidity is set to $2.4 \times 10^{-19}\ J$ for all cases, as the dependence of the membrane bending stiffness for different stages is not known. The additional simulation curve for the schizont stage marked "near spherical" corresponds to stretching a membrane of ellipsoidal shape with the axes $a_x = a_y = 1.2a_z$. Here, the membrane shear modulus is found to be 40 $\mu N/m$ in order to match the stress-strain response with the experiment, which is smaller than that for the biconcave-shape simulation. For the near-spherical cell geometry a membrane is subject to a stronger local stretching for the same uniaxial deformation compared to the biconcave shape. In the case of the

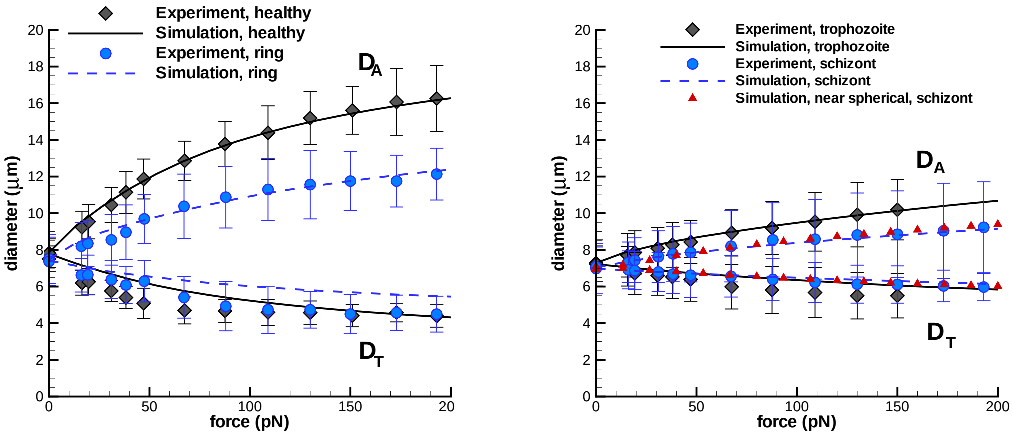

Figure 3.14: The stretching response of healthy and Pf-parasitized RBCs for different stages compared with the experiments in [190].

deflated biconcave shape the inner fluid volume can be deformed in response to stretching, while in the near-spherical shape the fluid volume applies an additional resistance onto the stretched membrane. Experiments show that for the schizont stage the RBC has a near-spherical shape, and therefore the ellipsoidal geometry should be more accurate. In conclusion, the cell geometry plays an important role and has to be closely modeled for accurate extraction of parameters from experiments. Figure 3.15 presents typical RBC shapes for the schizont stage using the original WLC-C model and the stress-free model for biconcave and near-spherical geometry. The WLC-C model shows strong local buckling due

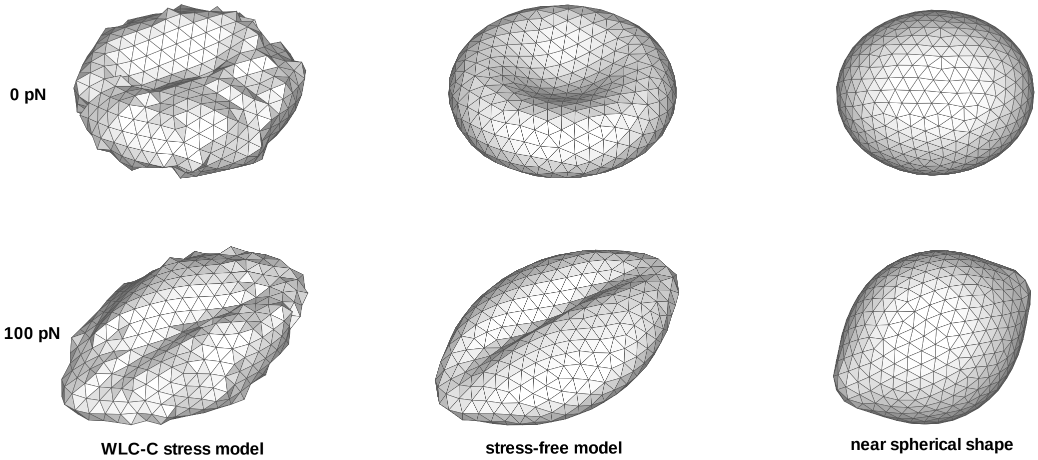

Figure 3.15: Malaria infected RBC shape evolution at the schizont stage for original and stress-free models, and near-spherical shape.

to local stress anomalies, which is not completely eliminated even for the stretching force of 100 pN, while the stress-free model yields a smooth RBC surface.

3.4 Rheology

The first experiments to obtain RBC rheological characteristics employed a creep test and cell extensional recovery [104] to derive the RBC relaxation time scale, which was found to be on the order of $t_c = 0.1$ seconds. However, this technique cannot provide a quantitatively accurate characteristic membrane time scale since whole cell deformations result in non-uniform strains and strain-rates along the RBC [213] as shown below. Recent experiments [167] used optical magnetic twisting cytometry (OMTC) to obtain the dynamic complex modulus of the membrane, a basic rheological characteristic of viscoelastic materials. In another set of experiments [161, 10], membrane thermal fluctuations were measured resulting in the complex modulus in qualitative agreement with OMTC. These experiments provide enough evidence for the RBC membrane to be viscoelastic.

RBCs parasitized by Plasmodium falciparum (Pf) become much stiffer than healthy ones and may change their morphology. In addition, cell rheological properties are greatly affected in malaria disease as shown in OMTC experiments [133]. Measurements of thermal fluctuations on the membrane surface [158] showed a significant decrease in fluctuations as the parasite develops, confirming the increase in RBC stiffness. Moreover, experiments [158, 133] with infected RBCs at different temperatures showed an additional membrane stiffening at febrile temperature (41^o C) in comparison with those at physiological temperature (37^o C).

Most of the current RBC models are purely elastic and lack viscous contribution in the membrane. As a result they cannot reproduce the single RBC response to time-dependent loads and may also yield an incorrect rheology of the cell suspension (blood). Further, our viscoelastic model is subjected to several rheological tests in comparison with the experiments, a topic that has not been previously addressed. Both healthy and Pf-parasitized RBCs (often denoted as Pf-RBCs) are considered.

3.4.1 Twisting torque cytometry

The twisting torque cytometry (TTC) is a numerical analog of the experimental technique OMTC [167], where a ferrimagnetic microbead is attached to the RBC top and is subjected to an oscillating magnetic field. In TTC, an attached to the membrane microbead is subjected to an oscillating torque. Bead response is measured in both experiments and simulations resulting in the dynamic complex modulus of healthy and infected RBCs as shown below.

3.4.1.1 Healthy RBCs

Figure 3.16 shows a sketch of TTC where a microbead is attached to the RBC top with an oscillating torque applied. In analogy with the experiments, the modeled RBC is attached to a solid surface, where the wall-adhesion is modeled by keeping fifteen percent of vertices stationary on the RBC bottom, while other vertices are free to move. The adhered RBC is filled and surrounded by fluids having viscosities much smaller than the membrane viscosity; thus, only the membrane viscous contribution is measured. The microbead is represented by a set of vertices on the corresponding sphere, that move as a rigid body. The attachment is simulated by including several RBC vertices near the microbead bottom into the rigid

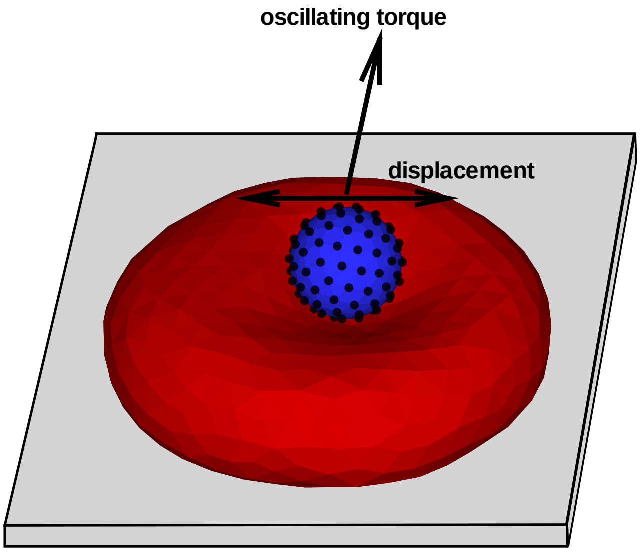

Figure 3.16: A sketch of the numerical setup of the twisting torque cytometry with the attached microbead subjected to the oscillating torque.

microbead motion, while the torque on the microbead is applied only to its vertices. Figure 3.17 presents a typical bead response for different torque frequencies obtained from TTC. The bead movement measured as the center-of-mass displacement maintains the same oscillating frequency compared to the torque per unit volume, but it is shifted by a phase angle ϕ depending on the oscillating frequency. For example, for a purely elastic material the phase angle ϕ is equal to zero independent of the torque frequency under the assumption of no inertial effects. For viscoelastic materials the phase angle increases with frequency as shown in figure 3.17. The linear complex modulus can be extracted from a dependence of the phase angle on the torque frequency as follows

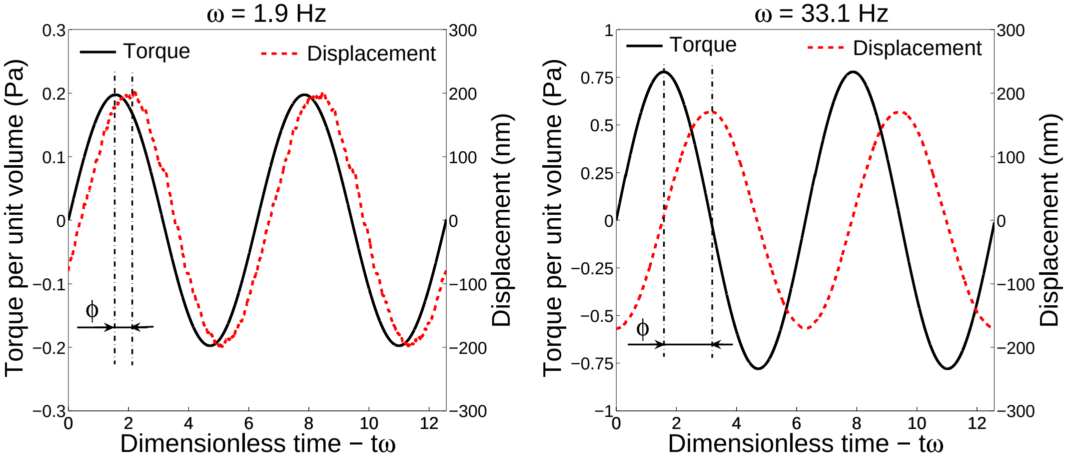

Figure 3.17: A characteristic response of an attached microbead subjected to the oscillating torque per unit volume (normalized by the bead volume) for different frequencies.

$$g'(\omega) = \frac{\Delta T}{\Delta d}\cos(\phi), \qquad g''(\omega) = \frac{\Delta T}{\Delta d}\sin(\phi), \tag{3.37}$$

where $g'(\omega)$ and $g''(\omega)$ are the *two-dimensional* storage and loss moduli (G' and G'' in 3D), and ΔT and Δd are the torque and bead displacement amplitudes. Under the assumption of no inertial effects the phase angle lies in the range between 0 and $\pi/2$, but it can be larger than $\pi/2$ otherwise.

Figure 3.18 presents components of the complex modulus compared with the experimental data [167]. We find a good agreement of the membrane moduli in simulations with the experimental data for the bending rigidity $k_c = 4.8 \times 10^{-19}\ J$ and the membrane viscosity $\eta_m = 0.022\ Pa \cdot s$. Twisting torque cytometry showed that the storage modulus assumes the following dependence $g'(\omega) \sim k_c^{0.65} Y_0^{0.65}$. Figure 3.18 shows dependence of g'

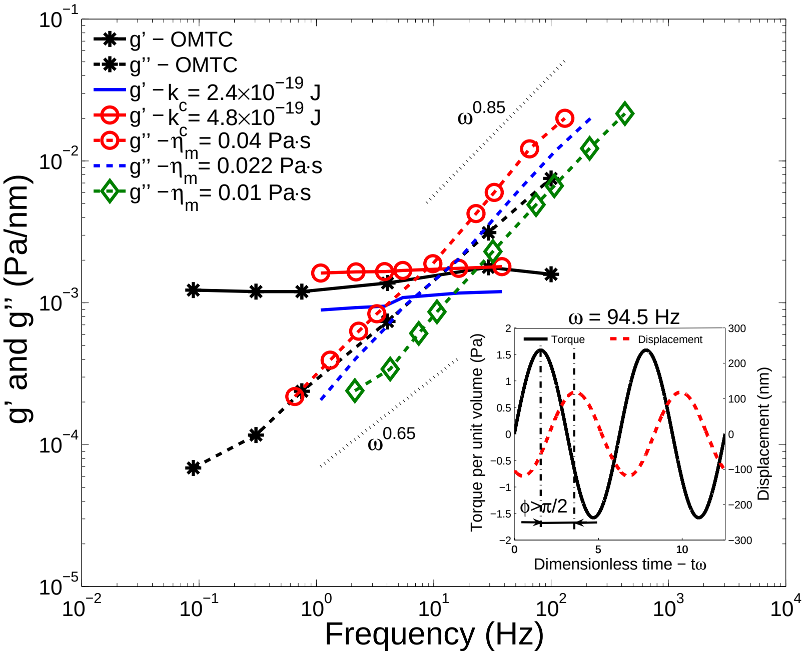

Figure 3.18: g' and g'' of healthy RBCs obtained from TTC simulations for different membrane viscosities and bending rigidities in comparison with the OMTC experiments [167]. The inclusion figure demonstrates presence of inertial effects in simulations at high frequencies of the torque.

on only the bending rigidity of the membrane since the Young's modulus of healthy RBCs was obtained and fixed by the RBC stretching tests described in section 3.3. Note that the comparison indicates that bending rigidity of a healthy RBC should be equal to about 4 to 5×10^{-19} J, which is twice larger than the value of $k_c = 2.4 \times 10^{-19}$ J used in many publications. The loss modulus g'' is independent of the membrane elastic properties and is governed by the RBC viscosity. Here, the time scale assumes the exponent $\alpha = 0.85$ and $\eta = \eta_m$ in equation (3.36) since the loss modulus shows similar dependence with respect to frequency. The exponent of g'' in simulations is equal to 0.85, while it was reported to be 0.64 in the experiments. This discrepancy may result from fitting errors in both simulations and experiments since data were fitted over only two orders of magnitude in frequency. In addition, we can define a RBC characteristic time t_c found as the g' and g'' intersection, which uniquely relates the membrane elastic properties and the viscous dissipation. From the intersection in figure 3.18 we obtain $t_c = 1/\omega_c \approx 0.1$ s, in agreement with the RBC characteristic relaxation time found in RBC recovery experiments [104].

The inset plot in figure 3.18 illustrates that for high frequencies inertial effects are observed in TTC simulations especially affecting the results for g'. Decreasing of the bead mass allows us to obtain rheological data for higher torque frequencies, but it may be computationally expensive since much smaller timesteps in simulations are required to ensure numerical stability. In addition, when the loss modulus (g'') dominates the storage modulus (g') the bead-displacement amplitudes become extremely small for a fixed torque resulting in difficulties to obtain reliable displacement measurements in experiments. However, in simulations it is possible to successfully detect bead displacements on the order of several nanometers.

3.4.1.2 Pf-parasitized RBCs

Here, the twisting torque cytometry technique is applied to Pf-RBCs at different stages of the parasite development. TTC for healthy RBCs in the previous section revealed that the storage modulus (g') depends on the membrane elastic properties and bending rigidity, while the loss modulus (g'') is governed by the membrane viscosity. The stretching tests on the parasitized RBCs in section 3.3.4 resulted in the shear modulus $\mu_0 = 14.5\ \mu N/m$ for the ring stage, 29 $\mu N/m$ for the trophozoite, and 60 $\mu N/m$ for the schizont at room temperature $T = 23^o$ C. However, potential changes in the bending stiffness and the membrane viscosity for different stages are not known, and therefore, we set $k_c = 2.4 \times 10^{-19}\ J$ and $\eta_m = 0.022$ $Pa \cdot s$ in all simulations. Figure 3.19 shows components of the complex modulus for healthy and Pf-RBCs at different stages. It also includes several data points for the frequency 0.75 Hz obtained in OMTC experiments [133]. Simulation results show the expected trend: increase in g' for the consecutive intra-erythrocytic stages since the shear modulus of the membrane is increased, while g'' does not change for different stages because the membrane viscosity is kept constant. Agreement between TTC and experiments is qualitative at best. Experimental data show an increase of g' for the progressing stages of the parasite development, but it appears to be less pronounced than that in the TTC simulations. Moreover, experiments show an increase in g'' which indicates a rise in the membrane or the internal fluid viscosity.

Several unresolved issues may contribute to the present discrepancies between the TTC simulations and the OMTC experiments. First, the shear modulus used in simulations was obtained by fitting the experimental data of RBC stretching with optical tweezers [190], where a whole cell was subjected to deformation, while the OMTC technique probes

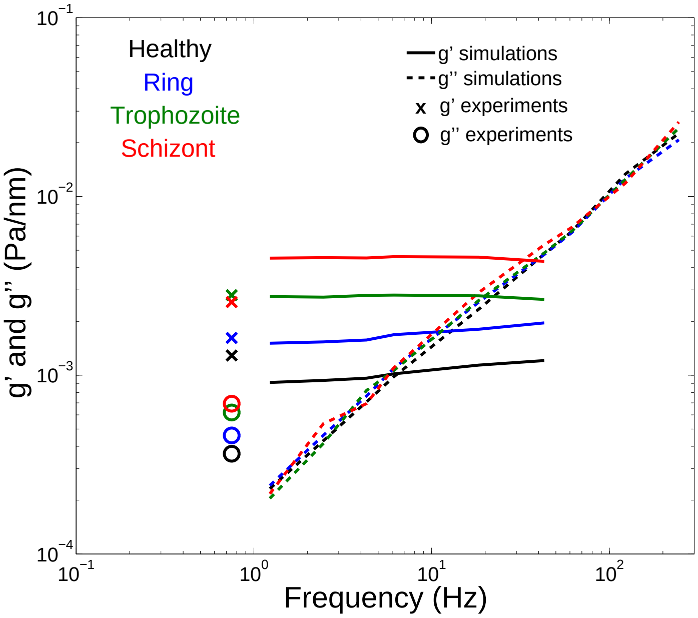

Figure 3.19: Components (g' and g'') of the complex modulus for healthy and Pf-parasitized RBCs at different stages of the parasite development obtained from TTC simulations. Experimental data [133] for the frequency 0.75 Hz are drawn in symbols.

membrane properties locally. Local properties may be non-isotropic resulting in deviations of the OMTC data. However, recent measurements of membrane thermal fluctuations [158] of parasitized RBCs for different stages showed similar shear moduli to those obtained by optical tweezers. Note that thermal undulations are directly correlated with the local membrane properties. Second, a potential change in the membrane bending rigidity during the parasite development would greatly affect measurements of the storage modulus as shown in the previous section for healthy RBCs. Third, presence of the growing parasite inside RBCs may strongly influence experimental measurements of the complex modulus especially for later intra-erythrocytic stages since its volume becomes comparable with that of the RBC. Finally, an alteration in the membrane or the internal fluid viscosity would influence measurements of the loss modulus as shown in the previous section. In conclusion, modeling of realistic RBCs in health and malaria disease requires more accurate and detailed experimental measurements of various RBC properties for different stages of the parasite development.

3.4.1.3 Healthy and Pf-parasitized RBCs at different temperatures

Recent OMTC experiments [133] showed a strong dependence of membrane rheological properties on temperature for healthy and Pf-infected RBCs. Specifically, the increase of temperature from the physiological value $T = 37^o\ C$ to the febrile $T = 41^o\ C$ results in considerable stiffening of Pf-parasitized RBCs. Analogous conclusions were made in the experiments that observed membrane thermal fluctuations [158] discussed in the next section. Table 3.4 outlines the shear moduli of healthy and Pf-RBCs for different temperatures obtained in the experiments [158]. Healthy and Pf-RBCs at ring stage do not show a significant change in their shear moduli at different temperatures, while trophozoite and schizont stages are characterized by a substantial increase in their membrane stiffness. Dependence of other membrane properties (e.g., bending rigidity, membrane viscosity) on temperature is not known, and therefore we assume $k_c = 2.4 \times 10^{-19}\ J$ and $\eta_m = 0.022\ Pa \cdot s$ in simulations that follow.

Temperature	$23^o\ C$	$37^o\ C$	$41^o\ C$
Healthy	6.3	5.8	4.9
Ring	14.5	14.5	20.4
Trophozoite	29	35	56.6
Schizont	60	71.8	95

Table 3.4: Shear moduli of healthy and Pf-parasitized RBCs in $\mu N/m$ at different temperatures obtained in [158].

We perform TTC simulations for healthy RBCs at different temperatures with the shear moduli outlined in table 3.4. Figure 3.20 presents components of the complex modulus for healthy RBCs at different temperatures and includes OMTC experimental data [133] for the frequency 0.75 Hz. The change in the complex modulus for healthy RBCs at different temperatures appears to be relatively small in simulations. A small decrease in g' with temperature elevation is found since the membrane shear modulus becomes smaller as shown in table 3.4. In contrast, the experiments show a gradual increase in the storage modulus as temperature rises, which indicates progressive membrane stiffening. This is in contradiction with several experiments (e.g., RBC micropipette aspiration [205], monitoring of membrane thermal fluctuations [158]), where a gradual membrane softening with temperature increase

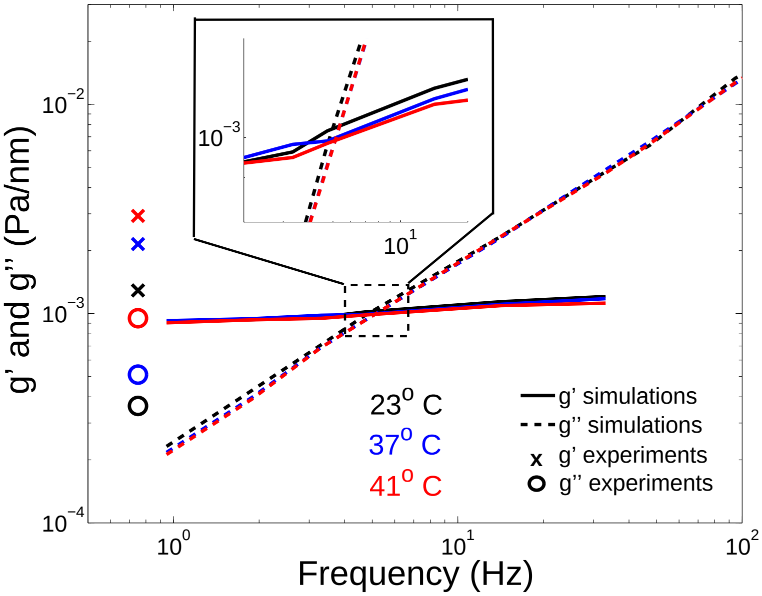

Figure 3.20: g' and g'' for healthy RBCs at different temperatures. Experimental data [133] for the frequency 0.75 Hz are drawn in symbols.

was found. Other experiments (e.g., ektacytometry [210], optical tweezers [141]) have shown a slight increase in the RBC shear modulus with temperature elevation, but statistical significance was not reached. Moreover, TTC simulations suggest that the increase of the shear modulus by $10\% - 30\%$ with changing temperature would result in a much smaller rise in g' than that found in the experiments (see figure 3.20). Hence, this discrepancy must be due to other changes in the membrane taking place at different temperatures. An increase in the membrane bending rigidity with increasing temperature would offer a possible explanation for the membrane's gradual stiffening found in the experiments. In order to quantitatively follow the experimental data in figure 3.20, the RBC bending stiffness should increase from its value at room temperature to that at $T = 41^o\ C$ by a factor between three and four according to the TTC simulation results in section 3.4.1.1. However, several experiments on lipid vesicles [47, 122] showed a slight decrease in the membrane bending rigidity with increasing temperature suggesting the same to be likely true for RBCs. Marinkovic et al. [133] proposed a significant role of entropic component to explain their experimental results since the RBC spectrin network is able to rearrange [49] under certain conditions such as metabolic activity or large strains.

Another characteristic feature of the experimental data [133] in figure 3.20 is the increase of the loss modulus g'' with increasing temperature indicating a rise in the membrane viscosity. The viscosity of fluids is known to decrease when temperature is elevated [175] suggesting the analogous behavior for the fluid-like lipid membrane of RBCs. The present discrepancies between the simulations and the experiments require further investigation.

Figure 3.21 shows storage and loss moduli of Pf-RBCs at the trophozoite stage (left) and the schizont stage (right) for different temperatures. The OMTC experimental data [133] for the frequency 0.75 Hz are also included. The TTC simulations show the expected trend: increase in g' since the membrane shear modulus is increased according to the data in table 3.4, that is in qualitative agreement with the experiments. Correspondence between the experiments and the simulations appears to be slightly better for trophozoites than schizonts; however, it is qualitative at best. Here, the discrepancies may be well due to unknown changes in the bending rigidity and the membrane viscosity for different temperatures, presence of the Pf-parasite, and potential metabolic activities discussed above. Hence, accurate experimental measurements of RBC properties at different parasite development stages and temperatures are of great interest.

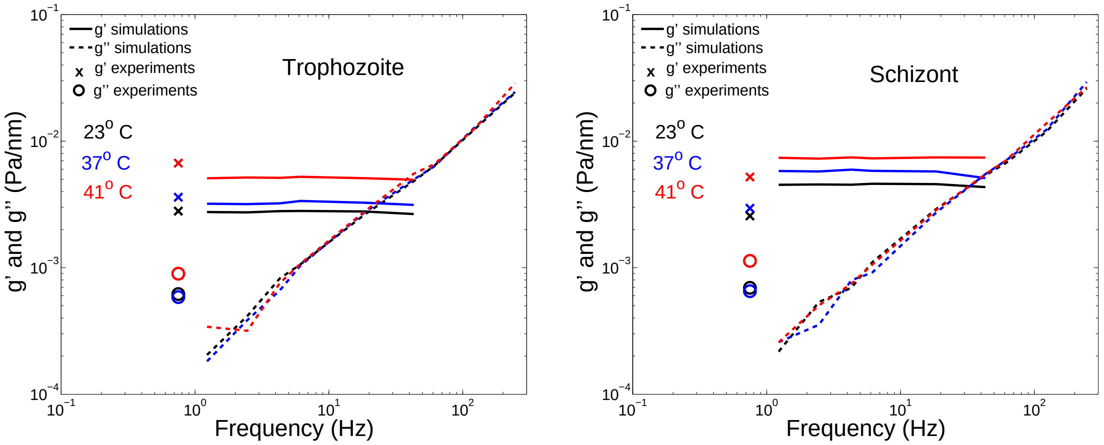

Figure 3.21: g' and g'' of Pf-RBCs at the trophozoite stage (left) and the schizont stage (right) for different temperatures. Experimental data [133] for the frequency 0.75 Hz are drawn in symbols.

3.4.2 Membrane thermal fluctuations

Thermal fluctuations of healthy and Pf-RBCs were measured in experiments using microrheology [10] by dynamical tracking of microbeads attached to the RBC surface and diffraction phase microscopy [161, 158], where instantaneous RBC-height maps were obtained. Thermal undulations are directly correlated with the membrane properties and can be used to derive the dynamics complex modulus.

3.4.2.1 Thermal fluctuation maps and RBC membrane properties

Diffraction phase microscopy experiments [158] monitored thermal fluctuations of an adhered to a solid surface RBC by measuring instant heights of the cell. Adhesion of the modeled RBC to a solid surface is performed by fixing a fraction of vertices on the RBC bottom, while other vertices are able to move. The cell is filled and surrounded by fluids with different viscosities. Thermal fluctuations on the RBC top are monitored in time. Figure 3.22 shows the instant thickness and fluctuation maps of a healthy RBC (A and C) and a Pf-parasitized RBC in trophozoite stage (B and D). Both RBCs have the same equilibrium shape (A and B), while the shear elastic modulus was set to 6.3 and 29 $\mu N/m$ for the healthy and Pf-RBCs in trophozoite stage, respectively. The images C and D indicate that the Pf-RBC has a smaller fluctuation amplitude than that of the healthy one in agreement with the results in [158].

A number of simulations is performed for different stages of the parasite development to identify dependence of thermal fluctuations on the membrane properties. Figure 3.23 presents membrane fluctuation distributions for different stages of Pf-RBCs at room temperature in comparison with the experiments [158]. Circles in figure 3.23 are the results of simulations employing the biconcave RBC shape (eq. (3.29)) with bending rigidity $k_c = 2.4 \times 10^{-19}\ J$. The strength of RBC adhesion here is characterized by the 0.13 fraction of vertices on the RBC bottom held stationary, while the corresponding shear moduli of Pf-RBCs at room temperature are given in table 3.4. Agreement between the distributions in experiments (solid lines) and simulations is found to be excellent for the case of healthy RBCs, while simulations for ring and trophozoite stages predict more narrow distributions than those in the experiments, and a wider distribution for the schizont stage. The curve in figure 3.23 plotted with “*” symbols corresponds to a simulation employing nearly spherical membrane (often observed in experiments) for the schizont stage, and yields a better agreement with the experiments. Hence, effective geometry and local curvature may affect thermal fluctuation measurements. However, shown discrepancies between the experiments and the simulations suggest that the shear modulus alone cannot provide an appropriate

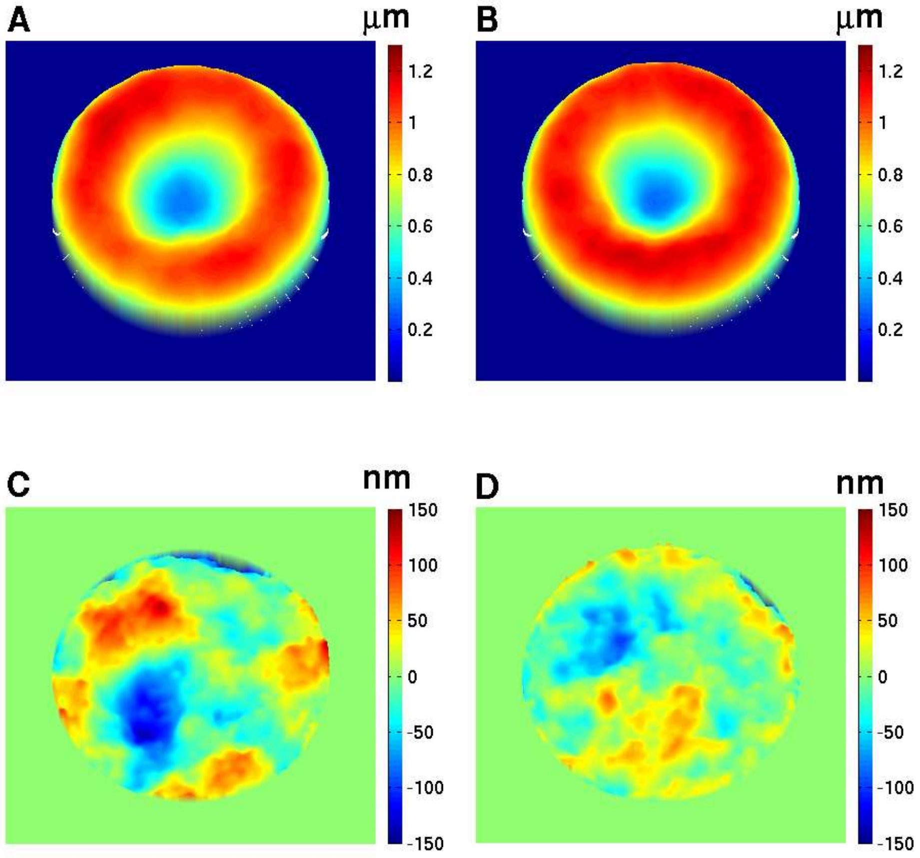

Figure 3.22: Instantaneous height and fluctuations of healthy RBC (A and C) and Pf-RBC in trophozoite stage (B and D). The instant fluctuation map is obtained by subtracting time-averaged cell shape from the instantaneous height map. Zero value in A and B corresponds to the half height of RBC.

description of thermal fluctuations.

Figure 3.24 shows dependence of fluctuation measurements on the experimental conditions (left) and the membrane properties (right). Circles in figure 3.24 are the full-width half-maximum (FWHM) values of the calculated distributions and the "*" symbols correspond to the FWHM values of the fitted Gaussian distributions, that are equal to $2\sigma\sqrt{-2\log(0.5)}$, where σ is the standard deviation. Figure 3.24 (left) shows that as the strength of RBC attachment characterized by the fraction of vertices held stationary decreases, the thermal fluctuations distribution widens since the FWHM values increase. The adhesion strength may be difficult to control in experiments; however, our simulation results indicate independence of thermal fluctuation measurements on the adhesion strength if the fraction of the fixed vertices is greater than 0.1. Furthermore, the simulation results

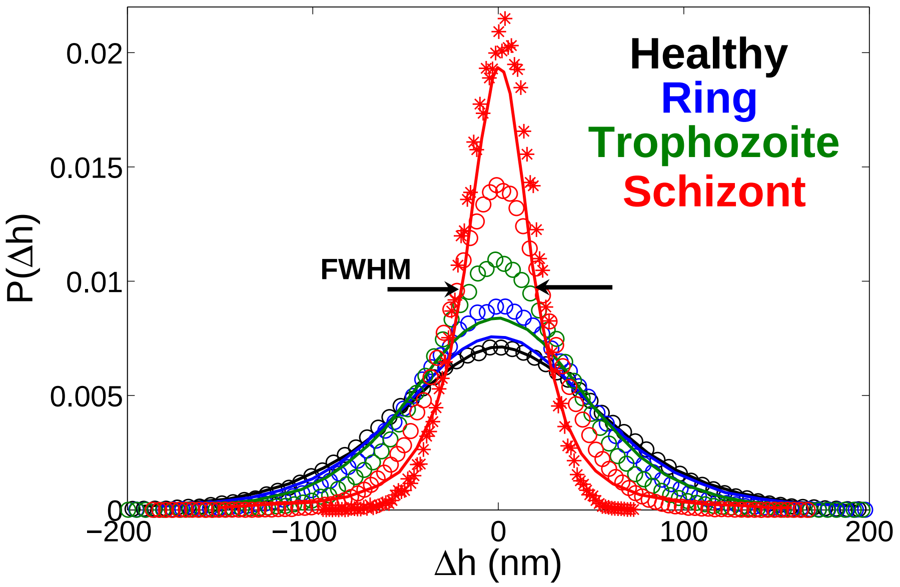

Figure 3.23: Membrane fluctuation distributions at different stages of Pf-RBCs monitored at room temperature ($T = 23^o\ C$). The experimental data [158] are drawn with solid lines, simulations employing the biconcave RBC shape are plotted with circles, and a simulation with a nearly spherical shape is shown by "*". FWHM identifies the full-width half-maximum value of the distribution curves.

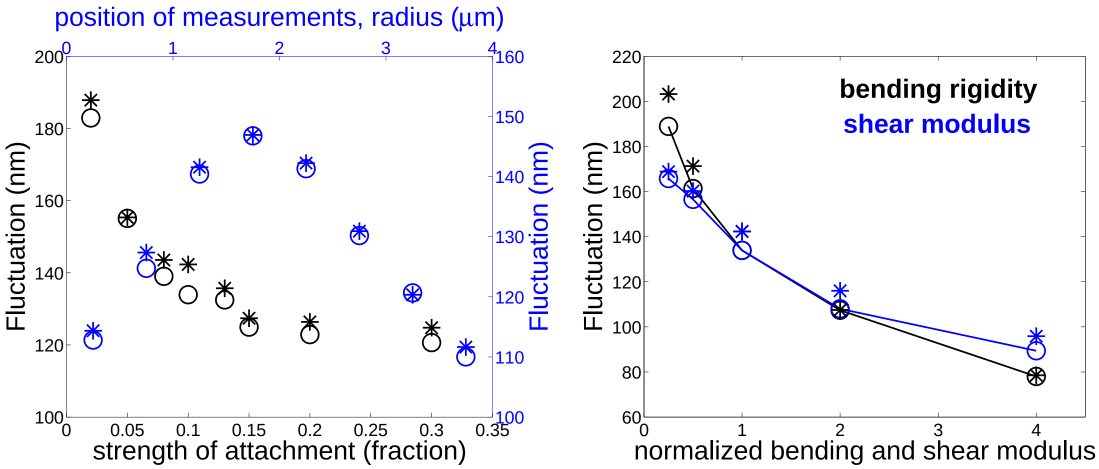

Figure 3.24: Sensitivity of fluctuations to the strength of attachment (vertex fraction) and the position of measurements (stripes of thickness 0.5 μm with different radii) (left). Dependence of fluctuations on the bending rigidity and the shear modulus normalized by healthy RBC values $k_c = 2.4 \times 10^{-19}\ J$ and $\mu_0 = 6.3\ \mu N/m$ (right). Circles are the FWHM values of the simulated distributions, and the "*" symbols are the FWHM of the fitted Gaussian distributions.

in figure 3.24 (left) show that thermal fluctuations may not be isotropic on the cell surface. Blue symbols are the FWHM measurements obtained for the circular areas of thickness 0.5

μm and different radii on the RBC top. Thermal fluctuations appear to be smaller in the RBC center and on the side compared with a maximum in-between. This can be partially explained by the RBC geometry since only height fluctuations are monitored here. In addition, a higher membrane curvature in central and side regions than that in the middle can contribute to damping of effective thermal fluctuations. Finally, presence of a rigid Pf parasite next to the Pf-RBC membrane may greatly affect fluctuation measurements. In light of the discussed issues, measurements of thermal fluctuations locally would provide more accurate and detailed information. Further, the FWHM values in simulations are averaged over a RBC surface area of radius 3 μm from the cell center.

Figure 3.24 (right) presents dependence of the FWHM values on the membrane bending rigidity and the shear modulus normalized by their healthy RBC values $k_c = 2.4 \times 10^{-19}$ J and $\mu_0 = 6.3$ $\mu N/m$. Both membrane properties strongly affect measurements of thermal fluctuations with a common trend: the stiffer the RBC, the smaller the fluctuation amplitudes characterized by FWHM values. These findings in combination with localized measurements of thermal fluctuations may provide a great opportunity to measure local Pf-RBC elastic and bending properties in experiments.

Pf-RBCs become stiffer as the parasite develops, and they show a significant stiffening when temperature is increased from the physiological value $T = 37^o$ C to the febrile $T = 41^o$ C observed in the experiments [158, 133] and discussed in section 3.4.1.3. In addition, febrile temperature can lead to irreversible changes in the membrane properties for later stages of Pf-RBCs, while healthy RBCs and those at the ring stage recover their elastic properties as temperature is lowered. Figure 3.25 shows the FWHM of thermal fluctuation distributions for different Pf-RBC stages at physiological and febrile temperatures. The shear moduli for different stages and temperatures are shown in table 3.4. The FWHM value of healthy RBCs at physiological temperature is slightly lower in simulations (blue circles) than that in experiments (black circles), while at room temperature agreement of thermal fluctuation distributions was excellent (see fig. 3.23). Hence, the increase in temperature from 23^o C to 37^o C and the small decrease in the shear modulus from 6.3 $\mu N/m$ to 5.8 $\mu N/m$ cannot fully explain an increase of thermal fluctuations as temperature is elevated from 23^o C to 37^o C. This suggests that there may be additional changes in the membrane properties (e.g., bending rigidity) or biochemical activities (e.g., metabolic) that influence thermal undulations when temperature is increased. An effective decrease in the membrane bending

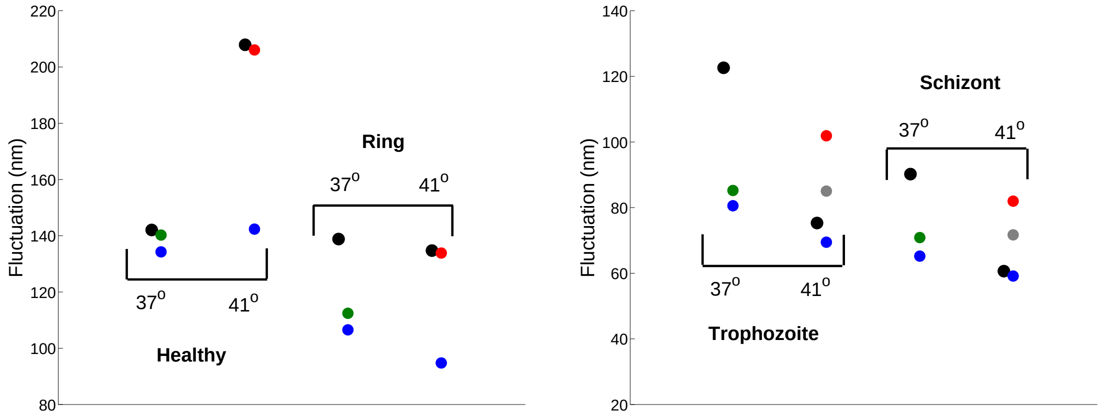

Figure 3.25: Pf-RBC FWHM of thermal fluctuation distributions for different stages of the parasite development at the physiological $T = 37^oC$ and the febrile $T = 41^oC$ temperatures. Black circles are the median values of FWHM in experiments [158], while other colors correspond to simulations. Blue circles assume the bending rigidity $k_c = 2.4 \times 10^{-19} J$, green $4k_c/5$, red $k_c/4$, and gray $k_c/2$. The corresponding shear moduli are outlined in table 3.4.

rigidity by about 20% as temperature reaches 37^o C (shown by the green circles) provides a good agreement between the simulations and the experiments. This seems to provide a plausible explanation since several experimental results on lipid vesicles [47, 122] show a slight decrease in bending rigidity with increasing temperatures. However, as we increase temperature to the febrile value, discrepancy between simulations (blue) and experiments (black) for healthy RBCs becomes dramatic. This difference can be reconciled by an effective bending rigidity to be four times lower (red circles) than $k_c = 2.4 \times 10^{-19}$ J at room temperature. Even though a sudden decrease in bending rigidity may potentially exist, it is more likely that other effects are involved. Thermal fluctuations may be influenced by metabolic activity such as the consumption of adenosine triphosphate (ATP) resulting in the spectrin network remodeling [49] and substantial enhancement of membrane undulations [88]. It is not clear whether metabolic activity was present in the experiments [158], nor whether it is actively triggered at the febrile temperature. In contrast, recent experiments [66] reported no dependence of membrane fluctuations on ATP. Thus, further investigation is required.

The FWHM values of the Pf-RBCs in figure 3.25 at physiological temperature are lower in simulations than those in experiments. This indicates a complex dependence of membrane thermal fluctuations on the membrane properties and potential metabolic activities. As an example, healthy and ring-stage RBCs at $T = 37^o\ C$ show comparable FWHM values in the experiments, while the corresponding shear modulus for the ring-stage is about 2.5 times higher than that of healthy RBCs. A decrease in the membrane bending rigidity is likely to take place for Pf-RBCs since the malaria parasite exposes intramembrane proteins that are known to affect membrane properties; however, it offers only partial explanation for the discrepancies found. Simulation results at the febrile temperature seem to show a better agreement with experiments for later stages of parasite development. However, we did not find any consistent trend that would properly correlate the experimental FWHM values with membrane properties at different stages and temperatures. Shown differences suggest that more reliable experimental data are needed in order to control a simultaneous interplay of RBC membrane properties and metabolic activities at different temperatures and Pf-RBC stages. In addition, local measurements of thermal fluctuations would be favorable to eliminate the existing anisotropy discussed above.

3.4.2.2 Complex modulus of healthy and Pf-RBCs

Microbeads attached to the cell surface were tracked in the microrheology experiments [10] resulting in the three-dimensional complex modulus G^* with components G' and G'', analogously to the two-dimensional version described in section 3.4.1.1. To mimic these experiments, the attached RBC is surrounded by a fluid of viscosity $\eta_o = 1 \times 10^{-3}\ Pa \cdot s$. In addition, the RBC is filled with a fluid of the viscosity $\eta_i = 5 \times 10^{-3}\ Pa \cdot s$ similar to the RBC cytosol which is a hemoglobin solution. The viscosity of hemoglobin solutions was measured in [33] yielding a range of $3 - 10 \times 10^{-3}\ Pa \cdot s$ for the physiologically relevant concentrations of hemoglobin. The membrane viscosity is set to $\eta_m = 0.022\ Pa \cdot s$. The mean square displacement (MSD) $< \Delta r^2(t) >$ of several points on the RBC top is measured. Theoretical developments in microrheology [99] provide a relation between MSD and G^* as follows

$$G^*(\omega) = \frac{k_B T}{CL(< \Delta r^2(t_\infty) > + i\omega < \Delta r^2(\omega) >)}, \tag{3.38}$$

where $i = \sqrt{-1}$, $< \Delta r^2(\omega) >$ is the unilateral Fourier transform of $< \Delta r^2(t) > - < \Delta r^2(t_\infty) >$, C is a constant, and L is a length scale. Note that the corresponding C and L depend on the physical problem and selected theoretical model. As an example, the

MSD of microbeads in a viscoelastic fluid can be well approximated by the generalized Stokes-Einstein relation, where $C = 6\pi$ and L is the bead radius. This interpretation was chosen by Amin et al. [10] for microbeads attached to the RBC surface. However, the Stokes-Einstein relation cannot be valid in this case since the membrane elastic properties are not taken into account. Several other models [99] attempt to incorporate effects of the elastic and bending properties, but there is no agreement whether a particular model yields quantitatively accurate results for RBC rheology. Therefore, we do not favor any specific theoretical model and will present our results for $G^*(\omega)$ up to a constant. Moreover, relative trends of the complex modulus with respect to frequency are more informative than the exact values.

Figure 3.26 shows the spectral density of healthy RBCs (left), and storage G' and loss G'' moduli (right) at room temperature. Theoretical predictions for viscoelastic vesicles [99] yield the asymptotic scaling of the spectral density with frequency obtained from MSD, when the tracked beads are much smaller than the membrane, as follows

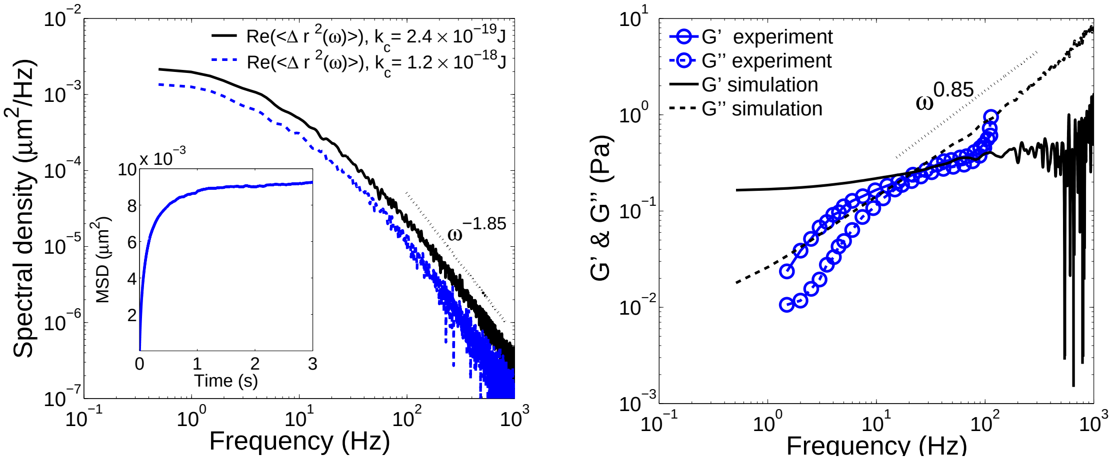

Figure 3.26: RBC spectral density of healthy RBCs (left) and the components of the complex modulus G^* (right) at room temperature obtained from MSD (inset plot). Dash-dotted lines are drawn to the eye to illustrate the power with respect to frequency. Experimental results [10] are obtained by dynamical tracking of microbeads attached to the RBC surface.

$$Re(<\Delta r^2(\omega)>)) \sim k_c^{-1/3}\omega^{-5/3}, \tag{3.39}$$

where Re is the real part. Similar exponents were found for actin-coated vesicles in the experiments [99]. Our simulation results for healthy RBCs show that $Re(<\Delta r^2(\omega)>)) \sim$

$k_c^{-0.26}$ which is close to the theoretical prediction of $-1/3$. This also indicates that the value of the MSD plateau (shown as inset in figure 3.26 (left)) at long times $< \Delta r^2(t_\infty) >$ is proportional to $k_c^{-0.26}$. Furthermore, the power of the spectral density at high ω is found to be -1.85 in simulations in agreement with $-5/3$ in equation (3.39). Figure 3.26 (right) presents a comparison of experimental and simulation results for the complex modulus of healthy RBCs. The time scale exponent used here is the same as in the twisting torque cytometry simulations $\alpha = 0.85$, while $\eta = \eta_o + \eta_i + \eta_m$ in equation (3.36). This is consistent with the exponent of G'' found to be 0.85. For the calculation of G^* (eq. (3.38)) we assumed that $C = 3\pi$ and $L = 0.25\ \mu m$ in agreement with those used in the experiments [10]. While the behavior of the loss modulus G'' with respect to frequency provides a reasonable agreement between the experimental and simulation data, the behavior of the storage modulus G' is clearly different. In simulations G' shows a plateau at low frequencies indicating that in this regime the RBC membrane is nearly elastic, which is typical for viscoelastic solid materials and is consistent with the twisting torque cytometry in section 3.4.1.1. However, G' found in the experiments shows a significant decrease at low frequencies typical for viscoelastic fluids. This disagreement may be well due to differences in measurement techniques since in simulations we measure three-dimensional RBC-membrane thermal fluctuations directly at the network surface, while in experiments displacement of the attached microbeads is tracked. Note that $G'(\omega) \sim k_c^{0.26} Y_0^{0.65}$. The scatter at high frequencies is due to data underresolution at short times.

Further, MSD measurements are performed for Pf-RBCs at different stages of the parasite development at room temperature. The shear moduli for various stages are outlined in table 3.4, while the bending stiffness and the membrane viscosity are set to $k_c = 2.4 \times 10^{-19}$ J and $\eta_m = 0.022\ Pa \cdot s$, respectively. Figure 3.27 shows components of the complex modulus for healthy and Pf-RBCs at different stages, $T = 23^o\ C$. We found a similar increase in G' as that in the twisting torque cytometry simulations in section 3.4.1.2 since Pf-RBCs become stiffer during the consecutive stages of the parasite development. The loss modulus G'' remains nearly the same for the progressing stages in agreement with the TTC simulations. Figure 3.28 presents the storage and loss moduli of healthy (left) and Pf-RBCs at the schizont stage (right) for different temperatures with the corresponding shear moduli given in table 3.4. Healthy RBCs show a slight decrease in the storage modulus with temperature, while Pf-RBCs at the schizont stage show an increase in G' in accordance with the TTC sim-

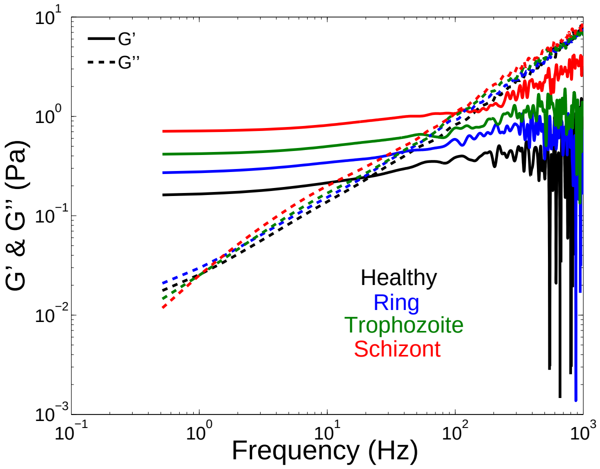

Figure 3.27: G' and G'' of healthy and Pf-parasitized RBCs at different stages of parasite development. Thermal fluctuation measurements at $T = 23^o\ C$.

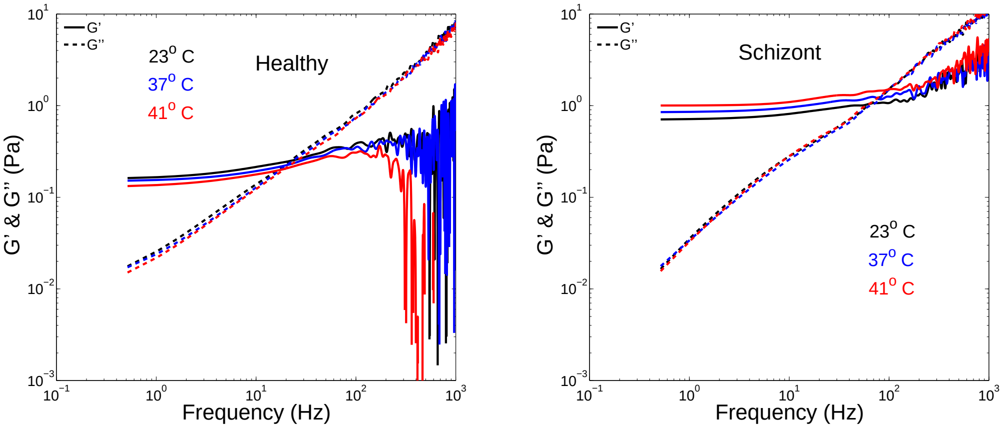

Figure 3.28: Components of the complex modulus for healthy (left) and Pf-RBCs at the schizont stage (right) for different temperatures.

ulations and the employed shear moduli. Agreement between the two-dimensional complex moduli from the twisting torque cytometry and the three-dimensional one obtained from measurements of thermal fluctuations indicates equivalence of these different rheological techniques.

3.4.3 Creep test and cell recovery

A creep test is the standard rheological technique to measure time-dependent deformation of a material under constant load or stress, while a recovery test provides dynamic relaxation of a material after deformation. The dynamic stretching and recovery of a whole RBC was performed by micropipette aspiration [104] and by optical tweezers [101]. The creep test on a single RBC was also done locally [167] using OMTC by subjecting an attached ferrimagnetic microbead to a constant magnetic field. The agreement among these experiments can be described by capturing the order of magnitude of the characteristic relaxation time. However, quantitative agreement among different experiments is poor, and the values of the obtained relaxation times may differ by the factor of $3 - 5$.

Several issues may contribute to this poor quantitative agreement such as geometry, stress and strain magnitudes, and simplified models to extract the parameters of interest. Whole cell stretching or recovery measures RBC rheological membrane properties on average since the membrane strains and stresses are not uniform along the cell due to a varying cell circumference along the stretching axes. In addition, various strain rates may greatly affect quantitative rheological predictions [213]. Moreover, whole cell stretching experiments subject a RBC to relatively high strains where a nonlinear response may be present, and hence applied linear rheological models may fail. Hence, local membrane deformation techniques (e.g., OMTC) are more favorable to measure bulk rheological properties of a RBC membrane since the applied loads are local and have much smaller magnitudes compared to whole cell deformations. Another complication which often arises in rheology of viscoelastic materials is that there exists a spectrum of relaxation times where a single relaxation time may be only relevant in a certain range of experimental conditions. The described difficulties can be successfully resolved in numerical simulations using realistic cell models to aid in the design and interpretation of experiments.

The numerical setup for the creep test followed by cell recovery is analogous to RBC stretching in section 3.3 observing a time-dependent RBC deformation. Thus, the total stretching force f is applied to N_- and N_+ vertices (figure 3.5) in negative and positive direction, respectively, while the axial cell diameter is monitored. Internal/external fluid viscosities are set to $\eta_i = 5 \times 10^{-3}\ Pa \cdot s$ and $\eta_o = 1 \times 10^{-3}\ Pa \cdot s$, respectively, while the membrane viscosity is varied. Our simulations showed that the characteristic time scale depends on the RBC membrane and fluid properties as $Y_0^{-0.75}$ and $\eta^{0.75}$, where $\eta = \eta_o + \eta_i + \eta_m$. Hence, the time scale exponent in equation (3.36) is set to $\alpha = 0.75$, which is consistent with the twisting torque cytometry and membrane thermal fluctuation tests presented above. The assumption of linear dependence ($\alpha = 1$) of the time scale with the membrane properties made in experiments [104] appears to be a rather crude approximation.

Figure 3.29 (left) shows creep tests of healthy RBCs for different membrane viscosities. The comparison between the experimental data and simulations suggests that the RBC membrane viscosity lies in the range of $0.02 - 0.06\ Pa \cdot s$. The main difference between the experiments is that the micropipette aspiration [104] deforms the whole cell with relatively high strains, while OMTC [167] applies deformations on the membrane locally with small strains. Figure 3.29 (right) illustrates differences in the creep response for distinct total applied forces. This demonstrates the complexity of the RBC membrane response which depends on total strains and strain-rates [213].

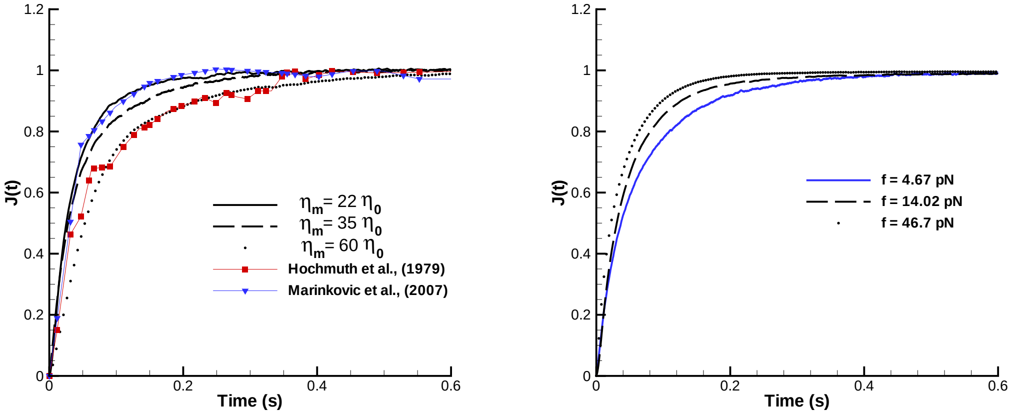

Figure 3.29: The normalized creep compliance ($f = 7\ pN$) for different membrane viscosities (left) and applied forces (right) with $\eta_m = 0.022\ Pa \cdot s$. The left figure also shows the creep test by micropipette aspiration [104] and by OMTC [167].

To study dynamics of RBC recovery after stretching with force f we introduce the time-dependent elongational index $e(t)$ analogously to that in [104] as follows

$$e(t) = \frac{(\lambda - \lambda_\infty)(\lambda_0 + \lambda_\infty)}{(\lambda + \lambda_\infty)(\lambda_0 - \lambda_\infty)} = \exp\left[-\left(\frac{t}{t_c}\right)^{\delta}\right], \tag{3.40}$$

where $\lambda = D_A/D_T$, λ_0 and λ_∞ correspond to the ratios at times $t = 0.0$ and $t = \infty$, t_c is the characteristic time, and δ is the exponent (*Note that in [104]* $\delta = 1$, *thus equation (3.40) is a generalization of the equation (11) in [104]*). Similar to the creep test, the time scale exponent here is set to $\alpha = 0.75$. Figure 3.30 (left) shows RBC recovery after deformation by the force of $7\ pN$, having $\eta_m = 0.022\ Pa \cdot s$. In case of $\delta = 1$ we observe a rather poor fit to RBC recovery, while the fit with $\delta = 0.7$ yields excellent agreement with the recovery dynamics. Figure 3.30 (right) demonstrates sensitivity of the recovery dynamics

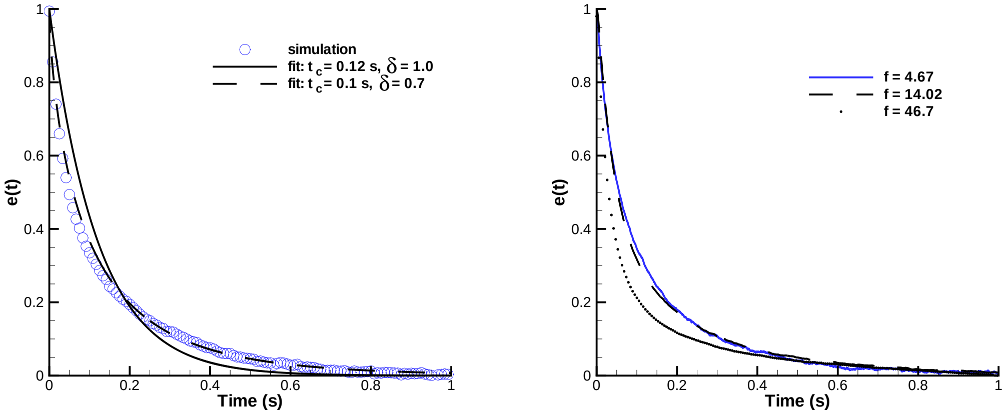

Figure 3.30: RBC recovery after deformation by the force of $f = 7\ pN$ for different fits (left) and after different stretching forces (right).

to the total stretching force (or initial stretch). The response is not sensitive to a small initial stretch; however, the recovery is very different in case of a high initial stretch, where non-linear effects may be present. In addition, we note that RBC recovery showed a long tail decay and it is important to have a long enough sample to correctly measure λ_∞, which may greatly affect the fitting parameters. Thus, the experiments on RBC recovery have to be observed for at least several seconds, in contrast to the RBC recovery [104] over about 0.5 s.

3.5 Dynamics

RBC dynamics in shear flow was investigated in experiments [197, 79, 80, 4] and in three-dimensional simulations [53, 159]. The behavior is mainly characterized by two regimes: tumbling at low shear rates and tank-treading at high shear rates. Several attempts were made to theoretically describe RBC behavior in shear flow [4, 181] depending on a number of cell properties (e.g., ellipsoidal geometry, membrane shear modulus, and viscosity) and flow conditions (e.g., shear rate, and viscosity contrast between external and internal fluids). We performed a number of simulations to quantify RBC dynamics in shear flow depending on the conditions mentioned above. A single RBC in Poiseuille flow in tubes having the diameter $8 - 15\ \mu m$ shows a transition from the biconcave shape to a parachute-like shape as the flow rate increases, as found in several experiments [198, 69] and in simulations

[150]. The biconcave-to-parachute transition will be characterized for different membrane properties.

3.5.1 RBC dynamics in shear flow

Experimental observations [197, 79, 80, 4] of a RBC in shear flow show a tumbling-to-tank-treading transition. This behavior is attributed to the existence of a minimum energy state of the RBC membrane shown by Fischer [79]. In these experiments a single RBC was subjected to the tank-treading motion for several hours, and after the flow was stopped the RBC would relax to its original biconcave shape having exactly the same relative positions of several attached microbeads as those before shearing. Thus, we need to exceed a certain energy barrier in order for a RBC to start tank-treading. Theoretical predictions [4, 181] for this behavior consider a RBC of an ellipsoidal shape tank-treading along the fixed ellipsoidal path. Here, the RBC dynamics depends on the membrane shear modulus, shear rate of the flow, and the viscosity contrast defined as $\lambda = (\eta_i + \eta_m)/\eta_o$. In case of $\lambda < 3$ the theories predict tumbling at low shear rates and tank-treading at high shear rates with a narrow intermittent region around the tumbling-to-tank-treading transition characterized by an unstable RBC behavior. Thus, RBC tumbling can be followed by tank-treading and vice versa. However, in case of $\lambda > 3$ there is a well-defined tumbling regime followed by an intermittent region, while stable tank-treading may not be present. The viscosity ratio of healthy RBCs in blood is much greater than three. In addition, the tank-treading state shows a RBC swinging motion around the average tank-treading axes with certain frequency and amplitude. Further, we use numerical simulations to observe RBC behavior and deformation in shear flow and to discuss reliability of the theoretical predictions.

A single RBC is placed in linear shear flow between two parallel walls. The viscosity of the external solvent is set to $\eta_o = 0.005\ Pa \cdot s$, while that for the internal cytoplasm, if present, has the same value of $\eta_i = 0.005\ Pa \cdot s$. When used, the membrane viscosity is set to $\eta_m = 0.022\ Pa \cdot s$ in consistency with the rheological results in section 3.4. Figure 3.31 shows RBC tumbling and tank-treading frequencies for different simulation setups versus shear rates in comparison with the experiments [197, 80]. A purely elastic cell with or without inner solvent (circles and squares) results in a significant overprediction of the tank-treading frequencies in comparison with the experiments since it does not have enough viscous dissipation exerted by the internal fluid. In principle, the internal solvent

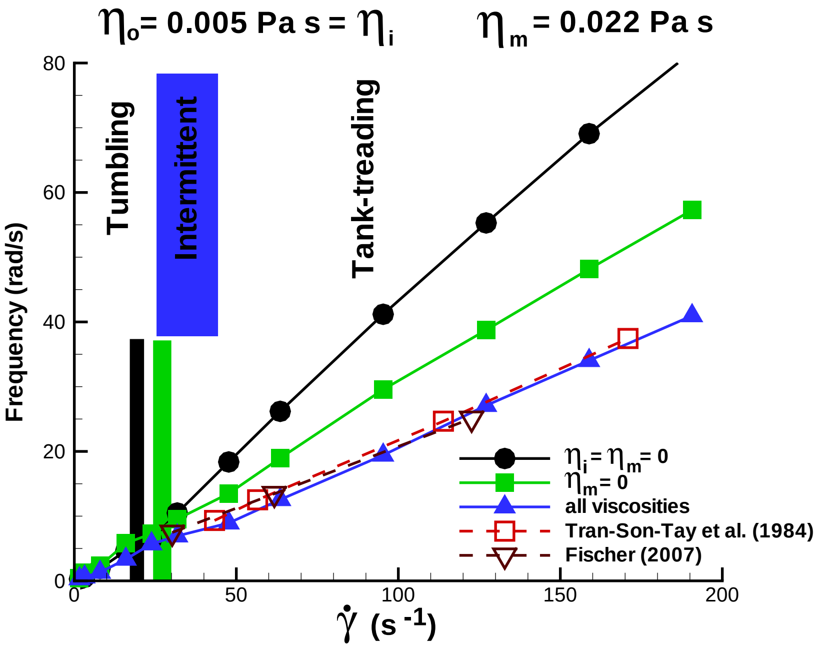

Figure 3.31: Tumbling and tank-treading frequency of a RBC in shear flow for different cases: 1) $\eta_o = 0.005\ Pa \cdot s$, $\eta_i = \eta_m = 0$ (circles); 2) $\eta_o = \eta_i = 0.005\ Pa \cdot s$, $\eta_m = 0$ (squares); 3) $\eta_o = \eta_i = 0.005\ Pa \cdot s$, $\eta_m = 0.022\ Pa \cdot s$ (triangles).

viscosity can be substantially increased in order to follow the experimental data. However, the RBC cytoplasm is a hemoglobin solution with a well-determined viscosity of about $0.005\ Pa \cdot s$ [33], and therefore additional viscous dissipation must be in the membrane. This is supported by the results of the third case (triangles) in figure 3.31 showing a good agreement with the experimental data. In contrast, the tumbling frequencies appear to be nearly independent of the involved viscosities since the RBC membrane is subject to nearly pure rotation. Moreover, presence of the internal fluid and the membrane viscosity slightly shifts the tumbling-to-tank-treading transition to higher shear rates marked by the intermittent region. From simulations we estimate the tank-treading energy barrier of a RBC to be about $E_c = 3$ to $3.5 \times 10^{-17}\ J$ found as a change in the membrane elastic energy during the tank-treading motion right after the tumbling-to-tank-treading transition has occurred. In the theoretical model by Skotheim and Secomb [181] this energy barrier E_c was set to $10^{-17}\ J$ in order to match the experimental data. In simulations as RBC tank-treads, the elastic energy difference increases with shear rate within about 20% of the E_c value indicating an increase in membrane deformations.

Note that in all cases a finite intermittent region in terms of shear rates is observed, but it becomes wider in the case of non-zero membrane viscosity. This is consistent with the experiments but not with the theoretical predictions. Similar results for the intermittent region were reported in simulations of viscoelastic vesicles by Kessler et al. [111]. This suggests that theoretical predictions describe RBC dynamics in shear flow qualitatively at best since they are based on several simplifications such as an ellipsoidal RBC shape and the fixed (ellipsoidal) RBC tank-treading path. Experiments by Abkarian et al. [4] and our simulations show that the RBC does not follow a fixed path and deforms along the tank-treading axis with strains of the order of $0.1-0.15$. Figure 3.32 (a) and (b) show several snapshots of tumbling and tank-treading RBC with the bending rigidity $k_c = 2.4\times10^{-18}\ J$ which is ten times higher than that often accepted for healthy RBCs. Our simulation results

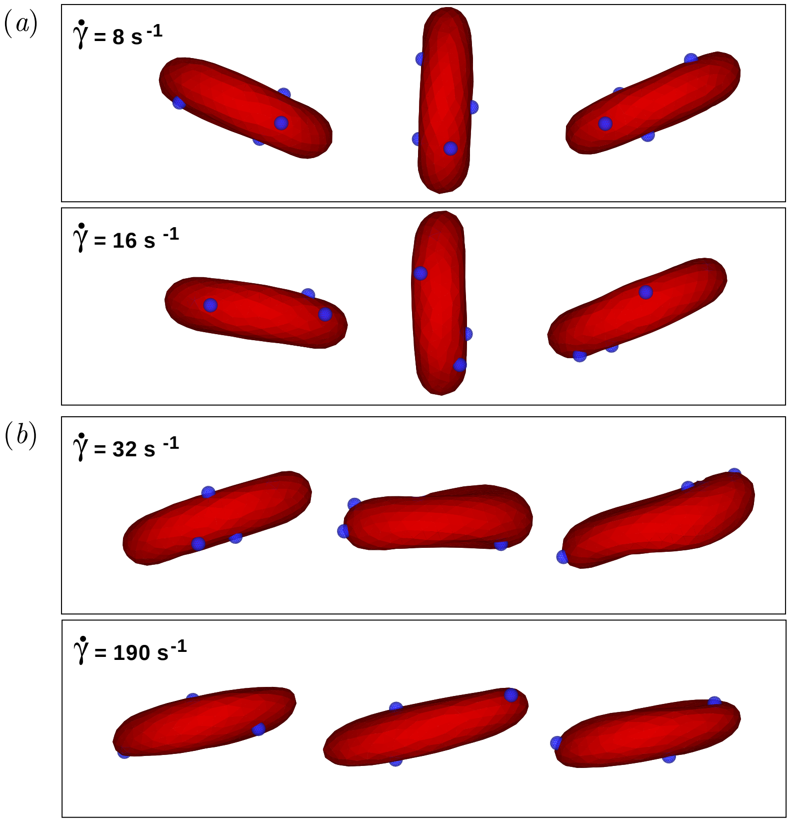

Figure 3.32: Snapshots of tumbling RBC (a) and tank-treading RBC (b) for different shear rates. The following parameters are used in simulations: viscosities $\eta_o = \eta_i = 0.005\ Pa\cdot s$, $\eta_m = 0.022\ Pa\cdot s$, bending rigidity $k_c = 2.4\times10^{-18}\ J$, and the Föppl-von Kármán number $\kappa = 85$. Blue particles are the tracing points.

show that the RBC deformation in shear flow depends on the relative ratio of membrane elastic and bending properties characterized by the Föppl-von Kármán number defined as follows

$$\kappa = \frac{Y_0 R_0^2}{k_c}, \tag{3.41}$$

where $R_0 = \sqrt{\pi A_0/4}$. Note that the theoretical models do not take into account membrane bending rigidity. The case in figure 3.32 corresponds to the Föppl-von Kármán number $\kappa = 85$. The tumbling-to-tank-treading transition occurs at shear rates of about $20-25\ s^{-1}$. The results show a negligible deformation during tumbling behavior, and small shape deformations during tank-treading right after the transition. In contrast, figure 3.33 (a) and (b) present analogous snapshots of a tumbling and tank-treading RBC with the bending rigidity $k_c = 2.4 \times 10^{-19}\ J$, and $\kappa = 850$. Here, we observe a significant shape

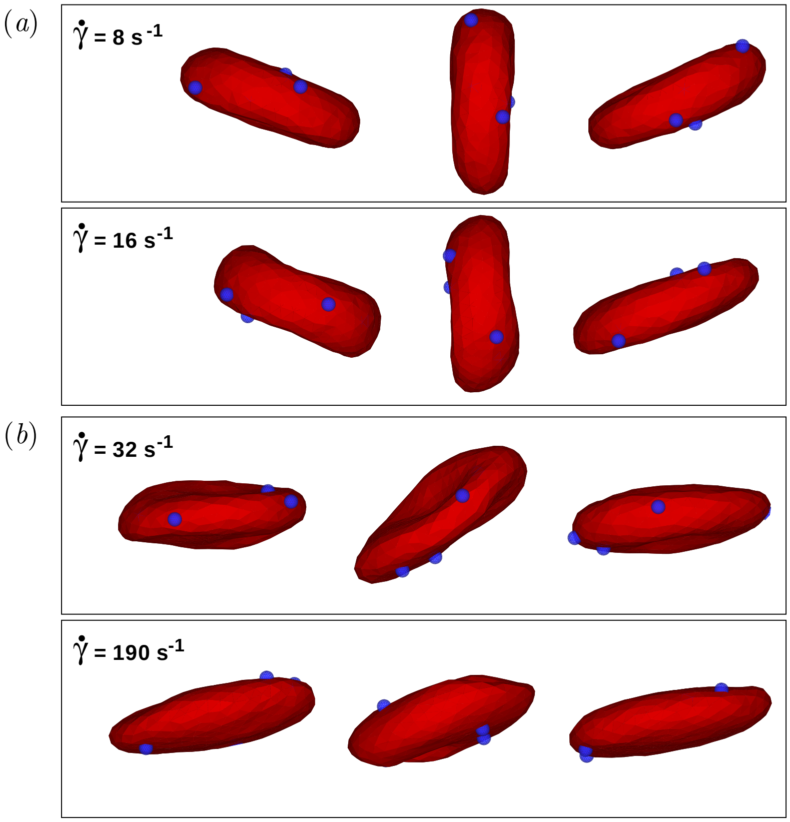

Figure 3.33: Snapshots of a tumbling RBC (a) and a tank-treading RBC (b) for different shear rates. The following parameters are used in simulations: viscosities $\eta_o = \eta_i = 0.005\ Pa \cdot s$, $\eta_m = 0.022\ Pa \cdot s$, bending rigidity $k_c = 2.4 \times 10^{-19}\ J$, and the Föppl-von Kármán number $\kappa = 850$. Blue particles are the tracing points.

deformation during tumbling and tank-treading. However, the corresponding frequencies are not strongly affected in comparison with the previous case of $\kappa = 85$. Further decrease of the membrane bending rigidity results in membrane buckling. A discrete network cannot adequately capture the membrane bending properties on length scales comparable with the characteristic size of the network elements. To rule out the possible effects of the membrane discretization we simulated RBCs discretized with $Nv = 1000$ and 3000 vertices that showed similar membrane deformations for the analogous Föppl-von Kármán number. Such findings raise a question about the magnitude of the RBC bending rigidity, which may be several times larger than the widely accepted value of $k_c = 2.4 \times 10^{-19}\ J$. Note that the rheological results in section 3.4.1.1 also support a larger value for the bending rigidity of healthy RBCs. Moreover, we comment on a potential change in the membrane shear modulus in the cases of Pf-parasitized RBCs. Increase in μ_0 gives a higher Föppl-von Kármán number, and also would proportionally increase the tank-treading energy barrier E_c resulting in a shift of the tumbling-to-tank-treading transition to higher shear rates.

From figures 3.32 and 3.33 it can be noticed that the RBC oscillates (swings) around the tank-treading axes with a certain frequency and amplitude. This behavior was also observed in experiments [4]. Figure 3.34 shows the average RBC tank-treading angle and swinging amplitude. The obtained values are consistent with the experimental data. The

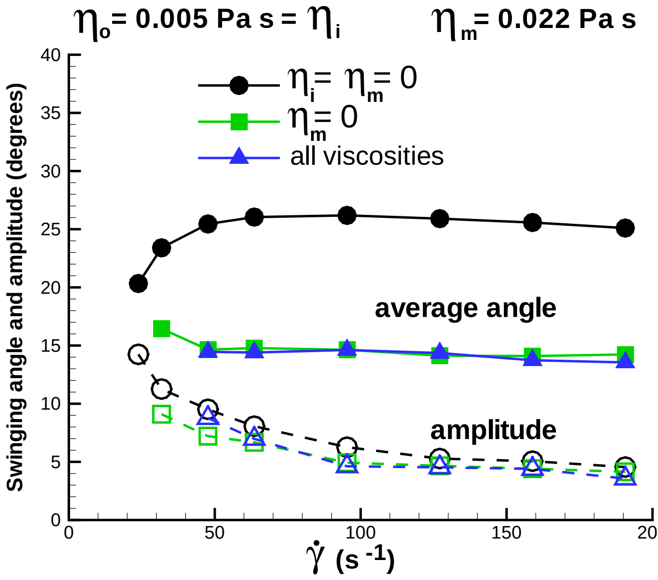

Figure 3.34: Swinging average angle (filled symbols) and amplitude (open symbols) in degrees for the three cases: 1) $\eta_o = 0.005\ Pa \cdot s$, $\eta_i = \eta_m = 0$ (circles); 2) $\eta_o = \eta_i = 0.005\ Pa \cdot s$, $\eta_m = 0$ (squares); 3) $\eta_o = \eta_i = 0.005\ Pa \cdot s$, $\eta_m = 0.022\ Pa \cdot s$ (triangles).

swinging average angle appears to be larger for a purely elastic membrane without cytosol, while that with cytosol shows no dependence of the inclination angle on the internal fluid and membrane viscosities. Furthermore, the swinging amplitude is not sensitive to fluid and membrane properties. Note that the swinging frequency is equal to exactly twice that of the tank-treading frequency.

3.5.2 RBC dynamics in Poiseuille flow

It was found in experiments [198, 69] that RBC dynamics in Poiseuille flow in tubes of a diameter comparable with the RBC size is characterized by a transition from biconcave to the parachute-like shape as the flow rate is increased. Figure 3.35 shows the parachute shape of a RBC simulated in a tube of diameter $9\mu m$. At low pressure gradients the fluid flow is weak and the RBC retains its biconcave shape, while as the pressure gradient is increased the RBC will transit into a parachute-like shape. The strength of the Poiseuille flow can be characterized in terms of the mean flow velocity defined as

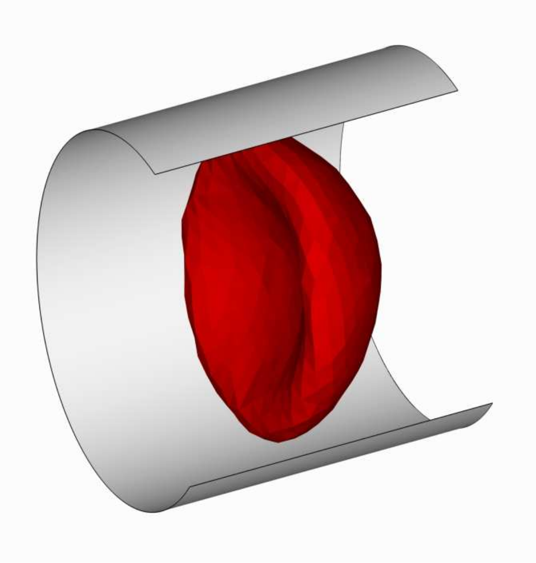

Figure 3.35: RBC parachute shape in Poiseuille flow in the tube having the diameter of $9\mu m$.

$$\bar{v} = \frac{1}{S}\int v(r)dS, \tag{3.42}$$

where S is the area of the tube cross-section, and $v(r)$ is the axial flow velocity. Note that for a Newtonian fluid $\bar{v} = v_c/2$, where v_c is the maximum flow velocity in the center. To identify the biconcave-to-parachute RBC transition we introduce the gyration tensor given as follows

$$G_{mn} = \frac{1}{N_v} \sum_i (r_m^i - r_m^C)(r_n^i - r_n^C), \tag{3.43}$$

where r^i are the RBC vertex coordinates, r^C is the center-of-mass, and m, n can be x, y, or z. The gyration tensor has three eigen-values which allow us to characterize the RBC shape. As an example, the gyration tensor for the equilibrium biconcave shape has two larger eigen-values corresponding to the cell diameter and one smaller corresponding to the RBC height. Thus, the biconcave-to-parachute transition can be characterized by the smallest eigen-value becoming larger as the RBC elongates along the flow axes. Figure 3.36 shows a dependence of the shifted eigen-value of the gyration tensor for different bending rigidities (left) and membrane shear moduli (right). The dashed line marks the biconcave-to-parachute transition depending on the mean flow velocity. The transition for healthy RBCs occurs at a mean flow velocity of about 65 $\mu m/s$. Cells having a larger bending rigidity or membrane shear modulus (Pf-RBCs) show the transition at stronger flows with a nearly linear dependence of the transition on the bending rigidity k_c and the shear modulus μ_0. These results are consistent with the numerical simulations of Noguchi and Gompper [150]. The eigen-values also show that stiffer capsules are subject to a smaller cell elongation along the flow for the same mean velocity. Therefore, stiffer cells exhibit a higher flow resistance in comparison with softer ones shown in figure 3.37. The relative apparent viscosity is defined

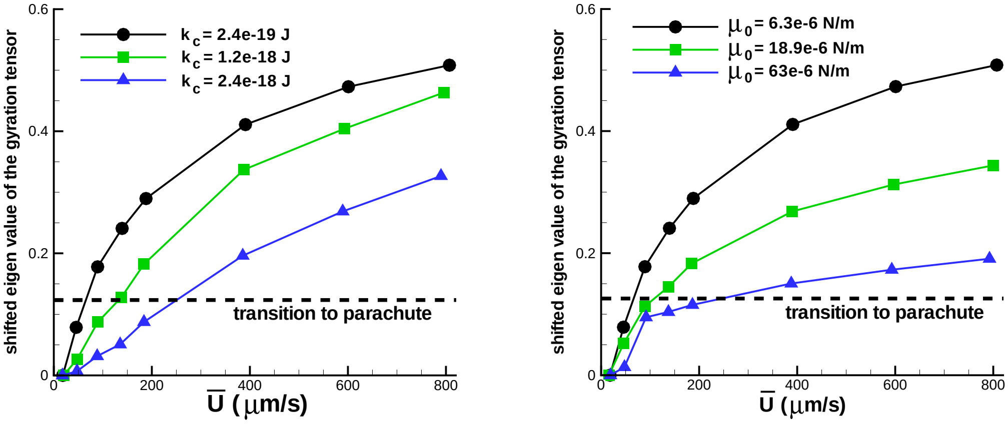

Figure 3.36: The shifted eigen-value of the gyration tensor for different bending rigidities (left) and membrane shear moduli (right). The shift is done by subtracting the eigen-value of the equilibrium biconcave shape. $C = 0.05$ is the volume fraction of a single RBC.

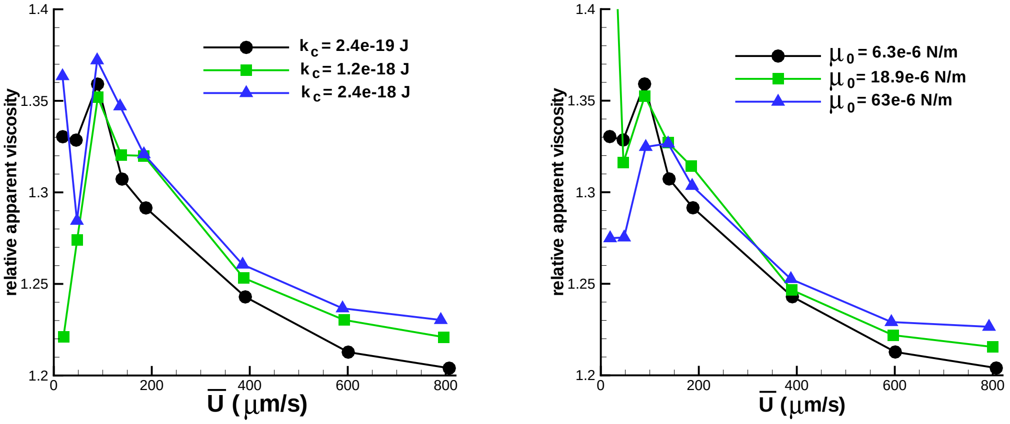

Figure 3.37: The relative apparent viscosity for different bending rigidities (left) and membrane shear moduli (right). $C = 0.05$ is the volume fraction of the single RBC.

as

$$\lambda_{app} = \frac{\eta_{app}}{\eta_o}, \qquad \eta_{app} = \frac{nfR_0^2}{8\bar{u}}, \tag{3.44}$$

where n is the particle number density, f is the force exerted on each particle, R_0 is the tube radius, and $\bar{u}$ is the mean flow velocity calculated from the simulated velocity profile according to equation (3.42). Note that nf is equal to the flow pressure drop $\Delta P/L$, where L is the tube length. Figure 3.37 shows a slight increase of the apparent viscosity for stiffer cells resulting in an increased flow resistance. The flow resistance increases by only several percent while the membrane properties are varied up to ten times. Such a small difference in the apparent viscosity is attributed to a very low cell concentration with the volume fraction of $C = 0.05$. For higher RBC volume fractions the apparent viscosity is more sensitive to a change in the RBC membrane properties.

3.6 Summary

We presented mesoscopic modeling of RBCs using the DPD method. In analogy with the spectrin network of real RBCs the membrane is represented as a network of interconnected viscoelastic springs supplying elastic and viscous membrane properties. The network takes into account the membrane bending resistance found for the lipid bilayer. Furthermore, it incorporates local and global area constraints providing membrane area-incompressibility, and volume constraint mimicking the incompressibility of the internal cytosol. The model is validated through a number of tests including membrane mechanics, rheology, and dynamics in shear and Poiseuille flows, and is used to represent healthy and Pf-parasitized RBCs.

The macroscopic properties of a membrane can be uniquely related to the network parameters using the derived analytical relations. This completely eliminates an adjustment of the model parameters. We also proposed a stress-free RBC model which leads to triangulation-independent membrane properties, while the other RBC models suffer from stress anomalies, which result in a triangulation-dependent deformation response and an anisotropic equilibrium shape. Mechanical properties of modeled healthy and Pf-RBCs are compared with the optical tweezers experiments yielding excellent agreement for different levels of coarse-graining starting from spectrin-level modeling ($N_v = 27344$ vertices) and ending with only $N_v = 100$ vertices for full membrane representation. However, we suggest that the minimum number of vertices to be used for the RBC membrane should be about $N_v = 250 - 300$ as the lower N_v may not accurately represent the RBC's smooth shape, which is of importance for RBC dynamics.

Here, we summarize the procedure for the RBC model. First, we obtain a triangulation of the equilibrium RBC shape defined by equation (3.29) for the given number of vertices N_v. This triangulation sets the required equilibrium lengths for the springs, triangle areas and the total RBC area and volume. Second, the modeled membrane shear modulus μ_0, area and volume constraint coefficients (eq. (3.7)) are chosen. This defines our RBC model parameters using equations (3.10, 3.13, 3.14 and 3.21). In addition, we need to set the membrane viscosity using equation (3.27). The length, energy unit, and time scales are then defined based on equations (3.33, 3.34, and 3.36). Here, we suggest the RBC diameter to be obtained through an equilibrium simulation rather than assuming it from the analytical RBC shape (eq. (3.29)) as they may be slightly different depending on the relative contributions of in-plane elasticity and membrane bending rigidity. After these two simple steps, the linear elastic properties of the model will match those of the real RBC. In addition, we mention that for large RBC deformations we may need to adjust the spring maximum-extension length which governs the non-linear RBC response. However, it is convenient to set the ratio $x_0 = l_0/l_{max} = 2.2$ for the WLC springs and $x_0 = 2.05$ for the FENE springs. We emphasize that our procedure does not involve parameter adjustments through numerical testing.

The RBC rheology was first probed by TTC showing a good agreement with the experiments for healthy RBCs having the membrane viscosity $\eta_m = 0.022\ Pa \cdot s$ at room temperature. The TTC results for healthy and Pf-RBCs at different temperatures showed rather qualitative agreement with the experiments since dependence of the membrane bending rigidity and viscosity for different stages of the parasite development on temperature are not known. The second rheological test monitored membrane thermal fluctuations. Calculated fluctuation distributions of healthy and Pf-RBCs show only partial agreement with those obtained in the experiments due to many uncertainties in the membrane properties and potential presence of metabolic activities. Complex moduli for healthy and Pf-RBCs at different temperatures derived from the mean square displacement of several points on the fluctuating membrane show consistent results with those obtained in TTC simulations. The third test followed time-dependent whole cell stretching and relaxation. We found that these tests result in a complex behavior due to the non-uniform cell strains and a dependence of the cell response on the applied stresses. In particular, such tests cannot accurately provide meaningful membrane characteristic relaxation time attempted in a number of experiments. In addition, the experiments attempt to fit linear relaxation models which appear to be a crude approximation while the power-law model is preferred. The comparison of the simulation results with the cell response obtained in experiments yields a membrane viscosity between 20 and 60 times that of water. The two former rheological measurements probed local membrane properties, and hence they are more reliable in comparison to the latter one. In addition, the two former tests raised a question about the magnitude of the membrane bending-rigidity and viscosity, where more accurate quantitative experimental predictions would be desired.

RBC dynamics was simulated in shear and Poiseuille flows. In shear flow a RBC shows two basic behaviors: tumbling at low-shear rates and tank-treading at high-shear rates. In addition, there exists a narrow intermittent region where RBC behaviors can interchange. Our model is able to quantitatively capture RBC dynamics in shear flow. However, the comparison of the simulation results with existing theoretical predictions revealed that theories can predict RBC behavior in shear flow qualitatively at best since they are based on a number of simplifications. The theories assume ellipsoidal RBC shape and RBC tank-treading along the fixed ellipsoidal path, while simulations show appreciable RBC deformations in the flow. Furthermore, bending rigidity is not taken into account in theoretical predictions, while RBCs in simulations may show strong membrane deformations within a shear-rate range around the tumbling-to-tank-treading transition. The RBC deformations depend on the relative membrane elastic properties and bending rigidity, and suggest that the RBC bending rigidity may be several times larger than $k_c = 2.4 \times 10^{-19}\ J$. Experimental data on RBC deformations around the tumbling-to-tank-treading transition are not available, but would provide potential confirmation of complex deformations observed in simulations. RBC dynamics in Poiseuille flow in a tube of 9 μm diameter showed a RBC transition to parachute-like shape occurring at a mean flow velocity of about 65 $\mu m/s$. This transition occurs at a larger mean flow velocity for stiffer cells having a higher bending rigidity or shear modulus. An order of magnitude increase in cell stiffness results in only several percent increase of the flow resistance in case of low RBC volume fractions ($C = 0.05$). The cell stiffness is expected to have a much more drastic effect for high volume fractions of RBCs.

Most of the current RBC models assume a purely elastic membrane, and therefore they are able to capture only its mechanical response. Our simulations show that the membrane viscosity has to be considered in order to correctly capture single RBC rheology and dynamics. The presented model is general enough and can be used in many simulation methods, such as Lattice Boltzmann, Brownian dynamics, immerse boundary method, multiparticle collision dynamics, etc. In addition, this model can be employed in simulations of RBCs in disease such as malaria and sickle cell anemia.

Chapter 4

Blood flow in health and malaria disease

4.1 Introduction

Blood is a physiological fluid that consists of erythrocytes or red blood cells (RBCs), leukocytes or white blood cells (WBCs), platelets, and various molecules suspended in plasma. Its main functions are the transport of oxygen and nutrients to cells of the body, removal of waste products such as carbon dioxide and urea, and circulation of molecules and cells which mediate the organism's defense and immune response and play a fundamental role in the tissue repair process. RBCs constitute approximately 45% of the total blood volume, WBCs around 0.7%, and the rest is taken up by blood plasma and its substances. Under healthy conditions RBCs have a biconcave shape of approximately 8 μm in diameter and are highly deformable, which allows them to pass through narrow capillaries with a diameter several times smaller than the RBC size. Due to a high volume fraction of RBCs, the rheological properties of blood are mainly determined by RBC properties.

In vitro experiments [68, 169, 165] of blood flow in glass tubes with diameters ranging from $3 - 4$ μm to 1000 μm have found a dependence of the apparent blood viscosity on the tube diameter, RBC volume fraction or hematocrit (H_t), cell aggregability, and flow rate. In tubes with diameters larger than $500 - 600$ μm blood can be assumed to be a nearly Newtonian fluid with a constant effective viscosity, while in smaller tubes it shows complex rheological behavior. The apparent blood viscosity reaches its minimum at the tube diameter of about 7 μm and shows a significant increase with respect to this minimum as the tube diameter decreases or increases. An increase of the apparent viscosity with increasing tube diameter is known as the Fahraeus-Lindquist effect [68]. This effect is attributed to a cross-stream migration of RBCs in tube flow leading to the formation of two phases [86, 32]: a flow core consisting mainly of RBCs and a cell-free layer (CFL) next to the tube wall devoid of cells. The CFL has a lower viscosity in comparison with the RBC core and serves as a lubrication layer reducing the effective blood viscosity [32].

The cross-stream migration of RBCs in tube flow is governed by cell-wall hydrodynamic interactions which drive the cells away from the wall and by cell-cell hydrodynamic interactions which tend to disperse RBCs [85]. The CFL formed by cell migration depends on the tube diameter, H_t value, and the flow rate, and is correlated with the apparent blood viscosity such that increasing CFL thickness reduces the apparent viscosity of blood.

In vivo experiments [164, 131, 115] of blood perfused through microvessels showed the Fahraeus-Lindquist effect mediated by a CFL formed next to the vessel walls. However, blood flow resistance in real microvessels is markedly higher than that in the microtubes [166, 206]. Microvessels in comparison with glass tubes are elastic, lined with endothelium, relatively short, and may be irregular in shape. These differences are likely to attenuate RBC migration resulting in a decreased CFL and an increased effective viscosity. In addition, irregularities at the vessel walls (e.g., geometry, glycocalyx layer) may contribute to spatial variations of the CFL which tend to diminish the effect of the CFL on the apparent blood viscosity [179].

Computational modeling of blood flow in microtubes or microvessels is challenging since a continuum description is not adequate and the motion of individual deformable cells have to be simulated explicitly. Several computational approaches to model blood flow as a suspension of cells have recently been developed. These include two-dimensional models [188, 15] and three-dimensional simulations [129, 54, 137]. Even though two-dimensional models may qualitatively capture the behavior of a RBC suspension, their quantitative predictions have to be considered cautiously, since RBC motion and deformation in a flow are inherently three-dimensional. Three-dimensional modeling of a RBC suspension is limited due to computational expense such that the number of cells modeled in [129, 137] was on the order of $O(10)$. Dupin et al. [54] were able to simulate blood flow in microchannels with a characteristic size up to 30 μm employing $O(10^2)$ RBCs.

We have developed an efficient parallel code which employs the multiscale RBC model described in chapter 3. This code allows us to simulate the total number of RBCs on the order of $O(10^4)$. Blood flow in tubes with diameters ranging from 10 μm to 40 μm is simulated for different H_t values. Flow velocity profiles, the Fahraeus-Lindquist effect, and the corresponding CFLs will be examined and compared with available experiments. In addition, the flow of a RBC suspension is simulated through a constriction of a microchannel with the characteristic size of 100 μm following the experiments by Faivre et al. [70]. In the experiments it was found that the CFL downstream is significantly enhanced in comparison with that upstream due to a "focusing" effect achieved through migration of cells to the channel center within the constriction. This effect will be examined for different constriction widths and lengths, viscosities of the suspending fluid, H_t values, and rigidities of the cell membrane, and will be compared with experiments. Finally, to demonstrate parallel efficiency of the developed code a flow in a microchannel 1 mm long and 100 μm wide is simulated with 5000 RBCs.

Blood flow may be significantly affected by altered RBC properties occurring in malaria disease. In malaria, RBCs become hosts of Plasmodium parasites which change the cell properties. Pf-parasitized RBCs lose their deformability [190, 158] due to membrane stiffening up to ten times higher than that of healthy cells. This can lead to capillary occlusions [38, 180]. Moreover, at the final stage of intra-erythrocytic parasite development (schizont) the formed parasitic vacuoles force the RBC to attain a near-spherical shape further impairing its ability to deform. An additional change in the RBC properties, which may dramatically alter blood flow, is cytoadherence of Pf-parasitized RBC to vascular endothelium and to other RBCs at later stages [23, 140, 51]. This appears to be a survival mechanism for the parasite, which otherwise may be destroyed while passing through the spleen [60].

Recent *in vitro* experiments [35, 212, 11] have examined adhesive dynamics of infected RBCs in microfluidic flow channels. In these experiments the channel walls were coated with purified protein ligands participating in cytoadherence (e.g., ICAM-1) or with mammalian CHO cells expressing such ligands. Adhesion dynamics of Pf-parasitized RBC on purified ICAM-1 showed rolling or "flipping" behavior in a wide range of shear rates without a detachment or an arrest of RBCs. In contrast to ICAM-1, adhesive dynamics on a surface coated with mammalian CHO cells showed that the majority of RBCs were firmly attached with infrequent complete detachment. This difference in behavior is not entirely understood.

It is believed that the stable binding of RBCs on mammalian CHO cells is not mediated by any unknown expressed proteins [11] and the difference is attributed to the flow microenvironment. Thus, numerical simulations of the RBC adhesive dynamics may be able to aid in understanding this issue.

The developed blood flow model is used for simulations of blood flow through microtubes in malaria. The increased flow resistance in malaria due to an increase in the RBC stiffness is quantified for a wide range of parasitemia levels. An adhesive dynamics model similar to that developed by Hammer and Apte [96] is implemented to simulate the adhesion of leukocytes and Pf-parasitized RBCs in various flows. The simulations of leukocyte adhesive dynamics serve as the model validation, since it has been extensively studied in experiments [9, 8, 90] and in simulations [96, 113, 119]. The adhesive behavior of Pf-parasitized RBCs is studied for a range of model parameters since, to the best of our knowledge, no data of specific bond properties are available. The "flipping" behavior of infected RBCs appears to be due to increased cell stiffness and the presence of a "rigid" parasite inside of the cells, whereas healthy RBCs under similar modeled adhesion conditions yield crawling dynamics. A comparison with the experiments [11] will be made where it is possible, and physical insights will be provided.

The chapter is organized as follows. Section 4.2 presents results on blood flow modeling in microtubes. Flow resistance and the corresponding CFLs are examined for healthy blood conditions and in malaria. Section 4.3 contains blood flow results in a microfluidic channel with a constriction. In section 4.4 the adhesive dynamics model is described and is used to simulate interactions of leukocytes and Pf-parasitized RBCs with an adhesive surface. A brief summary in section 4.5 concludes this chapter.

4.2 Blood flow

This section presents results on modeling of blood flow in microtubes in health and malaria disease. Blood is modeled as a suspension of RBCs using the WLC-POW model described in chapter 3. Blood flow is simulated in tubes of diameters ranging from 10 μm to 40 μm. Properties of the modeled cell suspensions flowing through tubes and corresponding cell-free layers are evaluated for different flow rates and tube hematocrit values. In addition, we simulate blood flow in malaria, where the cell suspension consists of a mixture of healthy and Pf-parasitized RBCs.

4.2.1 Modeling parameters

Blood is simulated with a number of RBCs suspended in a solvent. Here, a single fluid for both external and internal solvents was used, so that particle reflections at the membrane surface were omitted. Turning off reflections of solvent particles at the RBC membranes results in a reduction of the computational cost by two to three times as estimated from previous simulations. To approximate membrane impenetrability by solvent particles the DPD repulsive force (see section 2.2.2) between them and the membrane vertices of RBCs was employed. This does not fully guarantee separation of the internal and external fluids by the RBC membrane, but it nearly eliminates membrane crossing by solvent particles. To identify an effect of such a simplification we have run several simulations of blood flow in small tubes ($D = 10\ \mu m$) with the separation of the internal and the external fluids (through reflections), and no significant differences in the simulated blood properties with those obtained using the simplified model were found.

Suspended RBCs assumed the shear modulus $\mu_0 = 6.3\ \mu N/m$, the bending rigidity $2.4 \times 10^{-19}\ J$, and the membrane viscosity $\eta_m = 0.022\ Pa \cdot s$. We employed the WLC-POW model with the following parameters: $\mu_0^M = 100$, $x_0 = 2.2$, $k_a = 4900$, $k_d = 100$, and $k_v = 5000$ (see section 3.2 for details). The DPD interactions among different particle types (solvent (S) and wall (W) particles, RBC vertices (V)) are outlined in table 4.1. Random force coefficients for different interactions were obtained from equation (2.10) using the energy unit $k_BT = 0.0945$ calculated according to the energy scale in equation (3.34). The number densities of both solvent and wall were set to $n_S = n_W = 3$. The RBC volume was assumed to be slightly larger than that of the triangulated network ($V_0 = 92.45$), since there exist repulsive interactions between solvent particles and RBC vertices resulting in a

interaction	a	γ	r_c	$k(eq.(2.11))$
S-S and S-W	4.0	30.0	1.5	0.25
S-V, W-V	2.0	45.0	1.5	0.25
V-V	100.0	30.0	0.5	0.25

Table 4.1: DPD simulation parameters in blood flow simulations.

thin solvent-free layer next to the RBC membrane. The effective RBC volume was obtained from an analysis of the three-dimensional solvent distribution next to the membrane in an equilibrium simulation, and was set to $V' = 105$. Thus, the cell volume fraction or tube hematocrit was calculated as follows

$$H_t = \frac{N_c V'}{V_t}, \tag{4.1}$$

where N_c is the number of RBCs in the volume $V_t = \pi R^2 L$, R is the tube radius and L is the tube length.

Two types of excluded volume (EV) interactions among cells were considered. The first case is shown in table 4.1, where the repulsive force coefficient between membrane vertices a_{V-V} is set to 100. This method introduces a non-zero screening length between two membrane surfaces governed by the cutoff radius of the repulsive interactions $r_c = 0.5$. Hence, the choice of a smaller cutoff radius may result in overlapping of cells, while a larger one would increase the screening distance between cells which may be unphysical and may strongly affect simulation results at high volume fractions of RBCs. The second method to enforce EV interactions among cells employed reflections of RBC vertices on the membrane surfaces of other cells. The repulsive force coefficient in this case was set to $a_{V-V} = 2$ yielding the screening length between two RBC surfaces to be virtually zero. These two methods of EV interactions will be called "*repulsion*" and "*reflection*", respectively. In addition, several simulations employed a *net repulsion* of RBCs from the wall by setting the repulsive force coefficient between the wall particles and the cell vertices to $a_{W-V} = 30$. They employ "reflection" EV interactions and will be denoted as "*wall force*" further in text. This was done to minimize the effect of near wall density fluctuations of the suspending fluid, which influences simulation results of blood flow in small tubes ($D = 10\ \mu m$). Performance of the described methods is discussed below.

4.2.2 Blood velocity profiles

RBCs in Poiseuille flow migrate to the tube center forming a core in the flow. Figure 4.1 shows a sample snapshot of RCBs flowing in a tube of a diameter $D = 20\ \mu m$. A RBC core formation is clearly observed with a thin plasma layer (not shown) next to the tube walls called the *cell-free* layer (CFL). The cell core of the flow results in plug-like velocity profiles

Figure 4.1: A snapshot of RCBs in Poiseuille flow in a tube of a diameter $D = 20\ \mu m$. $H_t = 0.45$.

shown in figure 4.2 for tubes of diameters $D = 10\ \mu m$ (left) and $D = 40\ \mu m$ (right) for different H_t values. Velocity profiles and subsequent number density distributions are shown

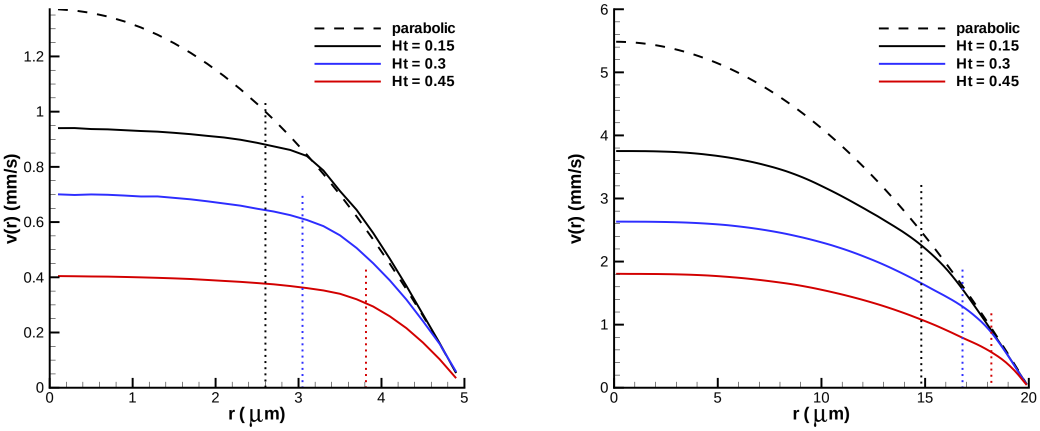

Figure 4.2: Typical velocity profiles of blood flow in tubes of diameters $D = 10\ \mu m$ (left) and $D = 40\ \mu m$ (right) for different H_t values employing “repulsion” EV interactions. Dashed lines show the corresponding parabolic profiles of the Newtonian plasma with no cells present for the same pressure gradients. Dotted lines indicate the corresponding CFL thicknesses.

over the half tube because of flow axisymmetry. Dashed lines in figure 4.2 correspond to the parabolic profiles of the Newtonian plasma in absence of the cells for the same pressure gradients $\Delta P/L$, where ΔP is the pressure drop over the tube length L. Velocity profiles are plotted in physical units, where the time scale was defined in equation (3.36) with $\alpha = 1.0$ and $\eta = 0.0012\ Pa \cdot s$ is the plasma viscosity. Velocity curves are averaged over the tube cross-section and over 2×10^5 time steps which corresponds to the total time of 0.1 seconds. Pressure gradients employed here are 2.633×10^5 Pa/m and 6.582×10^4 Pa/m for tubes of diameters 10 μm and 40 μm, respectively. In the case of low H_t (e.g., 0.15) the velocity profiles closely follow parabolic curves in the near-wall region. In the central region of the tube a substantial reduction in velocity is found for all volume fractions in comparison with the parabolic profiles indicating a decrease in the flow rate given by

$$Q = \int_A v(r) dA, \tag{4.2}$$

where A is the cross-sectional area. As the volume fraction of RBCs is increased the flow rate decreases for the same pressure gradient. For small tube diameters (e.g., $D = 10$ μm) we observe plug-flow profiles with a nearly flat velocity in the center, while for larger tubes the velocity profiles only slightly resemble plug-flow. Moreover, flat velocity profiles are extended to the tube walls for larger H_t values indicating a wider RBC core and smaller CFL. Table 4.2 presents blood flow characteristics for different tube diameters and H_t values. The table includes mean flow velocities defined as $\bar{v} = Q/A$, mean shear rates $\bar{\dot{\gamma}} = \bar{v}/D$, pressure gradients $\Delta P/L$, centerline flow velocities v_c, and the corresponding centerline

H_t	D (μm)	$\bar{v}$ (mm/s)	$\bar{\dot{\gamma}}$ (s^{-1})	$\Delta P/L$ (Pa/m)	v_c (mm/s)	v_p (mm/s)
0.15	10	0.61	61.22	2.633×10^5	0.94	1.37
0.3	10	0.47	47.03	2.633×10^5	0.7	1.37
0.45	10	0.286	28.6	2.633×10^5	0.4	1.37
0.15	20	1.172	58.6	1.316×10^5	1.87	2.74
0.3	20	0.933	46.64	1.316×10^5	1.44	2.74
0.45	20	0.566	28.32	1.316×10^5	0.87	2.74
0.15	40	2.23	55.74	6.582×10^4	3.75	5.48
0.3	40	1.66	41.55	6.582×10^4	2.63	5.48
0.45	40	1.11	27.65	6.582×10^4	1.81	5.48

Table 4.2: Blood flow characteristics for different tube diameters and H_t values employing "repulsion" EV interactions.

velocities v_p of the Newtonian plasma in absence of the cells. The mean flow velocities increase for tubes having larger diameters with comparable shear rates.

4.2.3 RBC and plasma distributions

Figure 4.3 shows center-of-mass distributions of RBCs in tubes of $D = 10$ μm (left) and $D = 40$ μm (right) for different cell volume fractions. The center-of-mass distributions for lower H_t values appear to be more confined around the tube centerline. This results in a larger cell-free layer that can be roughly estimated as $R - r_{c=0}$, where $r_{c=0}$ is the radius at which the probability of finding RBCs becomes zero. Even though the RBC distributions are directly correlated with the width of the RBC core in Poiseuille flow, they do not precisely define a boundary between the CFL and the RBC core, since they correspond to measurements of cell centers. In section 4.2.6 this boundary is defined based on instantaneous measurements of the edge of the cell core with respect to the centerline. Note that for the case of $D = 40$ μm the probability of finding a cell at $r = 0$ is very close to zero, which appears to be due to limited statistics in simulations since no cell centers may be located in the small neighborhood of $r = 0$ during the sampling time.

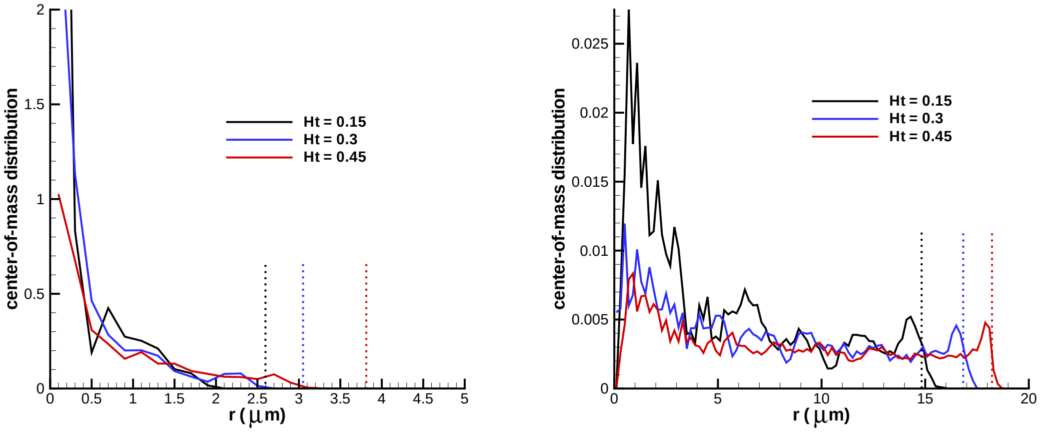

Figure 4.3: Center-of-mass distributions of RBCs in tubes of $D = 10$ μm (left) and $D = 40$ μm (right) for different H_t values with "repulsion" EV interactions. Dotted lines denote the corresponding CFL thicknesses.

To quantify RBC deformations along the flow direction (x) we introduce the x component of the cell radius of gyration $R_g^x(r)$ given by

$$R_g^x(r) = \left\langle \frac{1}{N_v} \sum_{i=1}^{N_v} (x_i - x_{cm}(r))^2 \right\rangle, \tag{4.3}$$

where N_v is the number of cell vertices, $\langle * \rangle$ denotes time averaging, x_i are the x coordinates of RBC vertices, and $x_{cm}(r)$ is the cell center-of-mass at r. Figure 4.4 presents $R_g^x(r)$ normalized by its equilibrium value $R_g^x(eq)$ in tubes of diameters 10 μm (left) and 40 μm (right) for different H_t. $R_g^x(eq)$ is calculated according to equation 4.3 for the RBC

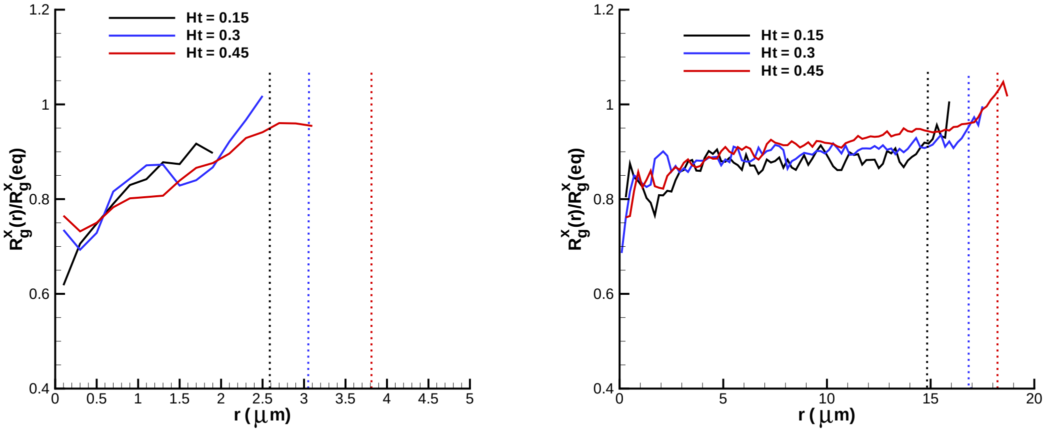

Figure 4.4: The x component of the RBC radius of gyration in tubes of $D = 10$ μm (left) and $D = 40$ μm (right) for different cell volume fractions using "repulsion" EV interactions. Dotted lines show the corresponding CFL thicknesses.

biconcave shape in equilibrium. The curves in figure 4.4 do not extend completely to the wall ($r = D/2$) since there are no cells in the CFL. The ratio $R_g^x(r)/R_g^x(eq)$ is larger in the near-wall region than in the tube center indicating stronger deformations of cells next to the wall due to larger shear rates. Moreover, the ratio in figure 4.4 appears to be independent of the H_t value.

Figure 4.5 presents the number densities of *blood plasma* normalized by their average values in tubes of diameters 10 μm (left) and 40 μm (right) for different H_t values. The average number density of blood plasma is given by $n_s^{avg} = N_s/V_t$, where N_s is the total number of solvent particles in the volume V_t. The plotted number density profiles show higher density values near the tube walls indicating the presence of CFL. In addition, density fluctuations are found next to the tube walls becoming more pronounced at high H_t

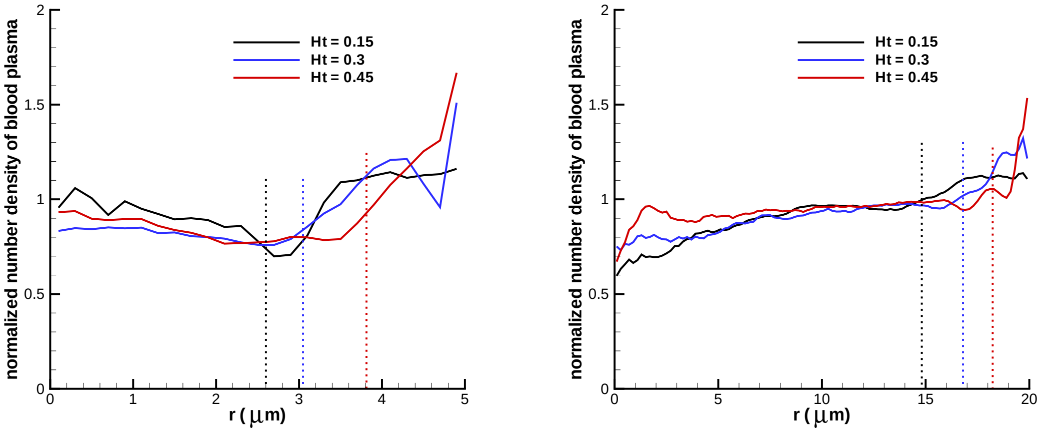

Figure 4.5: Number density profiles of the suspending solvent normalized by their average in tubes of diameters 10 μm (left) and 40 μm (right) for different RBC volume fractions using "repulsion" EV interactions. Dotted lines denote the corresponding CFL thicknesses.

values and small tube diameters. The effect of the existing near-wall density fluctuations will be discussed below.

4.2.4 Fahraeus effect

The Fahraeus effect was discovered in *in vitro* experiments of blood flow in glass tubes [67], which showed an increased value of discharge hematocrit (H_d) measured at the tube exit in comparison with that of the cell suspension before the tube entrance. H_d is defined as the volume fraction of RBCs exiting a tube per unit time. This effect is directly correlated with cell migration to the tube centerline. Hence, the RBC core is moving faster than the average blood velocity resulting in an increased H_d value measured at the tube discharge. We define H_d in simulations as follows

$$H_d = \frac{\bar{v}_c}{\bar{v}} H_t, \tag{4.4}$$

where $\bar{v} = Q/A$ and $\bar{v}_c$ is the average cell velocity calculated by averaging over velocities of all cell vertices and also averaged in time after the stationary state is reached. Pries et al. [165] have compiled a number of experiments on blood flow through glass tubes of different diameters at various H_t values to obtain an empirical relation between H_t and H_d given by

$$\frac{H_t}{H_d} = H_d + (1 - H_d)\left(1 + 1.7e^{-0.35D} - 0.6e^{-0.01D}\right), \tag{4.5}$$

where the tube diameter D is in μm. Figure 4.6 compares H_d values in simulations with those from equation (4.5) for different tube diameters and cell volume fractions. The left figure corresponds to the "repulsion" EV interactions among the cells with the parameters in table 4.1 that result in a small screening distance between two RBC membrane surfaces discussed in section 4.2.1. The right plot contains simulation results obtained with "reflection" EV interactions yielding essentially no screening length among RBCs. Agreement between simulations and empirical values from equation (4.5) is excellent for low H_t values, while discrepancies are found for large H_t and small tube diameters ($D = 10$ μm). EV interactions appear to be of importance at $H_t = 0.45$ since the cells are closely packed. The introduced screening length among the cells with "repulsion" EV interactions results in a wider RBC core compared with that using "reflection" EV interactions. This yields a smaller CFL and flow rate (shown in the next section) and consequently a smaller H_d value as seen in figure 4.6.

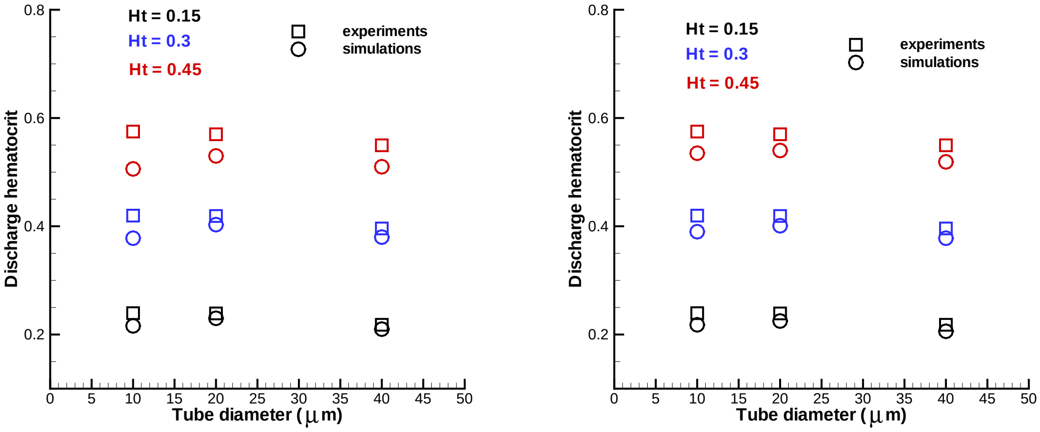

Figure 4.6: Discharge hematocrits for various RBC volume fractions and tube diameters in comparison with the approximation in equation (4.5). "Repulsion" (left) and "reflection" (right) EV interactions are employed.

The remaining discrepancies for small tube diameters are due to solvent density fluctuations next to the wall as shown in figure 4.5. Figure 4.7 presents H_d values from simulations using the "wall force" method (see section 4.2.1). Additional wall repulsion of RBCs re-

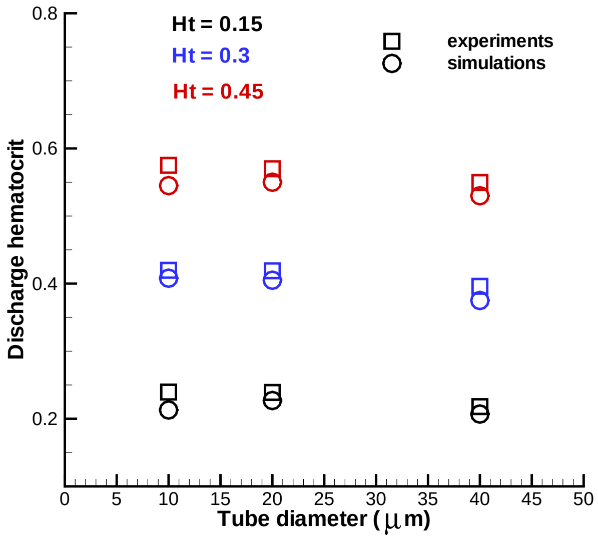

Figure 4.7: H_d for different RBC volume fractions and tube diameters obtained by the "wall force" method that utilize a net repulsion of cells from the wall.

duces the effect of near-wall density fluctuations of blood plasma in tubes of small diameters yielding good agreement of the simulated H_d values with those in *in vitro* experiments. Note that the repulsive wall does not affect the simulation results for low H_t values and large tube diameters since the CFL is wider than the distance of the effective cell-wall interactions.

In conclusion, the "wall force" method yields superior results for H_d in comparison with the other two considered approaches. The "repulsion" method for EV interactions introduces a non-zero screening distance among RBCs, which may be unphysical. Cell-cell hydrodynamic interactions mediated by the simulated blood plasma are likely to be affected by this screening layer among the cells. The "reflection" approach eliminates the effect of the artificial screening layer to yield better results compared with the "repulsion" method. However, both methods "repulsion" and "reflection" do not apply any treatments of the existing solvent density fluctuations near the walls. The "wall force" method extends the "reflection" approach to minimize the effect of density fluctuations. It proves to be the best approach and therefore, it is recommended for future runs.

4.2.5 Fahraeus-Lindquist effect

The Fahraeus-Lindquist effect [68] corresponds to a decrease in the apparent blood viscosity with decreasing tube diameter found in experiments of blood flow in glass tubes [165]. The apparent viscosity is defined as follows

$$\eta_{app} = \frac{\pi \Delta P D^4}{128 Q L} = \frac{\Delta P D^2}{32 \bar{v} L}. \tag{4.6}$$

The apparent viscosity increases for higher H_t values since higher cell crowding yields larger flow resistance. It is more convenient to consider the relative apparent viscosity defined as

$$\eta_{rel} = \frac{\eta_{app}}{\eta_s}, \tag{4.7}$$

where η_s is the solvent viscosity. Figure 4.8 shows the simulated η_{rel} values in comparison with the empirical fit to experiments [165] for the tube diameter range $10 - 40$ μm and H_t values in the range $0.15 - 0.45$. Simulations in the left figure employed "repulsion" EV interactions. They significantly overpredict the relative apparent viscosity for $H_t = 0.45$ and tube diameters of $10-20$ μm. The "reflection" EV interactions in the right figure yield better correspondence between the simulated viscosities and those from the experiments since a non-zero screening length among the cells is not implied *a priori*. These results are consistent with the H_d values discussed in the previous section. In addition, the remaining

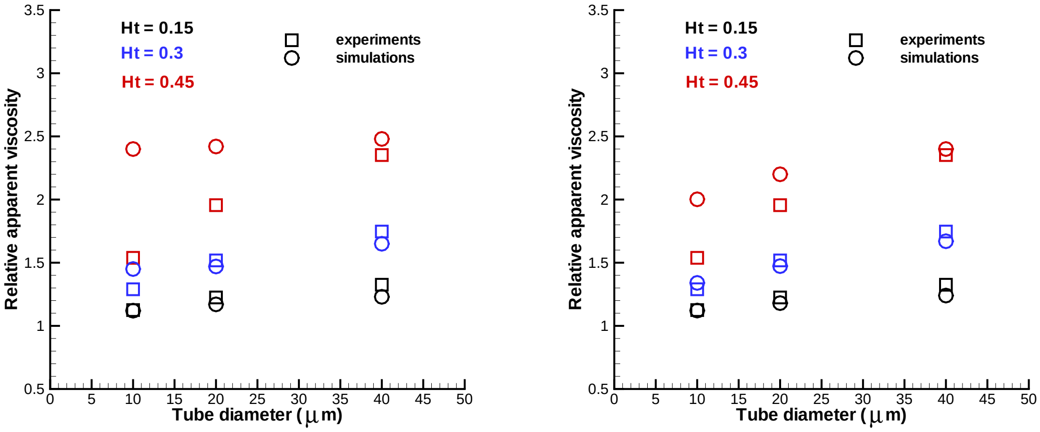

Figure 4.8: Relative apparent viscosity obtained with "repulsion" (left) and "reflection" (right) EV interactions in comparison with experimental data [165] for various H_t values and tube diameters.

discrepancies in η_{rel} for $H_t = 0.45$ are due the near-wall density fluctuations (figure 4.5) of the suspending plasma mentioned in section 4.2.4. To minimize influence of the solvent fluctuations an analogous set of simulations was performed with the "wall force" method shown in figure 4.9. Excellent agreement between simulations and experiments was found for this case. The "wall force" method appears to be the best among three considered approaches, which is consistent with the H_d values discussed in section 4.2.4 and with the corresponding CFLs presented next.

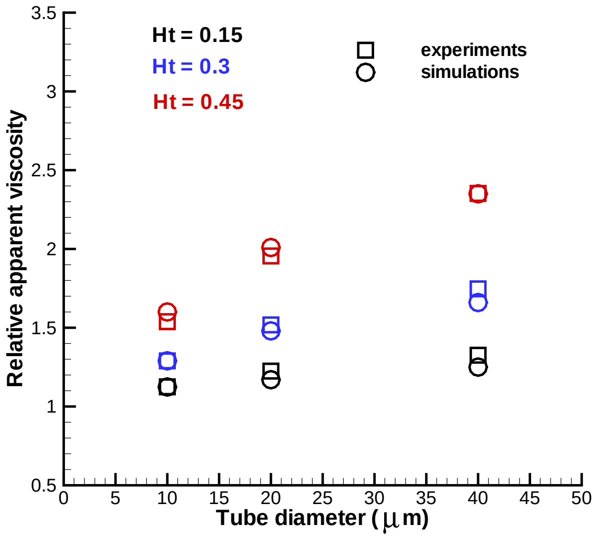

Figure 4.9: Relative apparent viscosity obtained with the "wall force" setup in comparison with experimental data [165] for different H_t values and tube diameters.

4.2.6 Cell-free layer

The CFL is a near-wall layer of blood plasma absent of RBCs (see figure 4.1) since they are subject to migration to the tube center in Poiseuille flow. The fluid viscosity of the CFL region is much smaller than that of the tube core populated with RBCs providing an effective lubrication for the core to flow. The thickness of the CFL is directly related to the Fahraeus and the Fahraeus-Lindquist effects. Thus, in small tubes the CFL thickness is significant with respect to the tube diameter resulting in a smaller relative apparent viscosity and larger H_d in comparison with those in larger tubes, where the CFL thickness becomes negligible with respect to the tube diameter.

To determine the CFL thickness δ we measured the outer edge of the RBC core (see figure 4.1) which is similar to CFL measurements in experiments [131, 115]. Figure 4.10 shows a sample CFL edge (left) from simulations and CFL thickness distribution (right) for $H_t = 0.45$ and $D = 20$ μm. The cell edge was measured by projecting cell vertices of a snapshot of RBCs on the $x - y$ plane, where curves of the RBC core minimum and maximum were fitted. Discrete samples of δ from the obtained curves were taken every 0.5 μm in x. In addition, several cell edge curves were extracted from a single snapshot by rotating the RBC core before projection on the $x - y$ plane, and a number of core snapshots corresponding to different times was averaged. A steep beginning of the CFL thickness distribution in figure 4.10 (right) characterizes the global minimum of the RBC core, while the slowly decaying tail corresponds to a number of cavities in the RBC core formed by two or more adjacent RBCs and shown in figure 4.10 (left). To characterize variations in CFL thickness the standard deviation (SD) σ_δ was calculated. Also, the persistence of spatial variation was obtained by calculation of the correlation length of the cell edge pattern given by

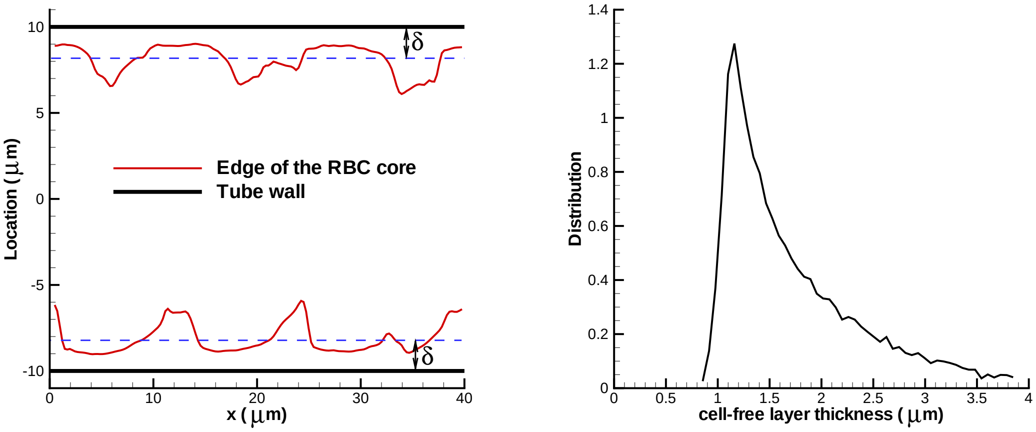

Figure 4.10: An example of a CFL edge (left) and CFL thickness distribution (right) for $H_t = 0.45$ and $D = 20$ μm.

$$C(d) = \left\langle (\delta(x) - \bar{\delta})(\delta(x+d) - \bar{\delta}) \right\rangle, \tag{4.8}$$

where $C(d)$ is the covariance of $(\delta(x) - \bar{\delta})$ and $(\delta(x+d) - \bar{\delta})$, $\bar{\delta}$ is the average CFL, and d is the separation length. The covariance decreases to zero with increasing d, and if $C(d') \approx 0$, then d' is the correlation length of the cell edge pattern. Table 4.3 presents the simulated correlation lengths for different H_t values and tube diameters. The correlation length of

	$H_t = 0.15$	$H_t = 0.3$	$H_t = 0.45$
$D = 10\ \mu m$	8.3	18.5	27.1
$D = 20\ \mu m$	8.5	18.3	27.8
$D = 40\ \mu m$	8.0	18.7	27.3

Table 4.3: Correlation lengths of the cell edge pattern for different tube diameters and H_t values.

the cell edge pattern increases for larger H_t since the cell core is denser. Note that in case of $H_t = 0.15$ the correlation length is comparable with the cell diameter indicating small correlations among separate cells. The lengths d' appear to be independent of the tube diameter which is in agreement with *in vivo* experiments [115] for the vessel diameter range of $20 - 50\ \mu m$. Furthermore, d' values found in [115] for $H_t = 0.42$ are in the range of $25 - 35\ \mu m$, which is consistent with the simulated values of $27 - 28\ \mu m$ for $H_t = 0.45$ in table 4.3.

Figure 4.11 shows CFLs for different tube diameters and cell volume fractions obtained using the "repulsion" and "reflection" EV interactions (left) and the "wall force" method in comparison with *in vitro* experiments [169] and *in vivo* experiments [131, 115] (right). Simulated CFLs are consistent with the described Fahraeus and Fahraeus-Lindquist effects.

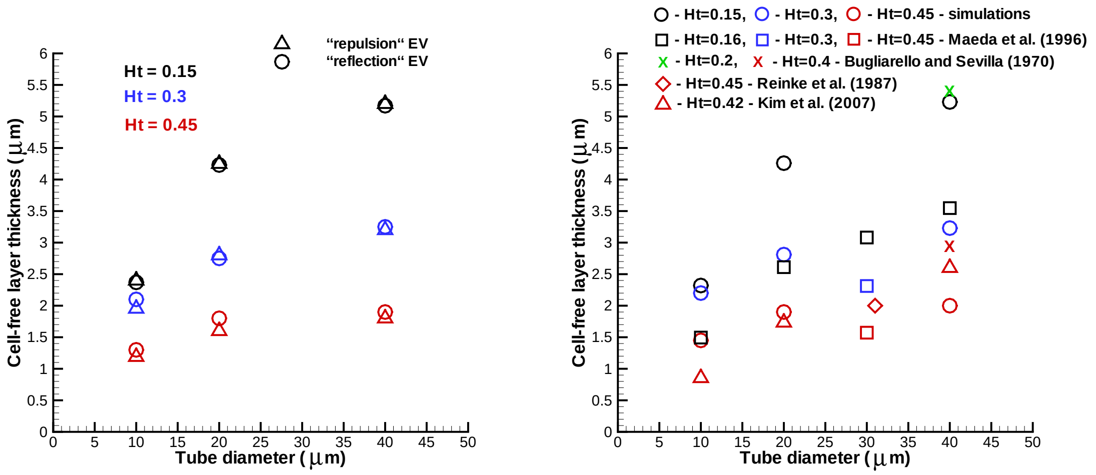

Figure 4.11: CFLs obtained in blood flow simulations employing the "repulsion" and "reflection" EV interactions (left) and the "wall force" setup in comparison with experimental data [169, 131, 115] (right) for various H_t values and tube diameters.

CFLs are wider for lower H_t values and larger tube diameters indicating migration of RBCs to the tube centerline. CFL thicknesses for different EV interactions in figure 4.11 (left) seem to have insignificant discrepancies. This appears to be true for larger tube diameters and lower cell volume fractions in agreement with the analogous independence of the relative apparent viscosity of a RBC suspension on EV interactions found in section 4.2.5. However, in case of small tube diameters and high H_t values even a small change in the CFL thickness may result in a considerable increase of the relative apparent viscosity. As an example, for the case of $D = 10\ \mu m$ and $H_t = 0.45$ the CFLs are 1.19 μm, 1.3 μm, and 1.45 μm for the "repulsion", "reflection" EV interactions, and the "wall force" method, respectively, while the corresponding η_{rel} values are 2.4, 2.002, and 1.6 (figures 4.8 and 4.9) showing a significant decrease.

A comparison of the simulated CFLs and those obtained in experiments in figure 4.11 (right) shows partial agreement. Note that our simulations mimic blood flow in rigid and long tubes. Thus, the CFL measurements are carried out after the stationary state is reached and cell migration can be neglected. Bugliarello and Sevilla [25] performed experiments of blood flow in glass tubes at various H_t values shown by the "x" symbols in figure 4.11 (right). The CFLs obtained in these experiments appear to be larger than the simulated values. Reinke et al. [169] conducted *in vitro* experiments of blood flow at $H_t = 0.45$ in glass tubes. The obtained CFL value for $D = 31\ \mu m$, $H_t = 0.45$ suitable for comparison (diamond symbol in figure 4.11 (right)) shows good agreement with simulations. Note that simulated CFLs lie within the range of a scatter in the available *in vitro* experimental data on CFLs. We are not aware of any other *in vitro* experimental measurements of CFLs suitable for comparison.

CFLs from *in vivo* experiments [131, 115] plotted in figure 4.11 (right) show satisfactory agreement with simulations for high H_t values ($H_t = 0.42 - 0.45$), while for low H_t the correspondence is rather poor. In fact, available *in vivo* measurements of CFLs show a scatter in the results. Yamaguchi et al. [209] found the CFL in cat cerebral microvessels to be approximately 4 μm (not shown in figure 4.11 (right)) and independent of vessel diameter. Maeda et al. [131] reported CFLs in the range of $1 - 1.8\ \mu m$ for vessel diameters $10 - 40\ \mu m$ at $H_t = 0.45$, where a rabbit mesentery was perfused. Kim et al. [115] obtained CFLs in the range of $0.5 - 3\ \mu m$ increasing from the diameter 10 μm to 50 μm at $H_t = 0.42$ where a rat cremaster muscle was used. The variability of *in vivo* measurements of the CFL and their discrepancies with simulations shown in figure 4.11 (right) may be due to several reasons such as the existence of the glycocalyx layer, variations in vessel width, use of a short vessel, close proximity of the site of CFL measurements to vessel bifurcations, vessel elasticity, and spatial resolution of the measurements.

The thickness of the glycocalyx layer is estimated to be on the order of $0.4 - 0.5\ \mu m$ [40, 202]. Experimental data of Kim et al. [115] shown in figure 4.11 (right) include the glycocalyx thickness and yield satisfactory agreement with simulations. Subtracting its average thickness from the experimental CFL values would result in very thin CFLs especially for small vessel diameters ($D = 10\ \mu m$) and yield further discrepancies in comparison with simulations. The other mentioned experimental sources do not explicitly state whether the thickness of the glycocalyx layer was included into CFL measurements. The largest discrepancies between simulated CFLs and those measured in *in vivo* experiments are on the order of the glycocalyx thickness for $H_t = 0.42 - 0.45$, while for lower H_t values discrepancies appear to be more significant.

Variations in vessel diameter may locally alter blood flow and impact CFL measurements. Maeda et al. [131] reported spatial variations in the vessel diameter on the order of several percent, while Kim et al. [115] estimated a potential error in CFL measurements to be approximately 10% due to the change in the vessel diameter. Even though variations in the vessel diameter seem to have a rather insignificant effect on CFL measurements, it may influence migration of RBCs to the center of the vessel which is the main mechanism for CFL development. Moreover, RBC migration strongly depends on the vessel length and flow non-uniformity due to nearby vessel bifurcations. The perfused vessel length was not specified in experiments and it may not be long enough to allow RBCs to fully migrate to the vessel center and to form a steady core of the flow. In simulations, periodic boundary conditions in the direction of the tube axes were employed, which is essentially equivalent to the infinite length of the tube, and complete migration of RBCs can be considered to be fully achieved. Incomplete migration of RBCs in short vessels would result in the smaller CFLs found in experiments [131] in comparison with those in simulations (figure 4.11 (right)). In section 4.3 a strong influence of the channel length on the CFL will be shown for the case of a RBC suspension flowing through a constriction in a microfluidic device.

Upstream flow conditions such as vessel bifurcations affect the width of the CFL [164, 59]. Kim et al. [115] reported a non-axisymmetric nature of CFL variations on opposite sides of the arteriole with a difference of 0.5 μm in the mean width of CFLs on the two sides. This difference in CFLs was attributed to a possible effect of upstream bifurcations. Note that the simulated CFLs here are found to be axisymmetric. Pries et al. [164] reported that an axisymmetric cell profile is recovered after at least ten vessel diameters downstream of a bifurcation. However, this distance may not be long enough to account for full RBC migration. At high H_t values CFLs may not be very sensitive to the discussed geometrical uncertainties present in the *in vivo* experiments, while at low H_t they may significantly affect measured CFLs. An example of this effect is shown in a microfluidic channel in section 4.3.

The CFLs obtained by Maeda et al. [131] plotted in figure 4.11 (right) are smaller than those obtained in the simulations. In accordance, the reported values of the relative apparent viscosity for the hardened vessels of diameters in the range of $25-35$ μm were 1.63, 2.0, and 2.83 for $H_t = 0.16$, 0.3, and 0.45, respectively. These viscosities are considerably higher than those found in *in vitro* experiments [165] (1.29, 1.65, and 2.19 for $D = 30$ μm and $H_t = 0.15$, 0.3, and 0.45), which provides an additional explanation for the discrepancies found. Finally, spatial resolution of the experimental measurements may contribute to the discrepancies between the simulated CFLs and those obtained in *in vivo* experiments. Kim et al. [115] reported that their spatial resolution was 0.4 μm, which is on the order of the thickness of the glycocalyx layer, while the spatial resolution was not specified in [131].

Figure 4.12 (left) presents SD values σ_δ of the CFL thickness. Spatial variations of the CFL thickness characterized by σ_δ appear to increase with tube diameter in agreement with experiments [115]. The observed discrepancies between simulated and experimental SD values may be due to the differences discussed in the previous paragraph. The obtained SD values of the CFL thickness appear to be independent of H_t and a model selected for EV interactions among cells (not shown here). Figure 4.12 (right) shows CFLs at $H_t = 0.45$ for different tube diameters and shear rates $\bar{\dot{\gamma}}$. The CFL thickness is slightly decreasing with increasing shear rate or equivalently flow rate. This is consistent with experiments [115], where the same trend was found for the range of shear rates $100-500$ s^{-1}. A decrease in the CFL thickness for higher flow rates is attributed to intensified hydrodynamic interactions among cells at higher shear rates that tend to expand the RBC core of the flow. Note that a decrease in the CFL thickness in this case may not necessarily result in an increase of the relative apparent viscosity because it corresponds to a characteristic viscosity of a

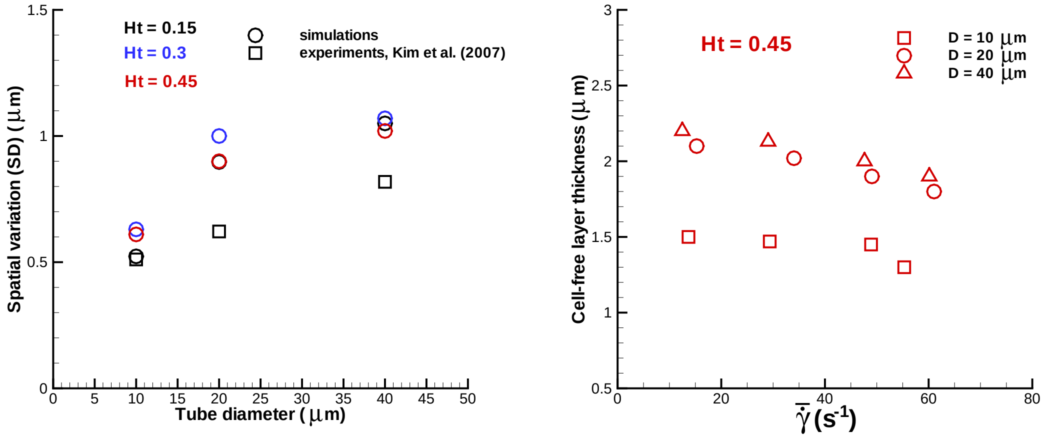

Figure 4.12: Spatial variations of the CFL thickness (SD) (left) and CFLs for different shear rates at $H_t = 0.45$ (right) for various H_t values and tube diameters. *In vivo* experimental data [115] for $H_t = 0.42$ are included in the left plot for comparison.

RBC suspension averaged over the tube cross-section. A suspension of RBCs shows a shear-thinning behavior with shear-dependent viscosity. Analysis of blood rheological properties is beyond the scope of this work; however, several examples of shear-thinning fluids (polymer melts and solutions) and the analysis of their rheological properties are presented in chapter 6. Finally, simulation results for a lower H_t than $H_t = 0.45$ did not show a statistically significant increase or decrease in the CFL thickness for shear rates in the range $10 - 100$ s^{-1}.

4.2.7 Increased flow resistance in malaria disease

Blood in malaria is simulated as a mixture of healthy and Pf-parasitized RBCs. Simulation parameters are the same as those in section 4.2.1 using the "wall force" method. Pf-parasitized RBCs are characterized by the membrane shear modulus $\mu_0 = 31.5$ $\mu N/m$ which is five times larger than that of healthy cells and corresponds to the trophozoite stage of parasite development. Other membrane properties (e.g., bending rigidity, viscosity) are identical to those of healthy RBCs. The percentage of Pf-parasitized RBCs with respect to the total number of cells in a unit volume is called parasitemia level. Several parasitemia levels (25%, 50%, and 100%) are considered for tube diameters $10 - 20$ μm and H_t values $0.3 - 0.45$. Parasitemia levels employed here are higher than those often found in clinical blood tests [24, 208, 95] of individuals suffering from malaria. At a parasitemia level above

0.2% an immune response is initiated and levels around 10% are found in very severe cases of malaria with high mortality [24, 208, 95]. Clinical tests are able to detect Pf-parasitized RBCs at a parasitemia level as small as $0.0001 - 0.0004\%$. Active malaria disease in most cases is characterized by parasitemia in the range of $0.5\% - 10\%$. Even though the parasitemia levels simulated here are beyond this range, we aim to span the full range of parasitemia $0\% - 100\%$ to evaluate dependence of blood flow properties on parasitemia levels. At low parasitemia levels differences in measured properties may not be significant and therefore, they would be difficult to detect. However, an estimation of a contribution of Pf-parasitized RBCs to blood flow properties at realistic parasitemia levels in malaria will be provided at the end of this section.

Figure 4.13 shows a snapshot of RCBs flowing in a tube of the diameter $D = 20\ \mu m$ at a parasitemia level of 25%. Healthy cells are drawn in red and Pf-parasitized RBCs in blue, while the total tube H_t is 0.45. The core of the flow is formed by the cells with a CFL next to the tube wall resulting in the plug-like velocity profiles presented in figure 4.14 for tubes of diameters $D = 10\ \mu m$ (left) and $D = 20\ \mu m$ (right) for different parasitemia levels at $H_t = 0.45$. Dashed lines are the corresponding parabolic profiles of Newtonian plasma in the absence of cells for the same pressure gradients given in table 4.2. An increase of the parasitemia level yields a decrease in flow rate shown by a decrease in velocity at the tube center.

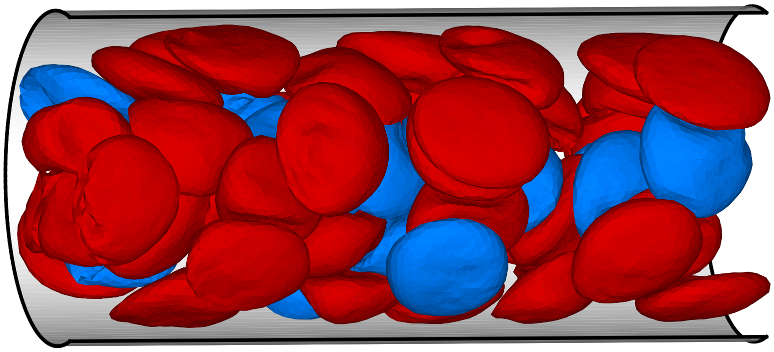

Figure 4.13: Healthy (red) and Pf-parasitized (blue) RCBs in Poiseuille flow in a tube of the diameter $D = 20\ \mu m$. $H_t = 0.45$, parasitemia level 25%.

Figure 4.15 shows the relative apparent viscosity of simulated blood in malaria for $H_t = 0.45$ (left) and $H_t = 0.3$ (right) at different parasitemia levels. The effect of parasitemia

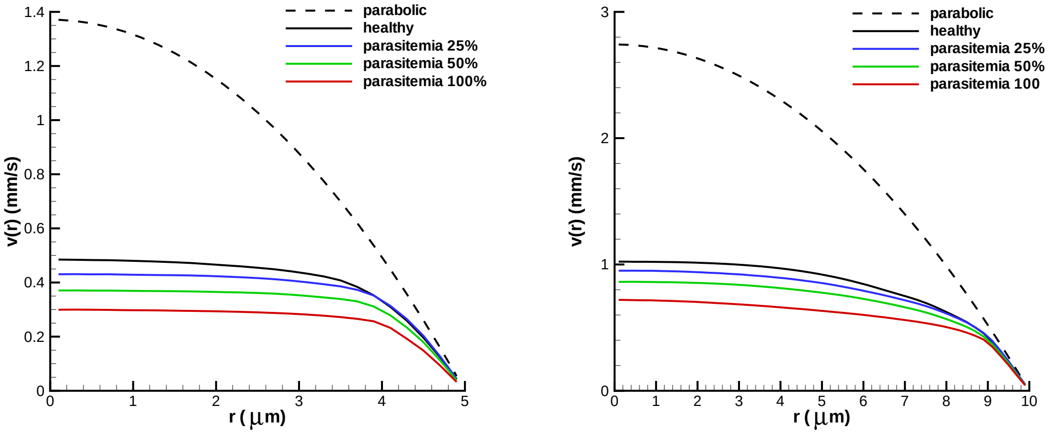

Figure 4.14: Velocity profiles of blood flow in malaria in tubes of diameters $D = 10\ \mu m$ (left) and $D = 20\ \mu m$ (right) for different parasitemia levels. $H_t = 0.45$. Dashed lines show the corresponding parabolic profiles of the Newtonian plasma with no cells present for the same pressure gradients.

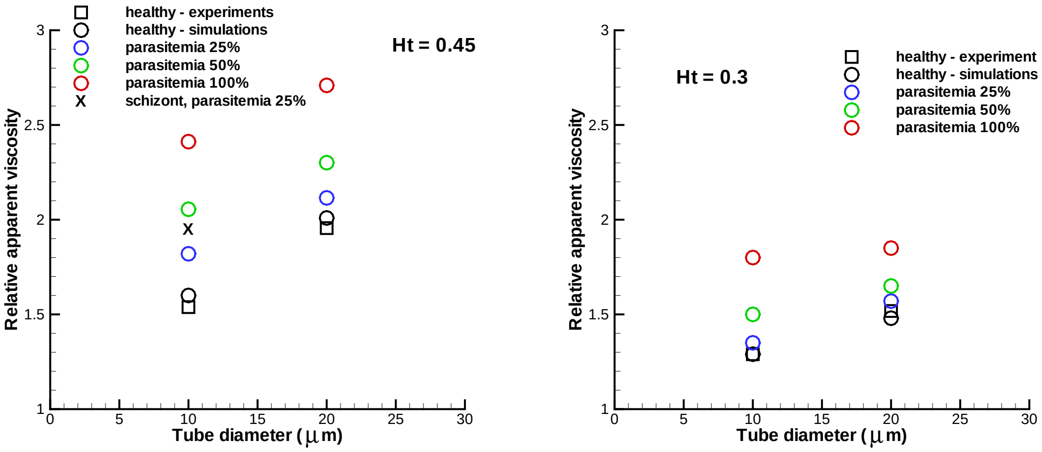

Figure 4.15: Relative apparent viscosity of blood in malaria with $H_t = 0.45$ (left) and $H_t = 0.3$ (right) for various parasitemia levels and tube diameters. Symbol "x" in the left figure corresponds to the schizont stage with a near-spherical shape (see section 3.3.4). Experimental data correspond to the empirical fit by Pries et al. [165].

level on flow resistance characterized by the relative apparent viscosity appears to be more prominent for small tube diameters and high H_t values. Thus, at $H_t = 0.45$ blood flow resistance in malaria may increase up to 50% in vessels of diameters around 10 μm and up to 43% for vessel diameters around 20 μm. For larger vessel diameters the difference between the increased flow resistance due to parasitemia and that of healthy blood decreases further. However, in the case of $H_t = 0.3$ the resistance is subject to a maximum increase by

40% for $D = 10\ \mu m$ and about 25% for $D = 20\ \mu m$ showing a weaker dependence than that for the case of $H_t = 0.45$. Moreover, an increase in the relative apparent viscosity due to parasitemia for the case of $H_t = 0.15$ is found to be on the order of 10% for $D = 10\ \mu m$ and about several percent for larger vessel diameters. Symbol "x" in figure 4.15 (left) presents flow resistance in malaria at 25% parasitemia level with the infected RBCs at schizont stage having a near-spherical shape (see section 3.3.4 for details). Besides the difference between near-spherical and biconcave shapes, the shear modulus of these cells is approximately two times larger than that of RBCs at throphozoite stage (most of the simulations shown). This results in a further increase in flow resistance when compared with RBCs at the trophozoite stage and the same parasitemia level. However, the increase is within 10% and is likely to be insignificant for realistic parasitemia levels as discussed below.

Figure 4.16 shows the corresponding CFLs of blood flow in malaria at $H_t = 0.45$ (left) and $H_t = 0.3$ (right) for different parasitemia levels and tube diameters. Simulated CFLs

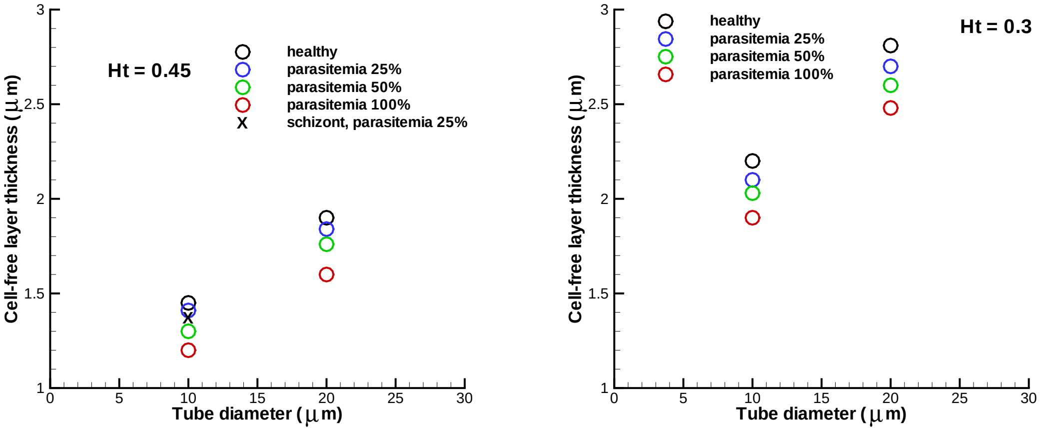

Figure 4.16: CFLs of simulated blood flow in malaria with $H_t = 0.45$ (left) and $H_t = 0.3$ (right) for various parasitemia levels and tube diameters. Symbol "x" in the left figure corresponds to the schizont stage with a near-spherical shape (see section 3.3.4).

are consistent with the results on the relative apparent viscosity presented above. The CFL thickness decreases with an increase in the parasitemia level resulting in larger blood flow resistance. A decrease in CFL thickness at a non-zero parasitemia is due to the increased stiffness of Pf-parasitized RBCs. Hence, stiffer cells are less compliant to deformations resulting in an impaired close packing of RBCs in the flow core in comparison with softer cells of healthy blood. This leads to an increase in the cell core width and consequently to a decreased CFL.

Finally, we comment on the increased blood flow resistance in capillaries and small arterioles for realistic parasitemia levels of less than 10% as found in the majority of malaria cases [24, 208, 95]. According to the simulation results shown above the increase in the relative apparent viscosity should be below $10-15\%$. Note that it is likely that the predicted resistance in simulations is underestimated due to a potential increase in membrane bending rigidity of Pf-parasitized RBCs and the presence of “rigid” parasites inside the cells discussed in chapter 3. An increase in bending rigidity as well as a rigid body inside the cells would further impair the ability of Pf-parasitized RBCs to comply with deformations in the flow and consequently prevent their close packing in the flow core. However, taking these changes into account may not yield a substantial increase in blood flow resistance in malaria at the realistic parasitemia levels. Hence, we estimate that the maximum increase in flow resistance in malaria to be 25%.

In fact, other conditions not considered in this section are more likely to significantly influence blood flow resistance in malaria. Stiffer Pf-parasitized RBCs can block small capillaries up to $5-6$ μm in diameter as shown in microfluidic experiments [180] and discussed in the introduction. In addition, the property of Pf-parasitized RBCs to adhere to each other and to vessel endothelium at later stages of parasite development may strongly impair blood flow in capillaries and small arterioles resulting in a substantial increase of flow resistance. This condition will be modeled and discussed in detail in section 4.4.

4.3 Blood flow through a constriction

In this section we systematically examine blood flow in a microchannel undergoing sudden constriction. An augmentation of the cell-free layer downstream of the constriction will be investigated for different microchannel geometries, hematocrit values, viscosities of a suspending fluid, and cell mechanical properties. Simulation results will be compared with experiments [70] and physical insights of an enhancement of the CFL thickness downstream of the constriction will be provided. In addition, we demonstrate the potential capability of the developed code for the blood flow model with a simulation employing 5000 RBCs. In general, we are able to simulate $O(10^4)$ of RBCs with a high parallel efficiency.

4.3.1 Microfluidic geometry and simulation parameters

The microfluidic channel geometry is sketched in figure 4.17. The channel is aligned with the x direction. W is the channel width being the same upstream and downstream, while w_c is the width of the constriction. L_u, L_c, and L_d are the lengths of upstream, constriction, and downstream parts, respectively. $W = 100$ μm, $L_u = 100$ μm, and $L_d = 200$ μm are kept the same in all simulations, while w_c is varied from 25 μm to 50 μm and the constriction length L_c from 50 μm to 200 μm. The channel height in z direction is equal to $H = 20$ μm. The simulated channel is assumed to be periodic in x and z.

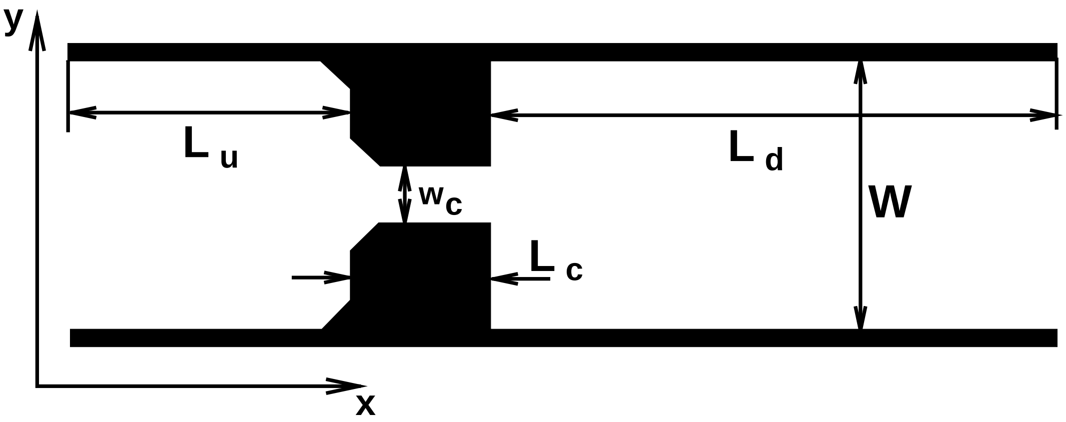

Figure 4.17: Sketch of the geometry of a microfluidic channel having sudden constriction.

The microfluidic geometry used in the simulations is similar to that in experiments [70]; however several disparities have to be pointed out. The fabricated channels in experiments are non-periodic in z with the height of 75 μm yielding a three-dimensional flow in contrast to a nominally two-dimensional flow in simulations. Furthermore, the experimental channels are non-periodic in x direction having an inflow and outflow and the lengths L_u and L_d are essentially longer than those employed in simulations. Finally, note that the corners at the end of the upstream part and the beginning of the constriction (see figure 4.17) are smoothed out in agreement with those found in experimental geometry. Influence of these differences between simulations and experiments on measured flow properties will be discussed below.

Table 4.4 presents the simulation parameters similar to those defined in table 4.1. The energy unit is set to $k_BT = 0.3$. The WLC-POW model is employed for RBCs with the parameters: $\mu_0^M = 100$, $x_0 = 2.2$, $k_a = 4900$, $k_d = 100$, and $k_v = 5000$ (see section 3.2

interaction	a	γ	r_c	$k(eq.(2.11))$
S-S and S-W	25.0	10.0	1.25	0.25
S-V, W-V	10.0	15.0	1.25	0.25
V-V	50.0	10.0	0.5	0.25

Table 4.4: DPD simulation parameters in blood flow through a microfluidic channel.

for details). The solvent viscosity is equal to 10.7 in DPD units. The simulated H_t values are 0.026 and 0.16 in agreement with those in experiments [70]. A uniform body force is applied to all DPD particles in the region of 50 μm in length from the channel entrance and in the region of 100 μm in length at the channel end to drive the flow. The uniform body force is equivalent to a constant pressure gradient which can be considered uniform in these regions. The pressure gradient in the region around the constriction is not constant, which voids the validity of application of the uniform body force in that area.

4.3.2 Typical flow profiles

Fluid flow in a microfluidic device is characterized by the Reynolds (Re) number defined as

$$Re = \frac{\rho_o Q}{\eta_o H}, \tag{4.9}$$

where ρ_o and η_o are the density and viscosity of the suspending solvent and Q is the total flow rate. Based on this definition the Re number employed in simulations is equal to approximately 5, while in experiments it is approximately 10^{-2}. Even though our Re number is larger than the experimental value, we will still attempt a comparison between simulations and experiments. An enhancement of the CFL downstream of the constriction appears to be mainly due to a cross-stream migration of cells in a microchannel flow, which is often characterized by a capillary number for cases of vesicles in a flow [26, 5]. We define the local capillary (Ca) number as follows

$$Ca = \tau\dot{\gamma}, \qquad \tau = \frac{\eta_o R_0}{Y}, \qquad \dot{\gamma} = \frac{Q}{w^2 H}, \tag{4.10}$$

where τ is the characteristic relaxation time of a cell, $\dot{\gamma}$ is the average shear rate, $R_0 = \sqrt{A/(4\pi)}$ is the characteristic cell size and A is the cell area; Y is the Young's modulus of a RBC, and w is the local channel width. The Ca number includes several characteristics of the simulated suspension such as the cell size, its rigidity, solvent viscosity, and the flow strength which govern RBC migration in microchannel flow. The Re number alone does not provide a sufficient characterization for the cell migration since it reflects only properties of the suspending fluid and the flow strength. In fact, in case of a small Re number (on the order of one or smaller) the Ca number appears to be the main characteristic parameter of the flowing suspension of RBCs.

Figure 4.18 shows the contour of the x component of velocity V_x normalized by V_{max} as well as the flow streamlines for $Re = 5$ and $H_t = 0.026$. V_{max} is the maximum flow velocity within the constriction. The streamlines show two symmetric recirculation regions downstream of the constriction. These regions become smaller if the Re number of the flow is decreased, while they would elongate for larger Re numbers. Figure 4.19 presents cross-sectional normalized velocity profiles extracted across the channel at $x = 140$ μm (left) and 50 μm after the constriction (right) for different constriction lengths L_c. The dashed line in the left figure corresponds to a Newtonian parabolic profile of the same flow rate. The velocity profiles in the constriction are nearly parabolic due to the low RBC volume fraction $H_t = 0.026$. Note that velocity profiles for different constriction lengths L_c are nearly identical since the flow appears to be very close to that of a Newtonian fluid.

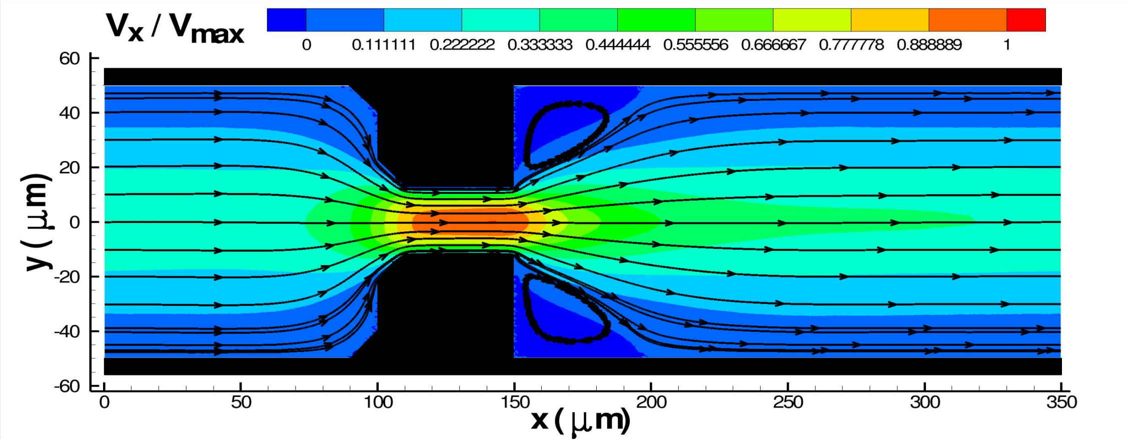

Figure 4.18: Flow streamlines and the contour of the x component of velocity V_x normalized by V_{max}. $Re = 5$ and $H_t = 0.026$.

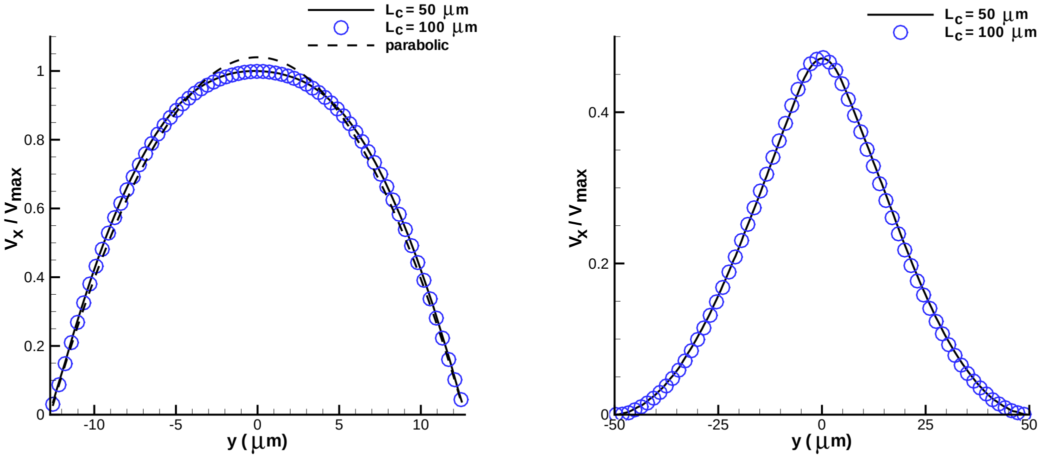

Figure 4.19: Normalized velocity profiles extracted across the channel at $x = 140\ \mu m$ (left) and 50 μm after the constriction (right) for different constriction lengths L_c. The dashed line in the left figure represents a parabolic Newtonian profile.

4.3.3 CFL measurements up- and downstream of the constriction

To measure CFLs upstream and downstream of the constriction, individual cells are tracked in simulations. Figure 4.20 shows a sample snapshot of RBCs in microchannel flow at $H_t = 0.026$. This plot illustrates that RBCs appear to be more confined around the flow centerline down the constriction resulting in an enhanced CFL downstream in comparison with that in upstream. To quantitatively estimate CFL thickness upstream (δ_u) and downstream (δ_d) trajectories of individual RBCs are recorded as shown in figure 4.21. These trajectories represent the center-of-mass motion of cells. The RBC core widths upstream

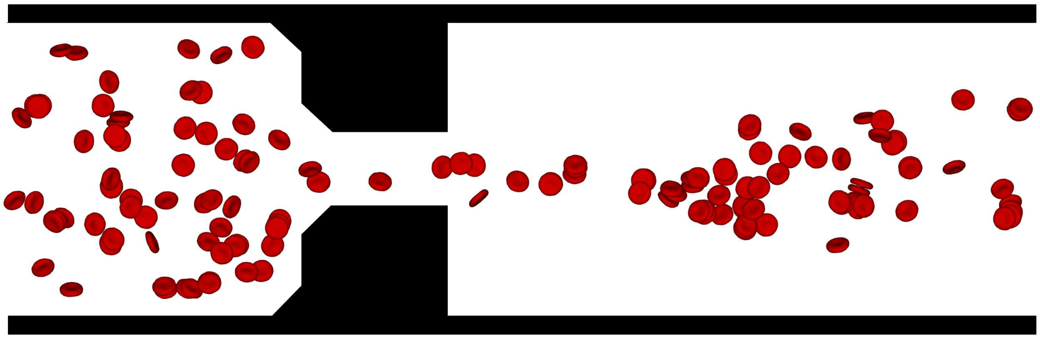

Figure 4.20: Snapshot of RBCs flowing through a constriction in a microchannel. $H_t = 0.026$.

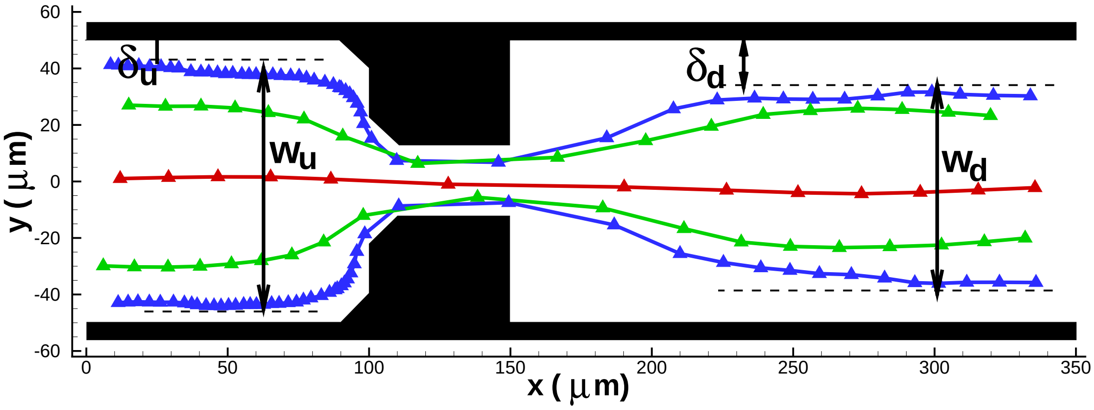

Figure 4.21: Trajectories of individual RBCs in microchannel flow to estimate CFL thicknesses and cell core widths upstream and downstream of the constriction.

and downstream are defined as

$$\begin{aligned} w_u &= \max_{x_i^u, j}\{y_c^j(x_i^u)\} - \min_{x_i^u, j}\{y_c^j(x_i^u)\} + 2R_0, \\ w_d &= \max_{x_i^d, j}\{y_c^j(x_i^d)\} - \min_{x_i^d, j}\{y_c^j(x_i^d)\} + 2R_0, \end{aligned} \tag{4.11}$$

where $y_c^j(x_i)$ is the y component of the RBC center-of-mass at the position x_i of a flowing cell, while index j runs over all cells in a simulation. The superscripts u and d denote upstream and downstream RBC positions, respectively. Consequently, the CFL thicknesses are found as $\delta_u = (W - w_u)/2$ and $\delta_d = (W - w_d)/2$. Note that the w_u and δ_u values in simulations may potentially depend on the initial conditions created by placing RBCs randomly in the flow domain since the upstream length of the microchannel is relatively short and CFL measurements are taken right after the flow startup. In order to eliminate dependence of the CFLs on inflow RBC distribution, L_u has to be long enough to provide ample time for RBC cross-stream migration and to achieve a steady-state cell distribution before the constriction. The length L_u is not specified in experiments [70] nor is the sensitivity of the CFL measurements on L_u tested. Our simulations are performed with $L_u = 100\ \mu m$ resulting in $\delta_u = 5.6\ \mu m$ and $w_u = 88.8\ \mu m$, while in experiments δ_u is found to be 4 μm. In addition, the use of periodic boundary conditions in simulations yields a persistent focusing of RBCs around the channel centerline since an increased CFL thickness downstream of the constriction is transfered further upstream due to periodicity. Therefore, simulations are advanced only for the time long enough to allow a single RBC to move two full channel lengths. Moreover, trajectories of RBCs showing their second passage through the constriction are discarded since they reflect a "double" focusing effect.

4.3.4 Enhancement of the downstream CFL for different conditions

CFLs downstream are affected by the cell distribution across the flow in front of the constriction. In light of the uncertainties in cell distribution upstream described in the previous section, comparisons of downstream CFLs obtained in simulations and experiments are expected to show a rather qualitative than quantitative agreement.

Figure 4.22 shows ratios w_d/w_u for different constriction widths w_c and lengths L_c in comparison with experiments [70]. It is clear that the constriction provides a mechanism for focusing RBCs around the centerline of the channel characterized by an enhanced CFL downstream compared with that upstream. The focusing effect can be explained by cross-stream migration of RBCs in microchannel flow due to cell-wall and cell-cell hydrodynamic interactions. In general, RBCs tend to migrate away from the walls due to a hydrodynamic

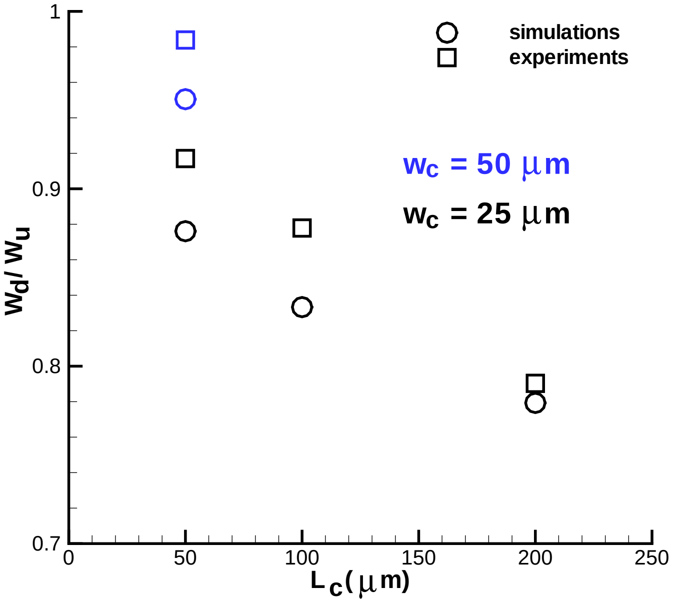

Figure 4.22: Ratio of the downstream and upstream widths of a RBC distribution w_d/w_u depending on the constriction width w_c and length L_c compared with experiments [70]. $H_t = 0.026$.

lift [26, 5]; however, under certain conditions (e.g., flow strength, cell concentration) RBCs are able to migrate away from the channel centerline attributed to hydrodynamic interactions among cells and their deformability. Similar migration effects are found for dilute and semi-dilute polymer solutions in Poiseuille flow, which are discussed in detail in chapter 5. RBC migration in the constriction appears to be the main reason for an enhanced CFL downstream. The cell distribution upstream may also contribute to the focusing effect as discussed in the previous section; nonetheless the cell distribution upstream is the same in all simulations due to an identical setup for the initial conditions.

The ratios w_d/w_u in figure 4.22 for different constriction widths and fixed $L_c = 50\ \mu m$ indicate a substantial increase in the downstream CFL for $w_c = 25\ \mu m$ in comparison with that of $w_c = 50\ \mu m$. In the case of $w_c = 50\ \mu m$ the cell drift to the channel centerline is weaker due to the smaller local shear rates than those in the case of $w_c = 25\ \mu m$ for the same flow rate Q. Thus, the local Ca number in the constriction is twice smaller for $w_c = 50\ \mu m$ than for $w_c = 25\ \mu m$. In addition, in case of $w_c = 50\ \mu m$ RBCs need to migrate a longer distance away from the walls in order to achieve a similar focusing effect as that found for the case of $w_c = 25\ \mu m$. Moreover, the drift velocity of solid particles in a rectangular channel flow [116] was found to be inversely-proportional to the square of their distance from the wall. Hence, the RBC drift is strongly attenuated when a cell is far enough from the walls, which may strongly affect the focusing effect in microchannels with larger w_c.

To identify an effect of the constriction length on the CFL downstream we performed several simulations for various L_c in the range of $50-200\ \mu m$ and fixed $w_c = 25\ \mu m$. Results are plotted in figure 4.22 showing a stronger cell focusing effect with increasing L_c. The CFL downstream is significantly enhanced in the case of a larger L_c due to longer times spent by flowing RBCs within the constriction resulting in their larger migration to the channel centerline. Thus, microfluidic channels with a narrow and long constriction yield the largest CFL thickness downstream. Finally, the comparison of simulation results with experiments in figure 4.22 shows a qualitative agreement of the CFL trends with respect to the constriction width and length.

Figure 4.23 presents the dependence of w_d/w_u on the viscosity of a suspending fluid for various L_c in comparison with experiments [70]. Increase in the solvent viscosity results in a larger Ca number of the flow, which enhances RBC migration towards the channel

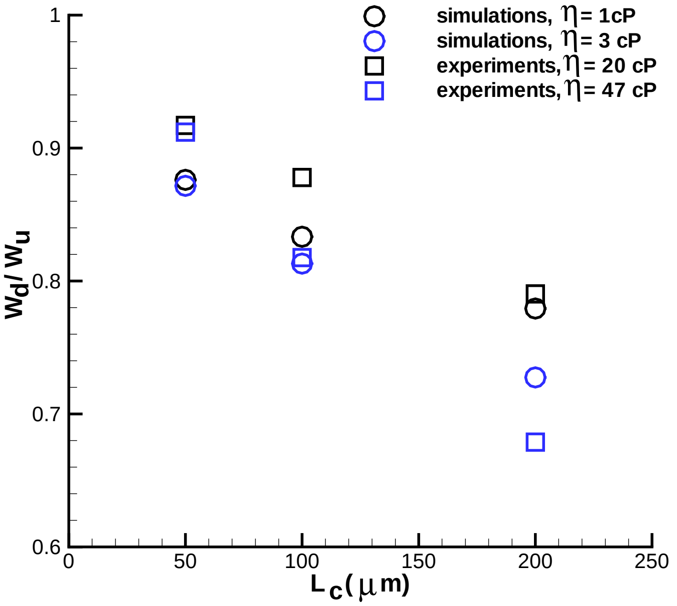

Figure 4.23: Ratio w_d/w_u with respect to the viscosity of a suspending fluid for different L_c compared with experiments [70]. $H_t = 0.026$.

centerline within the constriction and consequently, provides a more confined RBC distribution downstream. The simulation results for $\eta_o = 3\ cP$ show a gradual decrease in the w_d/w_u ratio with increasing L_c, which is consistent with the results for $\eta_o = 1\ cP$ discussed above. In experiments, higher viscosities of a suspending medium are employed showing a qualitatively similar dependence of the enhanced CFLs downstream on solvent viscosity.

The effect of RBC stiffness on the CFL thickness downstream of the constriction is shown in figure 4.24. Hardened RBCs assume a Young's modulus five times larger than $Y = 18.9\ \mu N/m$ of healthy RBCs. Hardened cells are subject to a weaker focusing effect in comparison with soft RBCs since their migration within the constriction is attenuated. In accordance, the Ca number for a suspension with hardened cells is smaller than that for healthy RBCs indicating the same conclusion. Experimental data in figure 4.24 are in qualitative agreement with simulation results.

4.3.5 Focusing effect for higher hematocrit values

Further, we examine the focusing effect for $H_t = 0.16$. Two microchannels with fixed $w_c = 25\ \mu m$ but different constriction lengths $L_c = 50\ \mu m$ and $L_c = 100\ \mu m$ are considered.

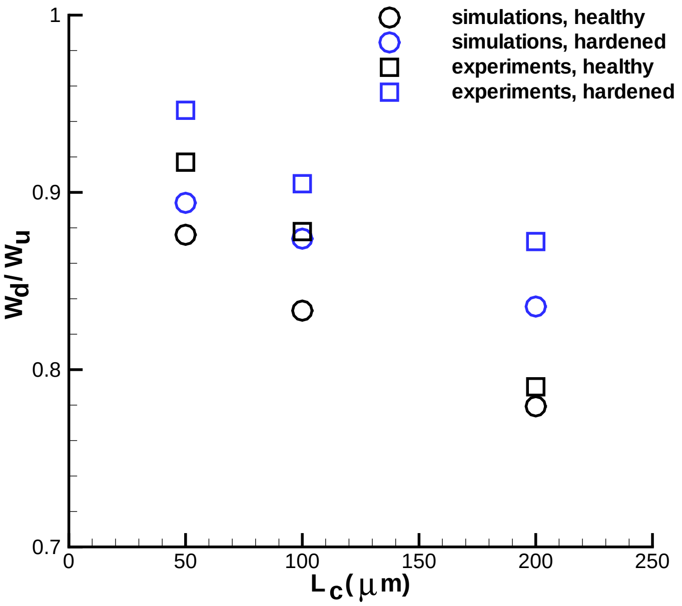

Figure 4.24: Ratio w_d/w_u with respect to cell stiffness for various L_c in comparison with experiments [70]. $H_t = 0.026$.

Figure 4.20 shows a snapshot of RBCs in a microchannel flow at $H_t = 0.16$. The plot visually shows an increase of the CFL thickness downstream in comparison with that upstream. To quantitatively characterize this CFL enhancement RBC trajectories are traced analogously to the aforementioned method used in simulations of suspensions with $H_t = 0.026$. Figure 4.26 compares ratios w_d/w_u for the two cases of $H_t = 0.16$ and $H_t = 0.026$ and different constriction lengths. In the case of $H_t = 0.16$ the focusing effect is substantially attenuated

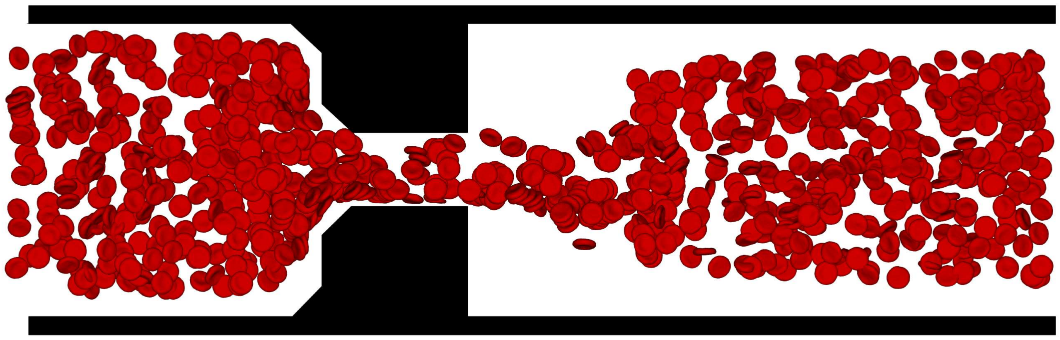

Figure 4.25: RBCs at $H_t = 0.16$ flowing through the constriction in a microchannel.

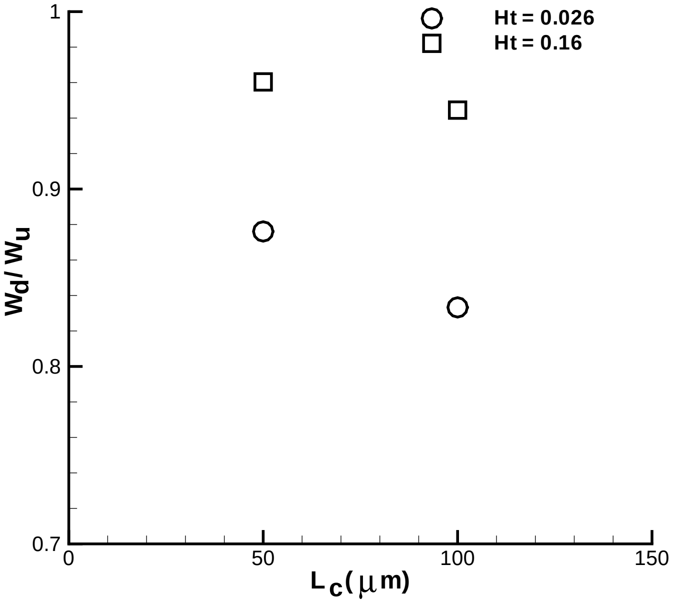

Figure 4.26: Ratios w_d/w_u for various L_c and H_t values 0.026 and 0.16.

in comparison with that of $H_t = 0.026$. In addition, an increase of the constriction length results in a weaker CFL enhancement downstream for larger H_t values. The microfluidic devices simulated here are proposed to be used to effectively separate RBCs and blood plasma in [70] presented for $H_t = 0.16$. Our simulation results suggest that the focusing effect in such microchannels can be successfully used for segregation of RBCs and blood plasma only in cases of relatively low cell volume fractions ($H_t \leq 0.15 - 0.2$). At the physiological H_t level of 0.45 the focusing effect will be insignificant voiding the efficiency of the use of such microchannels.

4.3.6 Computational work

Finally, we comment on the computational efficiency of the implemented parallel code for the blood flow model since these microchannel simulations correspond to relatively large simulation systems. As an example, the simulation system for the case of $H_t = 0.16$ and $L_c = 100\ \mu m$ contained 990 RBCs and 2.8×10^6 DPD particles and was run on 924 processors showing a parallel efficiency approximately equal to 90%. To further verify the scalability of the developed code we set up a simulation of the microchannel with the following dimensions: $L_u = 200\ \mu m$, $W = 100\ \mu m$, $w_c = 25\ \mu m$, $L_c = 100\ \mu m$, $L_d = 830\ \mu m$, and $H = 30\ \mu m$.

This simulation system contained 5000 RBCs and 1.14×10^7 DPD particles and was run on 3864 processors. The obtained parallel efficiency was approximately 85%. Note that these simulations test the weak scaling of parallel efficiency with the number of processors since the number of cores is increased proportionally to the size of the simulated system. Nevertheless, it proves scalability of the developed code up to at least 5000 CPUs with the number of simulated RBCs on the order of $O(10^4)$.

4.4 Adhesive dynamics of leukocytes and Pf-parasitized RBCs

In this section we describe the simulations of adhesive dynamics of leukocytes and Pf-parasitized RBCs with the endothelium lining blood vessel walls. The adhesive dynamics model is based on a stochastic formation/dissociation of bonds which correspond to receptor/ligand interactions. The model is able to successfully reproduce different types of the adhesive dynamics of cells such as firm adhesion, continuous rolling over a surface, and rolling in a "stop-and-go" manner. Cytoadhesive dynamics depends on a number of factors such as density of the available receptors and ligands, their interactions (e.g., bond formation/dissociation rates, bond strength), cell properties (e.g., cell shape, elasticity, bending rigidity), and flow conditions (e.g., shear rate, shear stress). The effect of some of those conditions will be examined for leukocytes and infected RBCs in malaria. In particular, Pf-parasitized RBCs show a "flipping" rather than "rolling" behavior attributed to an increased cell stiffness in comparison with that of healthy RBCs. A comparison with experiments will be provided where it is possible.

4.4.1 Adhesion model

Adhesion of cells to surfaces is mediated by the interactions between receptors and ligands which are the adhesion sites distributed on a cell and a surface, respectively. The adhesion model provides rules of formation and dissociation of bonds between receptors and ligands. The kinetics model of single bond dissociation was first offered by Bell [17], where the rate of bond dissociation was varying exponentially with the bond force. Dembo et al. [46] derived self-consistent expressions for the bond formation/dissociation rates following the Boltzmann distribution for the binding affinity. Based on these kinetics rates the first attempts to model cell adhesion used deterministic [97] and probabilistic [37, 96] approaches. The probabilistic model developed by Hammer and Apte [96] is commonly used in simulations and is known as *adhesive dynamics*.

Figure 4.27 shows a sketch of RBC adhesion. A potential bond (black lines in figure 4.27) may be formed only if it is close enough to a free ligand, which is characterized by the reactive distance d_{on}. A ligand is called free if it is not bound to any receptors. During the time a receptor is within the distance d_{on} to a free ligand, a bond can be formed with on-rate k_{on}. Reversely, existing bonds are ruptured with off-rate k_{off} or if their length exceeds the rupture distance d_{off}. The rates k_{on} and k_{off} are defined as follows

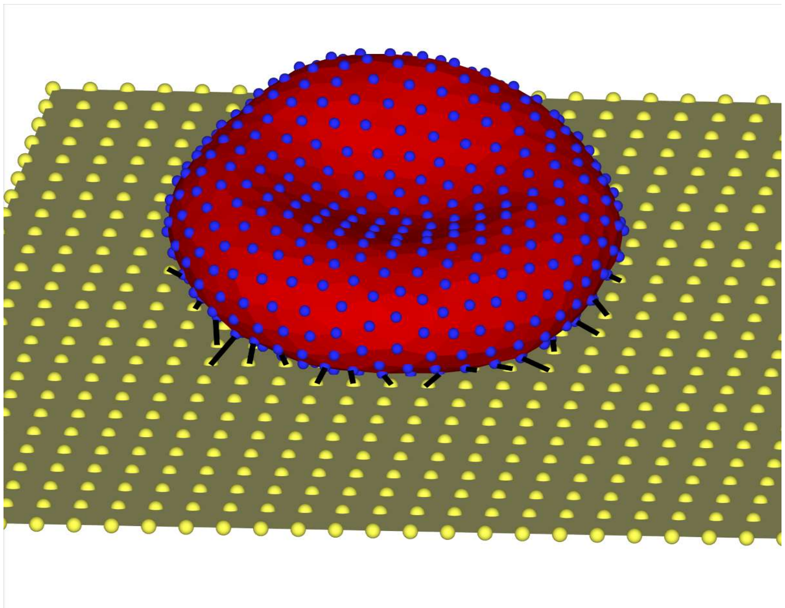

Figure 4.27: Sketch of RBC adhesion. Receptors are in blue, ligands in yellow, and black lines denote bonds.

$$\begin{aligned} k_{on} &= k_{on}^0 \exp\left(-\frac{\sigma_{on}(l-l_0)^2}{2k_BT}\right), \\ k_{off} &= k_{off}^0 \exp\left(\frac{\sigma_{off}(l-l_0)^2}{2k_BT}\right), \end{aligned} \tag{4.12}$$

where k_{on}^0 and k_{off}^0 are the reaction rates at the distance $l = l_0$ between a receptor and a ligand with the equilibrium spring length l_0 defined below. The effective on and off strengths σ_{on} and σ_{off} define a decrease or an increase of the corresponding rates within the interaction lengths d_{on} and d_{off}, and k_BT is the unit of energy. The force exerted on the receptors and ligands by an existing bond is given by

$$F(l) = k_s(l - l_0), \tag{4.13}$$

where k_s is the spring constant. The probabilities of bond formation and dissociation are defined as follows

$$P_{on} = \begin{cases} 1 - e^{-k_{on}\Delta t} & for \quad l < d_{on} \\ 0 & for \quad l \geq d_{on} \end{cases}, \quad P_{off} = \begin{cases} 1 - e^{-k_{off}\Delta t} & for \quad l < d_{off} \\ 0 & for \quad l \geq d_{off} \end{cases}, \tag{4.14}$$

where Δt is the time step in simulations. The described model is similar to the adhesive dynamics model developed by Hammer and Apte [96]. In their model $\sigma_{on} = \sigma_{ts}$ and $\sigma_{off} = k_s - \sigma_{ts}$, where σ_{ts} is the transition state spring constant.

During the course of a simulation the receptor/ligand interactions are considered every time step. First, all existing bonds between receptors and ligands are checked for a potential dissociation according to the probability P_{off}. A bond is ruptured if $\xi < P_{off}$ and left unchanged otherwise, where ξ is a random variable uniformly distributed on $[0, 1]$. If a bond is ruptured the corresponding ligand is available for new binding. Second, all free ligands are examined for possible bond formations. For each free ligand we loop over the receptors within the distance d_{on}, and bond formation is attempted for each found receptor according to the probability P_{on}. This loop is terminated when a bond is formed. Finally, the forces of all remaining bonds are calculated and applied.

Note that this algorithm permits only a single bond per ligand, while receptors may establish several bonds if several ligands are free within their reaction radius. This provides an additional capability for the adhesive dynamics model compared with that employing one-to-one interactions between receptors and ligands. Also, this assumption appears to furnish a more realistic representation of adhesive interactions of leukocytes and Pf-parasitized RBCs with a surface. The leukocyte membrane displays a large number of ruffles on its surface called microvilli [61, 143], and the cell adhesion is mediated by receptors concentrated on a small area of microvilli tips as shown in experiments [203]. Similarly, Pf-parasitized RBCs display a number of parasitic nanometer-size protrusions or knobs on the membrane surface [106, 103, 145], where receptors that mediate RBC adherence are clustered.

4.4.2 Scaling of model and physical units

To relate DPD non-dimensional parameters of the adhesive model to those in physical units we have to define length and time scales. The length scaling is based on the cell diameter and is defined as in equation (3.33). The time scale is given as follows

$$\tau = \frac{\dot{\gamma}^M}{\dot{\gamma}^P}\, s, \tag{4.15}$$

where $\dot{\gamma}$ is the characteristic shear rate of a flow, the superscripts "P" and "M" correspond to physical and model units, respectively, and "s" denotes seconds. Simulation parameters are chosen in such a way that this time scale is equivalent to that defined in equation (3.36) with $\alpha = 1$ and therefore, the following equality is satisfied

$$\frac{\dot{\gamma}^M}{\dot{\gamma}^P} = \frac{D_0^P}{D_0^M}\frac{\eta_o^P}{\eta_o^M}\frac{Y_0^M}{Y_0^P}, \tag{4.16}$$

where D_0 is the cell diameter, η_o is the external fluid viscosity, and Y is the cell Young's modulus. The scales of force and energy are then defined as follows

$$N^M = \frac{\eta_o^P}{\eta_o^M}\left(\frac{D_0^P}{D_0^M}\right)^2 \frac{\dot{\gamma}^P}{\dot{\gamma}^M} N^P, \qquad (k_BT)^M = \frac{\eta_o^P}{\eta_o^M}\left(\frac{D_0^P}{D_0^M}\right)^3 \frac{\dot{\gamma}^P}{\dot{\gamma}^M}(k_BT)^P, \tag{4.17}$$

where "N" denotes the Newton force unit. Note that the definitions above yield the same scales as in equations (3.35 and 3.34) if the equality in equation (4.16) is satisfied.

4.4.3 Adhesive dynamics of leukocytes in shear flow

Leukocyte or white blood cell (WBC) adhesion to the vascular endothelium is a crucial step in the immune response [185]. Rolling along the vessel wall allows WBCs to efficiently monitor for potential molecular signals, since the rolling velocity at the vessel wall is much smaller than that of the blood flow. In fact, microfluidic experiments [77] showed that WBCs adhere only above a critical threshold of shear. Firm adhesion of leukocytes is generally recognized as the final step of the WBC adhesive dynamics within a vessel with further cross-endothelium migration into the surrounding tissue.

Adhesion of WBCs to the endothelium is mediated by receptors from the selectin family which are known to have fast association and dissociation kinetics [121]. Trajectories of a rolling WBC are often characterized by a "stop-and-go" WBC motion rather than rolling with a constant velocity along the vessel wall [9, 27]. The sporadic rolling behavior is due to a stochastic nature of formation and dissociation of receptor-ligand bonds. However, at high shear rates WBC rolling was observed to be less erratic and showing smaller variations in rolling velocity than at low shear rates [27]. In addition, rolling at high shear rates is further stabilized by an increase in the number of receptor-ligand bonds [27].

Freely circulating WBCs are spherical in shape, while the attached or rolling leukocytes resemble a "tear-drop" shape. WBC deformations for the wall shear rates in the range $50 - 800\ s^{-1}$ were found to be up to 140% in *in vivo* experiments [78]. WBC deformability plays a significant role in the stability of rolling at high shear rates. The area of binding may increase three times at high wall shear rates [78]. In addition, a deformed WBC is subject to a smaller hydrodynamic drag than that of a solid sphere of similar size. Experiments with receptor-coated spheres [157] showed more erratic rolling in comparison with normal WBCs.

4.4.3.1 Simulation setup and physical parameters

A sketch of the simulation setup is shown in figure 4.28. A WBC membrane is represented by a network on a sphere with the radius $R = 5\ \mu m$ similar to the RBC membrane model described in chapter 3. The total number of receptors is $N_r = 1000$. Ligands are placed on the lower wall on a square lattice with the lattice constant $d = 0.25\ \mu m$. Linear shear flow is generated by the upper wall moving with velocity V, while the lower wall is kept

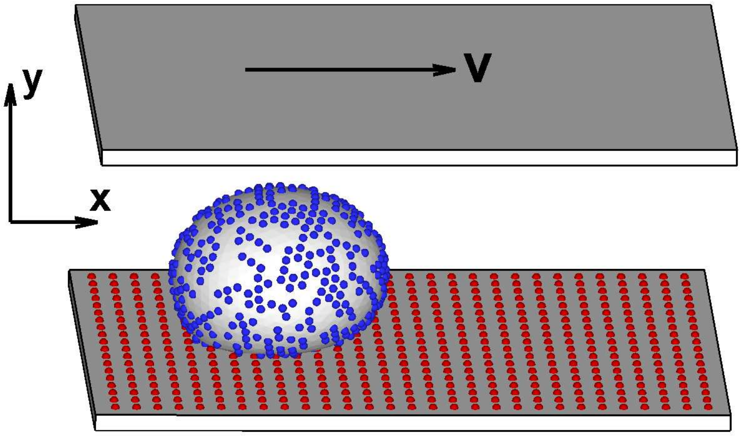

Figure 4.28: Sketch of a modeled WBC above the lower wall. Receptors are drawn in blue and ligands in red.

stationary. The domain dimensions are set to $40 \times 30 \times 20\ \mu m$ with periodicity in x (flow) and z directions. Simulation (in DPD units) and physical (in SI units) parameters are shown in table 4.5. Note that the receptor and ligand densities in simulations are smaller than those found in experiments [121], since we employ a coarse-grained model of a WBC (see section 3.2.7 for details). Thus, the receptor/ligand interactions in simulations correspond to *effective* bonds that may represent several physical bonds.

Parameters	Simulations	Physical	Typical values	Ref.
WBC radius (R)	5	$5 \times 10^{-6}\ m$	$4.5 - 5 \times 10^{-6}\ m$	[8]
Young's modulus (Y)	7720	$0.4 \times 10^{-3}\ N/m$	$0.3 - 1.2 \times 10^{-3}\ N/m$	[41, 108]
bending rigidity (k_c)	60	$3 \times 10^{-18}\ J$	$1 - 3 \times 10^{-18}\ J$	[214]
shear rate ($\dot{\gamma}$)	0.1	$100\ s^{-1}$	$50 - 300\ s^{-1}$	[28]
temperature (T)	0.0828	$310\ K$	$293 - 310\ K$	
external fluid viscosity (η_o)	20	$10^{-3}\ Pa \cdot s$	$1 - 3 \times 10^{-3}\ Pa \cdot s$	[28]
internal fluid viscosity (η_i)	54	$2.7 \times 10^{-3}\ Pa \cdot s$		
spring constant (k_s)	20000	$10^{-3}\ N/m$	$10^{-5} - 10^{-2}\ N/m$	[96, 82]
equilibrium spring length (l_0)	0.025	$25 \times 10^{-9}\ m$	$10 - 40 \times 10^{-9}\ m$	[46]
reactive distance (d_{on})	0.1	$10^{-7}\ m$		
rupture distance (d_{off})	0.1	$10^{-7}\ m$	$< 1.5 \times 10^{-7}\ m$	[135]
on strength (σ_{on})	10.0	$5 \times 10^{-7}\ N/m$	$-5 - 5 \times 10^{-3}\ N/m$	[46]
off strength (σ_{off})	1.0	$5 \times 10^{-8}\ N/m$	$-5 - 5 \times 10^{-3}\ N/m$	[46]
unstressed on rate (k_{on}^0)	$10^{-3} - 10$	$1 - 10^4\ s^{-1}$	$10^3 - 10^4\ s^{-1}$	[173]
unstressed off rate (k_{off}^0)	$10^{-5} - 10$	$10^{-2} - 10^4\ s^{-1}$	$0.5 - 300\ s^{-1}$	[8]
receptor density (n_r)	3.18	$3.18\ mol/\mu m^2$	$200 - 500\ mol/\mu m^2$	[121]
ligand density (n_l)	16	$16\ mol/\mu m^2$	$200 - 500\ mol/\mu m^2$	[121]

Table 4.5: Simulation (in DPD units) and physical (in SI units) parameters for leukocyte adhesive dynamics.

A WBC is placed at a distance of 50 nm from the lower wall. Before the flow startup, each simulation is run for 0.5 s in equilibrium ($V = 0$) to allow for initial binding of the WBC. After that the shear flow is started and WBC dynamics is monitored for 10 s. Besides receptor/ligand interactions a WBC is subject to the buoyant force $\Delta\rho V_{WBC} g$, where V_{WBC} is the WBC volume, g is the gravitational acceleration, and $\Delta\rho$ is the density difference between the internal and external fluids which is equal to 50 kg/m^3 [144]. Table 4.6 presents additional DPD parameters for interactions among particles representing external solvent (S_o), internal fluid (S_i), WBC vertices (V), and walls (W). Note that DPD interactions not included in table 4.6 are turned off. The WLC-POW model is employed for WBCs with the parameters: $\mu_0^M = 2000$, $x_0 = 2.2$, $k_a = 50000$, $k_d = 1000$, $k_v = 50000$, and $m = 2$ (see section 3.2 for details).

Interaction	a	γ	r_c	$k(eq.(2.11))$
$S_o - S_o$, $S_o - W$	4.0	9.15	1.5	0.25
$S_i - S_i$	4.0	20.0	1.5	0.25
$S_o - V$, $S_i - V$, $W - V$	2.0	20.0	1.5	0.25
$V - V$	0.0	9.15	1.0	0.25

Table 4.6: DPD parameters used in simulations of WBC dynamics. S_o and S_i denote external and internal solvent particles, V corresponds to WBC vertices, and W represents wall particles.

4.4.3.2 Simulation results of leukocyte dynamics

The simulations of WBC adhesive dynamics are performed for ranges of unstressed on and off rates shown in table 4.5. Similar ranges were considered in [119] for the adhesive dynamics of a solid spherical particle. Several states of WBC adhesive dynamics can be defined based on the average cell velocity $\bar{v}_c$ and pause time $\bar{\tau}_p$. The average pause time is calculated from the time sequence $\{\Lambda_i\}_{i=1...T}$ of WBC motion defined as

$$\Lambda_i = \begin{cases} 1 & \text{if} \quad v_c^i > 0.01V_m, \quad \text{in motion} \\ 0 & \text{if} \quad v_c^i \leq 0.01V_m, \quad \text{arrest} \end{cases}, \tag{4.18}$$

where i denotes a step in time, T is the total number of steps, $V_m = V/2$ is the flow velocity at the channel center, and $v_c^i = (x_c^i - x_c^{i-1})/\Delta t$ is the WBC center-of-mass velocity while x_c^i is the cell center-of-mass and Δt is the time interval. This sequence is then analyzed to calculate the average length of an arrest (average pause time) which is equivalent to the average length of continuous subsequences of zeros multiplied by Δt. The average cell velocity is defined as follows

$$\bar{v}_c = \frac{1}{T-1} \sum_{i=2}^{T} v_c^i. \tag{4.19}$$

The WBC dynamics is divided into four states according to the average pause time $\bar{\tau}_p$ and cell velocity $\bar{v}_c$:

1) *Firm adhesion:* the state of the WBC arrest which is characterized by $\bar{\tau}_p > 0.5$ s. Infrequent small jumps in the cell velocity are possible due to rare bond dissociation.

2) *Stop-and-go rolling:* the cell motion is described by frequent interchanges between WBC arrest and mobility. This state is defined by $0.1\ s < \bar{\tau}_p \leq 0.5\ s$.

3) *Stable rolling:* the state corresponds to WBC motion with a relatively stable rolling velocity. It is established if $\bar{\tau}_p \leq 0.1\ s$ and $\bar{v}_c < 0.8V_m$.

3) *Free motion:* the WBC is moving freely with the channel flow, when adhesion interactions are not able to resist a lift on the cell due to hydrodynamic flow. This state is characterized by $\bar{\tau}_p \leq 0.1\ s$ and $\bar{v}_c \geq 0.8V_m$.

The time interval is chosen to be $\Delta t = 0.01$ s. The simulations are run for 10 s, while data analysis is performed for times after 1 s to exclude flow startup effects.

Figure 4.29 presents the center-of-mass displacements (x_c) and velocities (v_c) for different WBC adhesion states. The “A” plots show that firm adhesion is characterized by relatively long times of cell arrests. However, rare events of sudden motion may be present due to erratic bond dissociation. They are represented by several submicron steps in the WBC displacement and the corresponding peaks in the cell velocity shown in figure 4.29 “A”. Note that WBC velocity fluctuates around the zero value and frequently displays small negative values; however, no net motion in the negative x direction is observed. This may be due to the presence of thermal fluctuations or a retraction of a WBC and its bonds to the surface after deformation by hydrodynamic flow, since the center-of-mass velocity

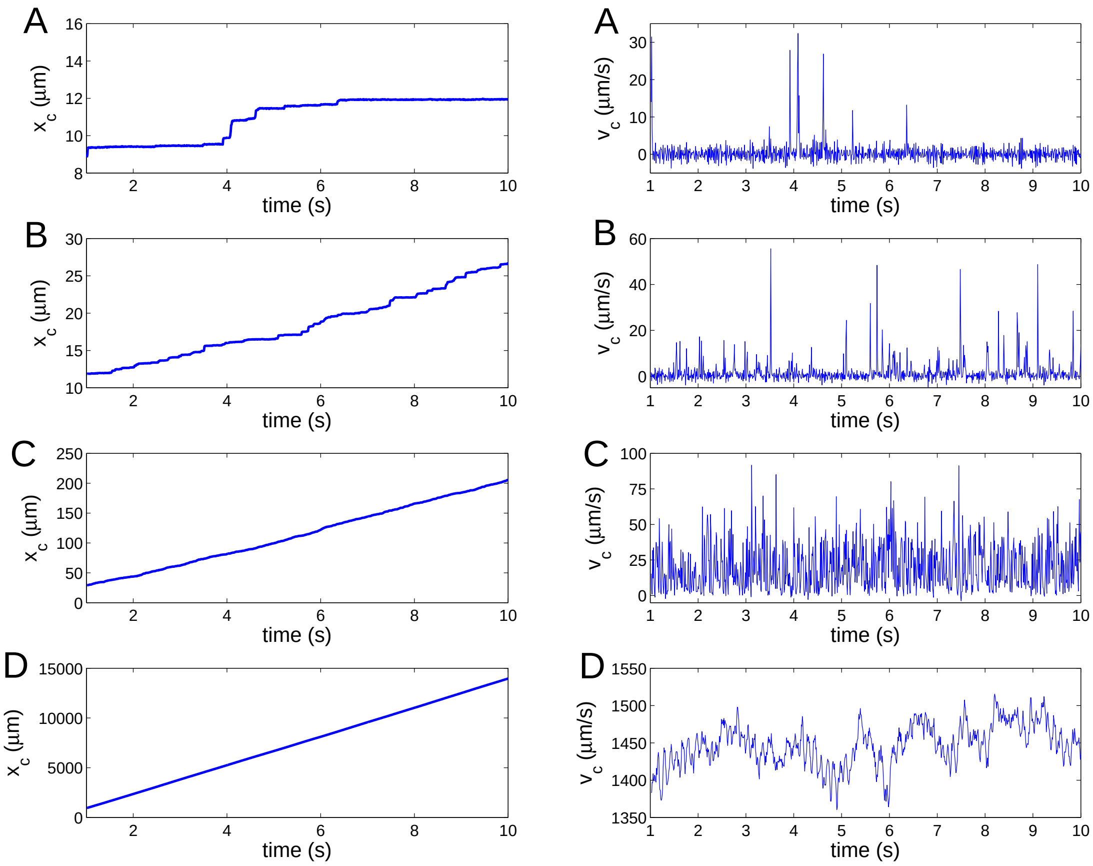

Figure 4.29: Center-of-mass displacements (x_c) and velocities (v_c) for various adhesion states of a WBC. A - firm adhesion, B - stop-and-go rolling, C - stable rolling, and D - free motion.

is measured based on current and previous positions with the time interval $\Delta t = 0.01$ s. The stop-and-go rolling shown in figure 4.29 "B" is well described by a staircase-like displacement directly related to frequent peaks in the cell velocity and intermittent WBC stops. In contrast, stable rolling is characterized by a near linear WBC displacement shown in figure 4.29 "C". Finally, under free motion (4.29 "D") WBCs move in shear flow near the channel center with the average velocity slightly lower than $V_m = 1500$ $\mu m/s$. The adhesive interactions are not strong enough to counterbalance cell-wall hydrodynamic interactions, which force WBCs to migrate to the channel center. After WBC detachment from the wall, no further adhesive interactions are encountered.

Figure 4.30 shows the WBC adhesion dynamics states for wide ranges of unstressed on

(k^0_{on}) and off (k^0_{off}) rates from table 4.5 normalized by the shear rate. This plot is called

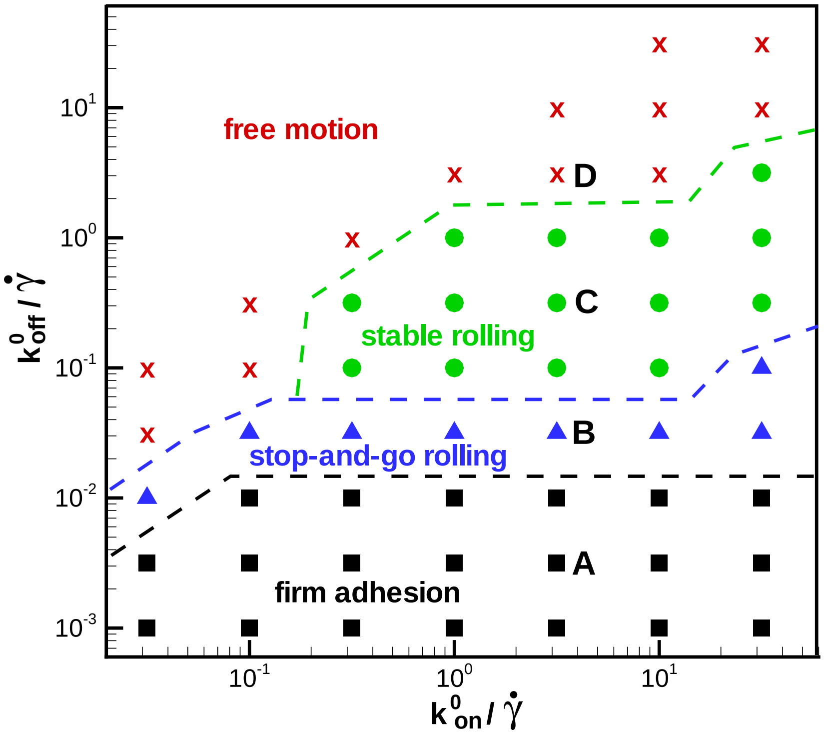

Figure 4.30: On-off state diagram of WBC adhesion dynamics states: firm adhesion (squares), stop-and-go rolling (triangles), stable rolling (circles), and free motion (crosses). The letters “A-D” mark simulations shown in figure 4.29. Dashed lines are drawn for the eye to identify regions corresponding to different states.

on-off state diagram similar to that by Korn and Schwarz [119]. Firm adhesion occurs if the bond dissociation rate is small. Under this condition bond rupture is a rare event, while bonds are formed with a faster rate to keep a WBC in arrest. At low values of k^0_{on} the border between firm adhesion and stop-and-go rolling motion (black dashed line in figure 4.30) is achieved by a proper balance between the association and dissociation rates. However, this border shows no dependence on the rate k^0_{on} at its high values. This behavior is due to a limited number of available receptors and ligands for binding. Thus, if there are no free receptors or analogously no free ligands left for binding, a further increase of k^0_{on} will have no effect on the firm adhesion of a WBC.

As we increase the bond dissociation rate k^0_{off} for a fixed k^0_{on}, WBC firm adhesion transits into the stop-and-go rolling state. Note that this behavior is observed in a thin stripe region of the on-off state diagram in figure 4.30 right above the "firm adhesion" region. In light of this, the stop-and-go rolling can also be thought of as an unstable firm adhesion. Hence, if the rate k^0_{off} becomes significant enough in comparison with k^0_{on} to allow relatively frequent random ruptures of bonds, a WBC is subject to a stop-and-go motion characterized by step-like displacements and velocity jumps shown in figure 4.29 "B".

Upon a further increase in k^0_{off} with respect to k^0_{on} a WBC shows stable rolling or detaches from the wall and undergoes a free motion in hydrodynamic flow. Note that stable rolling is only possible if the association rate is large enough to facilitate fast bond formation. Thus, stable WBC rolling on the wall can be described by a dynamic rupture of bonds at the back of the cell contact area and their quick formation at the front of a WBC. Figure 4.30 shows that for small k^0_{on} values, a WBC transits into a free motion above the border of the stop-and-go rolling region (blue dashed line). In addition, a WBC detaches from the wall if the bond dissociation rate becomes comparable with the rate of bond formation.

Figure 4.31 presents the corresponding on-off diagrams of the average WBC velocity (left) and the average pause time (right) for various states of leukocyte adhesive dynamics. The average cell velocity in the free motion region is above 1000 $\mu m/s$ confirming that

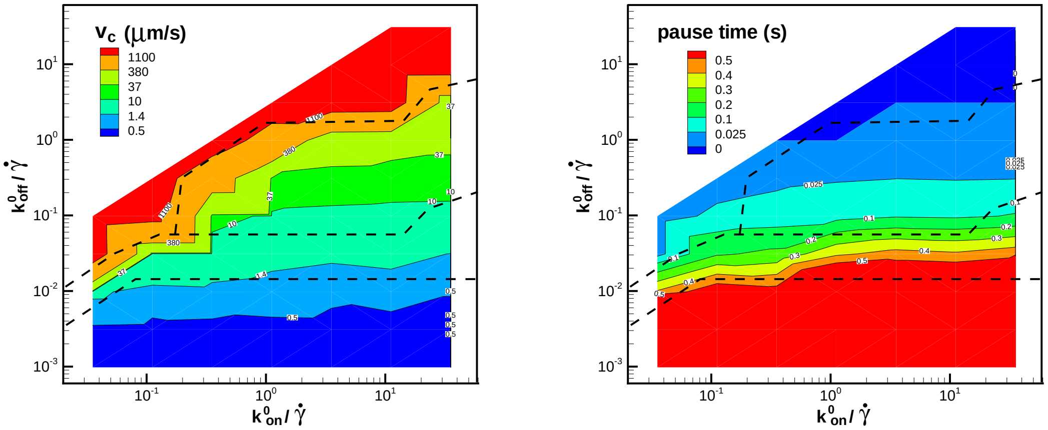

Figure 4.31: Contour plot of the on-off diagram of the average WBC velocity (left) and the average pause time (right). Dashed lines indicate regions of different states of leukocyte adhesive dynamics shown in figure 4.30.

no adhesive interactions between the WBC and the wall exist. In accordance, the average WBC pause time is zero in this region. In the region of stable rolling the average velocity is in the range of $10 - 400\ \mu m/s$ depending on the relative interplay between k^0_{on} and k^0_{off}, while the pause time is below 0.1 s. The stop-and-go motion yields the rolling velocity in the range of $1 - 70\ \mu m/s$ and the pause time between 0.1 s and 0.5 s. Finally, in the firm adhesion state the average velocity of WBCs is below 1.5 $\mu m/s$ with the pause times larger than 0.5 s. Kim and Sarelius [114] performed *in vivo* experiments of P-selectin-mediated leukocyte rolling in postcapillary venules and found the average WBC rolling velocity to be in the range of $20 - 30\ \mu m/s$ at the shear rate $\dot{\gamma} = 100\ s^{-1}$. This range of the rolling velocity fits well into the stable rolling region in figure 4.31 (left) with k^0_{off} in the range of $10 - 20\ s^{-1}$ and k^0_{on} in the range of $100 - 1000\ s^{-1}$. Firrell and Lipowsky [78] studied WBC rolling in mesenteric venules of rats and reported the average cell velocity in the range of $30 - 50\ \mu m/s$, which also falls into the stable rolling region in figure 4.31 (left). Smith et al. [183] found the characteristic pause time of selectin-mediated leukocyte rolling in a flow chamber to be approximately $0.1 - 0.2\ s$. This value corresponds to the stop-and-go WBC region in figure 4.31 (right). Despite some differences in the aforementioned experiments, the adhesive dynamics model is able to reproduce the WBC behavior found experimentally.

Figure 4.32 shows the on-off diagrams of the WBC contact area (left) and the deformation index (right). The contact area A_c and deformation index δ are defined as follows

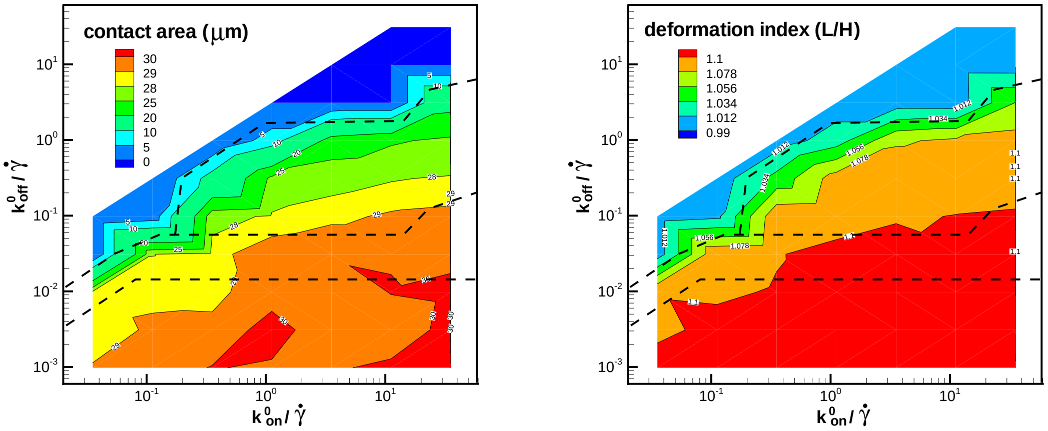

Figure 4.32: Contour plot of the on-off diagram of the WBC contact area (left) and the deformation index (right). Dashed lines indicate states of leukocyte adhesive dynamics shown in figure 4.30.

$$A_c = N_c \frac{4\pi R^2}{N_r}, \qquad \delta = \frac{L}{H}, \tag{4.20}$$

where N_c is the number of receptors the distance of which from the wall is smaller than $d_{on} = 100\ nm$, L is the WBC length, and H is its height. The maximum contact area of about 30 μm is found for the firm adhesion. Consistently, states of firm adhesion correspond to the maximum in the deformation index of approximately 1.1. A rolling WBC shows a smaller contact area and deformation index, while a freely moving WBC has zero contact area and a deformation index close to 1 indicating that the WBC remains spherical. A contact area of about 20 μm was found in *in vivo* experiments [78] at a shear rate of $\dot{\gamma} = 100\ s^{-1}$, which falls into the stable rolling region in figure 4.32 (left) in agreement with the aforementioned average cell velocity in the range of $30 - 50\ \mu m/s$.

Leukocyte adhesive dynamics also depends on the medium viscosity (η_o), bond spring constant (k_s), and densities of receptors (n_r) and ligands (n_l), which was studied in [119] through simulations of adhesive dynamics of a solid spherical particle. An increase in the solvent viscosity for a fixed shear rate was shown to shift the border of the firm adhesion region to lower off rate values, since cell arrest is sensitive to shear stress. At the same time the effect of η_o on rolling behavior was found to be insignificant because it mainly depends on the shear rate [156]. A change in the bond spring constant may have a more complex effect on the WBC adhesive dynamics. For example, a decrease in k_s may result in a considerable shrinking of the stable rolling behavior region, while an increase of k_s alters the firm adhesion region [119].

An increase in n_r or n_l would generally shift the borders of regions of different adhesion states to higher k_{off}^0 values, since more bonds can potentially be formed [119]. However, this conclusion is credible only if n_r and n_l are properly balanced or $n_r \approx n_l$. Note that if n_r is several times smaller than n_l as in our simulations (see table 4.5), a further increase in n_l may not have a significant effect on the WBC adhesive dynamics, since there may be no available receptors for binding.

Finally, WBC adhesive dynamics strongly depends on cell deformability [108, 156]. Softer cells have a larger contact area yielding an expanded firm adhesion region. In addition, a larger contact area has a stabilizing effect on rolling adhesion. More compliant cells are subject to stronger deformations under hydrodynamic flow showing a larger deformation index δ. This results in a lower hydrodynamic force on the cell due to the flow which stabilizes adhesive interactions [108, 156].

In conclusion, WBC adhesive dynamics is affected by many factors discussed above.

However, the developed model is able to capture various states of cell adhesion. Next, we apply the developed model to adhesive behavior of Pf-parasitized RBCs in malaria.

4.4.4 Adhesive dynamics of Pf-parasitized RBCs

Pf-parasitized RBCs undergo irreversible changes which significantly affect normal blood circulation. Membrane stiffness of infected cells may increase up to ten-fold which may create capillary occlusions [38, 180] and results in an increase of blood flow resistance discussed in section 4.2.7. Furthermore, cytoadherence of infected RBCs to the vascular endothelium may intensify formation of capillary physical blockages and strongly contribute to the blood flow resistance [23, 51].

Even though infected RBCs are virtually invisible to the immune system, freely circulating Pf-parasitized RBCs can be destroyed in the spleen [60]. Pf parasites expose adhesive proteins on the RBC membrane surface to mediate adhesion to the endothelium in order to survive for several days needed for their successful intra-cell development. This mechanism facilitates further progression of malaria; however, it may severely disrupt normal blood flow. Adherence of infected RBCs is believed to be the main cause of bleeding complications in cerebral malaria due to blockages of small vessels in the brain [6].

RBC adherence can occur in any individual suffering from malaria. However, some people are subject to severe forms of malaria, while others may show only slight symptoms with relatively high parasitemia levels. This is likely to be caused by differences in the adhesive properties of infected RBCs in distinct individuals. *In vitro* experiments [35, 212, 11] on cytoadherence of Pf-parasitized RBCs in flow chambers revealed that their adhesive dynamics can be strikingly different for distinct coatings of the flow chamber walls. Adhesive dynamics of Pf-parasitized RBCs on purified ICAM-1 is characterized by stable and persistent flipping (rolling) behavior for a wide range of wall shear stresses [11]. In contrast, dynamics of infected RBCs on grown mammalian CHO cells shows firm adhesion with a potential sudden detachment for the same range of wall shear stresses, even though they express the same type of ligands [11]. The basis of the behavior dissimilarity is attributed to a different flow micro-environment; however, it is not well understood.

Numerical simulations may aid in understanding the complex interactions between the exposed proteins of Pf parasites and ligands on a coated surface. The developed RBC model in combination with adhesive interactions described in section 4.4.1 is used to simulate adhesive dynamics of Pf-parasitized RBCs. Several model parameters are varied to identify their impact on the adhesive dynamics and to capture Pf-parasitized RBC behavior found in experiments [11].

4.4.4.1 Model and physical parameters

A Pf-parasitized RBC is modeled using the stress-free WLC-POW model described in section 3.2 with the following parameters: $\mu_0^M = 1000$, $x_0 = 2.2$, $k_a = 50000$, $k_d = 1000$, $k_v = 50000$, and $m = 2$. DPD parameters (see section 2.2.2) of interactions among external solvent (S_o), internal fluid (S_i), RBC vertices (V), and wall (W) particles are shown in table 4.7. Pair interactions which are not specified in table 4.7 are switched off.

Interaction	a	γ	r_c	$k(eq.(2.11))$
$S_o - S_o$, $S_o - W$	4.0	10.0	1.5	0.25
$S_i - S_i$	4.0	10.0	1.5	0.25
$S_o - V$, $S_i - V$, $W - V$	2.0	20.0	1.5	0.25
$V - V$	100.0	10.0	0.75	0.25

Table 4.7: DPD parameters used in the simulations of RBC adhesive dynamics in malaria.

The simulation setup is analogous to that shown in figure 4.28. Initially, an infected RBC is placed between two walls at the distance of 100 nm away from the lower wall. The cell has $N_r = 500$ receptors, while ligands on the lower wall are distributed on the square lattice with lattice constant $d = 0.5$ μm. The domain dimensions are the same as those used in the leukocyte adhesive dynamics simulations above, where shear flow is generated by moving the upper wall. Default adhesion parameters used in the simulations (DPD units) and the corresponding physical parameters in SI units are presented in table 4.8. The default parameters correspond to the schizont stage of intra-cell parasite development with the Young's modulus approximately ten times larger than that of healthy RBCs. An infected RBC is also subject to the buoyant force $\Delta\rho V_{WBC} g$ with $\rho = 50$ kg/m^3 analogously to that in the WBC dynamics simulations above. The adhesive dynamics of Pf-parasitized RBCs is monitored for several seconds.

Parameters	Simulations	Physical
RBC diameter (D)	7.82	7.82×10^{-6} m
Young's modulus (Y)	3926	16.8×10^{-5} N/m
bending rigidity (k_c)	8.66	3.7×10^{-19} J
shear rate ($\dot{\gamma}$)	0.3333	33.33 s^{-1}
temperature (T)	0.1	310 K
external fluid viscosity (η_o)	22	9.5×10^{-3} $Pa \cdot s$
internal fluid viscosity (η_i)	22	9.5×10^{-3} $Pa \cdot s$
spring constant (k_s)	400	1.71×10^{-5} N/m
equilibrium spring length (l_0)	0.0	0.0 m
reactive distance (d_{on})	0.35	3.5×10^{-7} m
rupture distance (d_{off})	0.35	3.5×10^{-7} m
on strength (σ_{on})	1.0	4.28×10^{-8} N/m
off strength (σ_{off})	0.3333	1.43×10^{-8} N/m
unstressed on rate (k^0_{on})	116.67	11667 s^{-1}
unstressed off rate (k^0_{off})	1.0	100 s^{-1}
receptor density (n_r)	4.0	4.0 $mol/\mu m^2$
ligand density (n_l)	4.0	4.0 $mol/\mu m^2$

Table 4.8: Default simulation (in DPD units) and physical (in SI units) parameters for RBC adhesive dynamics in malaria.

4.4.4.2 Dynamics of infected RBCs in comparison with experiments

The adhesive dynamics of Pf-parasitized RBCs in shear flow is studied for various wall shear stresses. The simulated RBC dynamics is compared with that found in experiments [11] for two cases of wall coatings: with purified ICAM-1 and with mammalian CHO cells. Figure 4.33 shows several successive snapshots of a cell rolling on the wall for the default setup. At the post-processing step, blue particles are added as tracers for visual clarity and distinct RBC snapshots are separated by shifting their x coordinate. The dynamics of the Pf-parasitized RBC is characterized by "flipping" behavior initiated first by the cell peeling off the wall due to the force of the hydrodynamic flow after flat RBC adhesion (the

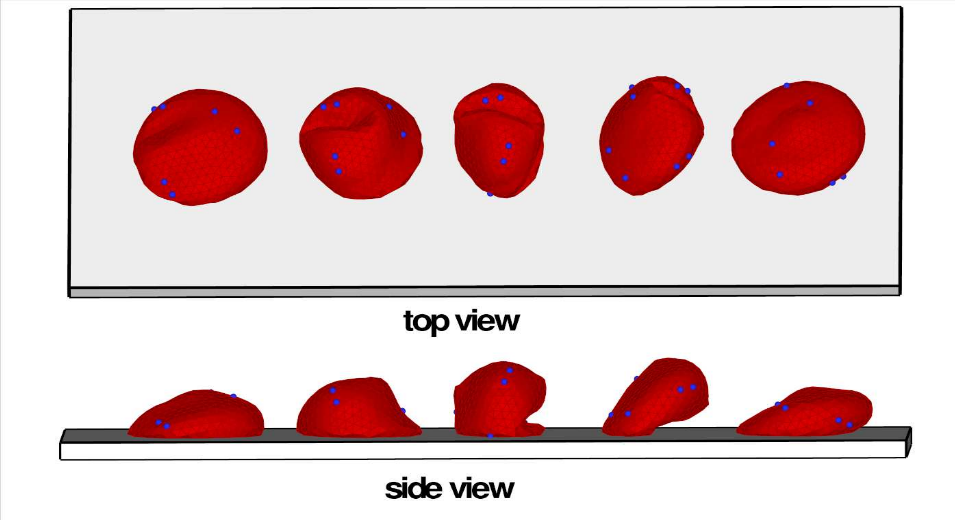

Figure 4.33: Top and side views of successive snapshots of a single flipping of an infected RBC for the default case. Coordinates along the wall for different snapshots are shifted in order to separate them for visual clarity. Blue particles are added as tracers during post-processing to illustrate the membrane dynamics.

first snapshot in figure 4.33). After the majority of the initial cell contact area with the wall is peeled off, a RBC flips over on its other side which is facilitated by the remaining small contact area with the wall. During these steps Pf-parasitized RBCs undergo strong membrane deformations as illustrated in figure 4.33. A similar behavior was found in experiments [11] of Pf-parasitized RBCs which showed flipping (rolling) along a wall coated with purified ICAM-1. In agreement with the simulations, RBCs in experiments also showed strong membrane deformations characterized by local membrane buckling.

Figure 4.34 presents the corresponding displacement along the x coordinate (left) and instantaneous RBC velocity (right). An infected RBC rolls in a relatively stable motion which resembles a staircase. The segments of smaller displacements correspond to the stage of a flat RBC adhesion followed by its slow peeling off the wall (see figure 4.33), while the fragments of larger displacements represent the stage of RBC fast flipping described above. The RBC velocity is in agreement with its displacement showing high peaks or fast cell motion during the time segments with larger displacements. The average cell velocity is approximately 5.8 $\mu m/s$. Figure 4.35 shows RBC displacement along the z cross-flow coordinate (left) and instantaneous contact area (right) for the default simulation. The displacement across the wall shows a jerky motion of an infected RBC within several microns. This is due to a discrete number of bonds and their random rupture or dissociation.

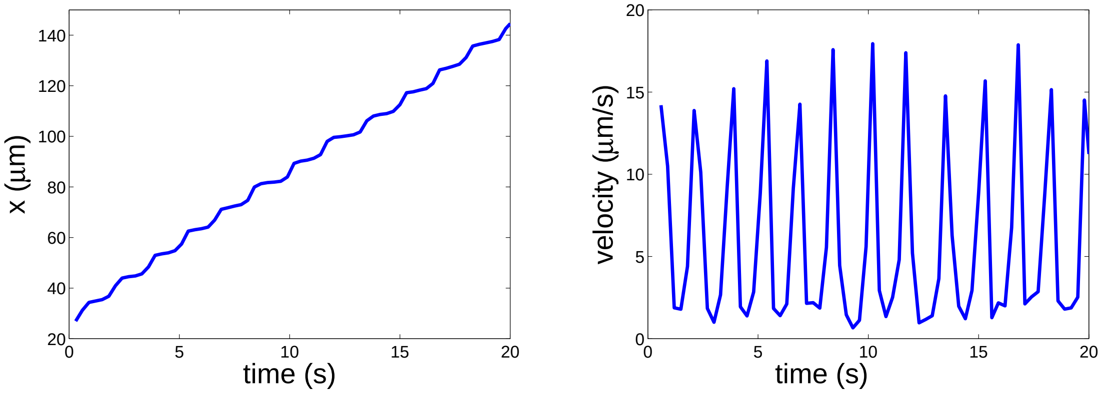

Figure 4.34: Pf-parasitized RBC displacement (left) and velocity (right) along the wall for the default case.

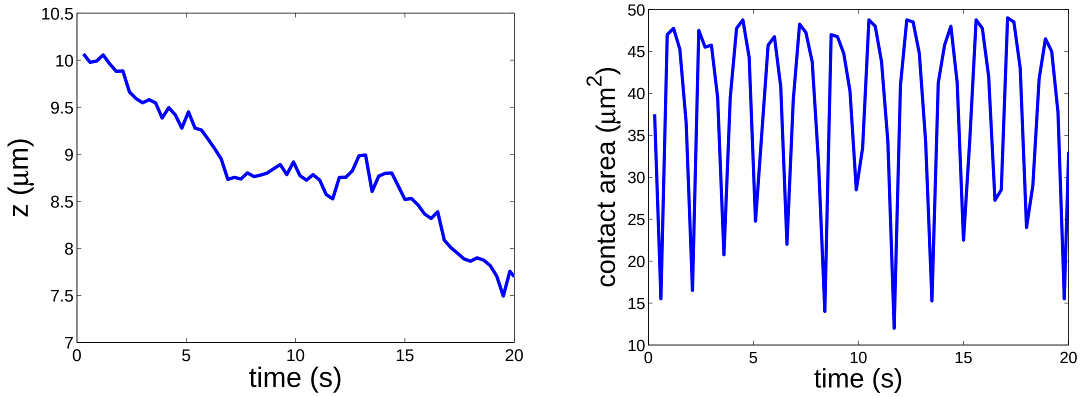

Figure 4.35: RBC displacement across the wall (left) and the cell contact area (right) for the default setup.

Thus, if there is a non-uniform distribution of bonds over the contact area at some instance of time, a Pf-parasitized RBC may be pulled to one side. In addition, the hydrodynamic force on the RBC may be non-zero in z direction, since the cell is not symmetric due to the local deformations shown in figure 4.33. The RBC contact area in figure 4.35 (right) is correlated with its displacement and velocity in figure 4.34. Minima in the contact area coincide with maxima in the RBC velocity corresponding to the stage of fast cell flipping from its one side to the other. The cell contact area remains within the range of $10 - 50$ μm^2, while the average value is equal to 38.6 μm^2.

To investigate the dependence of RBC adhesive dynamics on wall shear stress, the velocity of the upper plate is changed. Note that the shear rate is altered at the same time. However, the wall shear stress appears to be a key parameter which governs RBC adhesive dynamics, since adhered RBCs are driven by fluid stresses and roll along the wall with a much smaller velocity than that of the hydrodynamic flow.

Several initial simulations with a varying wall shear stress and other fixed parameters revealed that a Pf-parasitized RBC may exhibit firm adhesion at a shear stress lower than 0.317 Pa for the default case and can completely detach from the wall at higher wall shear stresses. At low shear stresses, adhesion forces are strong enough to counteract the stress exerted on the cell by hydrodynamic flow resulting in its firm sticking to the lower wall. On the contrary, at high shear stresses existing bonds do not provide sufficiently strong adhesive interactions which yields RBC detachment from the wall. RBC visualizations showed that its detachment at high shear stresses occurs during the relatively fast motion of RBC flipping, since the contact area at that step corresponds to its minimum. However, in experiments [11] Pf-parasitized RBCs which moved on a surface coated with the purified ICAM-1 showed persistent and stable rolling over long observation times and a wide range of wall shear stresses between 0.2 Pa and 2 Pa. This suggests that there must be a mechanism which stabilizes rolling of infected RBCs at high shear stresses. This fact is not surprising since for example leukocyte adhesion can be actively regulated depending on flow conditions and biochemical constituents present [185, 77].

To stabilize RBC binding at high shear stresses we introduce adaptivity of the bond spring constant (k_s) with a linear dependence on the flow shear stress. Thus, k_s is increased or decreased proportionally to an increase or decrease in the shear stress. Figure 4.36 presents the average rolling velocity of a Pf-parasitized RBC in comparison with experiments of cell rolling on a surface coated with purified ICAM-1 [11]. The simulated average velocities show a near-linear dependence on the shear stress and are in good agreement with experiments. An observed discrepancy at the highest simulated shear stress suggests that a further strengthening of cell-wall bond interactions may be required. However, the simulated value remains between the 10th and the 90th percentiles found in experiments.

The dependence of the RBC rolling velocity on shear stress found in experiments is clearly non-linear. Therefore, the assumption of linear dependence of k_s on the shear stress is likely to be an oversimplification. In addition, there may be a change in bond association and dissociation kinetics with shear stress which would be able to aid in rolling stabilization of infected RBCs at high shear rates. Our simulations suggest that adhesive dynamics of Pf-parasitized RBCs is not sensitive to a slight change (below $30\% - 40\%$) in k_{on}^0 and

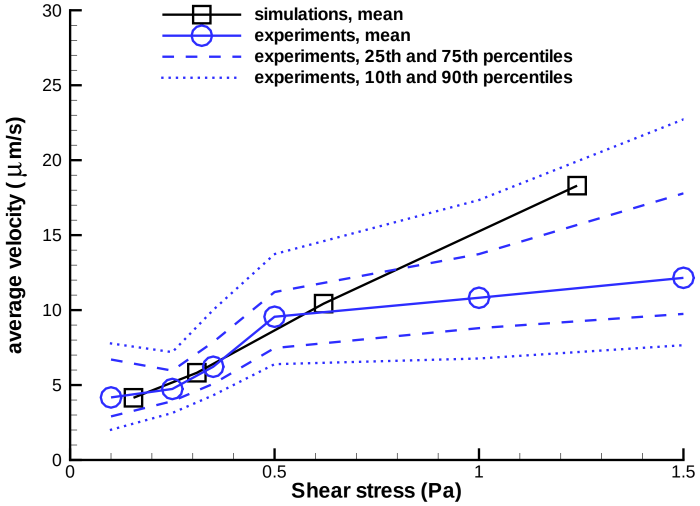

Figure 4.36: Average rolling velocity of infected RBCs depending on the shear stress in comparison with the experiments of cell rolling on purified ICAM-1 [11]. Experimental data include mean values and curves that correspond to the 10th, 25th, 75th, and 90th percentiles.

k^0_{off}; however, cell dynamics may be strongly affected if these parameters are changed considerably as seen in the leukocyte dynamics simulations in section 4.4.3. Moreover, experimental data show a much larger scatter in the average RBC velocity for different cells observed than that in simulations (not shown). This is likely to be related to non-uniform distributions of receptors on the RBC membrane and ligands on the wall. In the simulations, distributions of both receptors and ligands are fixed and are nearly homogeneous with approximately the same area occupied by each receptor or each ligand. A scatter in behavior among distinct RBCs in the simulations is solely related to the stochastic nature of the adhesive model. However, in experiments irregular distributions of receptors and ligands are likely to significantly contribute to a scatter in RBC adhesive dynamics. Next, we show an example where it appears to be important.

Antia et al. [11] also examined adhesive dynamics of Pf-parasitized RBCs on a surface covered with grown mammalian CHO cells. Most of the infected RBCs showed persistent firm adhesion with infrequent complete detachment. This behavior was not attributed to the presence of any other types of ligands which may be expressed by the mammalian CHO cells, since it is believed that they expose the same ligands as ICAM-1. The flow micro-environment was identified to potentially contribute to the difference in RBC adhesive dynamics on purified ICAM-1 and on mammalian CHO cells.

Adhesive behavior of Pf-parasitized RBCs, explored by means of a numerical simulation for various parameters, revealed several types of cell dynamics such as firm adhesion, RBC peeling off the surface followed by flipping from its one side to the other or by detachment from the wall, and very slow slipping along the wall. However, the video containing an example of RBC adhesive dynamics on the mammalian CHO cells from experiments [11] shows firm adhesion of Pf-parasitized RBCs for some time followed by a sudden detachment. In contrast, firm adhesion in simulations appears to always be stable with no detachment within the simulated time of approximately 30 s. Note that the RBC motion in experiments before the detachment displays very slow slipping along the surface due to the hydrodynamic flow and random collisions with other flowing RBCs. Considering RBC adhesive dynamics observed in simulations and experiments it is likely that the sudden complete detachment from the wall in this case is caused by RBC slipping into a wall region with a limited number of ligands available for binding.

To verify this hypothesis we run a simulation in which ligand sites are removed from the wall area between 30 μm and 40 μm in the x direction. RBC slipping along the wall is achieved for the following simulation parameters: $k_c = 1.85\times10^{-18}\ J$, $k_s = 3.42\times10^{-6}\ N/m$, and $\dot{\gamma} = 6.7\ s^{-1}$, while the other parameters are the same as in the default case (see table 4.8). Figure 4.37 presents RBC displacement along the x coordinate (left) and instantaneous velocity (right). RBC displacement shows a slow slipping along the surface continued up to an x coordinate between 30 μm and 40 μm, where a complete cell detachment occurs due to

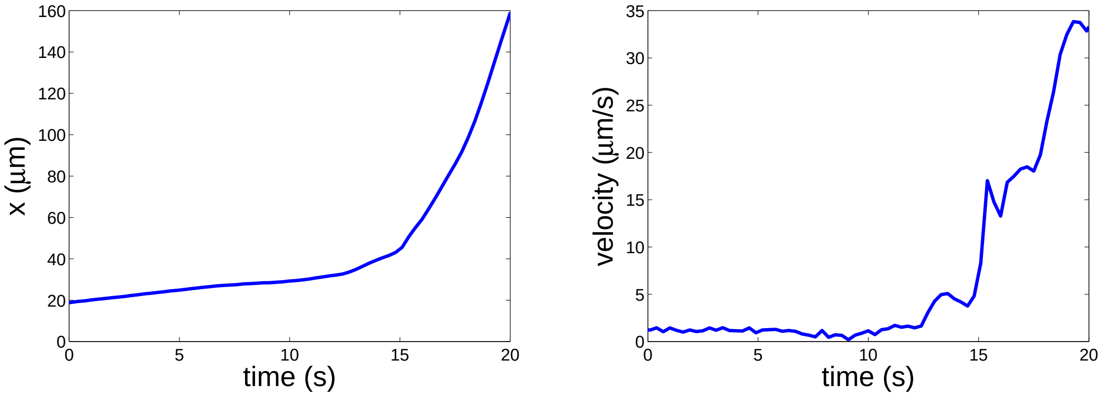

Figure 4.37: Displacement (left) and velocity (right) of a Pf-parasitized RBC along the wall for the case of sudden cell detachment.

no ligands present for binding. The corresponding cell velocity in figure 4.37 (right) confirms the described dynamics. The simulation results are in good qualitative agreement with the RBC dynamics on the mammalian CHO cells found in experiments [11]. At this time, no other change in physical parameters of cell adhesion was found to be able to reproduce this dynamics.

4.4.4.3 Dependence of RBC adhesive dynamics on membrane properties

In this section, the adhesive dynamics of Pf-parasitized RBCs in shear flow is described for different membrane properties such as bending rigidity and Young's modulus. Figure 4.38 presents several snapshots of a rolling RBC along a wall with the membrane bending rigidity five times larger than that for the default case. This plot illustrates that the membrane surface is much smoother than in the case of low bending rigidity in figure 4.33. High bending rigidity is able to resist stresses exerted by the hydrodynamic flow showing no local buckling of the membrane. However, the Pf-parasitized RBC experiences strong membrane deformations during the peeling stage of the flipping motion similar to those seen for RBCs with low bending resistance.

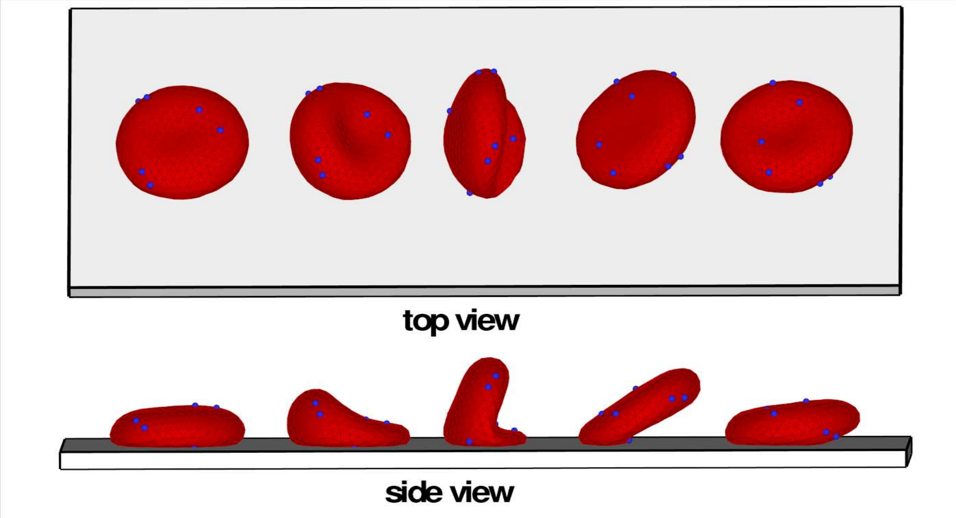

Figure 4.38: Top and side views of several snapshots of a rolling RBC with the bending rigidity $k_c = 1.85 \times 10^{-18}$ J. Coordinates along the wall for different snapshots are shifted in order to separate them for visual clarity. Blue particles are added as tracers during post-processing to show membrane dynamics.

Figure 4.39 shows the average rolling velocity (left) and the average contact area (right) with respect to the membrane bending rigidity normalized by its default value given in table 4.8. RBCs with lower bending rigidity roll with lower velocity along the wall than

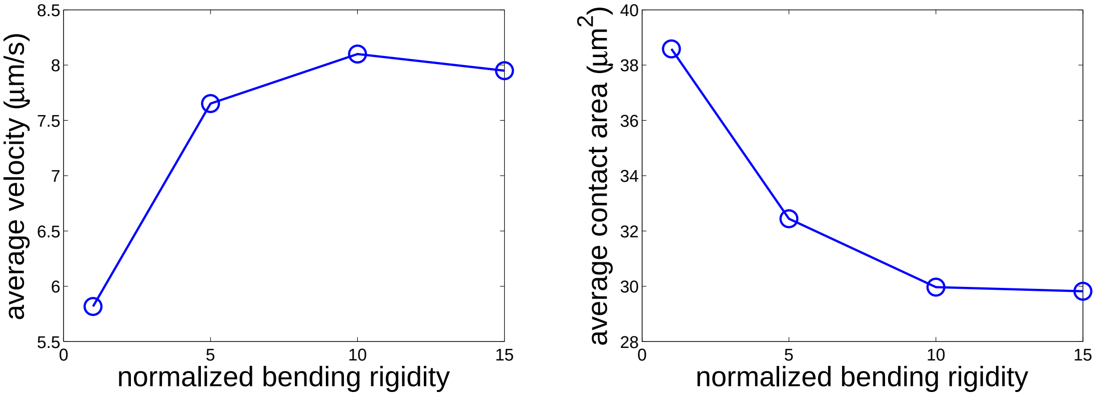

Figure 4.39: Average RBC rolling velocity (left) and average contact area (right) for different membrane bending rigidities normalized by 3.7×10^{-19} J.

those with higher bending resistance. Figure 4.39 (right) shows that more compliant RBCs form a larger contact area with the solid surface resulting in a larger number of bonds connecting cell receptors with the wall ligands. Hence, softer cells experience stronger binding interactions with the wall which slows down their rolling motion. Note that for normalized bending rigidities larger than approximately $7-8$, RBC rolling velocity and contact area seem to level off to constant values. This indicates that the RBC adhesive dynamics becomes independent of the membrane bending rigidity if the RBC is sufficiently stiff.

Further, the effect of the membrane Young's modulus on RBC adhesive dynamics is considered. The Young's modulus of Pf-parasitized RBCs increases during intra-cell parasite development which was discussed in section 3.3.4. The default case of RBC adhesive dynamics presented above corresponds to the last stage of parasite development (schizont stage) with the Young's modulus about ten times larger than that of a healthy RBC. However, adhesion of a Pf-parasitized RBC also occurs at the trophozoite stage of parasite development which precedes the schizont stage and is characterized by a five-fold increase in the membrane Young's modulus in comparison with that of healthy RBCs. Therefore, the Young's modulus in simulations is varied from its value for healthy RBCs ($Y = 18.9 \times 10^{-6}$ N/m) to that of the schizont stage given in table 4.8.

Figure 4.40 presents successive snapshots of a rolling RBC with the same membrane properties as a healthy RBC. The plotted sequence of RBC snapshots shows that the cell

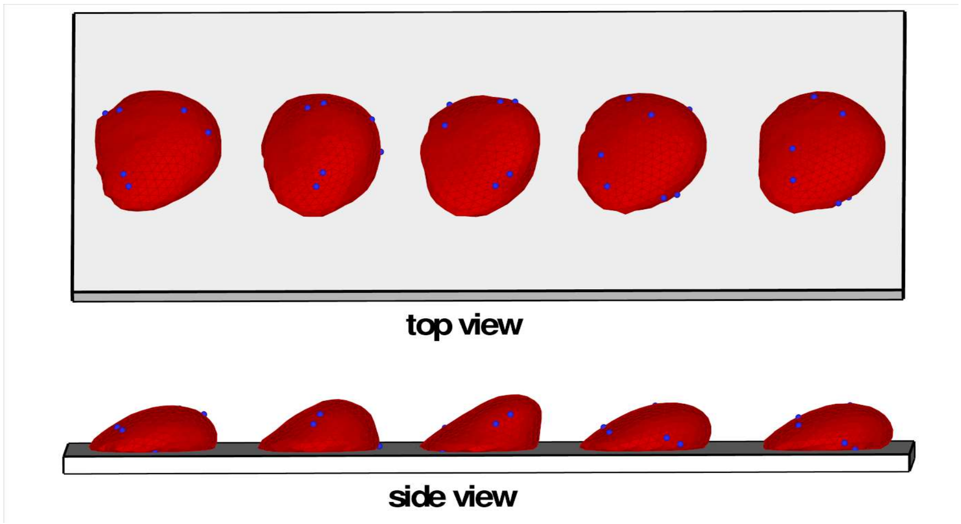

Figure 4.40: Top and side views of several snapshots of a rolling RBC with the Young's modulus $Y = 18.9 \times 10^{-6}\ N/m$. Coordinates along the wall for different snapshots are shifted in order to separate them for visual clarity. Blue particles are added as tracers during post-processing to show membrane dynamics.

crawls on the wall in contrast to the flipping dynamics found in the case of a high Young's modulus. The physics of this transition has the same basis as the tumbling-to-tank-treading transition in shear flow discussed in section 3.5. In order for a RBC to undergo a tank-treading motion in shear flow a certain energy barrier has to be exceeded. Hence, RBC tumbling in shear flow is observed if shear forces exerted by hydrodynamic flow are not strong enough to overcome the tank-treading energy barrier which depends roughly linearly on the membrane Young's modulus. By analogy, an adherent RBC crawls along the wall in a tank-treading like motion if the tank-treading energy barrier is exceeded by near-wall shear forces as seen in figure 4.40. However, a sufficient increase in the membrane Young's modulus hinders RBC tank-treading which forces the cell to peel off the surface with a consequent flipping from one side to the other. Thus, the flipping dynamics of Pf-parasitized RBCs is mediated by the increased membrane stiffness. In addition, it can be affected by the presence of a rigid parasite inside the cell which will be discussed in the next section.

Figure 4.41 shows the average rolling velocity (left) and the average contact area (right) with respect to the membrane Young's modulus normalized by its value for healthy RBCs. Stiffer RBCs roll with faster velocity, since their contact area is smaller than that of softer RBCs resulting in weaker adhesive interactions with the wall. A similar conclusion was

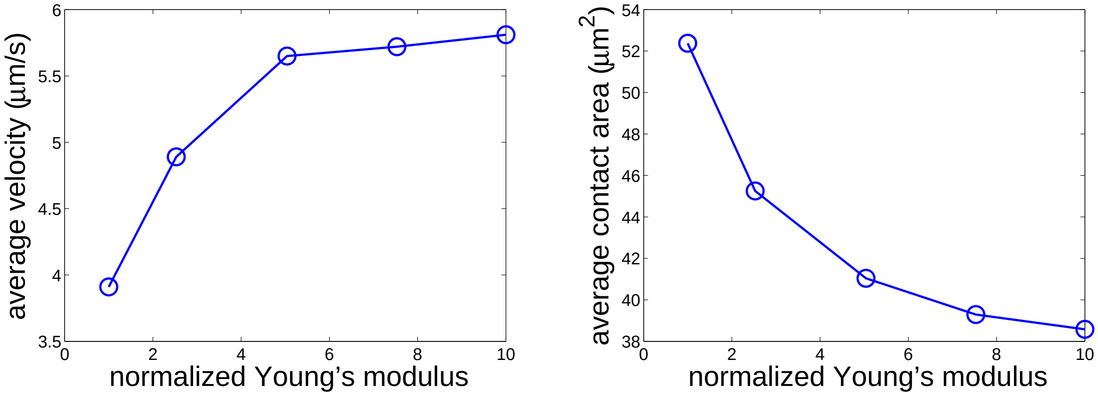

Figure 4.41: Average rolling velocity (left) and average contact area (right) for different Young's moduli normalized by the value $Y = 18.9 \times 10^{-6}\ N/m$.

drawn in simulations of leukocyte adhesive dynamics for varying membrane stiffness [108, 156]. Note that the transition from crawling dynamics to flipping behavior occurs at a Young's modulus of approximately three times larger than that of healthy RBCs. This confirms that Pf-parasitized RBCs at the trophozoite stage of parasite development are subject to flipping dynamics.

4.4.4.4 Influence of a rigid parasite on adhesive dynamics

Up to this point, Pf-parasitized RBCs were modeled as thin stiff membranes filled with a Newtonian fluid. Under realistic conditions Pf-parasitized RBCs contain a "rigid" parasite undergoing growth. Recent experiments [158] suggest that the volume of cytosol may be reduced three-fold in the later stages of intra-cell parasite development in comparison with that of healthy RBCs indicating that the parasite can take up a considerable volume inside a RBC. A sufficiently large parasite can provide a rigid backbone inside a RBC which may strongly affect RBC adhesive dynamics and contribute to the flipping behavior described above.

The parasite is modeled by a collection of DPD particles uniformly distributed within the cylindrical volume with a radius of 3.3 μm and a height of 0.2 μm. This set of particles is placed inside the modeled RBC and constrained to undergo rigid motion. In order to prevent the parasite body from crossing the RBC membrane, we introduce Lennard-Jones interactions between the parasite body particles and membrane vertices with the parameters $\epsilon = 1.0$ and $\sigma_{MD} = 0.5$ (see section 2.2.1 for details). However, the parasite swims freely in the RBC cytosol. The number of DPD particles that represents the RBC cytosol is reduced according to the volume occupied by the parasite body. The simulation parameters for the membrane and adhesive interactions are the same as in table 4.8. Figure 4.42 presents successive snapshots of a rolling RBC with a rigid parasite inside the cell. The plot confirms that the parasite body serves as a rigid backbone that contributes to RBC flipping dynamics. The RBC membrane displays local buckling due to its low bending rigidity, which is consistent with the RBC visualizations in figure 4.33. However, the RBC does not experience such a severe flexural deformation during cell peeling off the wall as observed in figures 4.33 and 4.38. Here, the parasite body constrains the RBC membrane by supplying a rigid support, which forces RBC flipping without a substantial bending.

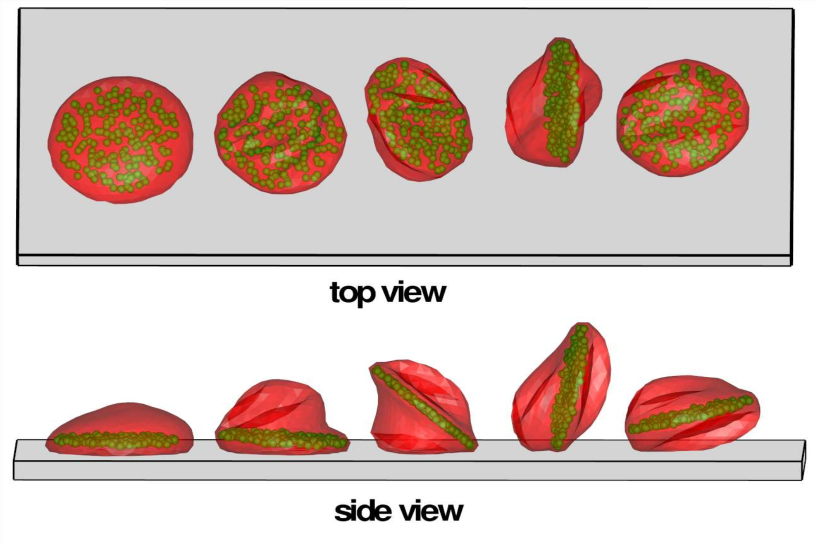

Figure 4.42: Top and side views of several snapshots of a rolling RBC with a parasite body inside the cell drawn in green. Coordinates along the wall for different snapshots are shifted in order to separate them for visual clarity. The RBC membrane is partially transparent.

Figure 4.43 shows the corresponding RBC displacement (left) and instantaneous velocity (right). RBC displacement and velocity display a more erratic pattern than that in figure 4.34. For example, the curves in figure 4.43 indicate that there are several time segments where the Pf-parasitized RBC shows firm adhesion for several seconds. Furthermore, firm adhesion may be followed by several fast flips of the RBC along the surface characterized by two closely located peaks of velocity around the time of 20 s. Visualizations of cell dynamics also revealed that the smaller peaks in cell velocity in figure 4.43 (right) correspond to a tank-treading like motion facilitated by the parasite body. This occurs due to the parasite

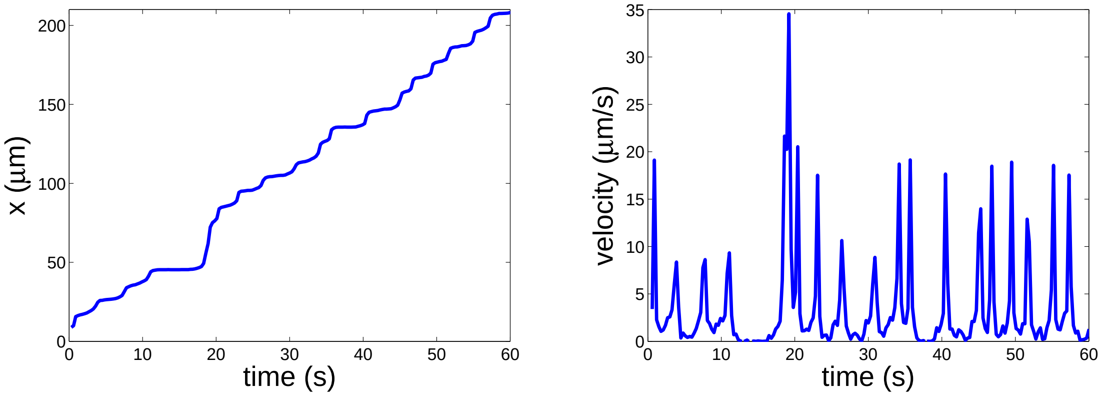

Figure 4.43: Infected RBC displacement (left) and velocity (right) along the wall for the case of explicit modeling of the rigid parasite body inside the cell.

being freely suspended in the RBC cytosol. A proper positioning of the parasite body inside the RBC may result in a stress on the front part of the membrane forcing the RBC into a crawling like motion. Figure 4.44 presents RBC displacement across the flow in z direction (left) and instantaneous contact area (right). These plots also display more

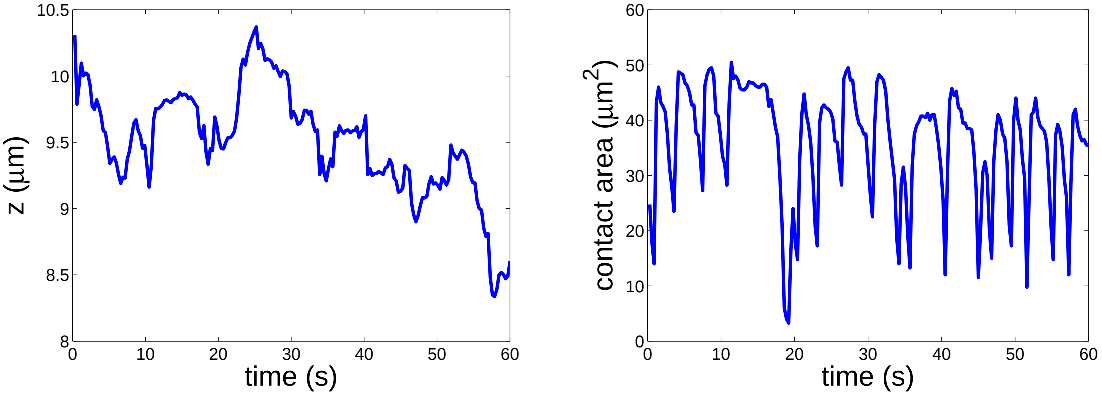

Figure 4.44: RBC displacement across the wall (left) and the cell contact area (right) for the case of explicit parasite modeling.

irregular patterns of the displacement across the flow and contact area than those in figure 4.35 consistent with the RBC displacement and velocity shown in the previous figure.

The presence of a rigid body inside a RBC significantly affects the RBC adhesive dynamics resulting in a more erratic behavior in comparison with the more regular adhesive dynamics of RBCs with no parasites. A thin disk to represent the parasite body was considered; however, a different geometrical form or size of the parasite may have a different effect on RBC adhesive dynamics. Therefore, an experimental characterization of the parasite geometry for different stages of parasite development would be of great interest. In addition, the modeled parasite body was freely suspended in the RBC cytosol, while under realistic conditions it is likely that the parasite has some attachments to the membrane, since it exposes adhesive proteins on the membrane surface to mediate binding to the wall. These unresolved issues require further experimental and numerical investigation.

4.4.4.5 Adhesion of Pf-parasitized RBCs in microchannel flow

A flow of a RBC suspension is simulated in a rectangular microchannel with the dimensions $100 \times 30 \times 50$ μm and periodicity in the x direction. This geometry is similar to a flow chamber employed in experiments [11]. The RBC suspension is characterized by $H_t = 0.1$ and a parasitemia level of 10% where the infected cells correspond to the schizont stage of intra-RBC parasite development with the parameters given in table 4.8. Ligand sites are placed on a square lattice on the lower wall in the y direction with the lattice constant $d = 0.5$ μm. The flow is driven by a uniform constant force applied to all particles to mimic the pressure gradient. In addition, RBCs are subject to the buoyant force which is set to be five times larger than that used in the previous simulations. This forces a faster contact between RBCs and the lower wall and facilitates a faster binding of Pf-parasitized RBCs to the wall to overcome the difficulty of a limited total time for which simulations can be advanced. The total physical time in simulations is limited by approximately one minute due to the computational expense, while the corresponding flow in experiments [11] was observed over $10 - 20$ minutes.

Figure 4.45 shows the velocity (V_x) contour of the flow of RBC suspension in a rectangular microchannel. The flow is nearly symmetric in y and z with the maximum velocity of approximately 150 $\mu m/s$ in the center of the microchannel. The maximum shear rate measured at the lower wall is equal to 27 s^{-1} which is close to the value in table 4.8 used previously for the default case. This yields a maximum wall shear stress of approximately 0.26 Pa.

After several seconds some Pf-parasitized RBCs may closely approach the lower wall where cell binding can occur. Figure 4.46 presents snapshots of three examples of binding of Pf-parasitized RBCs to the wall. The example "A" shows RBC binding when the cell is oriented nearly perpendicular to the wall. The RBC continues rolling along the wall for several seconds with a relatively small contact area. In "B", RBC binding starts with a

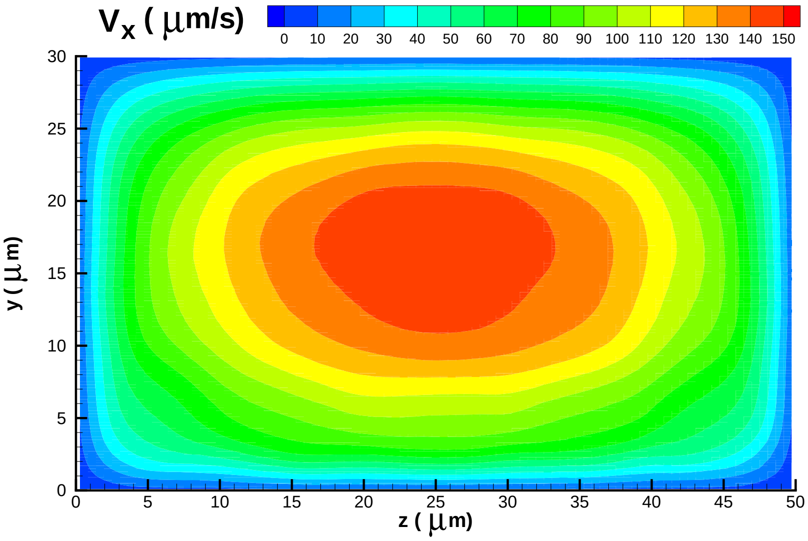

Figure 4.45: V_x velocity contour of the flow in a rectangular microchannel.

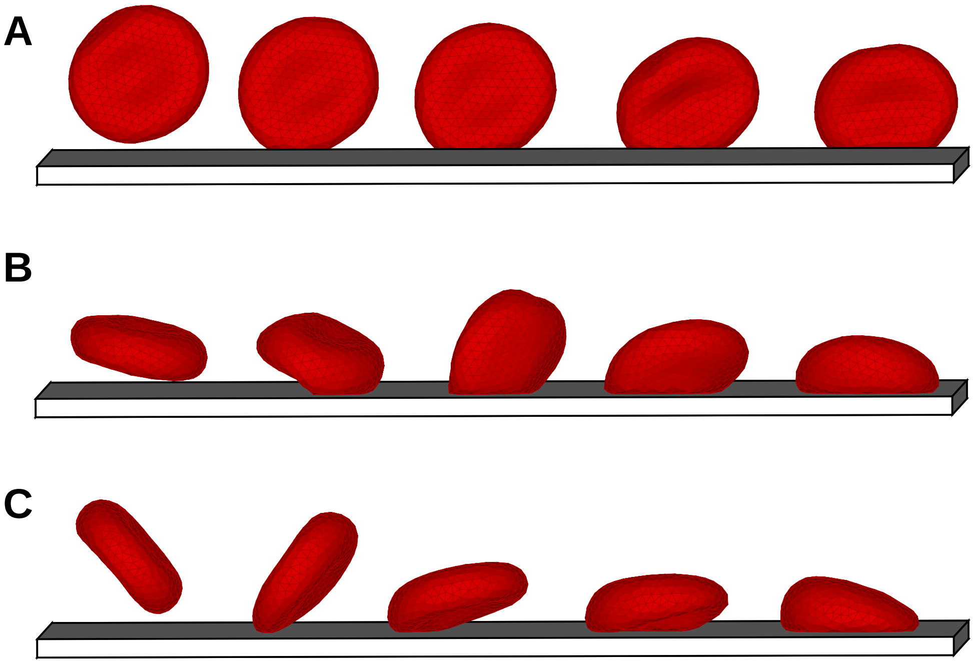

Figure 4.46: Snapshots of RBC binding to the lower wall of a microchannel. A - Pf-parasitized RBC binding with small contact area, B and C - binding with large contact area. Coordinates along the wall for different snapshots are shifted in order to separate them for visual clarity.

small contact area formed. Subsequently, the fluid flow forces the cell to flip from its one side to the other resulting in a binding with a large contact area. Example “C” illustrates

Pf-parasitized RBC binding to the wall where a large contact area is instantly formed. Figure 4.47 shows the corresponding displacements and instantaneous velocities for the three cases. In “A”, after initial binding to the wall a RBC continues rolling on its side

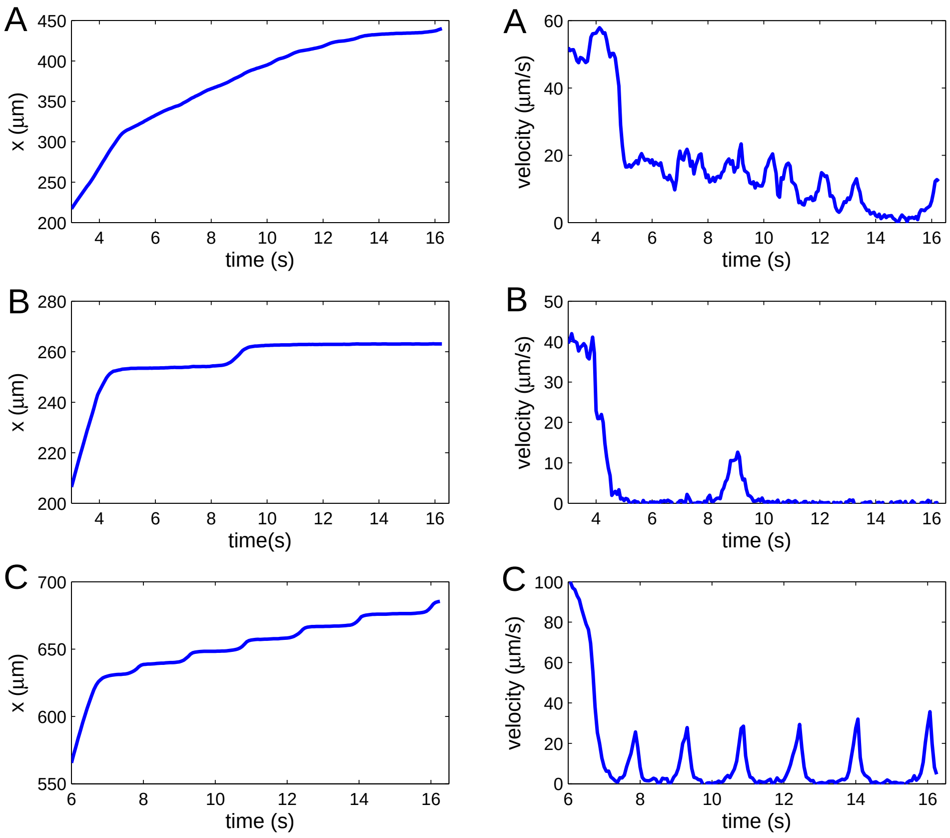

Figure 4.47: Pf-parasitized RBC displacements and instantaneous velocities for the three examples shown in figure 4.46.

for several seconds as confirmed by its displacement and velocity plots. Eventually, the infected RBC forms a larger contact area with the wall displayed by a substantial drop in its velocity at $t = 14$ s in figure 4.47 (A), since rolling on the side is not stable and is expected to be a transient behavior. Afterwards, the RBC exhibits flipping dynamics similar to that discussed in section 4.4.4.2. In contrast, adhesive dynamics of an infected RBC in example “B” shows a rapid strong binding with the wall followed by several seconds of cell arrest. Then, at $t = 9$ s the RBC flips from its one side to the other after which a repeated period of firm adhesion is observed. The z coordinate of the RBC initial binding site is equal to approximately 45 μm which is close to the channel corner. The local shear rate at $z = 45\ \mu m$ is equal to approximately 18 s^{-1} in comparison with the maximum wall shear rate of 27 s^{-1} resulting in a substantial decrease of local shear stresses on the RBC exerted by the hydrodynamic flow. The local shear stresses are likely to be too small to enforce persistent flipping dynamics, and hence, relatively long periods of firm adhesion are observed. The RBC adhesive dynamics in example "C" confirms this idea. The infected RBC shows a consistent flipping dynamics as seen in figure 4.47 (C). However, its position in the z coordinate is close to the middle of the microchannel, where the wall shear stress attains its maximum. The average rolling velocity after adhesion is equal to 6.1 $\mu m/s$ in agreement with that found in section 4.4.4.2. Note that all Pf-parasitized RBCs which formed binding with the wall remained bound for the rest of the simulation time. Similar observations were reported in experiments [11] of Pf-parasitized RBCs rolling on ICAM-1 in a flow chamber.

Simulation results on adhesive dynamics of Pf-parasitized RBCs in the microchannel illustrate complexity of cell behavior. Adhesive dynamics strongly depends on local microflow conditions due to varying shear stresses. Initial binding of infected RBCs may show a great variability in cell transient dynamics; however a strong binding with the wall is eventually formed yielding predictable flipping behavior or firm adhesion. In addition, freely flowing RBCs may collide with adhered cells affecting their adhesive dynamics.

4.5 Summary

In this chapter blood flow is simulated for healthy conditions and in malaria disease. Blood is modeled as a suspension of RBCs in a Newtonian fluid. Blood flow in microtubes under healthy conditions is simulated for different H_t values and tube diameters. Velocity profiles for different H_t values show an increase in blood flow resistance with an increase in H_t. RBC center-of-mass distributions indicate cell migration away from the wall to the tube center. This results in the formation of a CFL next to the tube wall and is related to the experimentally observed Fahraeus and Fahraeus-Lindquist effects.

The *Fahraeus effect* is characterized by a decrease in the discharge hematocrit when the tube diameter is increased, while the *Fahraeus-Lindquist* effect describes a decrease in the blood apparent viscosity with decreasing tube diameter. The developed blood flow model is able to closely capture changes in the discharge hematocrit and the relative apparent viscosity for H_t values in the range $0.15 - 0.45$ and tube diameters between 10 μm and 40 μm in comparison with those found in *in vitro* experiments.

Fahraeus and Fahraeus-Lindquist effects are directly related to the CFL next to the wall by providing an effective lubrication for the viscous RBC core to flow at much less friction. Simulated CFLs are in agreement with those found in *in vitro* and *in vivo* experiments; however, experimental CFL values show a considerable scatter which does not allow exact quantitative comparison. Discrepancies between the simulated CFLs and *in vitro* data are likely to be related to a potential RBC sedimentation, RBC aggregability, and differences in flow rates employed, while blood flow conditions *in vivo* are far more complex. In particular, CFLs *in vivo* are additionally affected by the presence of the glycocalyx layer, variations in vessel diameter, upstream flow conditions such as vessel bifurcations, and the length of a straight vessel segment where measurements are taken.

Blood flow in *malaria* is simulated for a range of parasitemia levels between 25% and 100%. Pf-parasitized RBCs are considerably stiffer than healthy RBCs resulting in an increase of blood flow resistance. The maximum increase in flow resistance by approximately 50% is found for the tube diameter $D = 10$ μm, $H_t = 0.45$, and parasitemia level of 100%. For larger tube diameters, lower H_t values, and lower parasitemia levels the increase in blood flow resistance is below 50%. In addition, the effect of RBC geometry is examined, since Pf-parasitized RBCs at the latest stage of intra-cell parasite development are found to have a near-spherical shape. Near-spherical geometry results in an additional increase in the blood flow resistance by approximately 10%. Based on the obtained simulation results, we estimate the increase in blood flow resistance in malaria to be below 25% because realistic parasitemia levels are below 10% for the most of the malaria cases. These results are based on the assumption of no adhesion of Pf-parasitized RBCs at the wall.

Blood flow through a *constriction* of a microfluidic channel shows the focusing effect described by an enhanced CFL downstream. This effect appears to be due to RBC cross-stream migration within the constriction to its center. The focusing effect is studied for different constriction widths and lengths, viscosities of the suspending medium, H_t values, and RBC membrane rigidities. More pronounced RBC focusing is achieved for narrower and longer constrictions, larger solvent viscosities, lower H_t values, and softer RBCs, since RBC migration to the constriction center is stronger for these conditions. The simulation results are in qualitative agreement with the corresponding experiments; however, quantitative comparison requires precise control of upstream flow conditions and RBC distribution which strongly affect RBC focusing. In addition, our results suggest that the focusing effect is likely to become negligible at high H_t values such as 0.45.

Adhesive dynamics of leukocytes and Pf-parasitized RBCs is simulated based on the stochastic bond formation/dissociation model. Freely circulating WBCs are spherical in shape, while adhered WBCs resemble a "tear-drop" like shape and show different adhesive dynamics depending on flow conditions and adhesive interactions. Four principal states of WBC adhesion in shear flow are defined based the average pause time and cell velocity: firm adhesion, stop-and-go rolling, stable rolling, and free motion. The on-off state diagram of WBC adhesion dynamics is calculated to identify regions of the defined states for various unstressed on and off rates. Firm adhesion occurs if the off-rate is below a critical value under which bond dissociation is an extremely rare event. Stop-and-go rolling is found in a narrow range of the off rates above the critical value for firm adhesion, where infrequent bond dissociations can occur resulting in an abrupt WBC motion. In contrast to the stop-and-go rolling, stable WBC rolling is characterized by a relatively continuous WBC motion along the wall and is achieved when the *on* and *off* rates are in a proper balance. Finally, free WBC motion is found when the rate of bond dissociation is more significant than the on-rate such that adhesive cell-wall interactions are not sufficiently strong to resist the hydrodynamic lift exerted by fluid flow. Available experimental data show good agreement with the simulation results and allow us to identify regions in the on-off state diagram that correspond to realistic conditions.

Pf-parasitized RBCs adhering to vascular endothelium in a flow show "flipping" dynamics. RBC flipping is characterized by the cell peeling off the wall due to forces exerted by the hydrodynamic flow with a subsequent flip from its one side to the other. This behavior appears to be due to an increased membrane stiffness of Pf-parasitized RBCs. Healthy RBCs under the same conditions of adhesive interactions crawl along the wall in a tank-treading motion. If the membrane Young's modulus is larger than approximately three times that of healthy RBCs, transition to flipping dynamics is observed because the tank-treading motion is hindered by a proportional increase in the tank-treading energy barrier. In addition, the adhesive dynamics of Pf-parasitized RBCs depends on the membrane bending rigidity. More compliant RBCs show stronger membrane deformations during adhesion. Also, they are able to form a larger contact area with the wall which slows down their rolling velocity in comparison to RBCs with higher membrane bending rigidity.

The simulated adhesive dynamics of infected RBCs is in agreement with experiments of Pf-parasitized RBCs rolling on ICAM-1 where flipping dynamics was observed for a wide range of wall shear stresses. Adhesive dynamics on mammalian CHO cells found in experiments shows prolonged firm adhesion of Pf-parasitized RBCs with a slight slipping on the wall and rare detachments. The firm adhesion is found to be exceptionally stable in simulations with no RBC detachments observed. Thus, our simulations suggest that this behavior is likely to be caused by an irregular distribution of ligands on the wall. Firmly adhered RBCs may slip into a region with a small number of ligands available for binding which would cause their detachment from the wall. In addition, several simulations are performed with explicit modeling of a rigid parasite inside infected RBCs. The presence of a rigid body inside RBCs strongly affects the simulated adhesive dynamics characterized by more irregular RBC flipping with short periods of intermittent firm adhesion. Adhesive dynamics of Pf-parasitized RBCs in a rectangular microchannel is further complicated by variations in local wall shear stresses and the presence of other healthy and infected RBCs in the flow.

In conclusion, the developed model is able to capture blood flow properties under healthy conditions and in malaria. It accurately reproduces blood flow properties and incorporates realistic adhesive interactions of WBCs and Pf-parasitized RBCs. The developed model may aid to make realistic predictions of the possible course of the malaria disease, and enhance current malaria treatments.

Chapter 5

Depletion layer and polymer migration in micro- and nano-channels for dilute polymer solutions

5.1 Introduction

Polymer depletion and cross-stream migration phenomena in micro- and nano-channels are important in microfluidic devices and a variety of biological systems. These effects might be relevant in physical processes such as adsorption, lubrication, wall-slip, and polymer transport. Depletion layers arise from steric wall repulsion [43, 13], when a polymer solution is placed in confined geometries. Depletion was observed in the region next to the fluid-solid interface in several experiments [72, 29], and was simulated using various methods including: Monte Carlo (MC) [138, 21, 18], Lattice Boltzmann (LBM) [199, 30], Brownian Dynamics (BD) [30, 112], and Dissipative Particle Dynamics (DPD) [139]. An asymptotic analytical solution [58] of the depletion layer for an ideal chain in the presence of purely repulsive wall predicts depletion to be effective at about of one radius of gyration from the confining surface. Therefore, in micro- and nano-channels the layer is often of the same order as the channel width, and greatly affects the polymer distribution across the channel.

In presence of flow (e.g. Poiseuille, Couette) the polymer migration phenomena changes the polymer distribution across the channel. Several experimental observations [72, 29] show polymer migration from the walls towards the channel centerline. However, simulations [199, 112, 139, 200] showed that polymer migration might proceed towards the walls as well as to the channel centerline. Two models of polymer migration which emphasize the importance of polymer hydrodynamic interactions were recently proposed by Graham et al. [130] and by Usta et al. [200]. The former predicts polymer migration away from the walls and attributes this effect to wall-polymer hydrodynamic interactions and a gradient in chain mobility. The latter states that polymer migration can proceed both away from and to the wall, and is determined by the balance of several effects: hydrodynamic lift, rotation, and drift of the polymer. Recent simulations [199, 30, 112, 139] of polymer migration in Poiseuille flow showed a development of two symmetric off-center peaks (local maxima) in the polymer distribution between the wall and the centerline. These peaks become more pronounced with increasing Peclet or Reynolds number. In contrast, the polymer distribution in Couette flow yielded a single local maximum at the channel centerline. Thus, the presence of two symmetric off-center peaks in pressure-driven Poiseuille flow appears to be related to variable shear rates. The above unresolved issues suggest further investigation.

Here we employ DPD [105, 92] to simulate the depletion layer and polymer migration. We systematically investigate the dependence of wall-polymer depletion on: the polymer model, level of chain representation, solvent quality and relative wall-polymer-solvent interactions. By means of suitable scaling of simulated depletion layers we compare our results to the asymptotic lattice theory solution [58] of depletion near a repulsive wall. Also, we investigate polymer migration in Poiseuille flow, and we offer an argument which attributes polymer migration to wall-polymer hydrodynamic interactions and to the well-known Segre-Silberberg effect [176, 177].

In the next section some details of the polymer models and the boundary conditions in DPD are presented. Section 5.3 contains simulation results for a polymer solution in a channel in the static case (no net flow), while section 5.4 presents migration results for dilute-solution Poiseuille flow at different Peclet and Reynolds numbers. We conclude in section 5.5 with a brief discussion.

5.2 Modeling details

5.2.1 Polymer models

The polymer model in our simulations is based on the well-known linear bead-spring polymer chain representation. Each bead in a polymer chain is subject to three DPD forces mentioned in section 2.2.2 and intra-polymer forces arising from neighboring bead-to-bead interactions. Here we consider flexible chains, so two consecutive segments of a chain have no preferred angle between them. Below we outline two spring laws which define force contributions of bead-to-bead interactions.

1) *FENE spring:* Each pair of particles connected by the Finitely Extensible Non-linear Elastic (FENE) spring is subject to the non-linear potential.

$$U_{FENE} = -\frac{k_s}{2} r_{max}^2 log \left[1 - \frac{|\mathbf{r}_i - \mathbf{r}_j|^2}{r_{max}^2} \right], \tag{5.1}$$

where r_{max} is the maximum spring extension and k_s is the spring constant. When the distance between two connected beads approaches r_{max}, the spring attractive force goes to infinity, and therefore the length greater than r_{max} is not allowed.

2) *Fraenkel spring:* Two connected beads interact through the quadratic potential with a fixed equilibrium length r_{eq}.

$$U_{Fraenkel} = \frac{k_s}{2} \left(|\mathbf{r}_i - \mathbf{r}_j| - r_{eq} \right)^2, \tag{5.2}$$

where k_s is the spring constant. In contrast to the FENE model, this type of spring virtually has no limit on the maximum allowed distance between two beads. However, the minimum of potential energy corresponds to the length r_{eq} which is preferred equilibrium inter-bead distance. Sometimes this model is also called the *harmonic* spring.

5.2.2 Wall boundary conditions

In order to enforce no-slip boundary condition (BC) at the fluid-solid interface we employ the equilibrium BC model with adaptive shear correction (EBC-S) [74]. At the pre-processing stage, the computational domain covers both fluid and solid wall regions and is assumed to be periodic in all directions. The hydrostatic simulation is run until the equilibrium state is reached. In the solid region the particles are then frozen at some instant of time, and later are used to model solid walls in combination with bounce-back reflection at the fluid-solid interface. In addition, we use an adaptive shear procedure illustrated in the figure 5.1. Subregions of the computational domain of width $L = r_c$ adjacent to the fluid-solid interface in both fluid and wall regions are considered. We divide the fluid and wall subregions into bins of height h, whose value determines the accuracy of the near-wall velocity profile. If the velocity profile changes in the direction parallel to the wall these subregions can be divided into bins along the wall. During the simulation, in each bin in the fluid subregion the time-averaged velocity $\mathbf{v}_{av}$ is collected over a specified number of time-steps. The velocities of the particles inside each bin in the wall subregion are set to be opposite, i.e. $-\mathbf{v}_{av}$, to the average velocity in the corresponding fluid subregion bin, which is symmetric with respect to the fluid-solid interface. The wall particles (shown as open circles) do not move in the simulations, and carry only the velocity information needed for the calculation of the dissipative force. A complete description of the BC model can be found in [74].

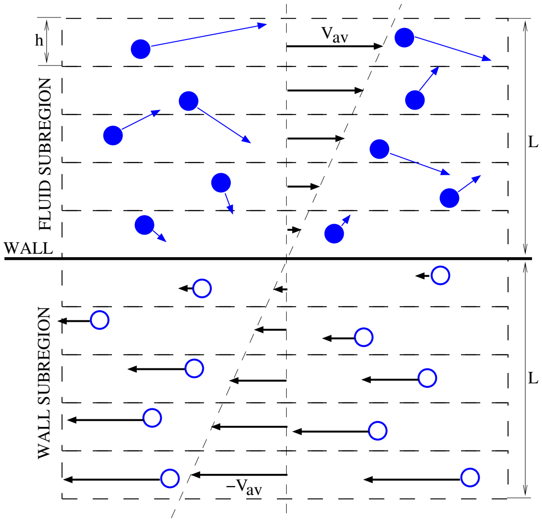

Figure 5.1: The equilibrium boundary condition with shear procedure (EBC-S).

5.3 Confined hydrostatics of dilute polymer solutions

In this section we present results of DPD simulations for the static case of dilute polymer solutions confined between parallel plates separated by gap H in the absence of any imposed flow. Dilute solutions are composed as a single polymer chain immersed in a Newtonian-like fluid solvent. Numerical measurements are taken of the polymer center-of-mass distribution, the bead distribution and the stresses across the channel.

Table 5.1 presents the parameters used in DPD simulations. The number density n of a solution includes solvent and polymer particles. The conservative force coefficients will be specified in text corresponding to a particular simulation. All simulations employed the modified velocity-Verlet integration scheme with $\lambda = 0.5$ [92], which corresponds to the standard velocity-Verlet scheme widely used in Molecular Dynamics simulations. The time step was set to 0.01. Solid walls were placed at $y = 0$ and $y = H$, and modeled by freezing DPD particles at equilibrium in combination with bounce-back reflection at the fluid-solid interface. The number density of the walls was that of fluid. In addition, adaptive shear procedure (EBC-S type) [74] was used in order to enhance dissipative interactions and ensure no-slip condition at the fluid-solid interface. For EBC-S we used a $1 \times 5 \times 1$ bin grid for all walls in order to compute the near-wall velocity profile and mimic a counter flow in the wall region.

n	r_c	γ	σ	k_BT
3	1	4.5	3	1

Table 5.1: DPD simulation parameters. Confined hydrostatics of dilute polymer solutions.

5.3.1 Simulations with several bead-spring models

Employing two different spring models we performed several DPD simulations of a chain in a static solvent in the channel described above. The polymer chain consists of 16 beads. Three sets of simulation parameters are shown in table 5.2, where a_{ss} is the repulsive force coefficient between solvent-solvent particles, a_{pp} - polymer-polymer (beads), a_{ps} - polymer-solvent, and a_{wp} - wall-polymer particles respectively. R_g is the polymer radius of gyration obtained from equilibrium simulations of dilute solution in large enough periodic domain.

spring	k_s	r_{max}	r_{eq}	a_{ss}	a_{pp}	a_{ps}	a_{wp}	R_g
FENE	10	2	N/A	25	25	17.5	17.5	1.6264
FENE	20	2.5	N/A	25	25	17.5	17.5	1.4437
Fraenkel	10	N/A	0.7	25	25	17.5	17.5	1.9207

Table 5.2: Simulation parameter sets for different bead-spring models.

The choice of repulsive interactions defines a polymer solution with good quality solvent, which was pointed out in [117]. The exponent k in equation (2.11) was set to 0.25 that corresponds to the kinematic viscosity of a fluid 0.54, which was obtained using the periodic Poiseuille flow method of [14]. The height of the channel H was set to $3R_g$. In the other two dimensions system is periodic and has a length more than $2H$ in order to ensure no dependence of the results from the domain size. The simulation times were set to allow the chain diffusion distance to be at least $40H$. Furthermore, 32 statistically independent copies (trajectories) of each simulation were run simultaneously on a Blue Gene TACC supercomputer. The combination of trajectories and long enough run times provided us with smooth chain center-of-mass results even though only one polymer chain is present in the simulation domain.

The results revealed that the polymer center-of-mass and the bead distributions across the channel collapse onto one curve for all three simulations. Figure 5.2 shows the center-of-mass distribution (left) and polymer bead distribution (right) for three polymer chains with the distance from the wall normalized by R_g. These and all subsequent distributions are shown over the half channel because of symmetry with respect to the centerline, and hence they have been normalized with area of one half. Thus, it appears that polymer distribution in dilute solution is independent of polymer model used, and is correlated only by a mesoscopic polymer characteristic length such as the radius of gyration or the end-to-end distance.

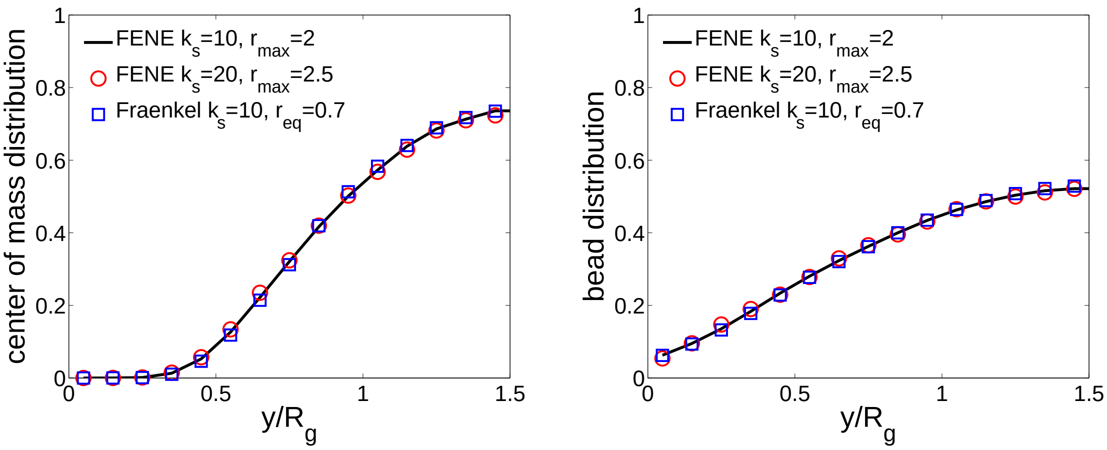

Figure 5.2: Center-of-mass (left) and bead (right) distributions for three $N = 16$ bead chains.

5.3.2 Effect of the solvent quality

Polymers and macromolecules can have dissimilar properties and behavior in different solvents. In fact, polymer characteristics can drastically change depending on the solvent quality. It is well-known that the quality of the solvent exhibits different scaling laws for static and dynamic polymer properties (e.g. R_g, D). Here we performed DPD simulations to identify the effect of solvent quality on the polymer distribution in the channel. We compare ideal chains to FENE chains in both poor and good solvents respectively. For a good solvent, polymer-solvent interactions are energetically favorable resulting in an expansion of polymer chains. For a poor solvent, polymer-polymer interactions are preferred yielding a contraction of polymer chains. Each chain consists of $N = 100$ beads and is placed in a channel of gap $H = 3R_g$. The simulation parameters are summarized in table 5.3. The different spring model for the ideal chain is required due to the absence of DPD repulsive interactions, which for a FENE spring would yield zero equilibrium distance between connected beads because it exerts only attractive force. However, Fraenkel spring exhibits a non-zero equilibrium length explicitly. Furthermore, the results shown in figure 5.2 exhibited no dependence on the spring model. The above parameters are chosen to match the solvent quality as in [117]. The exponent k (eq. 2.11) is set to 1.0, so that kinematic viscosity of the fluid is 0.2854.

spring	solvent	k_s	r_{max}	r_{eq}	a_{ss}	a_{pp}	a_{ps}	a_{wp}	R_g
FENE	good	20	2	N/A	25	25	17.5	17.5	4.7373
FENE	poor	20	2	N/A	25	25	25	25	3.9235
Fraenkel	ideal	10	N/A	0.7	0	0	0	0	3.5691

Table 5.3: DPD parameter sets for solvent quality calculations.

Figure 5.3 shows the center-of-mass distribution (left) and the polymer bead distribution (right) for the ideal (Fraenkel) polymer and FENE chains in poor and good solvents. In contrast to the insensitivity of the distributions to different polymer models (fig. 5.2), solvent quality has an effect on the polymer distribution. The ideal chain exhibits larger wall depletion (more confined distribution around the center) compared to chains in good and poor solvents. A good solvent yields the smallest wall depletion and poor solvent curve falls in-between good solvent and ideal chain. The wall depletion force on a chain is

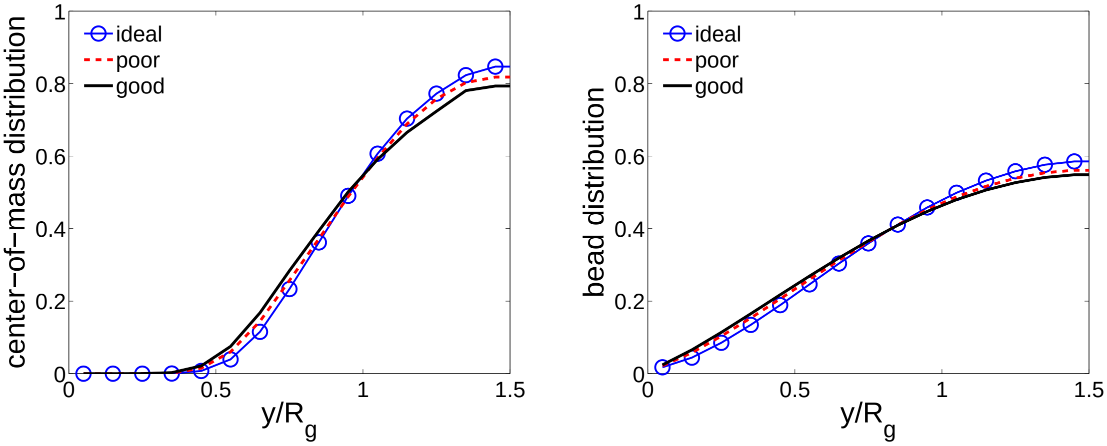

Figure 5.3: Effect of the solvent quality on the center-of-mass (left) and bead (right) distributions for $N = 100$ chains.

expected to be repulsive due to the cost in free energy for the loss of the available polymer configurations near the wall. Furthermore, the depletion potential and resulting wall force are weaker for chains with excluded volume (EV) interactions (good solvent) than for ideal chains as theoretically predicted by Schlesener et al. [170], where they concluded that EV interactions effectively reduce the depletion effect. As a result we observe larger wall depletion for ideal chains. This is illustrated by the pressure distribution across the slit. Figure 5.4 shows the excess pressure distribution in the channel with the virial contribution of pair interactions and without the inter-bead spring forces. Hence, only wall-polymer and solvent-polymer interactions contribute to the wall depletion. The excess pressure is obtained by subtraction of the equilibrium pressure in a large box. The pressure gradient for the ideal chain as we approach the wall from the centerline is larger than that of poor and good solvent. The larger pressure difference drives the polymer further away from the wall and contributes to larger wall depletion. The least pressure gradient and thus the smallest wall depletion was found for the good solvent case.

For complete analysis of the results we compute average polymer lengths in all three directions (x, y and z) across the channel which characterize relative polymer shapes in the slit. We define local radius of gyration depending on the distance from the wall y as

$$R_g(y) = \left[(R_g^x(y))^2 + (R_g^y(y))^2 + (R_g^z(y))^2\right]^{\frac{1}{2}}, \tag{5.3}$$

where $R_g^x(y) = \left\langle \frac{1}{N}\sum_{i=1}^{N}(x_i - x_{cm}(y))^2 \right\rangle$, $\langle\cdot\rangle$ denotes time averaging, x_i are bead coordi-

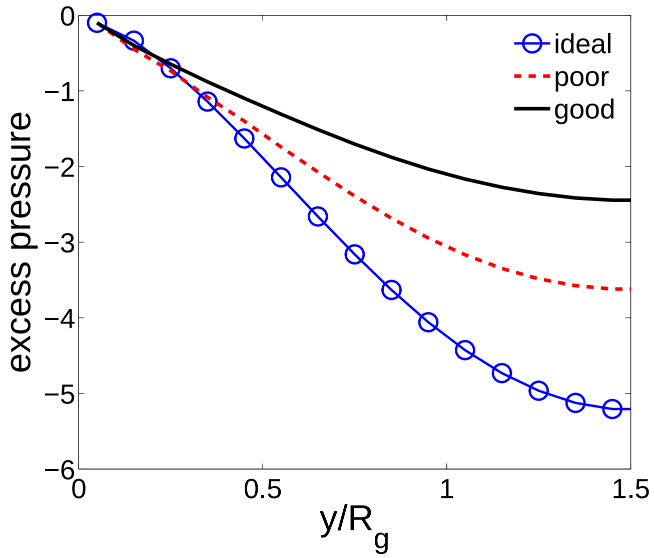

Figure 5.4: Excess pressure across the channel for $N = 100$ bead chain in solvents of different quality.

nates in the x-direction, and $x_{cm}(y)$ is the center of mass at y. $R_g^y(y)$ and $R_g^z(y)$ are defined analogously. Figure 5.5 presents the local radius of gyration normalized by the unconfined R_g (left) and the ratio of $R_g^x(y)$ and $R_g^y(y)$ (right) which identifies the relative polymer shape across the channel. The left-hand plot in the figure 5.5 shows that when confined in a slit

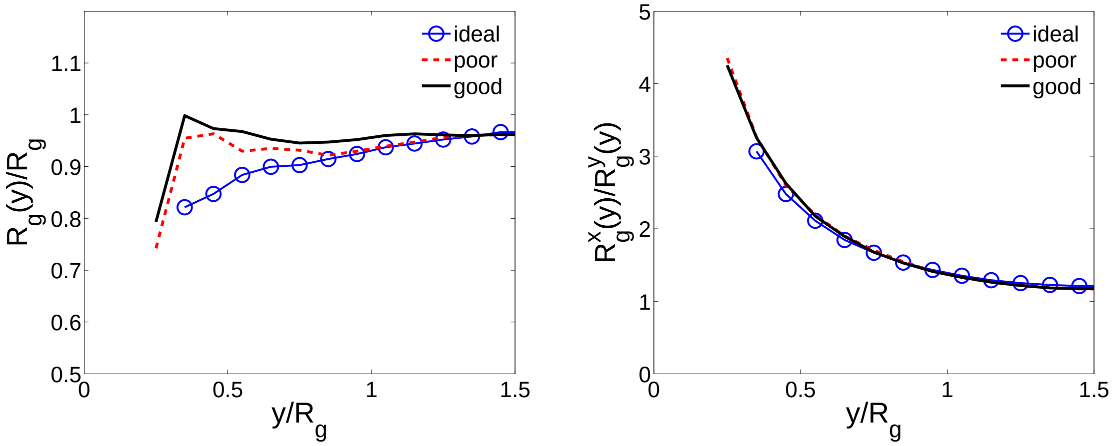

Figure 5.5: Local radius of gyration (left) and relative shape of the polymer (right) for $N = 100$ bead chain in solvents of different quality.

the polymer occupies a volume slightly smaller than it would in the unconfined state, and that the chain takes on a more compact volume as it approaches the wall. The right-hand plot of figure 5.5 shows that during the approach to the wall the chain elongates in the x- and z-directions relative to the y-direction, and that its shape is nearly independent of solvent quality. As expected by symmetry $R_g^z(y)$ was found to be statistically identical to $R_g^x(y)$.

5.3.3 Wall-polymer-solvent interactions

In the simulations presented above wall-polymer and solvent-polymer interactions were identical. These are neutral walls for which no explicit adsorption or repulsion is expected. However, real walls are known to induce adsorption or repulsion (electrostatic) of polymers. A manipulation of relative wall-polymer-solvent interactions enables us to explicitly introduce net-attractive or repulsive wall forces on the polymer. This might correspond to adsorption and repulsion respectively, but it requires further investigation. To this end, a polymer of $N = 25$ beads in a good solvent was placed in a slit of gap $H = 3R_g$. The simulation parameters are summarized in table 5.4. Figure 5.6 presents the center-of-mass (left) and the bead (right) distributions for both neutral and repulsive walls. These results are compared to the center-of-mass distribution obtained by Usta et al. in [199] using the LBM method for an $N = 16$ bead chain in a channel also of gap $H = 3R_g$. The repulsive wall exhibits larger depletion compared to neutral wall. Since the results of Usta et al. [199] fall between the neutral and the repulsive curves they correspond to a slightly repulsive wall. To verify that the boundary condition model (EBC-S) does not introduce extraneous effects, we have run analogous simulations using periodic BC's. Here, the computational domain is doubled in y-direction to give a gap of $2H = 6R_g$. The left half contains polymer solution confined between two parallel reflective walls at $y = 0$ and $y = H$, and the right half is filled with the solvent. The system is set to be periodic in y-direction. Such a setup corresponds to a perfectly neutral wall with no extraneous effects. The results were found to differ by no more than the statistical error.

spring	wall	k_s	r_{max}	a_{ss}	a_{pp}	a_{ps}	a_{wp}	R_g
FENE	neutral	10	2	25	25	17.5	17.5	2.1903
FENE	repulsive	10	2	25	25	17.5	25	2.1903

Table 5.4: DPD parameter sets used in wall-polymer-solvent interaction calculations.

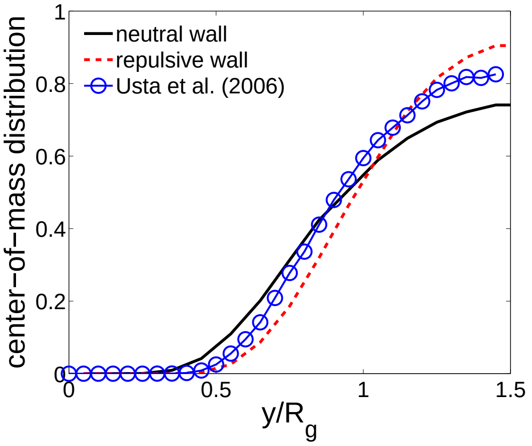

Figure 5.6: Effect of wall-polymer-solvent interactions on the center-of-mass (left) and bead (right) distributions for a $N = 25$ bead chain.

5.3.4 Effect of the channel width

To this point we have presented results for channels of fixed gap $H = 3R_g$. In this section the effect of channel width on the wall depletion layer is investigated with simulations of a $N = 16$ bead chain confined in slits having gaps of $H = 3R_g$, $4R_g$, $5R_g$, and $8R_g$, and with the parameters shown in table 5.5. Figure 5.7 presents the center-of-mass distribution of the simulated polymer confined in channels with gaps listed above. It also includes center-of-mass distributions normalized by their maximum magnitude c_{max} (correspondence is shown by arrows). For all channel widths the normalized distributions collapse onto a single curve which clearly demonstrates that the wall-polymer depletion region reaches no further than about $2.5R_g$. Consistency of this conclusion is tested by plotting the local radius of gyration normalized by the unconfined R_g and the ratio of components $R_g^x(y)$ and $R_g^y(y)$. Figure 5.8 shows that beyond a distance of about $2.5R_g$ both the local size (left) and the shape (right) of the polymer are unaffected by the wall.

spring	k_s	r_{eq}	a_{ss}	a_{pp}	a_{ps}	a_{wp}	R_g
Fraenkel	10	0.7	25	25	17.5	17.5	1.9207

Table 5.5: Simulation parameters for the channels of various gaps.

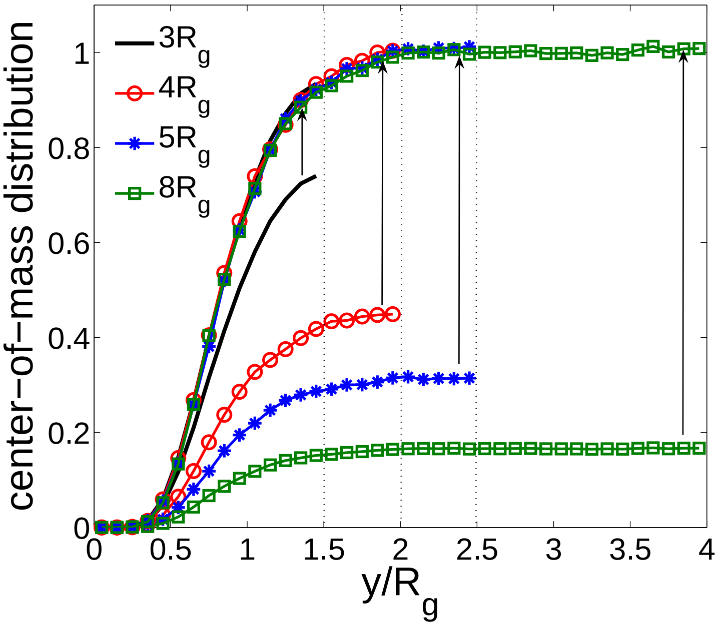

Figure 5.7: Influence of gap size on the center-of-mass distribution for a chain of $N = 16$ beads.

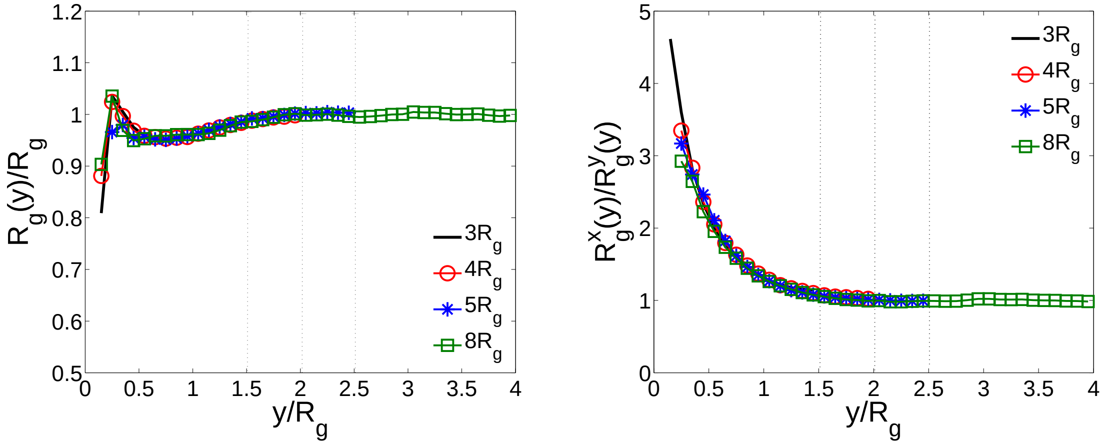

Figure 5.8: Local radius of gyration (left) and relative shape (right) for a chain of $N = 16$ beads for various gaps.

5.3.5 Effect of the number of monomers N

Many theoretical results in polymer physics are asymptotic in the limit of large bead number N. Examples are the scaling laws for the radius of gyration and for the diffusion coefficient. To test the level of chain representation on the depletion layer we performed simulations for a set of chains having bead numbers $N = 16$, 25, 100, and 500 in a channel of gap $H = 3R_g$, and with the parameters shown in table 5.6.

spring	k_s	r_{max}	a_{ss}	a_{pp}	a_{ps}	a_{wp}
FENE	10	2	25	25	25	25

Table 5.6: DPD parameters used in bead number effect simulations.

Figure 5.9 shows the calculated center-of-mass distributions for this set of chains, and also the LBM results for $N = 16$ in a channel of the same gap by Usta et al. [199]. The gap dimensions for the simulations discussed above assumed the appropriate characteristic length to be the unconfined R_g. An alternative length scale, independent of molecular concepts, is derivable from concentration distributions such as those of figure 5.9. This depletion layer thickness δ is defined as,

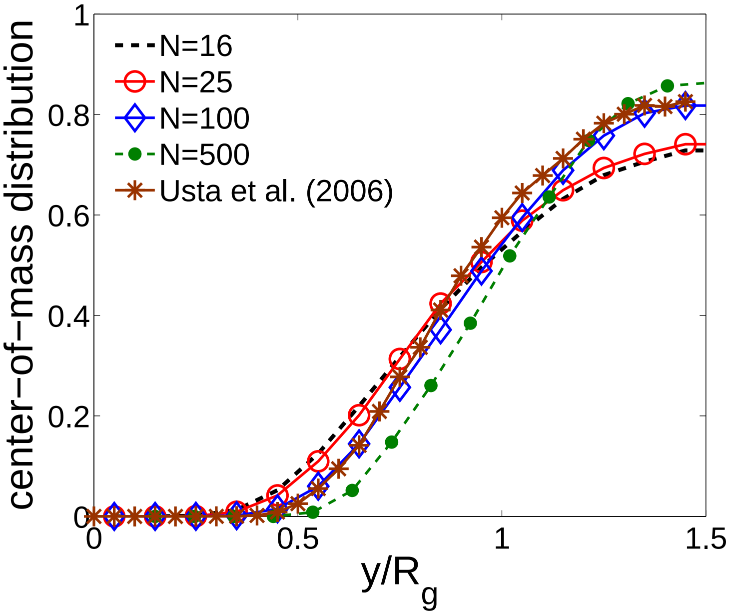

Figure 5.9: Effect of bead number N on the center-of-mass distribution in a slit of $H = 3R_g$.

$$\frac{\delta}{R_g} = \int_0^{\infty} (1 - \frac{c(z)}{c_{max}}) dz, \tag{5.4}$$

where $z = \frac{y}{R_g}$, $c(z)$ is the center-of-mass distribution and $c_{max} = max_{z \geq 0}[c(z)]$. From the distributions of figure 5.6 equation (5.4) yields $\frac{\delta}{R_g} = 0.837$ for the neutral wall, $\frac{\delta}{R_g} = 0.954$ for the repulsive wall, and for Usta et al. [199] $\frac{\delta}{R_g} = 0.868$.

Longer chains are subject to a stronger depletion effect measured as a larger depletion layer thickness. Thus, it appears that when the allowable configuration space is restricted to be a half-space the longer chains suffer a larger loss in free energy and are subject to larger steric depletion forces. However, the analytical solution of [58] for ideal chains assumes the center-of-mass distribution will converge to an asymptotic curve as N becomes very large. In the figure 5.10 the center-of-mass distributions, normalized by their maximum values c_{max}, for different bead numbers are compared with the asymptotic analytical solution. In the left-hand plot the distance from the wall is normalized by the equilibrium value of the radius of gyration R_g, and in the right-hand plot by the depletion layer thickness δ. The LBM results [199] are for an $N = 16$ bead polymer in a channel of width $H = 5R_g$. The curves in figure 5.10 show that, with lateral shifting, the numerical models closely capture the functional forms of the analytic solution, and that the depletion layer thickness provides the means for shifting the numerical distributions onto the analytic solution to produce an almost common curve. The agreement is remarkable since the numerical model features solvent explicitly represented by DPD particles whereas in the lattice model the solvent is implicit. Figure 5.10 (left) shows that, as expected, the shorter chains have distributions closer to the wall, and that as N goes from 100 to 500 the discrepancy between the numerical and the analytic distribution becomes vanishingly small. For the latter the small discrepancy may be due to the solution having been carried out with a poor solvent condition, which as previously noted slightly weakens the depletion. The LBM curve has the largest discrepancy probably due to the relative wall-polymer-solvent interactions mentioned in section 5.3.3

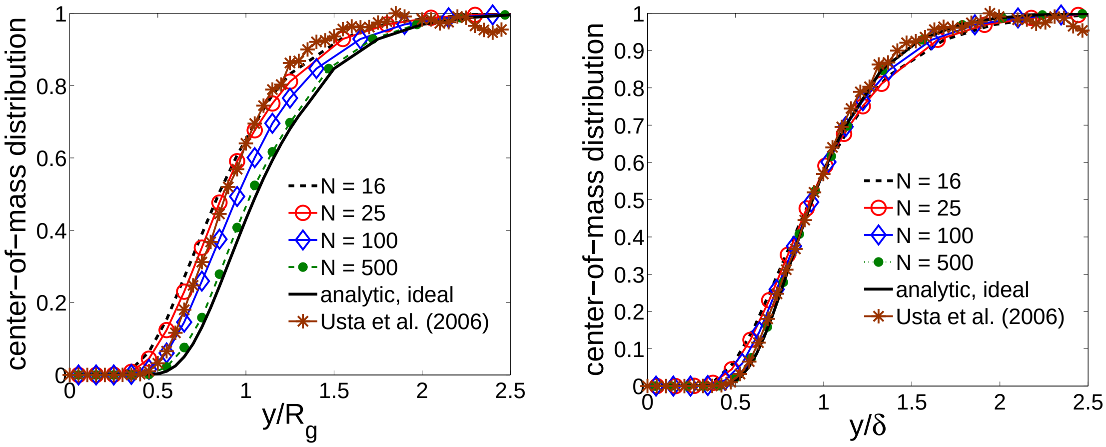

Figure 5.10: Normalized center-of-mass distributions for different bead numbers compared with the analytical solution. The wall distance y is normalized by the unconfined R_g (left) and depletion layer thickness δ (right).

and its small bead number N. In addition, our results agree well with the depletion layers calculated from Monte Carlo simulations by Berkenbos et al. [18] for tubes. They also investigated the limit of very small tubes, where the confinement greatly restricts the chain configurations. These distributions no longer resemble those in Figures 5.7 and 5.10.

For the same simulations figure 5.11 presents the local $R_g(y)$ normalized by its unconfined value (left) and the ratio of $R_g^x(y)$ and $R_g^y(y)$ (right). That the longest chains have the smallest normalized local $R_g(y)$ suggests that in the slit they adopt a more close-packed form than their smaller counterparts even though their relative shapes are about the same.

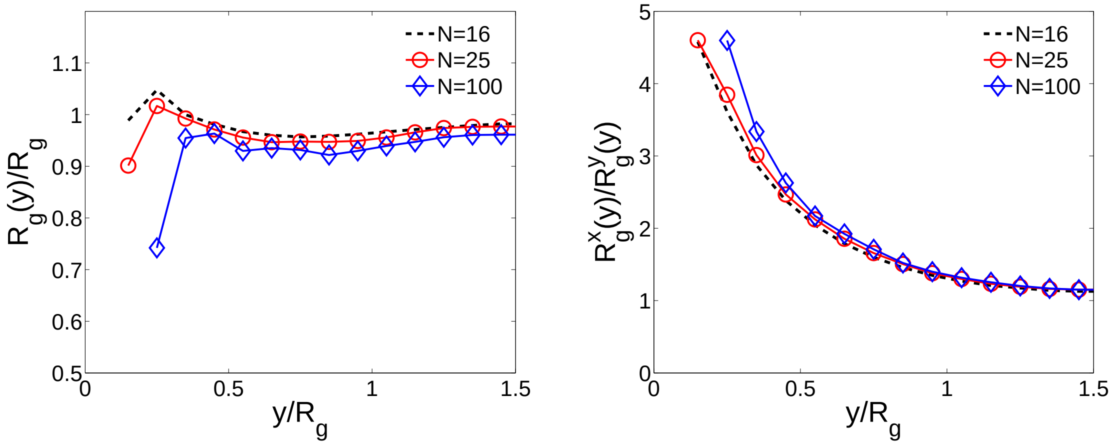

Figure 5.11: Local radius of gyration (left) and relative shape (right) of the polymer for various N.

5.4 Polymer dynamics in Poiseuille flow

This section results are presented for the Poiseuille flow of dilute polymer solutions confined between parallel plates separated by gap H. The Poiseuille flow is driven by a uniform pressure gradient as a force applied equally to both polymer and solvent DPD particles. Following [199] dynamic effects of the flow will be interpreted primarily with the Peclet number (Pe) defined as

$$Pe = \dot{\gamma}\frac{R_g^2}{D} = 4ScRe\frac{R_g^2}{H^2}, \tag{5.5}$$

where $\dot{\gamma} = 2V_c/H$ is the mean shear rate, V_c is the centerline velocity, and D is the polymer center-of-mass diffusion coefficient measured in equilibrium. The Schmidt number (Sc)

and the channel Reynolds number (Re) are defined respectively by

$$Sc = \frac{\nu}{D}, \qquad Re = \frac{V_c H}{2\nu} = \frac{\dot{\gamma} H^2}{4\nu}. \tag{5.6}$$

The discussion below invokes other Reynolds numbers based on the radius of gyration (Re_g) and Stokes-Einstein radius r_b [193] of a polymer bead (Re_b) which can be defined respectively as

$$Re_g = \frac{\dot{\gamma} R_g^2}{\nu}, \qquad Re_b = \frac{\dot{\gamma} r_b^2}{\nu}. \tag{5.7}$$

In some works [30, 112], Poiseuille flow results are interpreted in terms of the Weissenberg number $Wi = \tau\dot{\gamma}$, where τ is derived from the long-time relaxation of the stretched polymer chain in a stagnant solvent. Since both D and τ are derived from equilibrium data they differ by at most a constant for a given chain. Furthermore, Wi can be expressed as a product similar to equation 5.5 with Sc replaced by $\tau\nu/R_g^2$, which is also a purely material property.

5.4.1 Velocity profile

The Poiseuille velocity profile between walls placed at $y = 0, H$ for a Non-Newtonian fluid with a power-law shear-viscosity is given by

$$V(y) = V_c \left[1 - \left(\frac{y - H/2}{H/2} \right)^{1+\frac{1}{p}} \right], \qquad V_c = \frac{p}{1+p} \left(\frac{\rho f}{\kappa} \right)^{\frac{1}{p}} \left(\frac{H}{2} \right)^{1+\frac{1}{p}}, \tag{5.8}$$

where p is the power-law index, f the uniform driving force per unit mass, κ the power-law shear-stress coefficient and ρ the mass density.

Figure 5.12 shows velocity profiles for an $N = 100$ bead-chain solution in a gap of $3R_g$ at $Pe = 50$, 100, and 200. The calculated velocity profiles of the suspension are well-described by the power law (eq. 5.8) with $p = 0.88$. The dashed curves are the corresponding Newtonian profiles for $p = 1$. The average velocity of the particles within a slice Δy of the gap is assigned to be the local continuum velocity at the slice center. Hence continuum wall-velocities cannot be calculated directly. However, as expected from the particle boundary conditions, there appears to be no slip at the wall since nearby velocities extrapolate to zero within statistical error. The Re, Re_g and Re_b numbers scale linearly with Pe, and for the flow of $Pe = 200$ they are $Re = 39.49$, $Re_g = 17.55$, and $Re_b = 0.055$ respectively, where

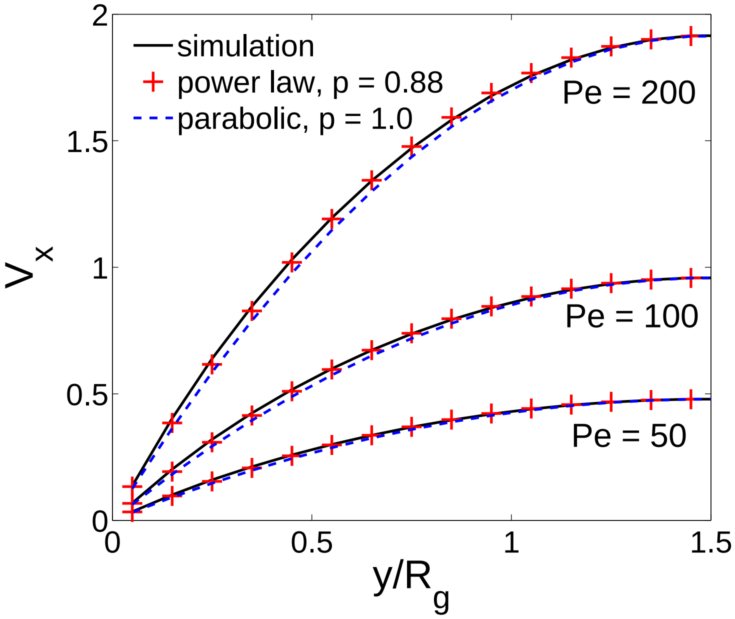

Figure 5.12: Poiseuille velocity profiles for several Pe's, $N = 100$.

$R_g = 3.9235$, $r_b = 0.22$, and $\nu = 0.2854$.

5.4.2 Polymer migration

In addition to the hydrostatic depletion already presented, Poiseuille flow gives rise to further cross-flow migration of the polymer. This dynamic migration was investigated with a chain of $N = 16$ beads with the parameters shown in table 5.7. The solvent viscosity for all cases is $\nu = 0.54$.

spring	k_s	r_{max}	a_{ss}	a_{pp}	a_{ps}	a_{wp}	R_g
FENE	10	2	25	25	25	25	1.36205

Table 5.7: Simulation parameters used in polymer migration calculations.

The simulations were performed at Pe numbers of 50, 100, and 200 for several channels. Figures 5.13, 5.14, and 5.15 correspond to the gap widths $H = 3R_g$, $5R_g$, and $8R_g$ respectively, and display the effect of the Pe and the Re numbers on the the results for: i) the center-of-mass distributions, ii) chain conformation distributions imaged by computation of the three components of the local radius of gyration $R_g^x(y)$, $R_g^y(y)$, $R_g^z(y)$ normalized by their equilibrium components $R_g/\sqrt{3}$. In the figures the mean of the distribution is displayed as a horizontal line.

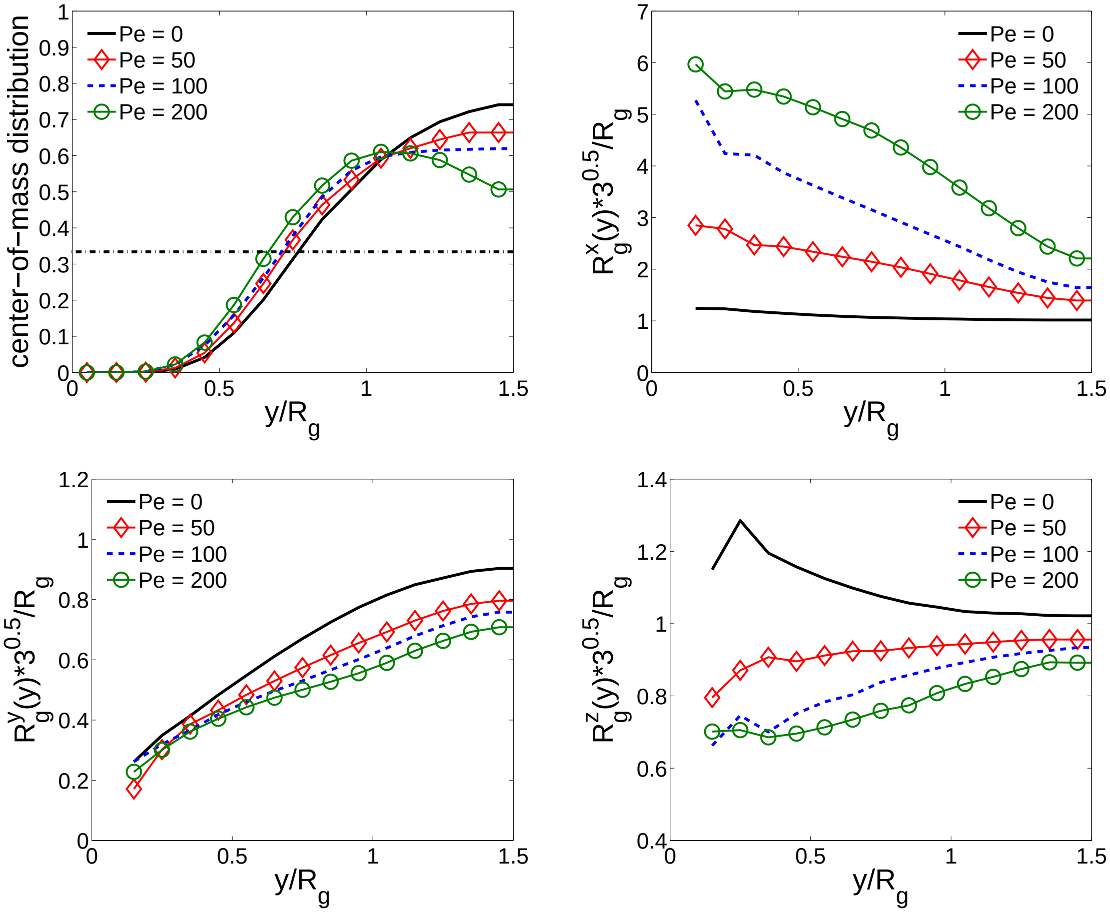

Figure 5.13: Polymer center-of-mass (upper left) and conformation distributions of R_g^x (upper right), R_g^y (lower left) and R_g^z (lower right) in Poiseuille flow, $N = 16$, $H = 3R_g$.

The center-of-mass distributions of figures 5.13, 5.14, and 5.15 respectively show the dynamic depletion layer to be steadily reduced relative to the hydrostatic case as Pe is increased, and that the effect is strongest for the smallest gap. In contrast, migration of polymer from the centerline towards the walls becomes more pronounced as the gap size increases, and between $Pe = 100$ and 200 the significant development is a distribution with two off-center peaks, which is consistent with previous work [199], and similar results obtained by various other methods were reported in [30, 112, 139, 200]. Factors contributing to cross-stream migration are listed by Usta et al. [200] as lift, rotation, stretching and drift of the polymer from the wall. Graham et al. [112] attribute migration to two effects: chain-wall hydrodynamics, and chain mobility gradients due to different conformations such as a stretched chain. The R_g-distributions show the chain to be strongly stretched in the flow

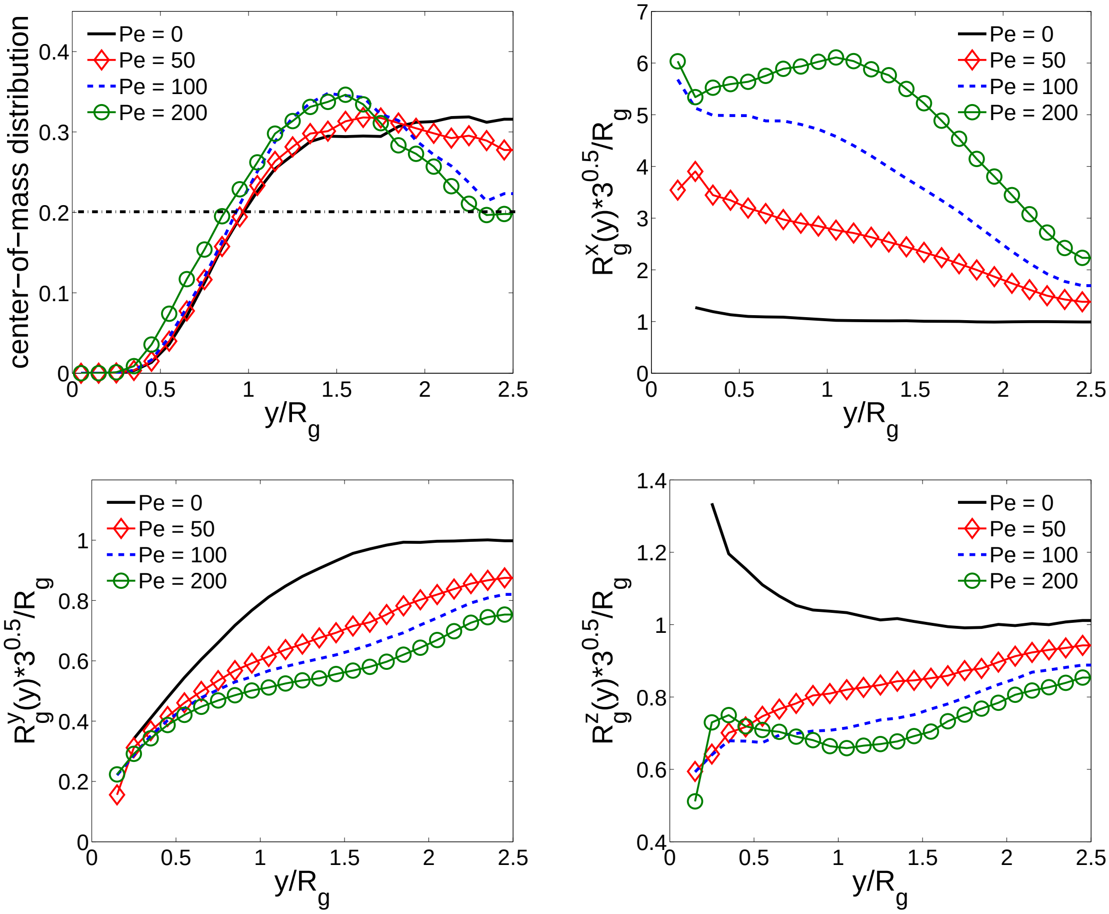

Figure 5.14: Polymer center-of-mass (upper left) and conformation distributions of R_g^x (upper right), R_g^y (lower left) and R_g^z (lower right) in Poiseuille flow, $N = 16$, $H = 5R_g$.

direction x when subjected to high shear rates. In view of the hydrostatic preference for the centerline region it seems counter-intuitive that a chain prefers to occupy the region of higher shear rates away from the centerline with its vanishing shear rate. It is plausible to attribute the forces which drive the chain away from the center to be similar to those that control the effect of Segre&Silberberg in which [176, 177] a neutrally-buoyant rigid sphere or ellipsoid [168] in a channel will migrate to an equilibrium position between wall and centerline due to the combined hydrodynamic effects of wall-particle interactions, velocity profile curvature and shear forces. The components of R_g show that, on average, the confined chain resembles an ellipsoid when viewed as an entity. However, flexibility and elasticity are not included explicitly in the Segre-Silberberg analysis although these factors are implicit in the definition (5.5) of the Peclet number. An alternative view is the chain as an ensemble of connected point-particles where each behaves as a sphere with a Stokes-Einstein radius [193], and

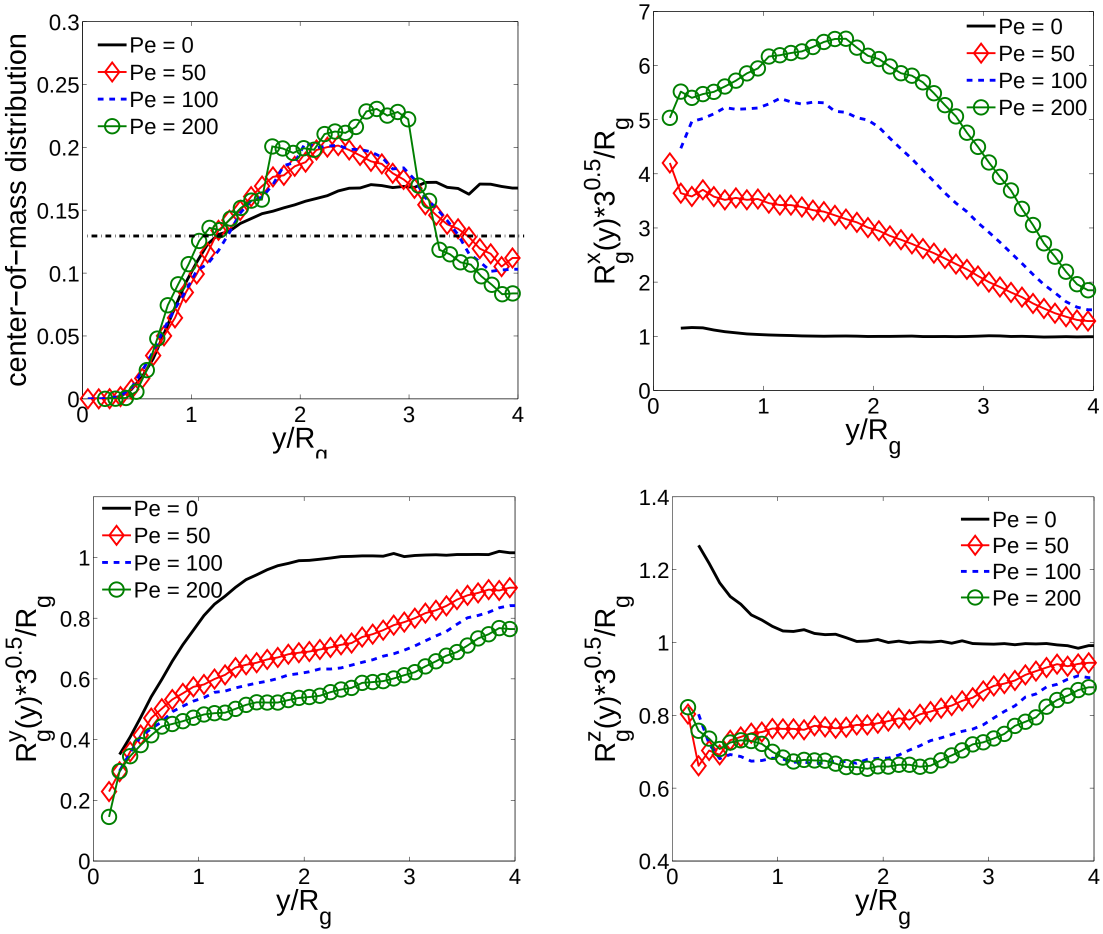

Figure 5.15: Polymer center-of-mass (upper left) and conformation distributions of R_g^x (upper right), R_g^y (lower left) and R_g^z (lower right) in Poiseuille flow, $N = 16$, $H = 8R_g$.

therefore is subject to the Segre-Silberberg forces. As reported in [201, 75] the Segre-Silberberg effect for a suspension of particles strongly depends on the ratio of particle size to the channel width and Reynolds number of the flow based on the particle size. For the case of $Pe = 200$ we have Re number in the range $28.4 - 201.2$ for the gaps $3R_g - 8R_g$, and $Re_g = 12.6$, $Re_b = 0.33$ respectively. In our simulations the Re numbers are in the range of those given in [75], where results for Poiseuille flow predict particle migration to a stable position in-between the wall and the centerline. This appears to support our interpretation of the above results as the Segre-Silberberg effect. The results are qualitatively similar for the three channels. However, wall-molecule interactions appear to be a determining factor for the polymer distribution in small channels ($H \simeq 3R_g$). Wall-polymer repulsive forces are dominant within a layer of about $2.5R_g$, and therefore in small slits the development of the off-center peaks in the distributions is observed only for relatively high Pe number when Segre-Silberberg forces are able to overwhelm wall steric repulsion. In contrast, for larger channels ($H \gtrsim 5R_g$) the off-center peaks in the polymer distributions appear at lower Pe, because wall-polymer forces act only within a near-wall layer and may not be present in the centerline region where shear forces have a migration effect. In addition, the distribution peaks coincide approximately with the maximum stretch ($\max\{R_g^x\}$, $\min\{R_g^z\}$) of the chain in the streamwise direction. The scatter in the distribution data clearly increases with channel size. This statistical defect for wider channels is a consequence of more expensive calculations for larger particle systems and longer times required for a chain to migrate a number of times across the slit.

The above argument suggests that polymer migration is characterized by at least three numbers: Pe, Re and R_g/H. In the presence of inertia ($Re > 0$) the Segre-Silberberg effect is to be expected, and this is in accord with the relatively high Re number cases presented above. Graham et al. [30] used the Brownian dynamics (BD) method to show ever increasing polymer migration towards the channel centerline with increasing Pe or Wi, where hydrodynamic inertia effects are excluded by use of only Stokes interactions for which the Segre-Silberberg effect vanishes. In particular, Stokes hydrodynamics accounts for very strong wall-polymer interactions. However as Wi increases, the channel Reynolds number must also increase. Analysis with linearized inertia, (time dependent [98] (p. 354), Oseen [22]) suggests that as inertia increases from zero the typical leading Stokes-interaction in the reciprocal distance is continuously replaced by the first-order inertial term typical of the unbounded case. This transition would appear to mark the inception of the Segre-Silberberg effect. The complexity of bead-spring suspensions does not permit 'a priori' estimates of this Re range, but the Re values actually realized are germane to an assessment of the effect in [30]. To this end we have performed a number of DPD simulations with greatly reduced Re number. A 16-bead polymer solution having viscosity $\nu = 14.019$ confined in the channel of $H = 3R_g$ is subject to Poiseuille flow at $Pe = 50$, 100 and 200. For $Pe = 200$ we have $Re = 0.041$, $Re_g = 0.018$, and $Re_b = 4.66 \times 10^{-4}$, respectively. Figure 5.16 shows the center-of-mass distribution and chain conformations. The center-of-mass distributions of figure 5.16 differ only slightly from the hydrostatic case, in accord with the often-used description of low Re flow as 'quasi-static'. In contrast, the chain conformations resemble those at high Re shown in figure 5.13 for the same H/R_g rather than the hydrostatic

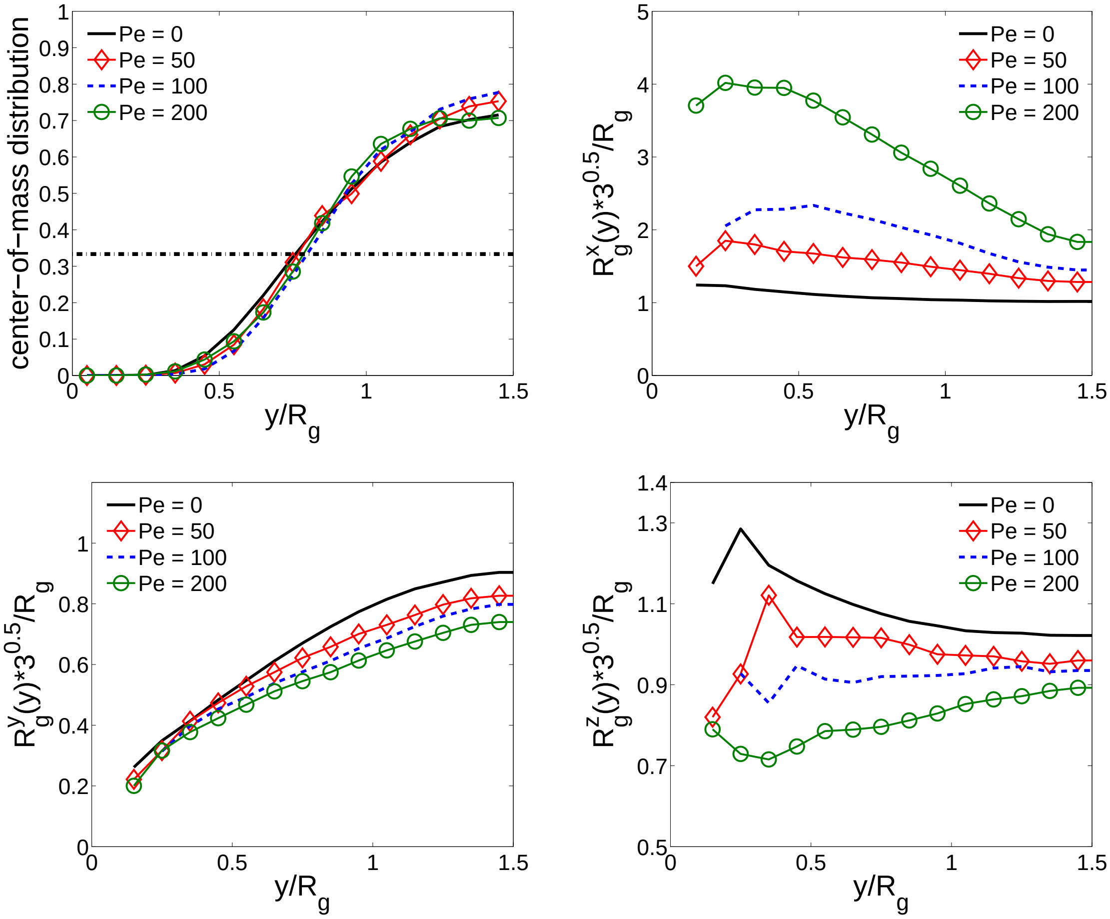

Figure 5.16: Polymer center-of-mass (upper left) and conformation distributions of R_g^x (upper right), R_g^y (lower left) and R_g^z (lower right) in Poiseuille flow, $N = 16$, $H = 3R_g$. Low Re number.

conformations of figure 5.8. Unfortunately, the BD results of Graham et al. [30] do not include the hydrostatic case which would provide a critical comparison with our results. For $Pe < 100$ polymer migration proceeds towards the channel centerline which suggests the dominance of wall-polymer interactions. However, as $Pe \rightarrow 200$ the center-of-mass distribution indicates a slight polymer migration away from the centerline which suggests that the Segre-Silberberg forces have become comparable with wall-polymer interactions. Moreover, evidence for the Segre-Silberberg effect at low Re number is provided by the perturbation theory of [201], the simulations of [75] and the experiments of [52]. In conclusion, the results of this work indicate that polymer migration is governed by the Pe, Re and R_g/H numbers which characterize wall-polymer interactions and the Segre-Silberberg effect. However, when $Re \rightarrow 0$ (approximately $O(10^{-3})$) the Segre-Silberberg effect is negligible and polymer migration is then governed only by Pe and R_g/H, in accord with [30, 112].

Other results, not included here, indicate that polymer migration in Poiseuille flow is independent of the segment spring model (FENE and Fraenkel), and is governed almost entirely by the three numbers mentioned above which incorporate the characteristic polymer length and time scales (eq. 5.5 and 5.6). However, we expect that increasing the number of beads in a chain will alter chain-wall interactions which this work has shown to affect migration. The hydrostatic results (fig. 5.10) suggest that for large enough N the migration effect should be independent of the chain representation. However, even in the static case 500-bead chains were subject to the statistical difficulties mentioned above, and reliable results will be even more expensive to attain in the dynamic case.

The effect of solvent quality on migration is investigated with the 16-bead chain employed above in the channels with gaps of $H = 3R_g$ and $4R_g$ for $Pe = 50$ and 100. Figure 5.17 shows the center-of-mass distribution for solvents of different quality. Results predict

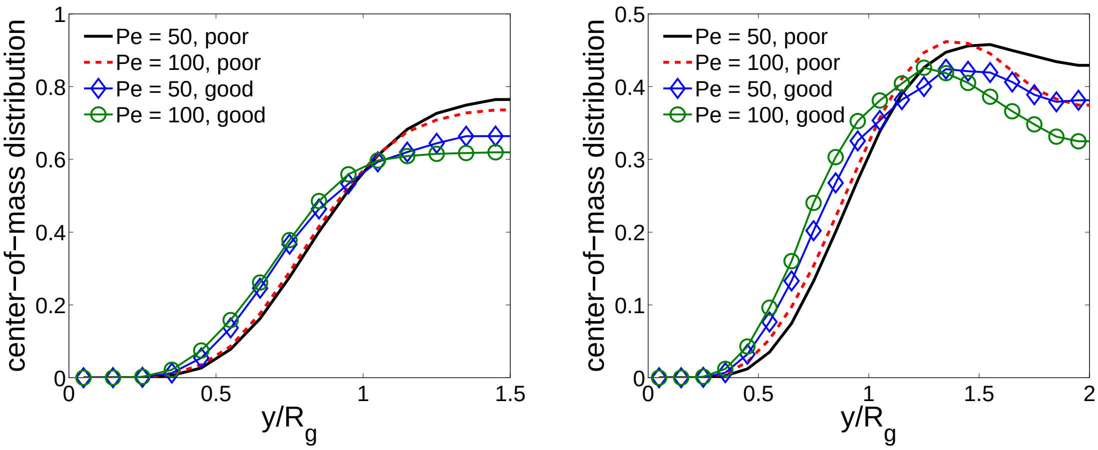

Figure 5.17: Influence of solvent quality on center-of-mass distributions for $Pe = 50, 100$, $H = 3R_g$ (left) and $H = 4R_g$ (right).

stronger migration away from the centerline for good solvents than poor solvents. We attribute this to weaker wall depletion of polymers in good solvents as was pointed out in section 5.3.2 for the static case, and potentially stronger Segre-Silberberg effect due to the larger volume taken up by chains in good solvents compared to the more compact, less swollen, shape in poor solvents. As in the results of figures 5.13, 5.14, 5.15 and 5.16 the migration effect in smaller channels is attenuated by the stronger chain-wall interactions.

5.5 Summary

For dilute polymer solutions in narrow channels we have investigated the hydrostatic depletion near walls for several bead-spring models, channel widths, number of beads, solvent quality and wall-polymer-solvent interactions. The channel width was varied from 3 to 8 times R_g, the unconfined polymer radius of gyration. The center-of-mass and bead distributions and polymer shape measured by the components of the local radius of gyration were found to be independent of the bead-spring model used in the simulations. Wall depletion and polymer shapes were found to be similar for channel gaps $H \gtrsim 3R_g$, and indeed distributions for all channel gaps collapse onto a single curve by normalization with the maximum concentration c_{max}, when other variables are fixed. The chain length specified with bead number N in the chain representation affects the depletion layer with short chains having narrower depletion layers than longer ones. However, as N becomes large ($N \gtrsim 500$) the depletion layer is independent of N, and the polymer distribution across the channel converges to the lattice-theory solution for ideal chains near a purely repulsive wall. By scaling the distance from the wall with δ, an integral measure of depletion layer thickness (eq. 5.4), the center-of-mass distributions for all N can be collapsed onto the lattice-theory asymptotic solution. Thus with appropriate scaling distributions for $N \sim O(10)$ adopt the shape of that of the very long, flexible chains of the lattice theory.

However, when a chain is immersed in a solvent of different quality its depletion layer properties change. A good solvent yields a thinner depletion layer than does a poor solvent, and by comparison the ideal chain has the strongest wall depletion. Finally, relative wall-polymer-solvent interactions or simply polymer boundary conditions also have a strong effect on the depletion layer. Potentially these interactions could be combined to control the depletion layer thickness and to model a wall adsorption.

In the dynamic case of Poiseuille flow we found that dilute polymer solutions exhibit slightly Non-Newtonian behavior with velocity profiles corresponding to a power law index of $p = 0.88$ (eq. 5.8). The hydrostatic depletion layer is affected by the flow, but beyond about a distance of $\delta \sim O(1)$ the center-of-mass distributions exhibit with increasing Pe and Re numbers ever stronger indications of migration toward an intermediate position between wall and centerline. At high enough Pe number Poiseuille flow induces in the distributions the new feature of two off-center peaks which correspond to the most probable channel positions. Simultaneously the chains tend to stretch out in the direction of the shear planes. Thus, chains prefer an intermediate position between wall and centerline and not the middle of the channel where the shear rate vanishes. We attribute this to the hydrodynamic Segre-Silberberg effect which forces spheres and ellipsoids away from the centerline due to the shear gradient in Poiseuille flow. At high enough Re when hydrodynamic forces prevail over Brownian fluctuations the quasi-stable polymer position in the channel appears to be determined by the balance of the wall-polymer hydrodynamic interactions and forces arising from Segre-Silberberg effect. In case of low enough Re number when the Segre-Silberberg effect becomes negligible polymer migration is governed by Pe number and proceeds mostly to the channel centerline due to wall-polymer interactions. We have shown that polymer migration is independent of the bead-spring model. However, the quality of the solvent, polymer boundary conditions, and the number of beads in the chain, all affect polymer migration in the slit. We expect no dependence on number of monomers for large enough N. Finally, two off-center peaks in the distribution develop at lower Pe in the larger channels which is consistent with the known interaction length of several R_g for wall-polymer depletion. Hence the migration effect is more pronounced in the channels of larger widths.

Chapter 6

Reverse Poiseuille flow - a virtual rheometer for complex fluids

6.1 Introduction

Particle models of complex fluids create the need for methods to calculate the simulated equivalents of the physical properties commonly measured in rheometers. The simulated and the measured properties can then be matched to calibrate the model's parameters. This operation is of great importance especially in mesoscopic simulations, where coarse-graining in space and time replaces known atomistic interactions with soft-type interactions among coarse entities each of which contains a possibly large number of atoms or molecules. For models of Newtonian fluids various methods have been employed for the calculation of viscosity and other transport coefficients, but for complex fluids not all of these methods are suitable or sufficiently accurate. Therefore, an efficient virtual rheometer is required to calculate macroscopic rheological properties of simulated complex fluids in a form suitable for convenient matching to the measured properties of experimental rheometry.

There are several virtual rheometers used in particle simulations to obtain shear properties, e.g, the plane Couette flow with Lees-Edwards periodic boundary conditions (LEC) [124], the Green-Kubo (G-K) relations [178, 102]. The periodic boundary conditions of LEC eliminate the need for explicit modeling of solid wall boundary conditions. This has the significant advantage of excluding unknown wall-effects, such as slip and density fluctuations, which seem to be endemic to *all* particle-wall models as they are currently known. However, since one LEC simulation yields data for only a single shear rate, it is computationally expensive, and therefore inefficient, because rheological properties are needed over a wide range of shear rates. On the other hand, the G-K relations require calculation of the stress autocorrelation function, which is very noisy and becomes computationally expensive when the characteristic relaxation time of a solution is large. In this chapter we investigate the use of reverse Poiseuille flow (RPF) as an alternative virtual rheometer for the calculation of the material functions of steady-state shearing from simulated velocity profiles. RPF was first applied to measure the viscosity of Newtonian fluids [14]. It consists of two parallel Poiseuille flows driven by uniform body forces, equal in magnitude but opposite in direction. Figure 6.1 shows the resulting velocity profiles (left) and shear stresses (right), where f is the imposed body force per unit mass and n is the number density. This arrangement, as with LEC, accommodates periodic boundary conditions, and again has the significant advantage of excluding unknown wall-effects, such as slip and density fluctuations. RPF has been applied successfully to Dissipative Particle Dynamics (DPD) simulations of dilute polymer solutions [73] and of colloidal suspensions [155]. These applications and examples in the chapter demonstrate RPF to be a general purpose virtual rheometer for the calculation of steady-state shear properties of a variety of non-Newtonian complex fluid models.

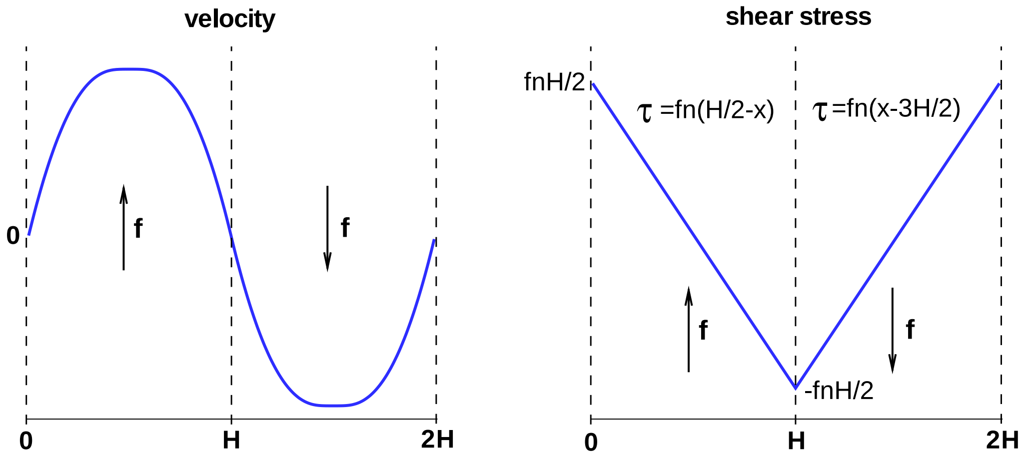

Figure 6.1: Typical velocity profile (left), and imposed shear stress (right) for the RPF arrangement. The wall shear-stress is $fnH/2$, where f is the imposed body force per unit mass and n is the number density.

We employ the Dissipative Particle Dynamics method (see section 2.2.2 for details) for the simulations that follow. However, it will be seen below that the only data required for the extraction of the material functions of steady shear flow are particle positions and velocities as functions of time. Hence the output from any particle based method that delivers those data can be similarly treated. For a system of free DPD particles, after the startup from rest following the sudden imposition of the driving force, the calculated velocity profiles at various times were found to be in good agreement with those predicted by the Navier-Stokes equation. Once the DPD-simulated velocity profiles become parabolic, the integrated bulk velocity or the maximum velocity yields calculated viscosities in good agreement with values calculated from Couette flow by LEC. With the viscosity and the elapsed time from startup in hand the Navier-Stokes solution can be used to check that the profile is indeed closely parabolic. For bead-chain systems or other complex structures no simple theoretical guide exists to determine the time to establish the steady-state since their rheology is unknown 'a priori', and they are taken to be unspecified non-Newtonian fluids. The steady velocity profiles are calculated for each prescribed linear shear-stress distribution determined by the imposed driving force. The shear rates across the profile must then be derived by numerical differentiation since the velocity profile has no simple mathematical representation. Simultaneously with the velocity profiles the complete stress system is calculated from the Irving-Kirkwood equation [107] in the form of stress-component profiles.

At very high shear rates DPD simulations fail when the mean velocities become much greater than the thermal fluctuating velocities. At low shear rates the fluctuations are overwhelming, and consequently the mean velocities become too small to be statistically significant. For Newtonian fluids, after the startup from rest following the sudden imposition of the driving force convergence to steady flow begins near the wall and moves gradually toward the centerline; thus long integration times are needed. This is analogous to the development of the velocity profile in turbulent flow in pipes where experience has shown that very long entrance lengths are required to complete the development near the centerline. The smoothness of the RPF velocity profiles tends to compensate for the errors due to numerical differentiation, and usually yields smoother rheograms when compared to the ones derived from the statistically measured stresses of Couette flow, in spite of its prescribed shear rate.

The chapter is organized as follows. In the next section we present the basic continuum equations and concepts of steady shear-rate rheology to be used to derive shear-dependent viscosities and normal stress differences of our non-Newtonian fluids. Section 6.3 demonstrates the use of the RPF virtual rheometer for monodisperse "melts" represented as identical chains, while section 6.4 presents results for mixtures of identical bead-spring chains in "good" solvents of free beads. In section 6.5 the time-temperature superposition is presented for melts at different temperatures. We conclude in section 6.6 with a brief discussion.

6.2 Rheological measurements and properties

For a given force f the RPF configuration shown in figure 6.1 of the introduction yields for the half-channel one steady-state velocity field calculated by the combination of time and ensemble averages. Shear rates $\dot{\gamma}(x)$ are then extracted from the measured velocity profile by numerical differentiation of fitted even-order polynomials for the central region, and cubic splines for the wall region. At cross-stream position x and time t elementary continuum analysis for any fluid in any shear flow requires the shear stress $\tau_{xy}(x,t)$ and the streamwise velocity $u(x,t)$ to satisfy the equation of motion

$$\rho\frac{\partial u}{\partial t} = \frac{\partial \tau_{xy}}{\partial x} - fn. \tag{6.1}$$

At the steady state ($\tau_{xy}(x,t) = \tau_{xy}(x)$) this momentum balance yields the linear shear stress profile shown in figure 6.1 (right) with the maximum absolute value of $fnH/2$ at the virtual walls (interfaces). This will be referred to as the imposed shear stress. In addition, the complete stress profile in the form of components (τ_{xy}, τ_{xx}, τ_{yy}, τ_{zz}) can be calculated from simulations using the virial theorem [39]. The calculated shear stress profile $\tau_{xy}(x)$ can be compared to the corresponding imposed profile to verify that the stresses calculated as statistical averages satisfy the continuum equation of motion, and that steady flow has been attained. With the shear rate $\dot{\gamma}(x) = du(x)/dx$ in hand the non-Newtonian shear viscosity $\eta(x)$, and the first and second normal stress coefficients $\Psi_1(x)$ and $\Psi_2(x)$ are derived from the stress components using the following definitions

$$\tau_{xy}(x) = \eta(x)\dot{\gamma}(x), \quad \tau_{yy}(x) - \tau_{xx}(x) = \Psi_1(x)\dot{\gamma}^2(x), \quad \tau_{xx}(x) - \tau_{zz}(x) = \Psi_2(x)\dot{\gamma}^2(x). \tag{6.2}$$

The non-Newtonian viscosity $\eta(x)$ will be calculated from the imposed shear stress so that its main source of error will be the shear rate $\dot{\gamma}(x)$ derived from the velocity profile by numerical differentiation. The calculated normal stress coefficients will be intrinsically more noisy since they are derived from the noisy calculated normal stresses and the square of the shear rate. For polymeric fluids the shear viscosity and normal stress coefficients typically approach constant values at low shear rates, and are called *zero-shear-rate* values. Very often this low-shear-rate Newtonian regime is experimentally inaccessible due to rheometer limitations. For the simulations of this work the zero-shear-rate values have to be extracted from the low shear rate region near the channel centerline where the velocity profile tends to flatten, and also it is the last region to converge to the steady state. Thus, larger errors in numerical differentiation should be anticipated in this region where the thermal fluctuations for both RPF and LEC dominate over the average shear rate.

6.3 Mono-disperse "melts"

The quotation marks applied in the title of this section serve to emphasize that while the construction of our simulation system appears to model a mono-disperse polymer melt it may not entirely represent the physical properties of real melts. The "melt" system here consists solely of flexible, mono-disperse bead-spring chains of $N = 2$, 5 and 25 beads connected by FENE springs (see section 5.2.1). There are no solvent particles. Table 6.1 outlines the parameters used in our DPD simulations, where n is the bead number-density.

n	r_c	a	γ	σ	k_BT	k eq.(2.11)	k_s	r_{max}
3	2.0	25.0	4.5	3.0	1.0	0.25	50.0	1.0

Table 6.1: DPD simulation parameters. Mono-disperse "melts".

The computational domain was set to $50 \times 20 \times 10$ in DPD units, which corresponds to a channel gap of $H = 25$ (see fig. 6.1). Initial chain configurations were assigned in the simulation domain by means of a three-dimensional random walk with the fixed step length of 0.6. RPF is driven by specification of f, a uniform constant force per DPD particle in the y-direction, positive on the left half and negative on the right half of the domain, respectively. The time step for all simulations was set to $\Delta t = 0.005$.

Several models exist to approximate the shear stress for non-Newtonian fluids in terms of the shear rate such as the power-law (eq. (5.8)) and the Ellis model [16]. Figure 6.2 shows velocity profiles (left) and normalized bead density (right) across the channel for chains of $N = 2$, 5 and 25 beads driven by $f = 0.25$. It also depicts the corresponding power-law

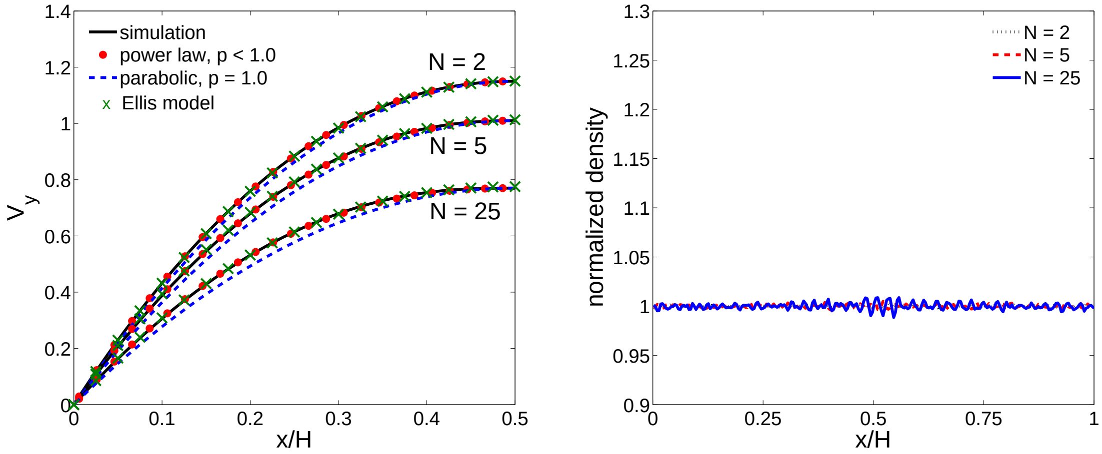

Figure 6.2: Velocity (left) and normalized bead density (right) profiles for three melts of $N = 2$, 5 and 25 bead chains. Power-law indices p are 0.898, 0.831, and 0.703 respectively.

fits (dots) and Ellis model fits (crosses) with indices $p = 0.898$ for $N = 2$, $p = 0.831$ for $N = 5$, and $p = 0.703$ for $N = 25$ bead chains. The power-law and Ellis model curves fit the simulated profiles extremely well. The parabolic Newtonian profiles with $p = 1$ (dashed lines) are plotted for contrast with the non-Newtonian curves of these "melts". The velocity profiles corresponding to the longer chains have smaller velocity maxima V_c and are flatter because these melts are more viscous and more strongly shear thinning (smaller p). In addition, figure 6.2 (right) shows that the bead density distribution is essentially uniform for all mono-disperse melts. The largest density deviations, within $1 - 2\%$ of the bulk density, were observed for the longest chains of $N = 25$ near the centerline. Absent for the system of pure mono-disperse chains is the cross-stream migration found for dilute and semi-dilute solutions [73, 199, 30, 112].

Figure 6.3 compares the imposed and the calculated shear stress for the melt of $N = 25$ beads as a consistency test. The overall excellent agreement between the assigned and the calculated shear stress distributions and the uniform density across the channel show that within the attainable statistical convergence the system of mono-disperse chains behaves as a homogeneous continuum. The negligible discrepancy in the near-wall region of thickness less than 1% of the channel width H appears to be a consequence of the the abrupt reversal of the driving force just beyond the wall. Comparison of calculated and imposed stress profiles for different driving forces showed that the discrepancy in the near-wall region vanishes as the driving force gets smaller. The periodicity of RPF suggests that as the ratio

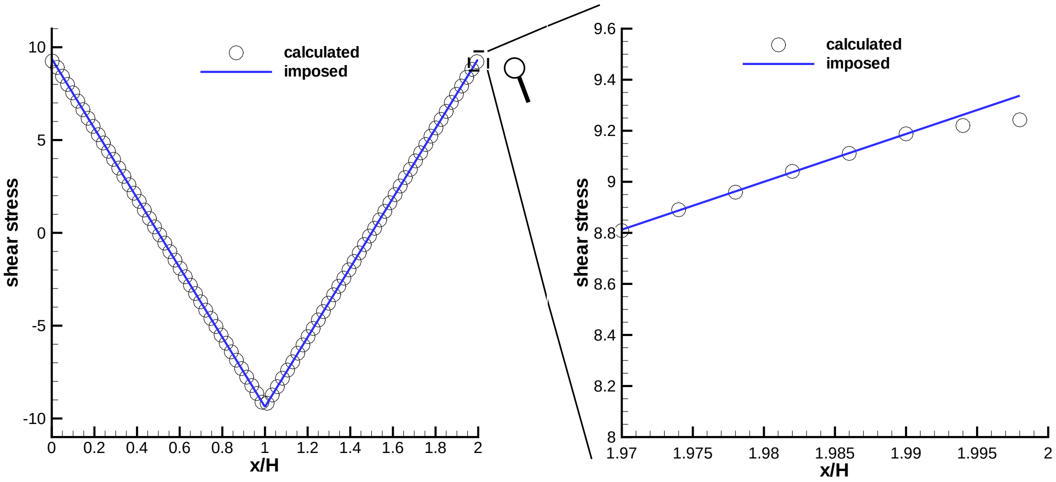

Figure 6.3: The calculated and imposed shear stress distribution (left) for the melt of $N = 25$ beads, and the near-wall region (right, expanded scale).

of particle size over H diminishes, this stress discrepancy will grow, and this will signal the breakdown of the continuum assumption. For the beads of this model, the Stokes-Einstein radius has been shown elsewhere [155] to be a plausible measure of particle size.

The regularity assumptions of continuum theory allow for the expansion of $V(x)$ in powers of x^2, and for the low shear rates near the centerline the leading terms are

$$V(x) = V_c - \frac{nf}{2\eta_0}x^2 + O(x^4). \tag{6.3}$$

This suggests that the central region of the velocity profile can be fitted well with even-order polynomials in x measured from the centerline, with the coefficient of x^2 furnishing the zero-shear rate viscosity η_0. The calculation of the non-Newtonian viscosity and the normal-stress coefficients (eq. (6.2)) requires the distribution of the shear rate $\dot{\gamma}(x)$ and the stress components $\tau_{xy}(x)$, $\tau_{xx}(x)$, $\tau_{yy}(x)$, and $\tau_{zz}(x)$ across the channel. For the viscosity the noise-free imposed shear-stress, $\tau_{xy}(x) = fn(H/2 - x)$ for $x \in [0, H]$ and $\tau_{xy}(x) = fn(x - 3H/2)$ for $x \in [H, 2H]$, is preferred (see fig. 6.1). For the normal-stress coefficients the only option is the computed stresses, and hence they are necessarily noisier than the viscosity. The required shear rates are extracted from the calculated velocity profiles by numerical differentiation for which the straightforward approach is to use finite-difference approximation based on a uniform grid of spacing Δx, defined as $x_i = i\Delta x$, $i = 0, ..., M$, where $M = \lfloor 0.5H/\Delta x \rfloor$. Constructed from the four halves of the reverse Poiseuille flow, an ensemble-average velocity profile is then interpolated with cubic splines and projected onto the grid $\{x_i\}$. This is appropriate for the near-wall region since polynomial interpolation is known to perform rather poorly for power-law functions (eq. (5.8)). Shear rates at points $x_{i+0.5}$ are then calculated from the second-order central difference $(V(x_{i+1}) - V(x_i))/\Delta x$.

Figure 6.4 presents the shear dependent viscosity (left) and the first and second normal-stress coefficients (right) for chains of $N = 25$. The curves denoted by crosses and circles in figure 6.4 (left) display the shear-dependent viscosity obtained by the numerical differentiation described above. The plot shows clearly how direct numerical differentiation works very well except at the very low shear rates of the central region where large errors in the central-difference estimate of the derivative appear as scatter in the viscosity and the normal-stress coefficients (symbols in figure 6.4 (right)). This scatter was reduced by two methods: firstly by filtering (smoothing) the original velocity data, and secondly by fits with low even-order polynomials. The solid line in figure 6.4 (left) is the result of applying the Savitzky-Golay filter [152] two to three times to the velocity data followed by the direct numerical differentiation. While filtering substantially reduces the low shear-rate scatter of the viscosity, it tends to smooth out data peaks such as the centerline maximum velocity V_c. Consequently, the flattened profile leads to under-prediction of the viscosity near the low shear-rate plateau, as can be seen in figure 6.4 (left). Smoothness for improved accuracy

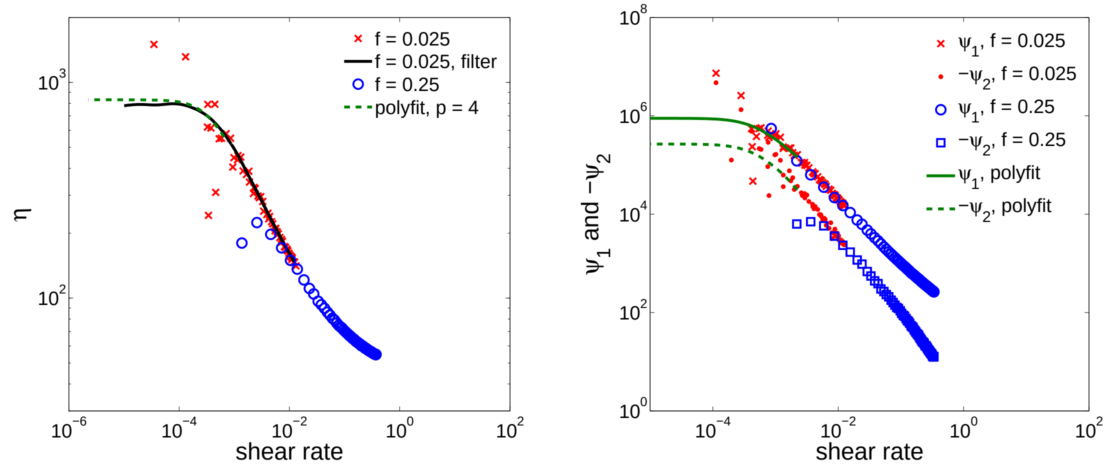

Figure 6.4: The shear dependent viscosity (left) and the first and second normal-stress coefficients (right) for 25-bead chains by direct numerical differentiation (symbols), and by curve filtering and fitting (solid and dashed lines).

of differentiation in the low shear-rate neighborhood of the Poiseuille flow centerline was achieved with fits of low-order polynomials in the small neighborhood where the velocity profile should be nearly parabolic (eq. (6.3)). The curves in figure 6.4 labeled “polyfit” employed a fourth-order polynomial fitted near the centerline by careful limitation of the region so that the term x^4 is not dominant. For the higher driving-force, $f = 0.25$, the zero-shear rate plateau cannot be obtained because the central region of the velocity profile is very narrow, and not resolvable by fitting with low-order polynomials. Hence, full curves of viscosity and normal-stress coefficients for a particular system require at least two simulations: the first with a low driving force f to resolve the zero-shear viscosity plateau, and subsequently one or more with higher $f's$ sufficient to provide overlapping resolution of the power-law region and possibly the high shear-rate plateau.

Figure 6.5 shows the shear dependent viscosity (left) and the first and second normal-stress coefficients (right) for chains of $N = 2$, 5, and 25 beads obtained by applying a combination of low-order polynomial fitting, filtering and numerical differentiation as described above. For each melt the solid and dashed curves are the results from two simulations of RPF carried out with non-dimensional forces $f = 0.025$ and 0.25 respectfully. The symbols in figure 6.5 denote analogous results obtained from simulations of plane Couette flow with Lees-Edwards boundary conditions (LEC). The excellent agreement over most of the shear-rate range between the RPF and the LEC results suggests that the steady shear-rate properties of these mono-disperse chains are material functions of the shear rate for any

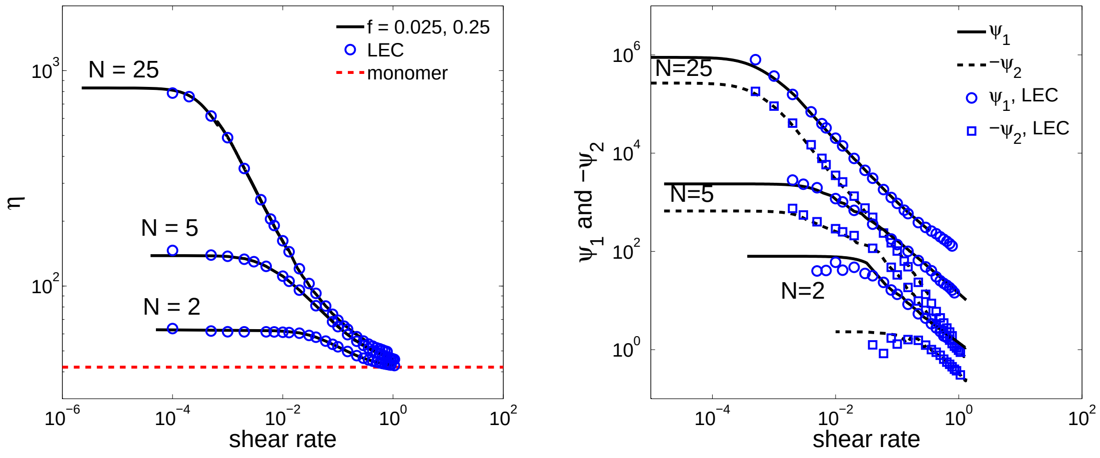

Figure 6.5: The shear dependent viscosity (left) and the first and second normal-stress coefficients (right) for chains of $N = 2$, 5, 25 beads.

steady shear flow. Hence, these fluids appear to behave macroscopically as homogeneous simple fluids in the sense of Noll [34]. The noticeable disagreement of the normal-stress coefficients for low shear rates, especially for 2-bead chains, is associated with the errors of the small calculated normal-stress differences as they approach zero. For LEC these coefficients exhibit increasing scatter at shear rates below the points shown in figure 6.5 (right), while for RPF the same coefficients at low shear rates can be successfully extracted by use of local, low-order polynomial fits of the calculated normal-stress difference data. This procedure is similar to the fits of velocity profiles near the centerline described above. Since the normal-stress differences in that region have nearly flat distributions it is essential to test the sensitivity of their coefficient plateaus to the chosen range of the fits.

An unexpected feature observed only for simulations by LEC for 2 and 5-bead chains at high-shear rates, and not for comparable ones by RPF, is that the first normal-stress coefficient becomes negative at high shear rates. Negative first normal stress coefficients are not observed in any experiments with such systems, and appear to be LEC model artifacts. It is not clear why the sign should switch only for short chains in constant-stress Couette flow, or why the Poiseuille flow stress-gradient is not subject to this artifact. Equation (5.8) is the integral of the equation of motion with the assumption of a power-law shear-stress shear-rate relation for the entire channel. The viscosity functions exhibited in figure 6.5 clearly show the power law region lies between the upper and lower viscosity plateaus. The best estimate of the power p is then the slope of the viscosity function taken to be $1 - 1/p$ at the inflection point. Table 6.2 shows that values of p derived from the viscosity function (p_2) agree fairly well with those obtained from the velocity profile fits (p_1). The table also shows asymptotic values of the mean relaxation time $\lambda_0 = 0.5\psi_1/\eta_0$ and the ratio $-\psi_2/\psi_1$ as $\dot{\gamma} \to 0$.

N	p_1	p_2	η_0	λ_0	$-\psi_2/\psi_1$
2	0.898	0.89	62.7	0.636	0.003
5	0.831	0.81	138.4	8.564	0.281
25	0.703	0.68	830.9	536.73	0.3

Table 6.2: Power-law index p_1 from velocity (fig. 6.2) and p_2 from viscosity (fig. 6.5), the zero shear-rate viscosity η_0, the mean relaxation time λ_0, and the normal stress coefficients ratio.

Note that in figure 6.5 (left) all viscosity curves converge to the same value (labeled “monomer”) at high shear rates which defines the high-shear rate plateau. Remarkably this value corresponds to the viscosity of the Newtonian DPD fluid having the same density of unchained or free beads (monomers) with the same interparticle forces. Figure 6.6 shows snapshots from visualizations of single, marked chains moving within ‘melts’ of unmarked chains at low shear rates (left) and high shear rates (right). At low shear rates the chains are entangled across the shear planes whereas at high shear rates they tend to completely disentangle, and are drawn out along, and are convected within the unstretchable shear planes. This implies a passive role for the spring connectors at high shear rates, and suggests why the monomer viscosity is the common plateau value for all N. Thus, in steady shear flow a typical chain behaves as follows: it *stretches* along the shear planes, and then *tumbles*. At high shear rates the tumble is constrained mostly within the shear planes, so that the chain ends are reversed within the same shear plane. Whereas at low shear rates, where fluctuations are dominant, the chain ends are frequently impelled across the shear planes, and so become entangled with chains in neighboring planes with different average velocities. The residence time for the stretching stage depends on the shear rate, bead interactions, and most importantly the chain length.

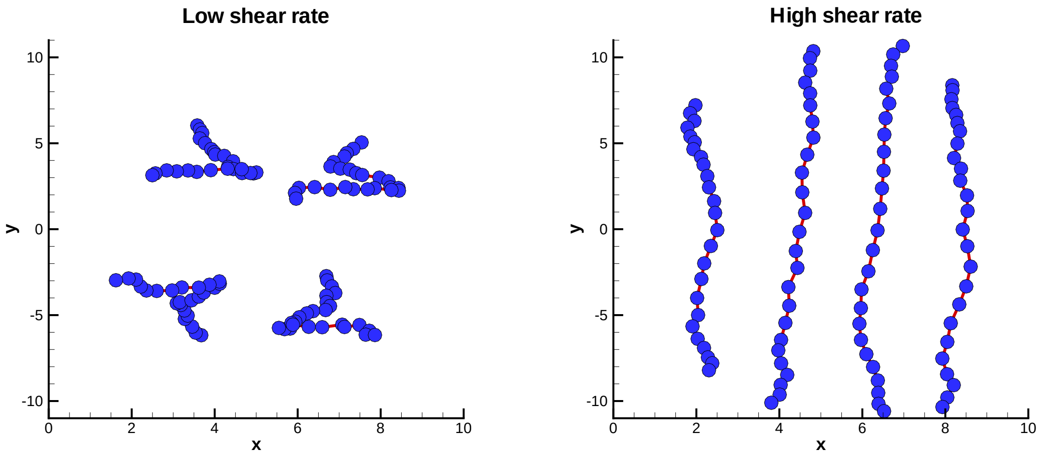

Figure 6.6: Collage of snapshots of a single 25-bead chain within a ’melt’ of unmarked chains at low shear rates (left) and at high shear rates (right) plotted on the same scale. Constant x defines the shear planes.

Note that each symbol in figure 6.5 corresponds to one LEC simulation for each prescribed shear rate. Even though the computational domain for all LEC simulations was

$10 \times 10 \times 10$ in DPD units or 10 times smaller by volume than the RPF domain, the total computational expense for the full material functions of comparable accuracy is several times larger for LEC than for RPF. In addition, statistical averaging of LEC stresses requires longer running times than those for RPF which combine both time and ensemble averages. Thus, the apparent advantage of an imposed shear rate in LEC is offset by the higher noise levels of the stresses. Whereas in RPF the shear stress distribution is prescribed, and the shear rate must be determined by numerical differentiation of the velocity profile. The latter operation turns out to be less noisy than the stress calculation because the statistical convergence of the velocity is more accurate and smoother than that of the stresses. This implies greater accuracy for the RPF viscosity function than for its normal-stress coefficients. A further advantage of RPF over LEC is its capability to extract the low shear-rate plateaus of the material functions. As a rheometer RPF performs similarly to experimental real steady-shear rheometers for which it is generally true that the viscosity function is more accurately measured than the normal-stress functions. Likewise the measurement of the low shear-rate plateaus is nearly always restricted by the limits of instrumental detection.

When the model fluids of mono-disperse chains were introduced above as "melts" the simulated properties can be compared with the corresponding properties of real melts. The viscosity data of a homologous series of undiluted polystyrenes with narrow molecular-weight distributions [89] exhibit a common power law over a five-fold range of molecular weights even though η_0 varies by several orders of magnitude. Hence the power-law exponents in table 6.2 suggest that if the models of this work are taken to represent whole polymers the bead number N alone is not a satisfactory proxy for molecular weight. In preliminary simulations the fluids of bead-spring chains were investigated with the cutoff radius r_c set to one, and the resulting viscosity functions were found to be only slightly non-Newtonian. Since the number of neighbor interactions increases as ${r_c}^3$ this shows the sensitivity of non-Newtonian response for such models. Thus, it should be possible to adjust model parameters to yield a series of fluids of mono-disperse bead-spring chains with power-law indices independent of N in agreement with experiment. This amounts to varying the viscosity of the "monomer" fluids, which in this study were held constant. However, the untangling visualized in figure 6.6 at high shear rates is not thought to occur for real polymers. Eventhough the data of [89], typical for whole polymers, do not extend beyond the power law regime it is usually accepted that at high shear rates these materials will exhibit a glassy response. Clearly the simplistic models employed in this work describe at best the rubbery regime. In spite of these limitations the ratios $-\psi_2/\psi_1$ as $\dot{\gamma} \rightarrow 0$ in table 6.2 are very close to the reptation theory prediction of 2/7 [120], except for N=2. The second normal-stress difference for 2-bead chains is very small at low shear rates, and the discrepancy of the ratio suggests that either the limit of detection has been reached or that dumbbells are a poor representation of a polymer.

Finally, it is necessary to relate DPD time scales to those of real polymer fluids. For both the mono-disperse undiluted polystyrenes of [89] and for poly-disperse melts, such as the polyethylenes of [120], the transition from the low shear-rate viscosity plateaus to the power-law regime occurs at shear rates $O(\lambda_0^{-1})$. This is also true for the simulated viscosity functions of this work, and so the matching of λ_0 provides the means to relate real and DPD time scales. Normal-stress data *for mono-disperse melts* are difficult to obtain [134, 174], and then the alternative is to derive λ_0 from low-frequency dynamic modulus measurements.

6.4 Semi-dilute solutions

In this section the RPF method is tested on several solutions of bead-spring chains in solvents of free DPD particles. Two chain-bead concentrations 25% and 50% were simulated for mono-disperse chains of 5- and 25-beads, respectively. Since chain beads and solvent particles have the same mass the chain-bead number density n or concentration corresponds to the chain-mass concentration. The computational domain is identical to the one described in section 6.3, and the simulation parameters are outlined in table 6.1. The solvent particles have the same interaction parameters as those of the polymer bead particles. For RPF two simulations for each solution were carried out corresponding to the imposed non-dimensional body forces of $f = 0.03$ and 0.3 for the 25% solutions, and $f = 0.05$ and 0.5 for the 50% solutions, respectively. Corresponding LEC simulations were also carried out over the same range of shear rates.

Figure 6.7 shows the shear dependent viscosity (left) and the first and second normal-stress coefficients (right) for the solution of $N = 25$ bead chains and concentrations 25% and 50%. The symbols in figure 6.7 correspond to LEC simulations of the same solutions, and the curves denoted by “direct” are extracted from the RPF simulations using local

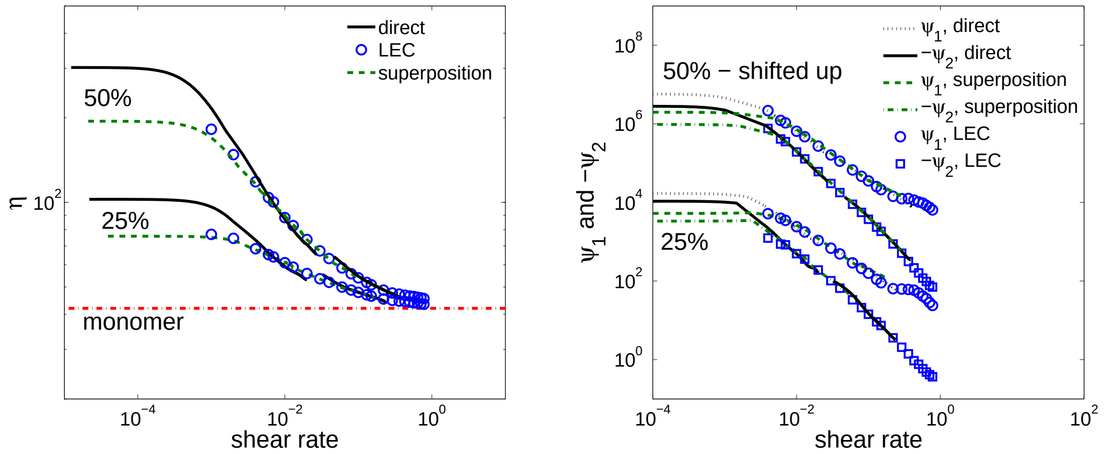

Figure 6.7: The shear dependent viscosity (left) and the first and second normal-stress coefficients (right) for the solution of $N = 25$ bead chains and mass concentrations 25% and 50%. For the 50% concentration in the right figure, all curves have been "shifted up" two orders of magnitude for visual clarity.

low-order interpolation, filtering and numerical differentiation as described above in section 6.3. Here, disagreement between RPF and LEC results is noticeable with different zero-shear rate viscosities and distinctive slopes in the power-law region. Macroscopically the shear stress for a mixture is constant in plane Couette, and the absence of a stress gradient is then compatible with uniform chain-bead concentration. The latter was found to hold at all shear rates for LEC, whereas in RPF the chain-bead concentration was found to be non-uniform. This behavior is attributed to the stress gradient across the channel.

Figure 6.8 presents the chain-bead densities across the channel normalized by their bulk values, for 25-bead solutions (left) and for 5-bead solutions (right) for two driving forces at each concentration. The effect of the Poiseuille stress gradient is a steeper and more confined concentration distribution in the central region for longer chains ($N = 25$), higher body forces and smaller chain-bead concentrations (25%). Figure 6.7 indicates higher viscosities relative to the LEC values in the lower shear-rate central region where the local concentration exceeds the bulk value, and vice versa in the high shear-rate wall region where the local concentration is depleted relative to the bulk value. The rheological properties of real polymer solutions at different concentrations are known to correlate by means of the empirical principle of time-concentration superposition. Here, we examine whether this principle applies to the DPD solutions described above, and in particular whether the solid "direct" curves of figure 6.7, which are discontinuous in the transition from the smaller to

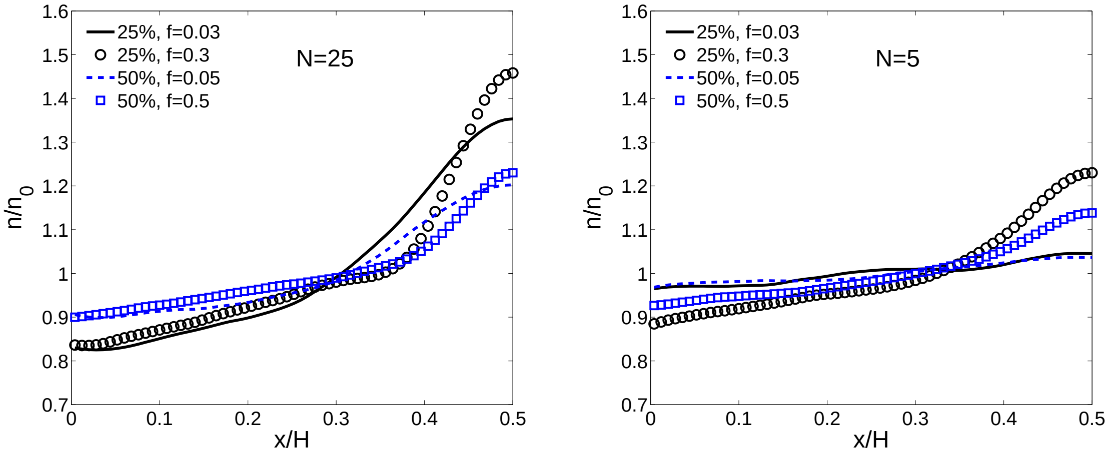

Figure 6.8: Normalized chain-bead number density distributions for 25-bead (left) and 5-bead solutions (right) for different bulk concentrations n_0 and body forces f.

the larger f, can be reconciled to lie on a single curve in agreement with the LEC points.

The zero-shear rate viscosity η_0 for concentrated solutions is assumed to be expressible as follows [19]

$$\eta_0 - \eta_s = \eta_s n[\eta]_0 e^{k' n[\eta]_0}, \tag{6.4}$$

where η_s is the solvent viscosity, n is the mass concentration (chain-bead number density here), $[\eta]_0$ is the intrinsic zero-shear rate viscosity, and k' is an arbitrary constant. It is assumed that $[\eta]_0 \sim M^a$, where M is the molecular weight and a is a power depending on the critical molecular weight. Thus, $[\eta]_0$ is constant for a given polymer chain, in this case chains of 5 and 25 beads, respectively. The superposition shift factor is formed as

$$a_n = \frac{\eta_0^{n_0} - \eta_s}{\eta_0^{n} - \eta_s} = \frac{\eta_s n_0[\eta]_0 e^{k' n_0 [\eta]_0}}{\eta_s n[\eta]_0 e^{k' n [\eta]_0}} = \frac{n_0}{n} e^{\alpha(n_0 - n)}, \tag{6.5}$$

where $\alpha = k'[\eta]_0$. Note that a_n is the shift factor only for $\eta - \eta_s$, and hence the total shifted viscosity is $(\eta - \eta_s)a_n + \eta_s$, whereas the normal-stress coefficients are shifted as $\psi_1 a_n^2$ and $\psi_2 a_n^2$, and the shear rate as $\dot{\gamma}/a_n$. Returning to figure 6.7 the curves denoted as "superposition" were obtained from the local concentration and the superposition shift factor a_n with $\alpha = 1.5$. The α value was found by superposition of LEC curves at the two concentrations (not shown). In the absence of LEC results α can be found by imposition of continuity on the shifted RPF results for different driving forces to yield the "superposition" curves in figure 6.7. The superposed RPF curves are continuous and agree well with the

LEC points, and thus, the principle of time-concentration superposition applies to the model solutions of 25-bead chains. Although large concentration gradients would appear to negate the use of the RPF configuration as a rheometer, useful measurements of bulk properties can be obtained for solutions where concentration superposition is applicable.

For the 5-bead chain solutions figure 6.9 shows that the time-concentration superposition as implemented above yields satisfactory results for the viscosity, and the second normal stress coefficient, but inconsistency between LEC and RPF results for the first normal stress coefficient. As expected the smaller concentration gradients (figure 6.8) relative to $N = 25$ reduce the deviations of the "direct" viscosity curves from the LEC points and their discontinuities are smaller than their $N = 25$ counterparts of figure 6.7 (left). Here, the time-concentration superposition, as described above, was applied with $\alpha = 0.75$ to yield excellent agreement between the LEC points and the RPF viscosity "superposition" curves. The scatter in the LEC normal-stress coefficient points indicates large errors as the shear rate is decreased to its lowest values. The surprising result is the behavior of the first normal-stress coefficient for which the LEC points decay faster with shear rate relative to the superposed RPF curves, and that the disagreement is worse for the more dilute 25% solution. Eventually ψ_1 by LEC becomes negative (not shown), while agreement between the second normal-stress coefficients remains very close. This artifact of the Couette flow appears to be a short-chain phenomenon, having been found above for the 2 and 5-bead

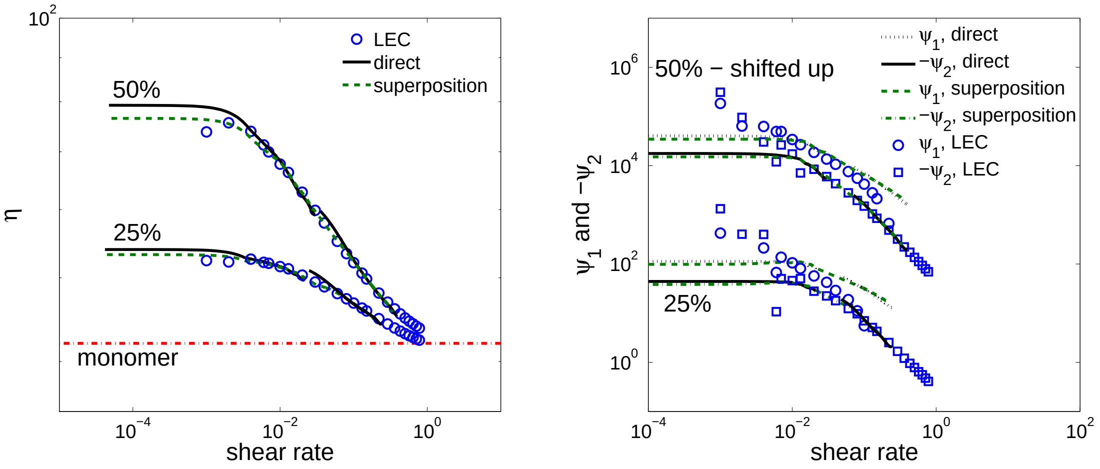

Figure 6.9: The shear dependent viscosity (left) and the first and second normal-stress coefficients (right) for solutions of 5-bead chains at concentrations of 25% and 50%. For the 50% concentration in the right figure, all curves have been "shifted up" two orders of magnitude for visual clarity.

melts and here for 25% solution of 5-bead chains. At the macroscopic level this suggests that bead-chain fluids may not always behave as simple fluids in the sense of Noll [34]. The large concentration changes across the channel indicate that the simulated solutions do not capture the diffusion behavior of real polymer solutions. Cross-stream migration effects of this magnitude are not known for polymer solutions flowing in channels of laboratory length scales. However, these results do suggest that concentration gradients will eventually appear for long enough channels due to the action of stress gradients.

Finally, table 6.3 outlines the power-law indices and zero shear-rate properties for the solutions of chains $N = 5$ and 25 beads at different concentrations. Here again, the mean relaxation time λ_0 defines the characteristic time scale in DPD solutions which is much smaller for short chains. The ratio $-\psi_2/\psi_1$ for all solutions appears to be larger than the value of 2/7 predicted by the reptation theory [120]. We attribute these differences due to errors in the second normal-stress coefficient, because its magnitude is comparable with statistical averaging errors as $\dot{\gamma} \to 0$.

N	concentration	p	η_0	λ_0	$-\psi_2/\psi_1$
5	25%	0.95	53.2	0.924	0.39
5	50%	0.9	76.5	2.26	0.43
25	25%	0.89	75.8	34.7	0.63
25	50%	0.78	194.5	50.7	0.49

Table 6.3: The power-law indices and zero shear-rate properties for the solutions of chains $N = 5$ and 25 beads at different concentrations.

6.5 Time-temperature superposition

Here we present the analysis of temperature dependence of the steady shear-rate properties of mono-disperse bead-chain melts. We employ time-temperature superposition, a well-established procedure [76] for real polymers, and the temperature analog of time-concentration superposition already described above. Although the method is mainly empirical, the scaling of both dependent and independent variables can be motivated by polymer theories at the mesoscopic level, such as the Rouse theory [120, 76]. In these theories, including the theory of rubber elasticity, the equilibrium Helmoltz free energy is generally athermal, i.e. linear in k_BT. This means that the entropy is entirely configurational (independent of k_BT), and thus the equation of state for the equilibrium pressure p is of the form

$$\frac{p}{k_BT} = f(n) = n + \sum_{i>1} b_i n^i. \tag{6.6}$$

Here, the second equality follows from the additional assumption that $f(n)$ has a virial expansion, and then its coefficients b_i must be constant. For molecules with spherical symmetry constant virial coefficients are a consequence of temperature-independent radial-distribution functions (RDF) [136]. The best-known example of the virial expansion for an athermal fluid is the hard sphere gas.

For the DPD fluids of this work the contribution to the excess pressure is calculated from the virial theorem as

$$\begin{aligned} p_{vir} &= \frac{1}{6V}\left[\sum_{i\neq j}\mathbf{r}_{ij}\mathbf{F}^C_{ij} + 2\sum_{s\in\{springs\}}\mathbf{r}_s\mathbf{F}^S\right] = \\ &= \frac{1}{6V}\left[a\sum_{i\neq j}\mathbf{r}_{ij}(1-\frac{r_{ij}}{r_c})\hat{\mathbf{r}}_{ij} + 2k_s\sum_s \mathbf{r}_s\frac{r_s}{1-r_s^2/r_{max}^2}\hat{\mathbf{r}}_s\right], \end{aligned} \tag{6.7}$$

where the forces were defined above in sections 2.2.2 and 5.2.1. For a fluid of free DPD particles at densities well beyond the ideal gas regime Groot & Warren [92] found from simulations the equation of state to be approximately $p = nk_BT + b_2n^2$, where b_2 is a constant proportional to the conservative force coefficient a. Pagonabarraga & Frenkel [153, 154] derived this result with multibody DPD (an enhanced version of the standard 2-body DPD employed here). However, Groot & Warren's simulations covered only one isotherm, and hence the temperature dependence of a was not considered. Statistical mechanics provides examples of mesoscopic forces whose expressions carry the prefix k_BT. The relevant one here is the Langevin force on a tethered chain, of which the FENE force [19] is an approximation. Since DPD beads are point particles which represent loose aggregates of many molecules it is plausible to assume their soft potentials also have the k_BT hallmark of mesoscopic forces. Hence, both the conservative force coefficient a and the spring constant k_s are assumed to be of the form

$$a = k_BTa_0, \qquad k_s = k_BTk_{s0}, \tag{6.8}$$

where a_0 and k_{s0} are the reference parameters corresponding to temperature $k_BT = 1$. Equation (6.7) suggests the equation of state will have the athermal form of equation (6.6). This was verified with equilibrium simulations of 5-bead chain melts for several bead densities n at three temperatures $k_BT = 0.5$, 1.0 and 1.5. The temperature was set by adjustment of the dissipative force coefficient according to $\gamma = \gamma_0/k_BT$, which from equation (2.10) means that σ was held constant. Table 6.4 summarizes the constant DPD parameters specified for simulations. Figure 6.10 shows the excess equilibrium pressure versus bead density at several temperatures simulated with the parameter scaling of equation (6.8). Clearly the curves for different temperatures plot as parallel lines on bi-logarithmic coordinates, which shift onto a single line by scaling the excess pressure with temperature. It is easily verified that the excess pressures at $n = 2$ satisfy $487.14/1.5 \approx 324.73 \approx 162.33/0.5$. In figure 6.10 the dashed reference line has slope 2 to show that the form of Warren & Groot [92] also holds for the bead-chain models provided the conservative force coefficient

r_c	a_0	γ_0	σ	k eq.(2.11)	k_{s0}	r_{max}
2.0	50.0	4.5	3.0	0.25	100.0	2.0

Table 6.4: DPD parameters for RPF simulations. Time-temperature superposition.

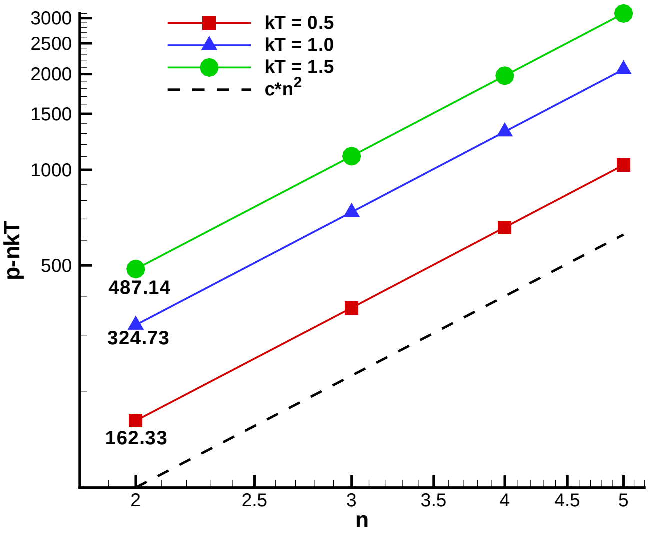

Figure 6.10: Log-log plot of the excess equilibrium pressure for different bead density at several temperatures. Melts of 5-bead chains.

scales according to equation 6.8. Although not shown here, the radial distribution function for these melts was verified to be independent of temperature which demonstrates the temperature-independent structure requirement of the athermal fluid.

For a melt of 5-bead chains with the bead density $n = 3$ RPF simulations were carried out at three temperatures, $k_BT = 0.5$, 1.0 and 1.5 in a $50 \times 20 \times 10$ box, with the constant simulation parameters given in table 6.4. To capture both the low and the high shear-rate plateaus of the viscosity function at each temperature runs were carried out for three non-dimensional body forces $f = 0.025$, 0.25 and 1.0. Figure 6.11 shows the resulting shear dependent viscosity (left) and the first and second normal-stress coefficients (right) at the three temperatures. Visual inspection of the shapes of these bi-logarithmic plots suggests that the curves can be superposed. Indeed, when the ordinates are normalized by their zero shear-rate values, and the shear rates are multiplied by the factor $a_T = \gamma(T)/\gamma(T_0)\eta_0(T_0)/\eta_0(T)$, then all the curves shift onto the $k_BT = 1.0$ curve. The superpositions are not shown since the deviations from the common curves are not visible on the scale of figure 6.11. For real polymers the shift factor is generally taken to be $a_T = \eta_0(T_0)/\eta_0(T)$. No rigorous argument can be given for including the dissipative force coefficient in the shear-rate shift factor. However, γ (dimension $time^{-1}$) is proportional to a time scale of the DPD system, and therefore this empiricism is not entirely surprising. The shear rate rendered dimensionless with the mean relaxation time λ_0 was demonstrated by Graessley [134] to be an alternative scaling for narrow distribution polystyrenes. Fig-

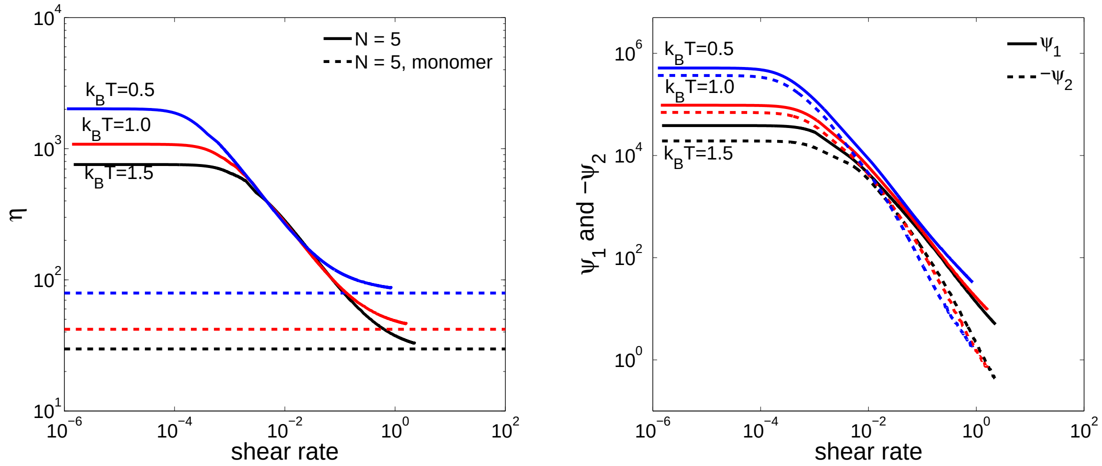

Figure 6.11: The viscosity function (left) and the first and second normal-stress coefficients (right) at three temperatures for 5-bead chains.

ure 6.12 shows the time-temperature superposition of the three viscosity curves. Here, the viscosity curves are normalized by its zero shear-rate value η_0, and the shear rate is scaled with the mean relaxation time λ_0 from table 6.5 analogously to the Graessley's scaling for polystyrenes [134]. This superposition suggests why the dissipative force coefficient γ appears in the shift factor a_T. Table 6.5 gives the power-law indices and the low shear-rate properties at the three temperatures. Compared to the 5-bead melt of figure 6.5, section 6.3, the 5-bead melt at $k_BT = 1.0$ of figure 6.11 exhibits much stronger shear-thinning. The difference between these chains is the doubling here of r_{max}, and hence the fully-extended contour length. This points to contour length rather than bead number as the chain prop-

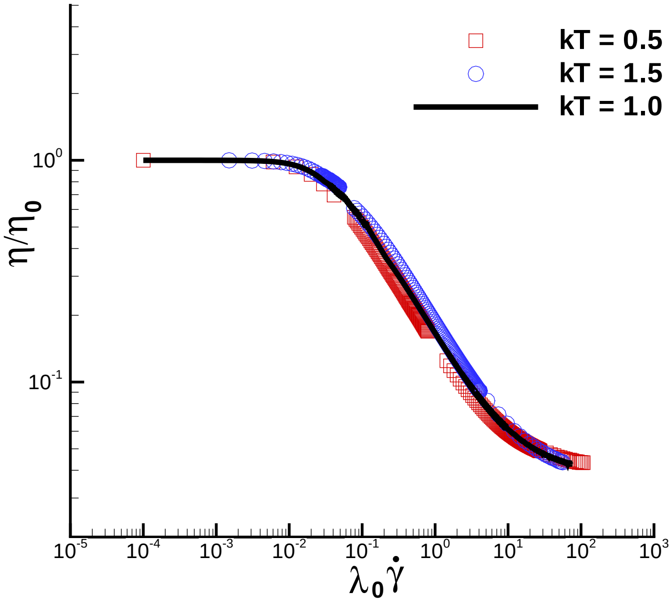

Figure 6.12: The time-temperature superposition of the shear-dependent viscosity for 5-bead chain melts at three temperatures.

k_BT	p	η_0	λ_0	$-\psi_2/\psi_1$
0.5	0.665	2015.2	128	0.7
1.0	0.665	1082.4	44.5	0.7
1.5	0.665	757.8	25.4	0.5

Table 6.5: The power-law indices and zero shear-rate properties for three temperatures.

erty that mainly determines the steepness of the viscosity function.

6.6 Summary

The virtual rheometer is a designation for the set of particle-based numerical methods which exist and are being further developed to simulate the many complex material systems studied in the laboratory by experimental rheologists. Such methods have matured to the point where today they can be considered useful adjuncts to experimental rheology, and with further development have the potential to transform theoretical rheology into a reliably predictive science. This will result in significant economies to enterprises engaged in dealing with complex fluids who now must rely on extensive and costly physical testing in order to utilize these materials. The concept of the Virtual Rheometer as a 'useful adjunct' is best appreciated by analogy to the role of the 'virtual wind tunnel' or 'virtual towing tank' in which simulation of aerodynamics and hydrodynamics has become an essential tool for the fluid mechanical design aspects of aircraft, ships and land vehicles.

Specifically, in this work we have demonstrated the use of reverse Poiseuille flow (RPF), illustrated in figure 6.1, as a virtual rheometer for the calculation of the steady shear-rate material functions from simulations of fluids based on particle models. Here the RPF virtual rheometer has been demonstrated with DPD simulations, but the concept is applicable to any particle based method, including MD, SPH or LBM. The reversal of the driving force over half the computational domain combined with periodic boundary conditions guarantees zero mean velocity on channel walls without imposition of real-wall boundary conditions with their known pitfalls. Hence, properties measured in RPF are bulk values. This was confirmed for a fluid of monodisperse chains in figure 6.2 which shows the bead density distribution to be uniform across the channel section, and in figure 6.3 which shows the shear stress calculated from the simulation data by the Irving-Kirkwood equation to be consistent with the imposed shear stress distribution determined from the continuum equation of motion. Further confirmation was provided by comparison of material functions derived from RPF simulations with those derived from simulations of plane Couette flow with Lees-Edwards boundary conditions (LEC), figure 6.5. This comparison is apt since the periodic boundary conditions of LEC imply that it also measures bulk values without the problems of real walls.

The purpose of this work has been to demonstrate how the shear-rate dependent properties of modeled complex fluids can be accurately and economically determined with the RPF rheometer. In doing so it was found that RPF has certain advantages over the conventional LEC configuration. Firstly, the latter determines material-function values for only one shear rate per simulation, whereas a single RPF simulation yields the same data for a wide range of shear rates from zero at the centerline to the wall value. Thus, even though the computational domain for the RPF configuration is several times larger than the LEC's, RPF yields the full rheogram at reduced computational cost compared to LEC. In practice, for shear thinning fluids driven by large body forces the flatness of velocity profiles near the centerline requires at least one simulation at the lowest possible force in order to resolve the low shear-rate viscosity plateau. One or two higher driving forces may be required to span the power law region and the approach to the high shear-rate plateau. Secondly, RPF values near the zero-shear rate plateaus appear to be more reliable than those derived from LEC. At very low shear rates stresses computed from the Irving-Kirkwood equation, required for LEC, are inevitably noisier due to the dominance of thermal fluctuations. The unexpected conclusion of this work is that shear rates derived by numerical differentiation of the RPF velocity distribution combined with prescribed shear stress is a less noisy operation than the prescribed shear rate of LEC combined with calculated shear stress. The computed normal-stress differences of RPF are more accurate than their LEC counterparts, since they are amenable to smoothing techniques as they are delivered as distributions across the cross-section.

The fluids composed of mono-disperse chains, referred to as melts, were shown to have steady shear-rate material functions of forms typical of polymer fluids. Furthermore, the material functions of the melts satisfy the principle of time-temperature superposition and their solutions the principle of time-concentration, which is typical of such fluids. However, in their present form these models only partially capture the behavior of real mono-disperse polymer melts and solutions. In particular, the tendency to complete disentangling of chains at high shear rates does not correspond to what little is known for real polymers; data are rare at shear rates approaching the upper viscosity plateau. Further understanding of coarse-graining of bead-chain models should allow the regime of shear rates up to the power law response can be brought into quantitative correspondence with the response of real polymer fluids. Although RPF yields only the steady shear response of a fluid, the examples of this work demonstrate it can quickly and economically yield insights into the adequacy of a particle model without the need for a complete rheological characterization. Hence, RPF will be a favored tool in the assessment of new and improved models.

Chapter 7

Summary and future work

The research described in this thesis is focused on multiscale modeling of blood flow and various polymeric systems which are part of soft matter. This work is driven by a rising importance of numerical simulations in such fields as biology, material science, and medicine and by a growing demand in multiscale approaches since many problems in systems biology and soft matter require modeling of a wide range of spatiotemporal scales. The main novel contributions of this work are as follows

- The Triple-Decker algorithm which interfaces atomistic, mesoscopic, and continuum flow regimes corresponding to MD, DPD, and NS methods. Distinct descriptions are formulated in different overlapping subdomains and are coupled through boundary conditions. The algorithm allows for a flexible and efficient decoupling of space and time scales which arise in different descriptions.

- A three-dimensional multiscale RBC model which incorporates realistic RBC membrane properties. The RBC membrane is constructed as a network of springs whose macroscopic properties are related to the network parameters through the developed theoretical analysis. This permits analytical calculation of the model parameters for targeted macroscopic membrane properties and therefore, no parameter adjustment is required. The RBC model includes a viscous contribution in the membrane to deliver its viscoelastic properties. In addition, it accounts for the separation of blood plasma and RBC cytosol by the membrane to allow the use of internal/external fluids with different viscosities which strongly affects RBC dynamics.

- A stress-free RBC model which eliminates artifacts of local non-vanishing membrane stresses due to a selected triangulation. This model permits to set a realistic membrane bending rigidity which is much lower than the in-plane membrane elasticity, while most of the existing models of similar type utilize very high bending rigidities to compensate for artifacts of local non-vanishing membrane stresses due to triangulation. The RBC model is able to adequately reproduce realistic RBC mechanics, rheology, and dynamics.

- Rheological measurements of RBC membrane properties by twisting torque cytometry and through the monitoring of membrane thermal fluctuations. The rheology of the modeled membrane is in agreement with available experiments. These measurements along with experimental data can also aid in the determination of some RBC membrane properties such as bending rigidity and membrane viscosity.
- Modeling of RBCs in malaria at different stages of intra-erythrocytic parasite development. RBC mechanics at different stages is accurately captured by the RBC model in comparison with experiments. The modeled RBC rheology shows a partial agreement with experiments indicating insufficient data provided by them. Thus, the RBC model can assist in the quantification of relative contributions to membrane rheology in malaria such as shear modulus, bending rigidity, membrane viscosity, presence of a rigid parasite inside RBCs, and potential metabolic activities.
- Modeling of blood flow under healthy conditions and in malaria. The simulated blood flow in microtubes is able to reproduce the well-known Fahraeus and Fahraeus-Lindquist effects and cell-free layers found in experiments. In addition, an increase in blood flow resistance in malaria in comparison with that under healthy conditions is quantified. Blood flow is simulated in a microfluidic channel with a constriction. The developed model can be used to simulate blood flow in microcirculation and in various microfluidic devices.
- Adhesive dynamics of Pf-parasitized RBCs in malaria. Adhesive dynamics of infected RBCs is found in agreement with that on ICAM-1 and on mammalian CHO cells in experiments. The effect of membrane properties on adhesive behavior is examined for different membrane Young's moduli and bending rigidities. In conclusion, flipping behavior observed for infected RBCs appears to be due to the increased stiffness of

the RBC membrane in malaria. The influence of a rigid parasite inside RBCs on the RBC's adhesive dynamics in shear flow is investigated showing more erratic adhesive behavior than that of RBCs absent of rigid parasites. The adhesion of Pf-parasitized RBCs in blood flow is simulated in a rectangular flow chamber showing significant effects of a microflow environment on the adhesive dynamics of infected RBCs.

- Polymer depletion and migration in micro- and nano-channels. The depletion of polymers is studied for various polymer models, solvent qualities, wall-polymer interactions, numbers of beads in polymer representation, and channel sizes. The simulated depletion layers are in agreement with the theoretical prediction of the depletion layer for ideal chains. Polymer migration in Poiseuille flow yields two off-center peaks in polymer bead distributions across the channel. The Serge-Silberberg effect is identified as one of the contributions to polymer migration.
- Reverse Poiseuille flow (RPF) - A numerical rheometer. The RPF method is proposed to be used for measurements of steady state rheological properties of complex fluids. The method is successfully applied to semi-dilute polymer solutions and melts. Time-concentration and time-temperature superposition principles are successfully applied to the simulated DPD systems. RPF can be used as an alternative numerical rheometer which allows to expand the range of flow conditions at which rheological measurements can be taken.

Despite the results in the thesis, multiscale modeling in blood flow and soft matter requires further tremendous developments and improvements in order to enable its practical use in medicine, material science, and biology. As an example, the Triple-Decker algorithm was applied to several cases of steady Newtonian flows. Further research is required to enable its application to unsteady flows and flows of complex fluids such as blood and polymeric suspensions. Moreover, blood flow modeling did not include numerous biological details and processes such as elastic vessel walls, glycocalyx layer, RBC aggregability, metabolic activities, etc. Blood flow in malaria exhibits an even higher level of complexity due to changes in RBC membrane properties and RBC adhesion to the vascular endothelium. Thus, the research in this thesis is one of the first steps towards realistic multiscale modeling of blood flow under healthy conditions and in malaria and modeling of polymeric systems.

Lastly, we propose several projects which should follow the research described in this thesis. The potential projects of interest include

- A further development of the Triple-Decker algorithm to enable its applicability to unsteady flows and flows of complex fluids. To simulate unsteady flows with the Triple-Decker method, an algorithm for modeling unsteady flow boundary conditions for particle methods such as DPD and MD is required. Similarly, BCs for flows of complex fluids are yet to be developed, requiring efficient algorithms for the insertion and deletion of simulated molecules or cells at inflow and outflow, respectively.
- The effect of RBC aggregability on blood flow and its resistance. Aggregation among RBCs can be incorporated into the blood flow model using, for example, the Morse potential for cell-cell interactions.
- Blood flow in complex geometries such as microfluidic devices and vessel bifurcations. Such simulations are likely to provide valuable insights for understanding blood flow resistance and CFL variations in the microcirculation.
- The effect of vessel elasticity and the glycocalyx layer on blood flow. This is another step towards more realistic simulations of blood flow in the microcirculation. Analogously to the RBC membrane, an elastic vessel can be modeled as a spring network with a large Young's modulus. The glycocalyx layer could be represented as a brush of semiflexible filaments attached to the vessel wall.
- Adhesion interactions among Pf-parasitized and healthy RBCs in malaria. Small cell aggregates are found in blood flow in malaria due to rosetting and autoagglutination. Rosetting is the attachment of healthy RBCs to Pf-parasitized erythrocytes, while autoagglutination is the adhesion among infected RBCs. These interactions can be potentially simulated using the adhesion model described in section 4.4. Alternatively, sufficiently strong attractive interactions among RBCs (e.g., Morse potential) may yield a good approximation of the adhesion of Pf-parasitized and healthy RBCs.
- Blood flow resistance in the microcirculation in malaria under realistic conditions which include the adhesion of Pf-parasitized and healthy RBCs as well as adhesive interactions of infected RBCs with the vessel wall. Here, complex vessel geometries can be considered and flow conditions for microvessel blockages could be identified.

- Bulk rheological properties of blood in health and in malaria. These include shear-dependent viscosity, normal-stress differencies, and the complex modulus.
- Possible segregation of healthy and Pf-parasitized RBCs in blood flow due to the difference in their membrane rigidities. The migration of Pf-parasitized RBCs towards the vessel walls in blood flow may facilitate their efficient adhesion to the wall.

Appendix A

RBC nodal forces from the defined energies

The modeled membrane is described by the potential energy $V(\{\mathbf{x}_i\})$ (eq. (3.1)) with the contributions defined in equations (3.2, 3.3, 3.5, 3.6, and 3.7). Derivation of the exact nodal forces corresponding to the outlined energies is performed according to equation (3.8) and is divided into several parts:

i) two-point interactions (e.g., springs),

ii) three-point interactions (e.g., hydrostatic elastic energy, area and volume conservation constraints),

iii) four-point interactions (e.g., bending between two adjacent faces).

The two-point or spring interactions defined in equations (3.3 and 3.5) yield the following forces

$$
\begin{aligned}
\mathbf{f}_{WLC}(l) &= -\frac{k_BT}{p}\left(\frac{1}{4(1-x)^2} - \frac{1}{4} + x\right)\hat{\mathbf{l}}_{ij}, \\
\mathbf{f}_{FENE}(l) &= -\frac{k_s l}{1-x^2}\hat{\mathbf{l}}_{ij}, \\
\mathbf{f}_{POW}(l) &= \frac{k_p}{l^m}\hat{\mathbf{l}}_{ij},
\end{aligned}
\tag{A.1}
$$

where $x = l/l_m$ and $\hat{\mathbf{l}}_{ij} = \vec{l}_{ij}/l$ is the vector of unit length between the spring ends i and j.

The three-point interactions may represent hydrostatic elastic energy (eq. (3.2)), area and volume conservation constraints (eq. (3.7)). Figure A.1 shows a sample triangular element of the membrane network. Here $\vec{a}_{ij} = p_i - p_j$ and i, j take the values 1, 2, or 3.

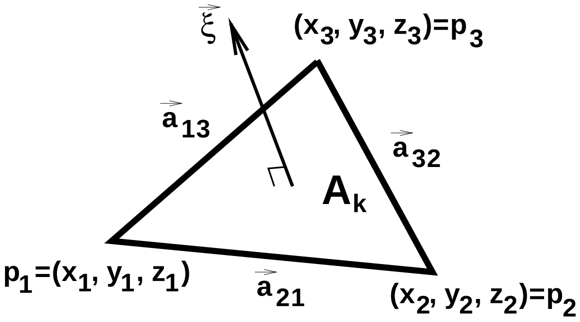

Figure A.1: Sketch of a triangular element of the network.

The normal $\vec{\xi}$ is equal to $\vec{a}_{21} \times \vec{a}_{31}$, where "×" defines the cross product. The area of the triangle is given by $A_k = |\vec{\xi}|/2 = \frac{1}{2}\sqrt{\xi_x^2 + \xi_y^2 + \xi_z^2}$. Then, the hydrostatic elastic energy for a single triangle results in the force given by

$$f_{s_i} = -\frac{\partial \left(C_q/A_k^q\right)}{\partial s_i} = \frac{q 2^q C_q}{(\xi_x^2 + \xi_y^2 + \xi_z^2)^{q/2+1}} \left(\xi_x \frac{\partial \xi_x}{\partial s_i} + \xi_y \frac{\partial \xi_y}{\partial s_i} + \xi_z \frac{\partial \xi_z}{\partial s_i}\right), \tag{A.2}$$

where s can be x, y, or z and i = 1, 2, or 3. Let us denote the coefficient in front of the parenthesis as follows

$$\alpha = \frac{q 2^q C_q}{(\xi_x^2 + \xi_y^2 + \xi_z^2)^{q/2+1}} = \frac{q C_q}{4 A_k^{q+2}}. \tag{A.3}$$

Thus, the nodal forces for the hydrostatic elastic energy term (eq. (3.2)) are given by the following expressions

$$\begin{aligned} (f_{x_1}, f_{y_1}, f_{z_1}) &= \alpha \left(\vec{\xi} \times \vec{a}_{32}\right), \\ (f_{x_2}, f_{y_2}, f_{z_2}) &= \alpha \left(\vec{\xi} \times \vec{a}_{13}\right), \\ (f_{x_3}, f_{y_3}, f_{z_3}) &= \alpha \left(\vec{\xi} \times \vec{a}_{21}\right). \end{aligned} \tag{A.4}$$

In case of the global area conservation constraint (the first term of V_{area} in equation (3.7)) we obtain

$$\begin{aligned} f_{s_i} &= -\frac{\partial\left[k_a(A-A_0^{tot})^2/(2A_0^{tot})\right]}{\partial s_i} = -\frac{k_a(A-A_0^{tot})}{A_0^{tot}}\frac{\partial A}{\partial s_i} = \beta_a \sum_{k\in 1\ldots N_t} \frac{\partial A_k}{\partial s_i} = \\ &= \beta_a \sum_{k\in 1\ldots N_t} \frac{1}{4A_k}\left(\xi_x^k \frac{\partial \xi_x^k}{\partial s_i} + \xi_y^k \frac{\partial \xi_y^k}{\partial s_i} + \xi_z^k \frac{\partial \xi_z^k}{\partial s_i}\right), \end{aligned} \tag{A.5}$$

where $\beta_a = -k_a(A - A_0^{tot})/A_0^{tot}$, the superscript k denotes the k-th triangle, and $i \in \{1, ..., N_v\}$. However, for a single triangle the nodal forces appear to have the same functional form as that in equation (A.4) with $\alpha = \beta_a/(4A_k)$. Similar to the global area constraint, the local area conservation constraint (the second term of V_{area} in equation (3.7)) results in the nodal forces for a single triangle as those in equation (A.4) with $\alpha = -k_d(A_k - A_0)/(4A_0A_k)$.

The global volume conservation constraint (eq. (3.7)) yields the following equation

$$f_{s_i} = -\frac{\partial\left[k_v(V-V_0^{tot})^2/(2V_0^{tot})\right]}{\partial s_i} = -\frac{k_v(V-V_0^{tot})}{V_0^{tot}}\frac{\partial V}{\partial s_i} = \beta_v \sum_{k\in 1\ldots N_t} \frac{\partial V_k}{\partial s_i}, \tag{A.6}$$

where $V_k = \frac{1}{6}(\vec{\xi^k} \cdot \vec{t_c^k})$, $(* \cdot *)$ denotes the dot-product, and $\vec{t_c^k} = (p_1^k + p_2^k + p_3^k)/3$ is the center-of-mass of the k-th triangle (see fig. A.1). The nodal forces for a single triangle derived for the volume constraint are as follows

$$\begin{aligned} (f_{x_1}, f_{y_1}, f_{z_1}) &= \frac{\beta_v}{6}\left(\vec{\xi}/3 + \vec{t_c} \times \vec{a}_{32}\right), \\ (f_{x_2}, f_{y_2}, f_{z_2}) &= \frac{\beta_v}{6}\left(\vec{\xi}/3 + \vec{t_c} \times \vec{a}_{13}\right), \\ (f_{x_3}, f_{y_3}, f_{z_3}) &= \frac{\beta_v}{6}\left(\vec{\xi}/3 + \vec{t_c} \times \vec{a}_{21}\right). \end{aligned} \tag{A.7}$$

Finally, the four-point interactions are encountered in the bending energy between two adjacent faces (eq. 3.6). Figure A.1 shows a sample geometry of two adjacent triangular elements of the membrane network. The triangle normals are defined as $\vec{\xi} = \vec{a}_{21} \times \vec{a}_{31}$, $\vec{\zeta} = \vec{a}_{34} \times \vec{a}_{24}$ and the corresponding areas as $A_1 = |\vec{\xi}|/2$, $A_2 = |\vec{\zeta}|/2$. The bending energy results in the following expression

$$f_{s_i} = -\frac{\partial\left[k_b(1-\cos(\theta-\theta_0))\right]}{\partial s_i} = -k_b \sin(\theta-\theta_0)\frac{\partial \theta}{\partial s_i}, \tag{A.8}$$

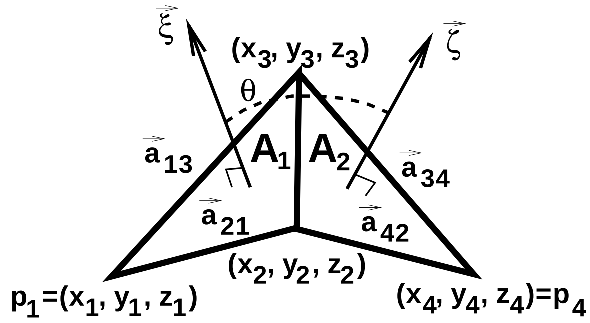

Figure A.2: A sketch of two adjacent triangular elements of the network.

where θ is the angle between the normals $\vec{\xi}$ and $\vec{\zeta}$. Here $\sin(\theta - \theta_0)$ can be expanded as $\sin\theta\cos\theta_0 - \cos\theta\sin\theta_0$, where $\cos\theta = (\frac{\vec{\xi}}{|\vec{\xi}|} \cdot \frac{\vec{\zeta}}{|\vec{\zeta}|})$ and $\sin\theta = \pm\sqrt{1-\cos^2\theta}$ taken with "+" if $([\vec{\xi} - \vec{\zeta}] \cdot [\vec{t}_c^1 - \vec{t}_c^2]) \geq 0$ and with "−" otherwise; $\vec{t}_c^1$ and $\vec{t}_c^2$ are the center of mass vectors of triangles 1 and 2, respectively. Further, we find the derivative of θ with respect to s_i given by

$$\frac{\partial\theta}{\partial s_i} = \frac{\partial\left[\arccos(\frac{\vec{\xi}}{|\vec{\xi}|} \cdot \frac{\vec{\zeta}}{|\vec{\zeta}|})\right]}{\partial s_i} = -\frac{1}{\sqrt{1-\cos^2\theta}}\frac{\partial\left[\frac{\vec{\xi}}{|\vec{\xi}|} \cdot \frac{\vec{\zeta}}{|\vec{\zeta}|}\right]}{\partial s_i}. \tag{A.9}$$

Analytical calculation of the derivatives above results in the nodal forces for the four-point interactions (see fig. A.2) as follows

$$\begin{aligned}
(f_{x_1}, f_{y_1}, f_{z_1}) &= b_{11}\left(\vec{\xi}\times\vec{a}_{32}\right) + b_{12}\left(\vec{\zeta}\times\vec{a}_{32}\right),\\
(f_{x_2}, f_{y_2}, f_{z_2}) &= b_{11}\left(\vec{\xi}\times\vec{a}_{13}\right) + b_{12}\left(\vec{\xi}\times\vec{a}_{34} + \vec{\zeta}\times\vec{a}_{13}\right) + b_{22}\left(\vec{\zeta}\times\vec{a}_{34}\right),\\
(f_{x_3}, f_{y_3}, f_{z_3}) &= b_{11}\left(\vec{\xi}\times\vec{a}_{21}\right) + b_{12}\left(\vec{\xi}\times\vec{a}_{42} + \vec{\zeta}\times\vec{a}_{21}\right) + b_{22}\left(\vec{\zeta}\times\vec{a}_{42}\right),\\
(f_{x_4}, f_{y_4}, f_{z_4}) &= b_{12}\left(\vec{\xi}\times\vec{a}_{23}\right) + b_{22}\left(\vec{\zeta}\times\vec{a}_{23}\right),
\end{aligned} \tag{A.10}$$

where $b_{11} = -\beta_b\cos\theta/|\vec{\xi}|^2$, $b_{12} = \beta_b/(|\vec{\xi}||\vec{\zeta}|)$, and $b_{22} = -\beta_b\cos\theta/|\vec{\zeta}|^2$ with $\beta_b = k_b(\sin\theta\cos\theta_0 - \cos\theta\sin\theta_0)/\sqrt{1-\cos^2\theta}$.

Appendix B

Analysis of the macroscopic properties of a hexagonal network

The derivation of shear and area-compression moduli for a regular hexagonal network is presented below. The Cauchy stress of an element of the hexagonal network shown in figure 3.2 is given by equation (3.9). The linear shear modulus is derived from a network deformation by applying a small shear strain γ as follows

$$\vec{r'} = \vec{r}\mathbf{E} = (r_x + r_y \frac{\gamma}{2};\ r_x \frac{\gamma}{2} + r_y), \qquad \mathbf{E} = \begin{pmatrix} 1 & \gamma/2 \\ \gamma/2 & 1 \end{pmatrix}, \tag{B.1}$$

and hence, $\vec{a'} = (a_x + a_y \frac{\gamma}{2};\ a_x \frac{\gamma}{2} + a_y)$ and $\vec{b'} = (b_x + b_y \frac{\gamma}{2};\ b_x \frac{\gamma}{2} + b_y)$ in figure 3.2. The shear deformation is area-preserving, and therefore only spring forces in equation (3.9) contribute to the network shear modulus. Expansion of the shear stress τ'_{xy} in Taylor series provides the linear shear modulus of the network as follows

$$\tau'_{xy} = \tau_{xy} + \left.\frac{\partial \tau'_{xy}}{\partial \gamma}\right|_{\gamma=0} \gamma + O(\gamma^2), \quad \mu_0 = \left.\frac{\partial \tau'_{xy}}{\partial \gamma}\right|_{\gamma=0}, \tag{B.2}$$

and thus,

$$\mu_0 = -\frac{1}{2A_0} \left.\frac{\partial \left[\frac{f(a')}{a'} a'_x a'_x + \frac{f(b')}{b'} b'_x b'_x + \frac{f(c')}{c'} c'_x c'_y \right]}{\partial \gamma}\right|_{\gamma=0}. \tag{B.3}$$

We differentiate the first spring term to obtain

$$\left.\frac{\partial\left(\frac{f(a')}{a'}a'_x a'_y\right)}{\partial\gamma}\right|_{\gamma=0} = \left.\left(\frac{\partial\frac{f(a')}{a'}}{\partial a'}\frac{\partial a'}{\partial\gamma}a'_x a'_y + \frac{f(a')}{a'}\frac{\partial a'_x a'_y}{\partial\gamma}\right)\right|_{\gamma=0} = \\ = \frac{(a_x a_y)^2}{a}\left.\frac{\partial\frac{f(a')}{a'}}{\partial a'}\right|_{a'=a} + \frac{f(a)a}{2}, \tag{B.4}$$

since $a'|_{\gamma=0} = a$, $\left.\frac{\partial a'}{\partial\gamma}\right|_{\gamma=0} = \frac{a_x a_y}{a}$, and $\left.\frac{\partial a'_x a'_y}{\partial\gamma}\right|_{\gamma=0} = a^2/2$. Note that $a = b = c = l_0$ and $f(a) = f(b) = f(c)$. In addition, using a geometrical argument, it can be shown that $(a_x a_y)^2 + (b_x b_y)^2 + (c_x c_y)^2 = 2A_0^2$. Hence, the network shear modulus can be calculated as

$$\mu_0 = -\frac{A_0}{l_0}\left.\frac{\partial\frac{f(r)}{r}}{\partial r}\right|_{r=l_0} - \frac{3f(l_0)l_0}{4A_0}, \tag{B.5}$$

where $A_0 = \sqrt{3}l_0^2/4$. Substitution of different spring forces into the equation above yields relations between corresponding spring parameters of the network and its macroscopic shear modulus outlined in equation (3.10).

The linear area-compression modulus K can be calculated from a small area expansion of the network element shown in figure 3.2. The in-plane pressure of the element is given in equation (3.11) including several contributions such as springs, hydrostatic elastic energy, and local and global area constraints. The corresponding area-compression modulus K is defined as

$$K = -A_0\left.\frac{\partial P}{\partial A}\right|_{A=A_0} = -\left.\frac{l_0}{2}\frac{\partial P}{\partial l}\right|_{l=l_0}. \tag{B.6}$$

Thus, the springs' contribution to the area-compression modulus is given by

$$K_S = -\frac{\sqrt{3}l_0}{2}\left.\frac{\partial\frac{f(l)}{l}}{\partial l}\right|_{l=l_0}, \tag{B.7}$$

while contributions from hydrostatic elastic energy, and local and global area constraints are as follows

$$K_A = \frac{q(q+1)C_q}{A_0^{q+1}} + k_a + k_d. \tag{B.8}$$

The sum of K_S and K_A for different network models (see section 3.2) yields the area-compression moduli outlined in equation (3.13).

Appendix C

Reflections of moving particles at moving triangular faces on the RBC surface

In order to prevent fluid particles to cross the RBC membrane, we perform reflections of them at the RBC surface. In addition, this allows us to have non-mixing external and internal fluids with different viscosities. The particle reflections are done at the triangular plaquettes that form the RBC membrane. Figure C.1 shows a moving particle **p** and a triangular element with vertices $\{\mathbf{s}_1, \mathbf{s}_2, \mathbf{s}_3\}$. The reflections are performed every time

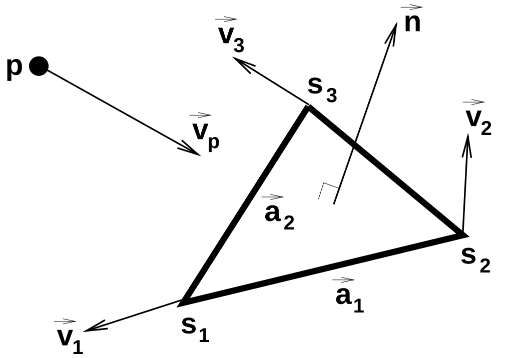

Figure C.1: Sketch of a moving particle **p** and a triangular element $\{\mathbf{s}_1, \mathbf{s}_2, \mathbf{s}_3\}$.

step of temporal integration since in DPD each particle moves ballistically (with constant velocity) within a single time step Δt. Hence, figure C.1 depicts a single time step, where each vertex $\mathbf{s}_i = (x_i, y_i, z_i)$, $i = 1, 2, 3$ of the triangle is moving with its constant velocity $\vec{v}_i$, while the particle $\mathbf{p} = (x_p, y_p, z_p)$ has the velocity $\vec{v}_p$. Motion of the vertices and the particle is given by

$$\begin{aligned} \mathbf{s}_i &= \mathbf{s}_i^o + \vec{v}_i t, \qquad i = 1, 2, 3, \\ \mathbf{p} &= \mathbf{p}^o + \vec{v}_p t, \end{aligned} \tag{C.1}$$

where $t \in [0, \Delta t]$ is time and the superscript "o" denotes a position at the beginning of the time step or at $t = 0$. The edge vectors $\vec{a}_1$, $\vec{a}_2$ and the triangle normal are defined as follows

$$\begin{aligned} \vec{a}_1 &= \mathbf{s}_2 - \mathbf{s}_1 = \mathbf{s}_2^o - \mathbf{s}_1^o + (\vec{v}_2 - \vec{v}_1)t = \vec{a}_1^o + \vec{d}_1 t, \\ \vec{a}_2 &= \mathbf{s}_3 - \mathbf{s}_1 = \mathbf{s}_3^o - \mathbf{s}_1^o + (\vec{v}_3 - \vec{v}_1)t = \vec{a}_2^o + \vec{d}_2 t, \\ \vec{n} &= \vec{a}_1 \times \vec{a}_2 = \vec{a}_1^o \times \vec{a}_2^o + \left(\vec{a}_1^o \times \vec{d}_2 + \vec{d}_1 \times \vec{a}_2^o\right) t + \left(\vec{d}_1 \times \vec{d}_2\right) t^2. \end{aligned} \tag{C.2}$$

As the initial check for a possible reflection within one time step, we verify that the particle trajectory has crossed the moving plane defined by the triangle vertices. The equation of the plane is given by

$$(\vec{n} \cdot \mathbf{s}) + n_d = n_x x + n_y y + n_z z + n_d = 0, \tag{C.3}$$

where n_d can be found as $-(\vec{n} \cdot \mathbf{s}_i)$ for any $i = 1, 2, 3$. To determine if the particle is on the positive or negative side of the plane normal, we define the following dot-products

$$b^o = \left(\vec{n}^o \cdot (\mathbf{p}^o - \mathbf{s}_1^o)\right), \qquad b^{\Delta t} = \left(\vec{n}^{\Delta t} \cdot (\mathbf{p}^{\Delta t} - \mathbf{s}_1^{\Delta t})\right), \tag{C.4}$$

where the superscript "Δt" denotes that the positions are at the time $t = \Delta t$. Thus, if the product $b^o b^{\Delta t}$ is positive, the particle did not cross the moving plane and no reflection is needed. Otherwise, if $b^o b^{\Delta t} \leq 0$, we find the intersection between the particle trajectory and the plane by solving the following equation with respect to t

$$(\vec{n} \cdot (\mathbf{p} - \mathbf{s}_1)) = 0. \tag{C.5}$$

Note that the equation above is cubic in t, and its roots are found using the Newton-Raphson method (see e.g., [163]). After the time t' of the intersection is obtained, the point of intersection can be calculated as $\mathbf{p}' = \mathbf{p}^o + \vec{v}_p t'$.

The point $\mathbf{p}'$ corresponds to the intersection of the particle path and the moving plane. An additional check, that $\mathbf{p}'$ is in the triangle, is necessary. For this we represent the vector $\vec{g}' = \mathbf{p}' - \mathbf{s}_1'$ in the coordinate system defined by $\vec{a}_1'$ and $\vec{a}_2'$ as follows

$$\vec{g}' = \xi \vec{a}_1' + \zeta \vec{a}_2', \tag{C.6}$$

where ξ and ζ are some scalars. Taking the dot-product of the equation above with $\vec{a}_1'$ and $\vec{a}_2'$, respectively, gives us the system of two equations from which ξ and ζ can be found as follows

$$\xi = \frac{(\vec{g}' \cdot \vec{a}_1')\,|\vec{a}_2'|^2 - (\vec{g}' \cdot \vec{a}_2')\,(\vec{a}_1' \cdot \vec{a}_2')}{|\vec{a}_1'|^2\,|\vec{a}_2'|^2 - (\vec{a}_1' \cdot \vec{a}_2')^2}, \qquad \zeta = \frac{(\vec{g}' \cdot \vec{a}_2')\,|\vec{a}_1'|^2 - (\vec{g}' \cdot \vec{a}_1')\,(\vec{a}_1' \cdot \vec{a}_2')}{|\vec{a}_1'|^2\,|\vec{a}_2'|^2 - (\vec{a}_1' \cdot \vec{a}_2')^2}. \tag{C.7}$$

Then, if $\xi \geq 0$, $\zeta \geq 0$, and $\xi + \zeta \leq 1$, the point $\mathbf{p}'$ lies within the triangle and the particle reflection has to be made.

The bounce-back reflection of the particle is performed as follows

$$\begin{aligned} \vec{v}_p^{new} &= 2\vec{v}' - \vec{v}_p, \qquad \vec{v}' = (1 - \xi - \zeta)\vec{v}_1 + \xi \vec{v}_2 + \zeta \vec{v}_3, \\ \mathbf{p}^{new} &= \mathbf{p}' + (\Delta t - t')\vec{v}_p^{new}, \end{aligned} \tag{C.8}$$

where the superscript “new“ denotes the new position and velocity of the particle after reflection. The described procedure is implemented in a loop to account for multiple reflections within one time step. In addition, for each fluid particle a linked-list of the triangles in a neighborhood of the particle is built to exclude unnecessary reflection checks and to substantially reduce computational cost.

Appendix D

Manual for creating initial conditions to be used in simulations

The code **data_domain.cpp** generates the initial conditions for DPD simulations. It reads the input file **domain.dat** where a configuration for the initial conditions has to be specified. The initial conditions are written to the file **data.out**. The input file domain.dat consists of the following

```
=====================================================
1:      589980 224100 149400 224100
2:      2 2 1 1
3:      1.0
4:      1.0
5:      0.0 100.0 -1.6 31.6 -1.6 51.6
6:      1     (number of lattice subdomains)
7:      1 0.25 99.75 0.0 0.0 0.0 50.0 200 1 101 0.0
8:      1     (number of random subdomains)
9:      1 0.01 99.99 0.01 29.99 0.01 49.99 420000 0.0
10:     1     (number of polymer subdomains)
11:     2 1 0.2 9.8 0.2 9.8 0.2 9.8 1 100 0.7 0 0.0
12:     1     (number of cell subdomains)
```

```
13:    2 2 1 1 0.0 0.0 0.0 0.0 0.0 0.0 1 1.0 0.0 rbc.dat
14:    1      (number of lattice cell subdomains)
15:    2 2 1 1 5.0 45.0 5.0 25.0 5.0 45.0 5 3 5 1.0 0.0 rbc.dat
16:    1      (number of template cell subdomains)
17:    1 1 2 2 1 1 1.3 23.2 0.0 0.0 0.0 0.0 10 1 1 0.8 0.0 rbc.dat template.dat
18:    1      (number of border subdomains)
19:    1 0 0.0 100.0 0.0 1.5 -26.5 26.5 0.0 -1.5 25.0 1 0 0 0.0
20:    box.dat
=======================================================
```

The very left column denotes the line numbers of the file.

Line 1: 589980 224100 149400 224100 - the total number of atoms, bonds, angles, and dihedrals in a DPD simulation.

Remarks: These numbers are read and written to the output file data.out. However, data_domain.cpp calculates and prints to the command window the correct number of atoms, bonds, angles, and dihedrals defined by a user. Therefore, if the values in domain.dat differ from the ones data_domain.cpp prints out, they need to be corrected either manually in data.out or by changing them in domain.dat and rerunning data_domain.cpp.

Line 2: 2 2 1 1 - the number of atom, bond, angle, and dihedral types used in a simulation, e.g., two atom types are numbered as type 1 and type 2.

Lines 3 and 4: 1.0 - the particle masses defined for each atom type.

Remarks: Note that the number of lines for particle masses has to match the total number of atom types in line 2. Therefore, if the number of atom types is 3, three lines have to be included in domain.dat to define all particle masses.

Line 5: 0.0 100.0 -1.6 31.6 -1.6 51.6 - x_{min}, x_{max}, y_{min}, y_{max}, z_{min}, z_{max} are the dimensions of the global computational domain defined as a rectangular cuboid.

Line 6: 1 (number of lattice subdomains) - the number of subdomains of single DPD particles placed on a lattice which are defined in the subsequent lines.

Line 7: 1 0.25 99.75 0.0 0.0 0.0 50.0 200 1 101 0.0 - atom type, x_{min}, x_{max}, y_{min}, y_{max}, z_{min}, z_{max}, N_x, N_y, N_z, and atom charge which define a lattice subdomain of single DPD particles. As an example, N_x DPD particles are placed equidistantly between x_{min} and x_{max} with the first one placed at x_{min} and the last one at x_{max} for the fixed y and z. Thus, this subdomain creates the total number of particles equal to $N_xN_yN_z$.

Remarks: The subdomains have to be fully inside the global domain defined in line 5. The number of subdomains in line 6 has to match the number of subsequent lines which define different subdomains. If the number of subdomains in line 6 is set to zero, line 7 has to be deleted.

Line 8: 1 (number of random subdomains) - the number of subdomains of single DPD particles placed randomly within the defined rectangular cuboid regions.

Line 9: 1 0.01 99.99 0.01 29.99 0.01 49.99 420000 0.0 - atom type, x_{min}, x_{max}, y_{min}, y_{max}, z_{min}, z_{max}, N, and atom charge. N DPD particles are placed randomly within the defined rectangular cuboid.

Remarks: The same restrictions as in line 7 are applied.

Line 10: 1 (number of polymer subdomains) - the number of subdomains of linear bead-spring polymers.

Line 11: 2 1 0.2 9.8 0.2 9.8 0.2 9.8 1 100 0.7 0 0.0 - atom type, bond type, x_{min}, x_{max}, y_{min}, y_{max}, z_{min}, z_{max}, N_p, N_b, l_0, index, and atom charge, where N_p is the number of polymers, N_b is the number of beads in a single polymer, and l_0 is the distance between any two connected beads. N_p polymers are placed in the defined rectangular cuboid. If index=0 each polymer is generated as a three-dimensional random walk with the step size l_0. If index=1, 2, or 3 each polymer is aligned with the x, y, or z directions, respectively.

Remarks: The same restrictions as in line 7 are applied. Also, note that for index=1, 2, 3 the starting bead for each polymer is placed randomly within the defined rectangular cuboid, while the other beads can be potentially placed outside the cuboid depending on N_b and l_0 since $x_{i+1} = x_i + l_0$ for $i = 1...N_b - 1$.

Line 12: 1 (number of cell subdomains) - the number of subdomains of cells placed randomly within the defined rectangular cuboid regions.

Line 13: 2 2 1 1 0.0 0.0 0.0 0.0 0.0 0.0 1 1.0 0.0 rbc.dat - atom type, bond type, angle type, dihedral type, x_{min}, x_{max}, y_{min}, y_{max}, z_{min}, z_{max}, N_c, scale, atom charge, and cell file, where N_c is the number of cells whose center-of-masses are placed randomly within the defined rectangular cuboid. The file rbc.dat contains the topology of a cell and will be provided. The parameter "scale" defines cell scaling such that the coordinates of cell vertices with respect to its center-of-mass are multiplied by the scale.

Remarks: The same restrictions as in line 7 are applied. In addition, the cell center-of-mass is placed within the defined rectangular cuboid, not the whole cell. The code will check for overlapping cells within a subdomain, but not for overlapping cells belonging to different subdomains. Thus, the dimensions of separate subdomains have to be chosen carefully. Also, note that if many cells have to be placed within a small subdomain, the code may be running an infinite loop since at some point there may be no free space left to insert a new cell due to the non-overlapping constraint. In this case, the code has to be stopped and the scale parameter needs to be set to a lower value.

Line 14: 1 (number of lattice cell subdomains) - the number of subdomains of cells whose center-of-masses are placed on a lattice.

Line 15: 2 2 1 1 5.0 45.0 5.0 25.0 5.0 45.0 5 3 5 1.0 0.0 rbc.dat - atom type, bond type, angle type, dihedral type, x_{min}, x_{max}, y_{min}, y_{max}, z_{min}, z_{max}, N_x^c, N_y^c, N_z^c, scale, atom charge, and cell file, where N_x^c, N_y^c, and N_z^c are the cell numbers for the lattice in each direction (see description for line 7). The "scale" and cell file are the same as in line 13.

Remarks: The same restrictions as in line 7 are applied. In addition, cell overlapping is not checked by the code. Therefore, the lattice dimensions have to be carefully chosen to guarantee no overlap among cells.

Line 16: 1 (number of template cell subdomains) - the number of subdomains of cell templates whose center-of-masses are placed on a lattice. The template file describes a cell filled and surrounded by different solvents and will be provided.

Line 17: 1 1 2 2 1 1 1.3 23.2 0.0 0.0 0.0 0.0 10 1 1 0.8 0.0 rbc.dat template.dat - atom type of the external solvent, atom type of the internal solvent, atom type of the cell vertices, bond type, angle type, dihedral type, x_{min}, x_{max}, y_{min}, y_{max}, z_{min}, z_{max}, N_x^c, N_y^c, N_z^c, scale, atom charge, cell file, and template file, where N_x^c, N_y^c, and N_z^c are the numbers for the lattice in each direction (see description for line 7). The "scale" here scales the whole template including the cell and the solvents.

Remarks: The same restrictions as in line 7 are applied. In addition, template overlapping is not checked by the code. Therefore, the lattice dimensions have to be carefully chosen to guarantee no overlap among templates.

Line 18: 1 (number of boundary subdomains) - the number of subdomains of boundary particles which are used to create solid boundaries constructed of frozen DPD particles.

Line 19: 1 0 0.0 100.0 0.0 1.5 -26.5 26.5 0.0 -1.5 25.0 1 0 0 0.0 - definition of a boundary subdomain which can be a rectangular cuboid or a cylindrical annulus region.

Note that the defined region is extracted from the boundary file box.dat defined in line 20.

Rectangular cuboid: atom type, 0, x_{min}, x_{max}, y_{min}, y_{max}, z_{min}, z_{max}, displacement in x, displacement in y, displacement in z, dummy, dummy, dummy, and atom charge. The particles within the defined cuboid are extracted from the boundary file box.dat defined in line 20 and are shifted in x, y, and z by the defined displacements.

Cylindrical annulus: atom type, 1, x_{min}, x_{max}, r_{min}, r_{max}, dummy, dummy, displacement in x, displacement in y, displacement in z, orientation, dummy, dummy, and atom charge, where r_{min} and r_{max} are the inner and outer radii of the annulus. Note that the central axis of the cylindrical annulus is always defined by two points $\{x_{min}, 0, 0\}$ and $\{x_{max}, 0, 0\}$. The particles within the defined cylindrical annulus are extracted from the boundary file box.dat defined in line 20 and are shifted in x, y, and z by the defined displacements. The orientation parameter allows to change the annulus alignment by swapping the order of writing x, y, and z into the output file. Thus, if orientation=1, 2, or 3 the cylindrical annulus is aligned with x, y, or z, respectively.

Remarks: The same restrictions as in line 7 are applied.

Line 20: box.dat - the boundary file from which all defined boundary regions are extracted. This file needs to be created separately.

Remarks: The coordinates of particles written in box.dat have to be in agreement with the proposed regions to be extracted. Otherwise, no boundary particles may be created.

The file data_domain.cpp can be compiled as “g++ data_domain.cpp -o data_domain” and be run as “./data_domain”.

Appendix E

Manual for the developed code

The developed code is based on LAMMPS Molecular Dynamics Simulator [2] distributed by Sandia National Laboratories as an open source code under the terms of the GPL license. The DPD code was built up on top of LAMMPS. Therefore, this manual describes only new implemented commands which are not included in the standard LAMMPS distribution. For the commands which are implemented in the standard LAMMPS distribution we will refer the reader to the on-line LAMMPS manual which can be found at "http://lammps.sandia.gov".

An input file required for running LAMMPS is called **in.cell** here; however, any name can be chosen. A sample input file in.cell is given below

```
=====================================================
1:      dimension 3
2:      units lj
3:      boundary p f f
4:      atom_style full 1
5:      neighbor 0.3 bin
6:      neigh_modify every 10 check no exclude type 3 3
7:      special_bonds 0.0 0.0 0.0
8:      lattice sc 1.0
9:      read_data data.cell
10:     group cells molecule > 0
11:     group wall type 3
```

12: group sol subtract all cells wall

13: group move join sol cells

14: group inner subtract cells cells

15: **bond_style wlc/pow/all/visc**

16: **bond_coeff 1 0.094523620928369 2.2 100 2.0 30.0 90.0**

17: **angle_style rbc**

18: **angle_coeff 1 0.0 1 4900.0 132.868 5000.0 92.452 100.0 0.14**

19: **dihedral_style bend**

20: **dihedral_coeff 1 6.117379786975386 0.0**

21: **pair_style dpd/verlet 1.5 1548482**

22: **pair_coeff 1 1 4.0 30.0 2.381473757088688 1.5 0.25**

23: **pair_coeff 1 2 2.0 45.0 2.916697770348037 1.5 0.25**

24: **pair_coeff 1 3 4.0 30.0 2.381473757088688 1.5 0.25**

25: **pair_coeff 2 2 2.0 30.0 2.381473757088688 0.5 0.25**

26: **pair_coeff 2 3 2.0 45.0 2.916697770348037 1.5 0.25**

27: **pair_coeff 3 3 0.0 0.0 0.0 1.0 1.0**

28: **fix 1 move dpd/verlet 0.5**

29: **fix 2 outer bound/rbc inner cells 0 1.0 1.7**

30: **fix 3 move solid/bound plane.dat**

31: **fix 4 move addforce 0 1.5 0.0 0.0**

32: timestep 0.00125

33: restart 500000 restart

34: **velocity_cyl_out move 1 25 1 20000 1 50000 0 50.304 0 5.155 0 5 vel**

35: **density_cyl_out move 1 25 1 20000 1 50000 0 50.304 0 5.155 0 5 dens**

36: temperature fl move partial 0 1 1

37: thermo_modify temp fl lost warn flush yes

38: thermo 1000

39: dump 1 cells atom 5000 cell.dump

40: dump_modify 1 scale no image do flush yes

41: run 3000000

===

Note that the very left column denotes the line numbers of the file. The lines in bold correspond to the newly implemented commands and will be explained below. The descriptions for other commands can be found in the LAMMPS manual [2]. This example file allows a simulation run of blood flow in a microtube with an appropriate input file data.cell (line 9) which has to be created separately (see appendix D for details).

The first word in each line is a command name which is followed by several parameters or options. Thus, each explanation describes a command first and after that identifies its parameters.

Line 4: **atom_style full 1** - the atom style used in simulations.

Syntax: atom_style style index

The atom_style command is a part of the original LAMMPS, but it was changed. In simulations with RBCs "style"=full, while a description for other atom styles can be found in the LAMMPS manual. In DPD simulations "index"=1 indicating that the code has to communicate particle's velocity information among neighboring processors.

Line 15: **bond_style wlc/pow/all/visc** - the bond style used in simulations.

Syntax: bond_style style

The bond_style command is a part of the original LAMMPS, but new additional bond styles were implemented. "Style"=wlc/pow/all/visc corresponds to the WLC-POW spring model defined in equations (3.3) and (3.5) with the viscous contribution in equations (3.24) and (3.25).

Line 16: **bond_coeff 1 0.094523620928369 2.2 100 2.0 30.0 90.0** - the bond parameters for the previously defined bond style.

Syntax: bond_coeff bond_type k_BT x_0 μ_0 m γ^C γ^T

Parameters for the WLC-POW spring model with viscous contribution which are defined in equations (3.3), (3.5), (3.24), and (3.25). μ_0 is the macroscopic shear modulus of the RBC membrane defined in equation (3.10). Note that the parameters p and k_p in equations (3.3), (3.5) are automatically calculated inside the code for the targeted μ_0.

Line 17: **angle_style rbc** - the angle style used in simulations.

Syntax: angle_style style

The angle_style command is a part of the original LAMMPS, but new additional angle styles were implemented. "Style"=rbc is related to the last term in equation (3.2) and the area and volume constraints in equation (3.7).

Line 18: **angle_coeff 1 0.0 1 4900.0 132.868 5000.0 92.452 100.0 0.14** - the angle parameters for the previously defined angle style.

Syntax: angle_coeff angle_type C_q q k_a A_0^{tot} k_v V_0^{tot} k_d A_0

Parameters for the last term in equation (3.2) and the area and volume constraints in equation (3.7). Note that for the stress-free RBC model $C_q = 0.0$ and A_0 is a dummy parameter which is ignored.

Line 19: dihedral_style bend - the dihedral style used in simulations.

Syntax: dihedral_style style

The dihedral_style command is a part of the original LAMMPS, but new additional dihedral styles were implemented. "Style"=bend corresponds to the RBC energy defined in equation (3.6).

Line 20: dihedral_coeff 1 6.117379786975386 0.0 - the dihedral parameters for the previously defined dihedral style.

Syntax: dihedral_coeff dihedral_type k_b θ_0

Parameters for the RBC bending energy defined in equation (3.6).

Line 21: pair_style dpd/verlet 1.5 1548482 - the style of pair interactions used in simulations.

Syntax: pair_style dpd/verlet r_c seed

The pair_style command is a part of the original LAMMPS, but new additional pair styles were implemented. "Style"=dpd/verlet corresponds to the three DPD forces defined in equation (2.8). r_c is the DPD cutoff radius (see section 2.2.2), and "seed" is used to set different seeds for the random number generator on distinct processors.

Lines 22-27: pair_coeff 1 1 4.0 30.0 2.381473757088688 1.5 0.25 - the pair interaction parameters for the previously defined pair style.

Syntax: pair_coeff i j a γ σ r_c k

Parameters for DPD pair interactions between particles of atom type i and particles of atom type j. Other parameters define DPD forces which are described in section 2.2.2.

Lines 28-31: fix 1 move dpd/verlet 0.5 - the fix command describes various manipulations of the simulated system by a user.

Syntax: fix fixID group name parameters

"fixID" is the unique fix number, "group" is a group of particles to which this fix is applied, "name" is the fix unique name, and "parameters" is a list of the fix parameters.

fix 1 move dpd/verlet 0.5 - the modified velocity-Verlet algorithm with $\lambda = 0.5$ [92].

fix 2 outer bound/rbc inner cells 0 1.0 1.7 - implements dynamic bounce-back reflections of particles on the RBC membrane. “Outer” is the group of particles which are reflected on the outside of the RBC membrane, “inner” is the group of particles which are reflected from the inside of the RBC membrane, and “cells” is the group of RBCs. “0” indicates bounce-back reflections. “1.0” is the maximum distance of particles from the RBCs membrane within which particle reflections are considered. “1.7” is the cutoff radius for communications of RBC vertices among neighboring processors.

fix 3 move solid/bound plane.dat - implements particle reflections and solid boundary conditions (BCs) which are described in the file “plane.dat” with the following syntax

```
========================================================
5       - number of boundary shapes
1.5 0.5 0      - distance and reflection specifications
1 1.0 1.0 4.0 2 250 0 group      - adaptive shear force
1 100 1.0 0 force.dat group      - pressure force
“five lines that describe boundary shapes“
========================================================
```

Distance and reflection specifications: r_{norm} r_{tang} $refl$ - First two numbers are the normal and tangential maximum distances of particles from boundary shapes within which particle reflections and BCs are considered. “$refl$”=0 defines bounce-back reflections, while “$refl$”=1 corresponds to specular reflections.

Adaptive shear force: on/off r_s α exponent N_d iter side group - see section 2.2.1 for details. “exponent” is the exponent of the weight function and N_d is the number of statistical cells in the normal direction to a boundary, where flow velocities are sampled. “iter” is the number of time steps between the adaptive shear force updates and “group” is the group of particles to which shear force is applied. “side”=0, 1, and 2 means that the adaptive shear force is applied on both sides, on the side of the shape normal, and on the opposite side of the shape normal, respectively.

Pressure force: on/off N_p r_p side force.dat group - applies the pressure force defined in equation (2.7) and written into the file force.dat with N_p entries. “side” and “group” are the same as for the adaptive shear force.

Boundary shapes: The possible boundary shapes are triangular plaquette (index 1), parallelogram (index 2), cylinder (index 3), and sphere (index 4). Note that the number of lines describing boundary shapes has to match the number of shapes defined in line 1 of the plane.dat file.

1) Triangular plaquette: 1 x_0 y_0 z_0 x_1 y_1 z_1 x_2 y_2 z_2 v_x v_y v_z side - $\{x_0,y_0,z_0\}$, $\{x_1,y_1,z_1\}$, $\{x_2,y_2,z_2\}$ are the vertices of a triangle and $\{v_x,v_y,v_z\}$ is the velocity at the boundary defined by the triangle. "side"=0, 1, 2, and 3 defines no particle reflections, reflections on the side of the triangle normal, reflections on the opposite side of the triangle normal, and on both sides, respectively. The triangle normal is defined as $\vec{n} = ((\vec{x_1} - \vec{x_0}) \times (\vec{x_2} - \vec{x_0}))$.

2) Parallelogram: 2 x_0 y_0 z_0 x_1 y_1 z_1 x_2 y_2 z_2 v_x v_y v_z N_1 N_2 side - $\{x_0,y_0,z_0\}$, $\{x_1,y_1,z_1\}$, $\{x_2,y_2,z_2\}$ are the three vertices of a triangle which corresponds to a half of the parallelogram and $\{v_x,v_y,v_z\}$ is the velocity at the boundary defined by the parallelogram. N_1 and N_2 define a regular mesh on the parallelogram to apply adaptive shear force in each cell of the mesh separately. The "side" parameter is the same as for triangular plaquette.

3) Cylinder: 3 x_0 y_0 z_0 x_1 y_1 z_1 r v_x v_y v_z N_z N_θ side - $\{x_0,y_0,z_0\}$ and $\{x_1,y_1,z_1\}$ define cylinder axes and r is the cylinder radius. N_z and N_θ define a regular mesh on the cylinder. The "side" parameter: 0 - none, 1 - outside, 2 - inside, and 3 - both sides.

4) Sphere: 4 x_0 y_0 z_0 r v_x v_y v_z N_ϕ N_θ side - $\{x_0,y_0,z_0\}$ is the sphere center and r is the sphere radius. The "side" parameter is the same as for cylinder.

fix 4 move addforce 0 1.5 0.0 0.0 - exerts force on each particle in the defined group. Syntax: fixID group addforce 0 f_x f_y f_z.

Lines 34-35: velocity_cyl_out move 1 25 1 20000 1 50000 0 50.304 0 5.155 0 5 vel - defines a mesh for statistics accumulation.

Syntax: velocity_cyl_out group N_x N_r N_θ start each every x_{min} x_{max} y_0 r z_0 dummy name The mesh is defined in the cylindrical coordinates, where the cylinder has to be aligned with the x direction. N_x, N_r, and N_θ are the divisions along the x, radial, and angle coordinates. "start" is the time step of the sampling start, "each" is the sampling frequency (for example, sampling every time step if each=1), and "every" is the total number of time steps in the sample. "name" corresponds to the beginning of the written output file. The ending of the file is automatically added as ".N_t.plt" where N_t is the current time step. The above command samples flow velocity. In addition, particle density can be sampled as density_cyl_out with the same syntax. The sampling mesh can be also defined in the Cartesian coordinates as follows

Syntax: velocity_out group N_x N_y N_z start each every x_{min} x_{max} y_{min} y_{max} z_{min} z_{max}

name

Here, a rectangular cuboid is defined with the number of cells N_x, N_y, and N_z in each direction. Many other flow parameters can be sampled with this command: density (density_out), temperature (temperature_out), stress (stress_out), etc.

In addition, we include several commands that were implemented to simulate adhesion of WBCs and Pf-parasitized RBCs.

1) **bond_style break/visc** - defines bond dissociation rules described in section 4.4.1.

2) **bond_coeff bondID parameters** - the bond parameters for the previously defined bond style. The choice of parameters is as follows

i) rbc $k_B T$ x_0 μ_0 m γ^C γ^T

ii) ligand k_s l_0 k_{off}^0 σ_{off} $k_B T$ d_{off}

where the first option defines bond parameters of a RBC described in **line 16:** above. The second option describes bond parameters of adhesive interactions which can be found in section 4.4.1.

3) **pair_style dpd/create** l_t b_t **each** r_c - defines bond formation rules described in section 4.4.1. l_t is the atom type of ligand particles, b_t is the bond type of adhesion bonds, and r_c is the DPD cutoff radius. "each" characterizes active receptors (available for binding) on the RBC. Thus, if the atom ID of a RBC vertex is divisible by "each", this vertex represents an active receptor site.

4) **pair_coeff i j parameters** - the pair interaction parameters for the previously defined pair style. The choice of parameters is as follows

i) dpd a γ σ r_c k

ii) create k_s l_0 k_{on}^0 σ_{on} $k_B T$ d_{on}

iii) stick D_e r_0 β r_c

iv) lj ϵ σ_{lj} γ σ r_c k

where i) defines standard DPD interactions described in **lines 22-27:** above. ii) describes bond parameters of adhesive interactions which can be found in section 4.4.1. iii) defines Morse interactions given by the Morse force

$$F(r) = 2D_e\beta\left[\exp\left(2\beta(r_0 - r)\right) - \exp\left(\beta(r_0 - r)\right)\right], \tag{E.1}$$

where D_e is the well depth of the potential, r_0 is the equilibrium distance, and β characterizes the range of attractive interactions. Finally, iv) defines Lennard-Jones interactions with the DPD thermostat which are described in section 2.2.1.

More detailed information on how to compile, use, and run LAMMPS we refer the reader to the on-line LAMMPS manual which can be found at “http://lammps.sandia.gov”. In addition, a more detailed manual for the developed code is maintained by the CRUNCH group at Brown University and is available upon request.

Bibliography

[1] *Gridgen*. Pointwise, Inc., http://www.pointwise.com.

[2] *LAMMPS Molecular Dynamics Simulator*. Sandia National Laboratories, http://lammps.sandia.gov.

[3] *Physiome Project*. http://www.physiome.org and http://www.europhysiome.org.

[4] M. Abkarian, M. Faivre, and A. Viallat. Swinging of red blood cells under shear flow. *Physical Review Letters*, 98:188302, 2007.

[5] M. Abkarian, C. Lartigue, and A. Viallat. Tank treading and unbinding of deformable vesicles in shear flow: Determination of the lift force. *Physical Review Letters*, 88:068103, 2002.

[6] S. Adams, H. Brown, and G. Turner. Breaking down the blood.brain barrier: signaling a path to cerebral malaria? *Trends in Parasitology*, 18:360–366, 2002.

[7] M. P. Allen and D. J. Tildesley. *Computer simulation of liquids*. Clarendon Press, New York, 1987.

[8] R. Alon, S. Chen, K. D. Puri, E. B. Finger, and T. A. Springer. The kinetics of L-selectin tethers and the mechanics of selectin-mediated rolling. *Journal of Cell Biology*, 138:1169–1180, 1997.

[9] R. Alon, D. A. Hammer, and T. A. Springer. Lifetime of the P-selectin-carbohydrate bond and its response to tensile force in hydrodynamic flow. *Nature (London)*, 374:539–542, 1995.

[10] M. S. Amin, Y.-K. Park, N. Lue, R. R. Dasari, K. Badizadegan, M. S. Feld, and G. Popescu. Microrheology of red blood cell membranes using dynamic scattering microscopy. *Optics Express*, 15(25):17001–17009, 2007.

[11] M. Antia, T. Herricks, and P. K. Rathod. Microfluidic modeling of cell-cell interactions in malaria pathogenesis. *PLoS Pathogens*, 3(7):939–945, 2007.

[12] R. Ata and A. Soulaimani. A stabilized SPH method for inviscid shallow water flows. *International Journal for Numerical Methods in Fluids*, 47(2):139–159, 2005.

[13] D. Aussere, H. Hervet, and F. Rondelez. Concentration dependence of the interfacial depletion layer thickness for polymer solutions in contact with nonadsorbing walls. *Macromolecules*, 19(1):85–88, 1986.

[14] J. A. Backer, C. P. Lowe, H. C. J. Hoefsloot, and P. D. Iedema. Poiseuille flow to measure the viscosity of particle model fluids. *Journal of Chemical Physics*, 122:154503, 2005.

[15] P. Bagchi. Mesoscale simulation of blood flow in small vessels. *Biophysical Journal*, 92:1858–1877, 2007.

[16] H. A. Barnes, J. F. Hutton, and K. Walters. *Introduction to rheology.* Elsevier, New York, 1989.

[17] G. I. Bell. Models for the specific adhesion of cells to cells. *Science*, 200:618–627, 1978.

[18] A. Berkenbos and C. P. Lowe. Mesoscopic simulations of accelerated polymer drift in microfluidic capillaries. *Journal of Chemical Physics*, 127:164902, 2007.

[19] R. B. Bird, R. C. Armstrong, and O. Hassager. *Dynamics of polymeric liquids:Fluid mechanics.* Wiley, New York, second edition, 1987.

[20] D. H. Boal. *Mechanics of the cell.* Cambridge University Press, Cambridge, 2002.

[21] P. G. Bolhuis, A. A. Louis, J. P. Hansen, and E. J. Meijer. Accurate effective pair potentials for polymer solutions. *Journal of Chemical Physics*, 114(9):4296–4311, 2001.

[22] H. Brenner. The Oseen resistance of a particle of arbitrary shape. *Journal of Fluid Mechanics*, 11:604–610, 1961.

[23] H. Brown, T. T. Hien, N. Day, N. T. H. Mai, L. V. Chuong, T. T. H. Chau, P. P. Loc, N. H. Phu, D. Bethe, J. Farrar, K. Gatter, N. White, and G. Turner. Evidence of blood-brain barrier dysfunction in human cerebral malaria. *Neuropathology and Applied Neurobiology*, 25(4):331–340, 1999.

[24] L. J. Bruce-Chwatt. DNA probes for malaria diagnosis. *Lancet*, 1:795, 1984.

[25] G. Bugliarello and J. Sevilla. Velocity distribution and other characteristics of steady and pulsatile blood flow in fine glass tubes. *Biorheology*, 7:85–107, 1970.

[26] I. Cantat and C. Misbah. Lift force and dynamical unbinding of adhering vesicles under shear flow. *Physical Review Letters*, 83:880–883, 1999.

[27] S. Chen and T. A. Springer. An automatic braking system that stabilizes leukocyte rolling by an increase in selectin bond number with shear. *Journal of Cell Biology*, 144:185–200, 1999.

[28] S. Chen and T. A. Springer. Selectin receptor-ligand bonds: Formation limited by shear rate and dissociation governed by the Bell model. *Proceedings of the National Academy of Sciences USA*, 98(3):950–955, 2001.

[29] Y. L. Chen, M. D. Graham, J. J. de Pablo, K. Jo, and D. C. Schwartz. DNA molecules in microfluidic oscillatory flow. *Macromolecules*, 38(15):6680–6687, 2005.

[30] Y.-L. Chen, H. Ma, M. D. Graham, and J. J. de Pablo. Modeling DNA in confinement: A comparison between the brownian dynamics and lattice boltzmann method. *Macromolecules*, 40(16):85–88, 2007.

[31] Y. I. Cho and K. R. Kensey. Effects of the non-Newtonian viscosity of blood on hemodynamics of diseased arterial flows. Part 1: Steady flows. *Biorheology*, 28:241–262, 1991.

[32] G. R. Cokelet and H. L. Goldsmith. Decreased hydrodynamic resistance in the two-phase flow of blood through small vertical tubes at low flow rates. *Circulation Research*, 68:1–17, 1991.

[33] G. R. Cokelet and H. J. Meiselman. Rheological comparison of hemoglobin solutions and erythrocyte suspensions. *Science*, 162:275–277, 1968.

[34] B. D. Coleman, H. Markovitz, and W. Noll. *Viscometric flows of non-Newtonian fluids.* Springer-Verlag, New York, 1966.

[35] B. M. Cooke, A. R. Berendt, A. G. Craig, J. MacGregor, C. I. Newbold, and G. B. Nash. Rolling and stationary cytoadhesion of red blood cells parasitized by Plasmodium falciparum: separate roles for ICAM-1, CD36 and thrombospondin. *British Journal of Haematology*, 87:162–170, 1994.

[36] B. M. Cooke and R. L. Coppel. Cytoadhesion and Falciparum malaria: Going with the flow. *Parasitology Today*, 11:282–287, 1995.

[37] C. Cozens-Roberts, D. A. Lauffenburger, and J. A. Quinn. Receptor-mediated cell attachment and detachment kinetics. I. Probabilistic model and analysis. *Biophysical Journal*, 58:841–856, 1990.

[38] H. A. Cranston, C. W. Boylan, G. L. Carroll, S. P. Sutera, J. R. Williamson, I. Y. Gluzman, and D. J. Krogstad. Plasmodium falciparum maturation abolishes physiologic red cell deformability. *Science*, 223:400–403, 1984.

[39] C. G. Cray and K. I. Gubbins. *Theory of molecular fluids.* Clarendon Press, Oxford, 1982.

[40] E. R. Damiano. The effect of the endothelial-cell glycocalyx on the motion of red blood cells through capillaries. *Microvascular Research*, 55:77–91, 1998.

[41] E. R. Damiano, J. Westheider, A. Tozeren, and K. Ley. Variation in the velocity, deformation, and adhesion energy density of leukocytes rolling within venules. *Circulation Research*, 79:1122–1130, 1996.

[42] M. Dao, J. Li, and S. Suresh. Molecularly based analysis of deformation of spectrin network and human erythrocyte. *Materials Science and Engineering C*, 26:1232–1244, 2006.

[43] P. G. de Gennes. *Scaling concepts in polymer physics.* Cornell University Press, Ithaca, 1979.

[44] R. Delgado-Buscalioni and P. V. Coveney. Continuum-particle hybrid coupling for mass, momentum, and energy transfers in unsteady fluid flow. *Physical Review E*, 67(4):046704, 2003.

[45] R. Delgado-Buscalioni and P. V. Coveney. USHER: an algorithm for particle insertion in dense fluids. *Journal of Chemical Physics*, 119(2):978–987, 2003.

[46] M. Dembo, D. C. Torney, K. Saxman, and D. A. Hammer. The reaction-limited kinetics of membrane-to-surface adhesion and detachment. *Proceedings of the Royal Society B: Biological Sciences*, 234:55–83, 1988.

[47] R. Dimova, B. Pouligny, and C. Dietrich. Pretransitional effects in dimyristoylphosphatidylcholine vesicle membranes: Optical dynamometry study. *Biophysical Journal*, 79:340, 2000.

[48] D. E. Discher, D. H. Boal, and S. K. Boey. Simulations of the erythrocyte cytoskeleton at large deformation. II. Micropipette aspiration. *Biophysical Journal*, 75(3):1584–1597, 1998.

[49] D. E. Discher and P. Carl. New insights into red cell network structure, elasticity, and spectrin unfolding. *Cellular and Molecular Biology Letters*, 6(3):593–606, 2001.

[50] D. E. Discher, N. Mohandas, and E. A. Evans. Molecular maps of red cell deformation: hidden elasticity and in situ connectivity. *Science*, 266:1032–1035, 1994.

[51] A. M. Dondorp, E. Pongponratn, and N.J. White. Reduced microcirculatory flow in severe falciparum malaria: Pathophysiology and electron-microscopic pathology. *Acta Tropica*, 89:309–317, 2004.

[52] D. H. Douglas-Hamilton, N. G. Smith, C. E. Kuster, J. P. W. Vermeiden, and G. C. Althouse. Particle distribution in low-volume capillary-loaded chambers. *Journal of Andrology*, 26(1):107–114, 2005.

[53] M. M. Dupin, I. Halliday, C. M. Care, L. Alboul, and L. L. Munn. Modeling the flow of dense suspensions of deformable particles in three dimensions. *Physical Review E*, 75(6):066707, 2007.

[54] M. M. Dupin, I. Halliday, C. M. Care, and L. L. Munn. Lattice boltzmann modeling of blood cell dynamics. *International Journal of Computational Fluid Dynamics*, 22(7):481–492, 2008.

[55] A. Dupuis, E. M. Kotsalis, and P. Koumoutsakos. Coupling lattice Boltzmann and molecular dynamics models for dense fluids. *Physical Review E*, 75(4):046704, 2007.

[56] W. Dzwinel, K. Boryczko, and D. A. Yuen. A discrete-particle model of blood dynamics in capillary vessels. *Journal of Colloid and Interface Science*, 258(1):163–173, 2003.

[57] C. D. Eggleton and A. S. Popel. Large deformation of red blood cell ghosts in a simple shear flow. *Physics of Fluids*, 10(8):1834, 1998.

[58] E. Eisenriegler and R. Maassen. Center-of-mass distribution of a polymer near a repulsive wall. *Journal of Chemical Physics*, 116(1):449–450, 2002.

[59] G. Enden and A. S. Popel. A numerical study of plasma skimming in small vascular bifurcations. *Journal of Biomechanical Engineering*, 116:79–88, 1994.

[60] C. R. Engwerda, L. Beattie, and F. H. Amante. The importance of the spleen in malaria. *Trends in Parasitology*, 21:75–80, 2005.

[61] S. L. Erlandsen, S. R. Hasslen, and R. D. Nelson. Detection and spatial distribution of the beta 2 integrin (Mac-1) and L-selectin (LECAM-1) adherence receptors on human neutrophils by high-resolution field emission SEM. *Journal of Histochemistry and Cytochemistry*, 41:327–333, 1993.

[62] D. L. Ermak. A computer simulation of charged particles in solution. II. Polyion diffusion coefficient. *Journal of Chemical Physics*, 62:4197, 1975.

[63] P. Espanol. Fluid particle model. *Physical Review E*, 57(3):2930, 1998.

[64] P. Espanol and P. Warren. Statistical mechanics of dissipative particle dynamics. *Europhysics Letters*, 30(4):191–196, 1995.

[65] E. A. Evans and R. Skalak. *Mechanics and thermodynamics of biomembranes.* CRC Press, Inc., Boca Raton, Florida, 1980.

[66] J. Evans, W. Gratzer, N. Mohandas, K. Parker, and J. Sleep. Fluctuations of the red blood cell membrane: relation to mechanical properties and lack of ATP dependence. *Biophysical Journal*, 94(10):4134–4144, 2008.

[67] R. Fahraeus. The suspension stability of the blood. *Physiological Reviews*, 9:241–274, 1929.

[68] R. Fahraeus and T. Lindqvist. Viscosity of blood in narrow capillary tubes. *The American Journal of Physics*, 96:562–568, 1931.

[69] M. Faivre. Red blood cells and vesicles. *PhD thesis, Marselle, France*, 2007.

[70] M. Faivre, M. Abkarian, K. Bickraj, and H. A. Stone. Geometrical focusing of cells in a microfluidic device: an approach to separate blood plasma. *Biorheology*, 43:147–159, 2006.

[71] X. Fan, N. Phan-Thien, S. Chen, X. Wu, and T. Y. Ng. Simulating flow of DNA suspension using dissipative particle dynamics. *Physics of Fluids*, 18(6):063102, 2006.

[72] L. Fang, H. Hu, and R. G. Larson. DNA configurations and concentration in shearing flow near a glass surface in a microchannel. *Journal of Rheology*, 49:127–138, 2005.

[73] D. A. Fedosov, G. E. Karniadakis, and B. Caswell. Dissipative particle dynamics simulation of depletion layer and polymer migration in micro- and nanochannels for dilute polymer solutions. *Journal of Chemical Physics*, 128(14):144903, 2008.

[74] D. A. Fedosov, I. V. Pivkin, and G. E. Karniadakis. Velocity limit in DPD simulations of wall-bounded flows. *Journal of Computational Physics*, 227(4):2540–2559, 2008.

[75] J. Feng, H. H. Hu, and D. D. Joseph. Direct simulation of initial value problems for the motion of solid bodies in a Newtonian fluid. Part 2. Couette and Poiseuille flows. *Journal of Fluid Mechanics*, 277:271–301, 1994.

[76] J. D. Ferry. *Viscoelastic properties of polymers*. Wiley, New York, third edition, 1980.

[77] E. B. Finger, K. D. Puri, R. Alon, M. B. Lawrence, U. H. von Andrian, and T. A. Springer. Adhesion through L-selectin requires a threshold hydrodynamic shear. *Nature (London)*, 379:266–269, 1996.

[78] J. C. Firrell and H. H. Lipowsky. Leukocyte margination and deformation in mesenteric venules of rat. *American Journal of Physiology*, 256:H1667–H1674, 1989.

[79] T. M. Fischer. Shape memory of human red blood cells. *Biophysical Journal*, 86(5):3304–3313, 2004.

[80] T. M. Fischer. Tank-tread frequency of the red cell membrane: Dependence on the viscosity of the suspending medium. *Biophysical Journal*, 93(7):2553–2561, 2007.

[81] E. G. Flekkoy, G. Wagner, and J. Feder. Hybrid model for combined particle and continuum dynamics. *Europhysics Letters*, 52(3):271–276, 2000.

[82] J. Fritz, A. G. Katopodis, F. Kolbinger, and D. Anselmetti. Force-mediated kinetics of single P-selectin/ligand complexes observed by atomic force microscopy. *Proceedings of the National Academy of Sciences USA*, 95(21):12283–12288, 1998.

[83] Y. C. Fung. *Biomechanics: Mechanical properties of living tissues.* Springer-Verlag, New York, second edition, 1993.

[84] M. Fyta, S. Melchionna, E. Kaxiras, and S. Succi. Coupling Lattice Boltzmann with atomistic dynamics for the multiscale simulation of nano-biological flows. *Computing in Science and Engineering*, arXiv:0710.1272v1, 2007.

[85] H. L. Goldsmith. Red cell motions and wall interactions in tube flow. *Federation Proceedings*, 30:1578–1590, 1971.

[86] H. L. Goldsmith, G. R. Cokelet, and P. Gaehtgens. Robin Fahraeus: evolution of his concepts in cardiovascular physiology. *American Journal of Physiology*, 257:H1005–H1015, 1989.

[87] N. S. Gov. Active elastic network: cytoskeleton of the red blood cell. *Physical Review E*, 75(1):011921, 2007.

[88] N. S. Gov and S. A. Safran. Red blood cell membrane fluctuations and shape controlled by ATP-induced cytoskeletal defects. *Biophysical Journal*, 88:1859–1874, 2005.

[89] W. W. Graessley. *Advances in polymer science.* Springer-Verlag, New York, 1974.

[90] A. W. Greenberg, D. K. Brunk, and D. A. Hammer. Cell-free rolling mediated by L-selectin and Sialyl Lewis reveals the shear threshold effect. *Biophysical Journal*, 79:2391–2402, 2000.

[91] R. D. Groot and K. L. Rabone. Mesoscopic simulation of cell membrane damage, morphology change and rupture by nonionic surfactants. *Biophysical Journal*, 81(2):725–736, 2001.

[92] R. D. Groot and P. B. Warren. Dissipative particle dynamics: Bridging the gap between atomistic and mesoscopic simulation. *Journal of Chemical Physics*, 107(11):4423–4435, 1997.

[93] N. G. Hadjiconstantinou. Hybrid atomistic-continuum formulations and the moving contact-line problem. *Journal of Computational Physics*, 154(2):245–265, 1999.

[94] N. G. Hadjiconstantinou, A. L. Garcia, M. Z. Bazant, and G. He. Statistical error in particle simulations of hydrodynamic phenomena. *Journal of Computational Physics*, 187(1):274–297, 2003.

[95] T. Haenscheid. Diagnosis of malaria: a review of alternatives to conventional microscopy. *Clinical and Laboratory Haematology*, 21:235–245, 1999.

[96] D. A. Hammer and S. M. Apte. Simulation of cell rolling and adhesion on surfaces in shear flow: general results and analysis of selectin-mediated neutrophil adhesion. *Biophysical Journal*, 63:35–57, 1992.

[97] D. A. Hammer and D. A. Lauffenburger. A dynamical model for receptor-mediated cell adhesion to surfaces. *Biophysical Journal*, 52:475–487, 1987.

[98] J. Happel and H. Brenner. *Low Reynolds number hydrodynamics*. Prentice-Hall, Inc., Englewood Cliffs, NJ, 1965.

[99] E. Helfer, S. Harlepp, L. Bourdieu, J. Robert, F. C. MacKintosh, and D. Chatenay. Microrheology of biopolymer-membrane complexes. *Physical Review Letters*, 85(2):457–460, 2000.

[100] W. Helfrich. Elastic properties of lipid bilayers: theory and possible experiments. *Z. Naturforschung C*, 28:693–703, 1973.

[101] S. Henon, G. Lenormand, A. Richert, and F. Gallet. A new determination of the shear modulus of the human erythrocyte membrane using optical tweezers. *Biophysical Journal*, 76:1145–1151, 1999.

[102] D. M. Heyes, P. J. Mitchell, P. B. Visscher, and J. R. Melrose. Brownian dynamics simulations of concentrated dispersions: viscoelasticity and near-newtonian behaviour. *Journal of the Chemical Society, Faraday Transactions*, 90:1133 – 1141, 1994.

[103] M. Ho and N. J. White. Molecular mechanisms of cytoadherence in malaria. *American Journal of Physiology*, 276:C1231–C1242, 1999.

[104] R. M. Hochmuth, P. R. Worthy, and E. A. Evans. Red cell extensional recovery and the determination of membrane viscosity. *Biophysical Journal*, 26(1):101–114, 1979.

[105] P. J. Hoogerbrugge and J. M. V. A. Koelman. Simulating microscopic hydrodynamic phenomena with dissipative particle dynamics. *Europhysics Letters*, 19(3):155–160, 1992.

[106] R. J. Howard. Malarial proteins at the membrane of Plasmodium falciparum-infected erythrocytes and their involvement in cytoadherence to endothelial cells. *Progress in Allergy*, 41:98–147, 1988.

[107] J. H. Irving and J. G. Kirkwood. The statistical mechanical theory of transport processes. IV. The equations of hydrodynamics. *Journal of Chemical Physics*, 18:817–829, 1950.

[108] S. Jadhav, C. D. Eggleton, and K. Konstantopoulos. A 3-D computational model predicts that cell deformation affects selectin-mediated leukocyte rolling. *Biophysical Journal*, 88:96–104, 2005.

[109] W. Janke. Statistical analysis of simulations: Data correlations and error estimation. *Proceedings of the Euro Winter School Quantum Simulations of Complex Many-Body Systems: From Theory to Algorithms, John von Neumann Institute for Computing (NIC)*, 10:423–445, 2002.

[110] G. E. Karniadakis and S. J. Sherwin. *Spectral/hp element methods for CFD.* Oxford University Press, Oxford, 2005.

[111] S. Kessler, R. Finken, and U. Seifert. Swinging and tumbling of elastic capsules in shear flow. *Journal of Fluid Mechanics*, 605:207–226, 2008.

[112] R. Khare, M. D. Graham, and J. J. de Pablo. Cross-stream migration of flexible molecules in a nanochannel. *Physical Review Letters*, 96:224505, 2006.

[113] D. B. Khismatullin and G. A. Truskey. Three-dimensional numerical simulation of receptor-mediated leukocyte adhesion to surfaces: effects of cell deformability and viscoelasticity. *Physics of Fluids*, 17:031505, 2005.

[114] M. B. Kim and I. H. Sarelius. Role of shear forces and adhesion molecule distribution on P-selectin-mediated leukocyte rolling in postcapillary venules. *American Journal of Physiology*, 287:H2705–H2711, 2004.

[115] S. Kim, L. R. Long, A. S. Popel, M. Intaglietta, and P. C. Johnson. Temporal and spatial variations of cell-free layer width in arterioles. *American Journal of Physiology*, 293:H1526–H1535, 2007.

[116] C. J. Koh, P. Hookham, and L. G. Leal. An experimental investigation of concentrated suspension flows in a rectangular channel. *Journal of Fluid Mechanics*, 266:1–32, 1994.

[117] Y. Kong, C. W. Manke, W. G. Madden, and A. G. Schlijper. Effect of solvent quality on the conformation and relaxation of polymers via dissipative particle dynamics. *Journal of Chemical Physics*, 107(2):592–602, 1997.

[118] J. Koplik and J. R. Banavar. Corner flow in the sliding plate problem. *Physics of Fluids*, 7(12):3118, 1995.

[119] C. B Korn and U. S. Schwarz. Dynamic states of cells adhering in shear flow: From slipping to rolling. *Physical Review E*, 77(4):041904, 2008.

[120] R. G. Larson. *The structure and rheology of complex fluids.* Oxford University Press, Oxford, NY, 1999.

[121] M. B. Lawrence and T. A. Springer. Leukocytes roll on a selectin at physiologic flow rates: distinction from and prerequisite for adhesion through integrins. *Cell*, 65:859–873, 1991.

[122] C.-H. Lee, W.-C. Lin, and J. Wang. All-optical measurements of the bending rigidity of lipid-vesicle membranes across structural phase transitions. *Physical Review E*, 64(2):020901, 2001.

[123] J. C. Lee and D. E. Discher. Deformation-enhanced fluctuations in the red cell skeleton with theoretical relations to elasticity, connectivity, and spectrin unfolding. *Biophysical Journal*, 81(6):3178–3192, 2001.

[124] A. W. Lees and S. F. Edwards. The computer study of transport processes under extreme conditions. *Journal of Physics C*, 5:1921–1928, 1972.

[125] K. Ley, C. Laudanna, M. I. Cybulsky, and S. Nourshargh. Getting to the site of inflammation: the leukocyte adhesion cascade updated. *Nature Reviews Immunology*, 7:678–689, 2007.

[126] J. Li, M. Dao, C. T. Lim, and S. Suresh. Spectrin-level modeling of the cytoskeleton and optical tweezers stretching of the erythrocyte. *Biophysical Journal*, 88:3707–3719, 2005.

[127] J. Li, G. Lykotrafitis, M. Dao, and S. Suresh. Cytoskeletal dynamics of human erythrocyte. *Proceedings of the National Academy of Sciences USA*, 104(12):4937–4942, 2007.

[128] J. Lidmar, L. Mirny, and D. R. Nelson. Virus shapes and buckling transitions in spherical shells. *Physical Review E*, 68(5):051910, 2003.

[129] Y. Liu and W. K. Liu. Rheology of red blood cell aggregation by computer simulation. *Journal of Computational Physics*, 220:139–154, 2006.

[130] H. Ma and M. D. Graham. Theory of shear-induced migration in dilute polymer solutions near solid boundaries. *Physics of Fluids*, 17(8):083103, 2005.

[131] N. Maeda, Y. Suzuki, J. Tanaka, and N. Tateishi. Erythrocyte flow and elasticity of microvessels evaluated by marginal cell-free layer and flow resistance. *American Journal of Physiology*, 271(6):H2454–H2461, 1996.

[132] A. Malevanets and R. Kapral. Mesoscopic model for solvent dynamics. *Journal of Chemical Physics*, 110(17):8605–8613, 1999.

[133] M. Marinkovic, M. Diez-Silva, I. Pantic, J. J. Fredberg, S. Suresh, and J. P. Butler. Febrile temperature leads to significant stiffening of Plasmodium falciparum parasitized erythrocytes. *American Journal of Physiology: Cell Physiology*, 296:C59–C64, 2009.

[134] J. Mark, K. Ngai, W. Graessley, L. Mandelkern, E. Samulski, J. Koenig, and G. Wignall. *Physical properties of polymers.* Cambridge University Press, Cambridge, third edition, 2004.

[135] B. T. Marshall, K. K. Sarangapani, J. Wu, M. B. Lawrence, R. P. McEver, and C. Zhu. Measuring molecular elasticity by atomic force microscope cantilever fluctuations. *Biophysical Journal*, 90:681–692, 2006.

[136] D. A. McQuarrie. *Statistical mechanics.* Viva Books Private Limited, New Delhi, India, 2000.

[137] J. L. McWhirter, H. Noguchi, and G. Gompper. Flow-induced clustering and alignment of vesicles and red blood cells in microcapillaries. *Proceedings of the National Academy of Sciences USA*, 106(15):6039–6043, 2009.

[138] A. Milchev and K. Binder. A polymer chain trapped between two parallel repulsive walls: A Monte-Carlo test of scaling behavior. *European Physical Journal B*, 3(4):477–484, 1998.

[139] J. A. Millan, W. Jiang, M. Laradji, and Y. Wang. Pressure driven flow of polymer solutions in nanoscale slit pores. *Journal of Chemical Physics*, 126:124905, 2007.

[140] L. H. Miller, D. I. Baruch, K. Marsh, and O. K. Doumbo. The pathogenic basis of malaria. *Nature*, 415:673–679, 2002.

[141] J. P. Mills, M. Diez-Silva, D. J. Quinn, M. Dao, M. J. Lang, K. S. W. Tan, C. T. Lim, G. Milon, P. H. David, O. Mercereau-Puijalon, S. Bonnefoy, and S. Suresh. Effect of plasmodial RESA protein on deformability of human red blood cells harboring Plasmodium falciparum. *Proceedings of the National Academy of Sciences USA*, 104(22):9213–9217, 2007.

[142] D. T. Mirijanian and G. A. Voth. Unique elastic properties of the spectrin tetramer as revealed by multiscale coase-grained modeling. *Proceedings of the National Academy of Sciences USA*, 105(4):1204–1208, 2008.

[143] K. L. Moore, K. D. Patel, R. E. Bruehl, F. Li, D. A. Johnson, H. S. Lichenstein, R. D. Cummings, D. F. Bainton, and R. P. McEver. P-selectin glycoprotein ligand-1 mediates rolling of human neutrophils on P-selectin. *Journal of Cell Biology*, 128:661–671, 1995.

[144] L. L. Munn, R. J. Melder, and R. K. Jain. Analysis of cell flux in the parallel plate flow chamber: implications for cell capture studies. *Biophysical Journal*, 67:889–895, 1994.

[145] E. Nagao, O. Kaneko, and J. A. Dvorak. Plasmodium falciparum-infected erythrocytes: qualitative and quantitative analyses of parasite-induced knobs by atomic force microscopy. *Journal of Structural Biology*, 130:34–44, 2000.

[146] X. Nie, S. Chen, and M. O. Robbins. Hybrid continuum-atomistic simulation of singular corner flow. *Physics of Fluids*, 16(10):3579, 2004.

[147] X. Nie, M. O. Robbins, and S. Chen. Resolving singular forces in cavity flow: multiscale modeling from atomic to millimeter scales. *Physical Review Letters*, 96:134501, 2006.

[148] X. B. Nie, S. Y. Chen, W. N. E, and M. O. Robbins. A continuum and molecular dynamics hybrid method for micro- and nano-fluid flow. *Journal of Fluid Mechanics*, 500:55–64, 2004.

[149] H. Noguchi and G. Gompper. Dynamics of fluid vesicles in shear flow: Effect of the membrane viscosity and thermal fluctuations. *Physical Review E*, 72(1):011901, 2005.

[150] H. Noguchi and G. Gompper. Shape transitions of fluid vesicles and red blood cells in capillary flows. *Proceedings of the National Academy of Sciences USA*, 102(40):14159–14164, 2005.

[151] S. T. O'Connell and P. A. Thompson. Molecular dynamics-continuum hybrid computations: a tool for studying complex fluid flows. *Physical Review E*, 52(6):5792–5795, 1995.

[152] S. J. Orfanidis. *Introduction to Signal Processing.* Prentice-Hall, Englewood Cliffs, NJ, 1996.

[153] I. Pagonabarraga and D. Frenkel. Non-ideal DPD fluids. *Molecular Simulation*, 25:167, 2000.

[154] I. Pagonabarraga and D. Frenkel. Dissipative particle dynamics for interacting systems. *Journal of Chemical Physics*, 115:5015, 2001.

[155] W. Pan. Single particle DPD: Algorithms and applications. *PhD Thesis, Brown University*, 2009.

[156] V. Pappu and P. Bagchi. 3D computational modeling and simulation of leukocyte rolling adhesion and deformation. *Computers in Biology and Medicine*, 38:738–753, 2008.

[157] E. Y. Park, M. J. Smith, E. S. Stropp, K. R. Snapp, J. A. DiVietro, W. F. Walker, D. W. Schmidtke, S. L. Diamond, and M. B. Lawrence. Comparison of PSGL-1 microbead neutrophil rolling: microvillus elongation stabilizes P-selectin bond clusters. *Biophysical Journal*, 82:1835–1847, 2002.

[158] Y.-K. Park, M. Diez-Silva, G. Popescu, G. Lykotrafitis, W. Choi, M. S. Feld, and S. Suresh. Refractive index maps and membrane dynamics of human red blood cells parasitized by Plasmodium falciparum. *Proceedings of the National Academy of Sciences USA*, 105(37):13730–13735, 2008.

[159] I. V. Pivkin and G. E. Karniadakis. Accurate coarse-grained modeling of red blood cells. *Physical Review Letters*, 101(11):118105, 2008.

[160] A. S. Popel and P. C. Johnson. Microcirculation and hemorheology. *Annual Review of Fluid Mechanics*, 37:43–69, 2005.

[161] G. Popescu, Y.-K. Park, R. R. Dasari, K. Badizadegan, and M. S. Feld. Coherence properties of red blood cell membrane motions. *Physical Review E*, 76(3):031902, 2007.

[162] C. Pozrikidis. Numerical simulation of cell motion in tube flow. *Annals of Biomedical Engineering*, 33(2):165–178, 2005.

[163] W. H. Press, B. P Flannery, S. A. Teukolsky, and W. T. Vetterling. *Numerical Recipes in C: The Art of Scientific Computing.* Cambridge University Press, Cambridge, 1992.

[164] A. R. Pries, K. Ley, M. Claassen, and P. Gaehtgens. Red cell distribution at microvascular bifurcations. *Microvascular Research*, 38:81–101, 1989.

[165] A. R. Pries, D. Neuhaus, and P. Gaehtgens. Blood viscosity in tube flow: dependence on diameter and hematocrit. *American Journal of Physiology*, 263(6):H1770–H1778, 1992.

[166] A. R. Pries, T. W. Secomb, T. Gessner, M. B. Sperandio, J. F. Gross, and P. Gaehtgens. Resistance to blood flow in microvessels in vivo. *Circulation Research*, 75:904–915, 1994.

[167] M. Puig-de Morales-Marinkovic, K. T. Turner, J. P. Butler, J. J. Fredberg, and S. Suresh. Viscoelasticity of the human red blood cell. *American Journal of Physiology: Cell Physiology*, 293:597–605, 2007.

[168] D. Qi, L. Luo, R. Aravamuthan, and W. Strieder. Lateral migration and orientation of elliptical particles in Poiseuille flows. *Journal of Statistical Physics*, 107(1):101–120, 2002.

[169] W. Reinke, P. Gaehtgens, and P. C. Johnson. Blood viscosity in small tubes: effect of shear rate, aggregation, and sedimentation. *American Journal of Physiology*, 253:H540–H547, 1987.

[170] F. Schlesener, A. Hanke, R. Klimpel, and S. Dietrich. Polymer depletion interaction between two parallel repulsive walls. *Physical Review E*, 63(4):041803, 2001.

[171] K. Schulten and I. R. Epstein. Recombination of radical pairs in high magnetic fields: a path integral-Monte Carlo treatment. *Journal of Chemical Physics*, 71:309, 1979.

[172] W. W. Schultz, N. Y. Lee, and J. P. Boyd. Chebyshev pseudospectral method of viscous flows with corner singularities. *Journal of Scientific Computing*, 4(1):1–24, 1989.

[173] U. S. Schwarz and R. Alon. L-selectin-mediated leukocyte tethering in shear flow is controlled by multiple contacts and cytoskeletal anchorage facilitating fast rebinding

events. *Proceedings of the National Academy of Sciences USA*, 101(18):6940–6945, 2004.

[174] T. Schweizer, J. Hosettler, and F. Mettler. A shear rheometer for measuring shear stress and both normal stress differences in polymer melts simultaneously: the MTR 25. *Rheologica Acta*, 47:943–957, 2008.

[175] C. J. Seeton. Viscosity-temperature correlation for liquids. *Tribology Letters*, 22(1):67–78, 2006.

[176] G. Segre and A. Silberberg. Radial particle displacements in Poiseuille flow of suspensions. *Nature*, 189:209–210, 1961.

[177] G. Segre and A. Silberberg. Behavior of macroscopic rigid spheres in Poiseuille flow. Part 1. Determination of local concentration by statistical analysis of particle passages through crossed light beams. *Journal of Fluid Mechanics*, 14:115–135, 1962.

[178] S. Sen, S. K. Kumar, and P. Keblinski. Viscoelastic properties of polymer melts from equilibrium molecular dynamics simulations. *Macromolecules*, 38(3):650–653, 2005.

[179] M. Sharan and A. S. Popel. A two-phase model for flow of blood in narrow tubes with increased effective viscosity near the wall. *Biorheology*, 38:415–428, 2001.

[180] J. P. Shelby, J. White, K. Ganesan, P. K. Rathod, and D. T. Chiu. A microfluidic model for single-cell capillary obstruction by Plasmodium falciparum-infected erythrocytes. *Proceedings of the National Academy of Sciences USA*, 100:14618–14622, 2003.

[181] J. M. Skotheim and T. W. Secomb. Red blood cells and other nonspherical capsules in shear flow: Oscillatory dynamics and the tank-treading-to-tumbling transition. *Physical Review Letters*, 98:078301, 2007.

[182] B. F. Smith, P. E. Bjorstad, and W. D. Gropp. *Domain decomposition: parallel multilevel methods for elliptic partial differential equations.* Cambridge University Press, Cambridge, 1996.

[183] M. J. Smith, E. L. Berg, and M. B. Lawrence. A direct comparison of selectin-mediated transient, adhesive events using high temporal resolution. *Biophysical Journal*, 77:3371–3383, 1999.

[184] T. Soddemann, B. Duenweg, and K. Kremer. Dissipative particle dynamics: A useful thermostat for equilibrium and nonequilibrium molecular dynamics simulations. *Physical Review E*, 68(4):046702, 2003.

[185] T. A. Springer. Traffic signals on endothelium for lymphocyte recirculation and leukocyte emigration. *Annual Review of Physiology*, 57:827–872, 1995.

[186] H. Strey, M. Peterson, and E. Sackmann. Measurement of erythrocyte membrane elasticity by flicker eigenmode decomposition. *Biophysical Journal*, 69(2):478–488, 1995.

[187] S. Succi. *The Lattice Boltzmann equation for fluid dynamics and beyond.* Oxford University Press, Oxford, 2001.

[188] C. Sun and L. L. Munn. Particulate nature of blood determines macroscopic rheology: a 2D lattice-Boltzmann analysis. *Biophysical Journal*, 88:1635–1645, 2005.

[189] M. Sun and C. Ebner. Molecular-dynamics simulation of compressible fluid flow in two-dimensional channels. *Physical Review A*, 48(8):4813–4818, 1992.

[190] S. Suresh, J. Spatz, J. P. Mills, A. Micoulet, M. Dao, C. T. Lim, M. Beil, and T. Seufferlein. Connections between single-cell biomechanics and human disease states: gastrointestinal cancer and malaria. *Acta Biomaterialia*, 1:15–30, 2005.

[191] Y. Suzuki, N. Tateishi, M. Soutani, and N. Maeda. Deformation of erythrocytes in microvessels and glass capillaries: effect of erythrocyte deformability. *Microcirculation*, 3(1):49–57, 1996.

[192] A. H. Swihart, J. M. Mikrut, J. B. Ketterson, and R. C. MacDonald. Atomic force microscopy of the erythrocyte membrane skeleton. *Journal of Microscopy*, 204:212–225, 2001.

[193] V. Symeonidis, B. Caswell, and G. E. Karniadakis. Schmidt number effects in dissipative particle dynamics simulation of polymers. *Journal of Chemical Physics*, 125:184902, 2006.

[194] M. Takeuchi, H. Miyamoto, Y. Sako, H. Komizu, and A. Kusumi. Structure of the erythrocyte membrane skeleton as observed by atomic force microscopy. *Biophysical Journal*, 74:2171–2183, 1998.

[195] A. Tartakovsky, P. Meakin, T. D. Scheibe, and R. E. West. Simulations of reactive transport and precipitation with smoothed particle hydrodynamics. *Journal of Computational Physics*, 222:654–672, 2007.

[196] G. Tomaiuolo, V. Preziosi, M. Simeone, S. Guido, R. Ciancia, V. Martinelli, C. Rinaldi, and B. Rotoli. A methodology to study the deformability of red blood cells flowing in microcapillaries in vitro. *Ann Ist Super Sanita*, 43(2):186–192, 2007.

[197] R. Tran-Son-Tay, S. P. Sutera, and P. R. Rao. Determination of RBC membrane viscosity from rheoscopic observations of tank-treading motion. *Biophysical Journal*, 46(1):65–72, 1984.

[198] K. Tsukada, E. Sekizuka, C. Oshio, and H. Minamitani. Direct measurement of erythrocyte deformability in diabetes mellitus with a transparent microchannel capillary model and high-speed video camera system. *Microvascular Research*, 61(3):231–239, 2001.

[199] O. B. Usta, J. E. Butler, and A. J. C. Ladd. Flow-induced migration of polymers in dilute solution. *Physics of Fluids*, 18(3):031703, 2006.

[200] O. B. Usta, J. E. Butler, and A. J. C. Ladd. Transverse migration of a confined polymer driven by an external force. *Physical Review Letters*, 98:098301, 2007.

[201] P. Vasseur and R. G. Cox. The lateral migration of a spherical particle in two-dimensional shear flows. *Journal of Fluid Mechanics*, 78:385–413, 1976.

[202] H. Vink and B. R. Duling. Identification of distinct luminal domains for macromolecules, erythrocytes, and leukocytes within mammalian capillaries. *Circulation Research*, 79:581–589, 1996.

[203] U. H. von Andrian, S. R. Hasslen, R. D. Nelson, S. L. Erlandsen, and E. C. Butcher. A central role for microvillous receptor presentation in leukocyte adhesion under flow. *Cell*, 82:989–999, 1995.

[204] Y. C. Wang and G. W. He. A dynamic coupling model for hybrid atomistic-continuum computations. *Chemical Engineering Science*, 62:3574–3579, 2007.

[205] R. Waugh and E. A. Evans. Thermoelasticity of red blood cell membrane. *Biophysical Journal*, 26(1):115–131, 1979.

[206] S. Weinbaum, J. M. Tarbell, and E. R. Damiano. The structure and function of the endothelial glycocalyx layer. *Annual Review of Biomedical Engineering*, 9:121–167, 2007.

[207] T. Werder, J. H. Walther, and P. Koumoutsakos. Hybrid atomistic-continuum method for the simulation of dense fluid flows. *Journal of Computational Physics*, 205(1):373–390, 2005.

[208] R. J. Wilkinson, J. L. Brown, G. Pasvol, P. L. Chiodini, and R. N. Davidson. Severe falciparum malaria: predicting the effect of exchange transfusion. *Quarterly Journal of Medicine*, 87:553–557, 1994.

[209] S. Yamaguchi, T. Yamakawa, and H. Niimi. Cell-free plasma layer in cerebral microvessels. *Biorheology*, 29:251–260, 1992.

[210] Y. Yawata. Red cell membrane protein band 4.2: phenotypic, genetic and electron microscopic aspects. *Biochimica et Biophysica Acta*, 1204:131–148, 1994.

[211] F. Yilmaz and M. Y. Gundogdu. A critical review on blood flow in large arteries; relevance to blood rheology, viscosity models, and physiologic conditions. *Korea-Australia Rheology Journal*, 20:197–211, 2008.

[212] B. G. Yipp, S. Anand, T. Schollaardt, K. D. Patel, S. Looareesuwan, and M. Ho. Synergism of multiple adhesion molecules in mediating cytoadherence of Plasmodium falciparum-infected erythrocytes to microvascular endothelial cells under flow. *Blood*, 96:2292–2298, 2000.

[213] Y.-Z. Yoon, J. Kotar, G. Yoon, and P. Cicuta. The nonlinear mechanical response of the red blood cell. *Physical Biology*, 5:036007, 2008.

[214] D. V. Zhelev, D. Needham, and R. M. Hochmuth. Role of the membrane cortex in neutrophil deformation in small pipets. *Biophysical Journal*, 67:696–705, 1994.